Experiments on EHD injection, interaction and electrocoalescence of water droplet pairs in oil

You Xia

Communauté
UNIVERSITÉ Grenoble Alpes

THÈSE

Pour obtenir le grade de

DOCTEUR DE LA COMMUNAUTÉ UNIVERSITÉ GRENOBLE ALPES

Spécialité : **Mécanique des fluides, Energétique, Procédés**

Arrêté ministériel : 25 mai 2016

Présentée par **You XIA**

Thèse dirigée par **Jean-Luc REBOUD**

préparée au sein du **Laboratoire G2Elab**

dans **l'École Doctorale I-MEP2**

Experiments on EHD Injection, Interaction and Electrocoalescence of Water Droplet Pairs in Oil

Thèse soutenue publiquement le **18 Juillet 2016**

devant le jury composé de :

Mr Laurent BERQUEZ

Professeur des universités, Université P. Sabatier Toulouse – Rapporteur.

Mr Christophe LOUSTE

Maître de conférences HDR, Université de Poitiers - Rapporteur

Mme Nelly BONIFACI

Chargée de recherche CNRS, G2Elab - Membre

Mr Francis McCLUSKEY

Professeur des universités, Université Grenoble Alpes – Président.

Mr Philippe MOLINIE

Professeur assistant, SUPELEC - Membre

Mr Jean-Luc REBOUD

Professeur des universités, Université Grenoble Alpes – Membre.

Preface

This work was funded by the project “Fundamental understanding of electrocoalescence in heavy crude oils”; co-ordinated by SINTEF Energy Research. The project was supported by The Research Council of Norway, under the contract no: 206976/E30, and by the following industrial partners: Wärtsilä Oil & Gas Systems AS, Petrobras and Statoil ASA.

First I want to express my thanks to SINTEF (the research center of Norway) for enabling such an interesting joint work. I thank Mr Lars Lundgaard for his warm welcome at meeting, and Asmund Ervik for his interesting discussion at G2ELab, Grenoble. I express my gratitude to my supervisor Pr Jean-Luc Reboud for his teaching and patience. He does not only fill me with his scientific knowledge and skills, but also gives me the urge to surpass myself. I also thank Dr Pierre Atten for his guidance through my PhD studies.

Thanks to the jury members of my PhD defense, Pr Laurent Berquez, Pr Christophe Louste, Dr Nelly Bonifaci, Pr Francis McCluskey and Dr Philippe Molinie for their thorough review of my work and for all their encouraging comments and insightful remarks. Especially I am grateful to Pr Francis McCluskey for his help in English corrections of my manuscript.

In addition I thank to all the members of my equip MDE with whom I spent four years for my graduate study. Their kindness and helps accompany me to go through these years, and make me to have more confidence on myself.

Content

Nomenclature

R_{cap} (mm)	Inner radius of used needle tip.
a (mm/s^2)	Drop approach acceleration.
Δe (mm)	Drop pair inter distance between the two facing surfaces.
H (mm)	Height between the needle tip and the upper surface of the electrode below.
D (mm)	Drop diameter.
r (mm)	Drop radius.
$\boldsymbol{U}$ (mm/s)	Drop falling velocity.
V (kV)	Voltage applied on the electrode in the test cell.
V_{low} (kV)	Minimum voltage required to deform water meniscus.
t_{cap} (ms)	Capillary time.
t_{μ} (ms)	Viscous time.
h (mm)	Height of the water meniscus.
t (ms)	Duration of the electric pulses.
V_{min} (kV)	Minimum voltage to begin drop injection.
$V_{0.1mm}$ (kV)	Voltage applied to obtain a drop of 0.1 mm in diameter.
V_{max} (kV)	Maximum voltage for single drop injection.
k (m^{2}V^{-1}s^{-1})	Mobility coefficient.
E (V/m)	Electric field.
j (C/m^2)	Surface charge.
ℓ (m)	Distance between falling drop pair centre to centre.
ε_r	Relative permittivity.
σ (N/m)	Interfacial tension.
μ (Pa.s)	Viscosity.

ρ_o (kg/m^3)	Oil density.
ε_0	Permittivity of vacuum: $\varepsilon_0 = 8.85*10^{-12}$ F/m.
L	Characteristic length (often refers to the diameter of droplet).
$We = \frac{\rho_o U^2 L}{\sigma}$	Weber number.
$Re = \frac{\rho_o U L}{\mu_o}$	Reynolds number.
$Oh = \frac{\mu_o}{\sqrt{\rho_o \sigma L}}$ $Oh = \frac{\sqrt{We}}{Re}$	Ohnesorge number.
$Eo = \frac{\Delta \rho g r^2}{\sigma}$	Eötvös number.
$\varepsilon_c = \frac{\varepsilon_r \varepsilon_0 E^2 r}{\sigma}$	Electrocapillary number.
$\boldsymbol{U}_{Stokes} = \frac{2}{9}\frac{\Delta \rho r^2 \boldsymbol{g}}{\mu}$	Stokes velocity.

Introduction

Though the use of crude oil dates back over a millennium, it has nearly become ubiquitous over the last century. In the petroleum industry, refined products of crude oil are used in many domains, such as the chemical industry, plastics, synthetic fibers, fuel, lubricant… The formation of crude oil varies over a very long time while the consumption rate is fast. Thus worldwide depletion of crude oil comes into question. For an oil field, extraction of crude oil under the earth's crust will reduce the underground pressure to a point that the latter can no longer drive oil through wells. The method of oil extraction by injecting water and gas into oil reservoirs was commonly applied. When the crude oil and co-produced water and gas pass from the wellhead to the manifold, there is generation of oil-in-water or water-in-oil emulsions. Water-cut can sometimes be higher than 80%, greatly increasing the crude oil volume and generating extra transportation cost. Moreover inorganic salts insoluble in oil are removed by washing or desalting the crude oil with relatively fresh water. Even at lower water-cut, water droplets in oil enhance the corrosion of instruments and should be removed before the refinery processes.

A fast rate of separation and a low value of residual water in the crude oil (typically few tenths of percent in weight) are desirable. Since the density of water is larger than that of oil, sedimentation allows the separation of large water drops. However, at low water-cut the emulsified small water droplets are particularly difficult to remove because the settling velocity in viscous oil decreases dramatically. Emulsion separation into oil and water can then be improved by adding chemical demulsifiers, by increasing the temperature of the emulsion to reduce the viscosity, or by increasing the drops size by merging them. This last is enhanced by applying electrostatic fields that promote coalescence and appears as the best way to speed up the demulsification process.

To optimize electrocoalescence with variable crude oil qualities, improvement of the understanding of the dynamics of water-oil interfaces and validation of numerical models is desirable. Consequently,

it is necessary to provide detailed experimental data on the electrocoalescence of very small droplets. Therefore, the aim of the present PhD is to perform experiments on small droplet pairs falling in stagnant model oil under DC and AC electric fields.

The first chapter of the thesis gives an overview of crude oil demulsification process using electrocoalescence. Former drop coalescence studies in laboratory conditions are presented, as drop collision in air in meteorology or coalescence under electric field of different liquid-in-liquid cases. Attention is paid to different parameters influencing the drop coalescence process in gas or liquid medium. Existing numerical studies and experimental investigations are presented.

The second chapter presents actual existing drop injection methods with their advantages and disadvantages. Experimental set-ups for drop injection, including test cell design and measurement devices are also presented. Image processing of visualizations and measurement techniques (with related uncertainties) of physical properties such as temperature, interfacial tension, viscosity and density are discussed. Finally model oil properties are summarized.

The third chapter focuses on the well-controlled generation of very small droplets in the model oils. As proposed by Raisin (2011), droplet-on-demand generation by the electrohydrodynamic (EHD) method is obtained by applying high voltage electric pulses to a pendant water meniscus. This EHD injection method using Multi-Stage Pulses (MSP) is improved for drop injection into new oils. Influencing parameters are taken into account to perform droplet injections in the range of 20-300 micrometers in diameter. It is observed that most of the droplets are not electrically neutral and improvements to the Multi-Stage Pulses are proposed to reduce the droplet electric charge. Use of drop falling velocities is also proposed to characterize the drop size and electric charge, with the related uncertainties.

The fourth chapter illustrates a dual drop injection method from a single needle, for generating axisymmetric configurations of droplet pairs aligned with the electric field and gravity. Influence of hydrodynamic and electrostatic interactions between droplets are taken into account to characterize with accuracy the droplet pair size and charge. For that, the different forces acting on the droplets are presented and simplified models are discussed.

The fifth chapter presents the experimental cases of electrocoalescence of droplet pairs under DC and AC electric fields and summarizes a first data set of 70 different cases. Examples of the analysis of the transient evolution of drop pair spacing and a discussion of some observed phenomena are proposed. Finally improvements are suggested for further experiments.

Chapter 1. Previous studies on droplet coalescence

1.1 Introduction

Droplets coalescence phenomenon appears in liquid – gas or liquid – liquid two phase media, from nature as raindrop generation and falling, to industry use (sprays, emulsions, chemical or biological processes…). The major topic of our work will concern an immiscible liquid – liquid two phase medium, specifically the coalescence of water droplets in oil under electric field. For droplet coalescence to take place, application of forces is involved, both external and internal. Droplet collision or attraction can bring into contact droplet interfaces, which play main roles in merging or bouncing processes. For drop merging processes, the coalescence will appear spontaneously driven by capillary forces of the droplets, under condition that separation forces remain smaller than capillary forces. If any extra force terms disturb this coalescence process, the coalescence will sometimes not be complete and partial coalescence or even no coalescence would appear. In this way, the coalescence efficiency comes onto stage, which can be expressed as the combination of a probability of contact and a ratio of total to partial coalescence.

This chapter presents first the context of crude oil extraction and refinery, where water drop coalescence techniques are used to break down water- in crude oil emulsions. Then an overview of research on liquid droplet coalescence is proposed, from early works on liquid droplets in gas, involved in meteorological studies, to later investigations of droplet coalescence in liquid-liquid medium...

1.2 Water in oil

1.2.1 Crude oil presence in history

Crude oil, also referred to as petroleum, is a brown to black liquid composed mainly of hydrocarbons, located under the Earth's crust. It is originally formed by organic matter which sediments and accumulates through biodegrading transformation, and is then compressed and heated over millions of years (Tissot & Welte 2013).

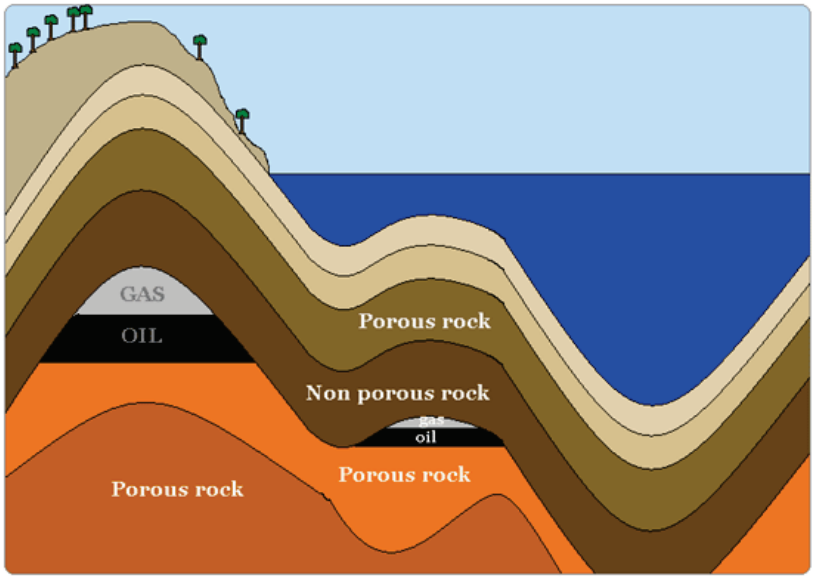

Fig 1.1. Location of crude oil under Earth crust (http://www.green-planet-solar-energy.com/fossil-fuel-formation.html).

The use of crude oil has a long history which dates back to about five to six thousand years before Christ (Simanzhenkov & Idem 2003). In Greece, the crude oil was used as a kind of medicine to heal diseases in fourth to fifth century. Also the well-known 'Greek Fire' which made use of petroleum as a combustible, served as a military weapon in many battles in the seventh century. The Greeks put the mixture of asphalt (another physical form of known petroleum) with other chemical compounds on the end of sticks, and then threw them when lit. According to manuscript of (Herodotus 457AD), the ancient Greek historian, construction of Babylon walls used asphalt which was thrown up by the Euphrates river. In India, a huge pool constructed about five thousand years ago in Mohengo – Daro used a thin Asphalt layer on the pool wall as water resistant material (Simanzhenkov & Idem 2003). With advancement of history, more and more products have been derived from petroleum. Up to now there are many petroleum products such as plastics, ink, motor oils, gasoline and so on. With

this increase of petroleum consumption, depletions of crude oil fields come into question. For oil productions, when the crude oil is extracted from an oil field, it often contains different proportions of water and other chemical or solid species. The water content is brine because it is a solution of salt, and this water content is always highly undesirable. Moreover, during maturation of the oil field the underground pressure is no longer sufficient to drive crude oil flow along producing well, thus gas and water are injected into the oil layer through a separate well, to increase the pressure inside. This process is called oil field recovery and the water injection can increase drastically water content inside crude oil, even to 80 % or 90 % (Raisin 2011). Finally, the high salinity inside crude oil is the major cause of corrosion in equipment. To reduce the salinity dilution water is introduced into oil body to dissolve brine water droplets. This process is called desalting during crude oil refinery (Speight 2014). For such water contents inside crude oil, large water drops can be separated from the oil body by gravity effect. When the water cut is lowered to about 17 wt%, the average drop diameters is from 0.06 to 0.4 mm (Borges et al. 2015). Thus other techniques other than the use of gravity are needed to treat the water emulsions.

When crude oil was first pumped from a well, apart from the hydrocarbon components it contained a quantity of water, chemical compounds such as nitrogen, oxygen, sulfur, and metallic species (Speight 2015). Thus refinery process is needed to treat the crude oil. The first petroleum industry was founded in 1859 (Speight 2014). Since then vast research has been carried out on crude oil refinery, among which one part concerns water emulsion breakup. Chemical method of dehydration in crude oil consists of adding chemical surface active agents which can remove already existing emulsifying agents inside crude oil, neutralize repulsive electrical charge on droplets, prevent small particles such as clays, drilling muds and ion sulfides from staying on the droplet surfaces in order to facilitate small droplets merging into large drops, so as to separate them by gravitational effect (Balson & Britain 2002).

The first attempt to separate water - oil emulsion with the help of electric fields was performed by Cottrell and Speed in 1911. They found that when two electrodes with sufficient applied voltage were immerged in oil medium, the water droplets could form a chain between them. Coalescence between the adjacent drops in the chain could occur and form larger drops which then fell out of the chain under gravity effect, leading to phase separation (Cottrell & Speed 1911). They also invented a separator with electric applications (Cotrell 1911). The method of emulsion separation using electric fields is different than that by chemical agents because the former only uses electric forces to promote coalescence between drops, while the latter focus on the chemical compositions of the oil – water surroundings. (Pearce 1954) observed the chain formation of droplets in crude oil emulsion

under electric fields as illustrated by Fig 1.2 below. In his research the water cut of the oil is 11 % and the diameters of the coalesced drops can be as small as 0.05 mm.

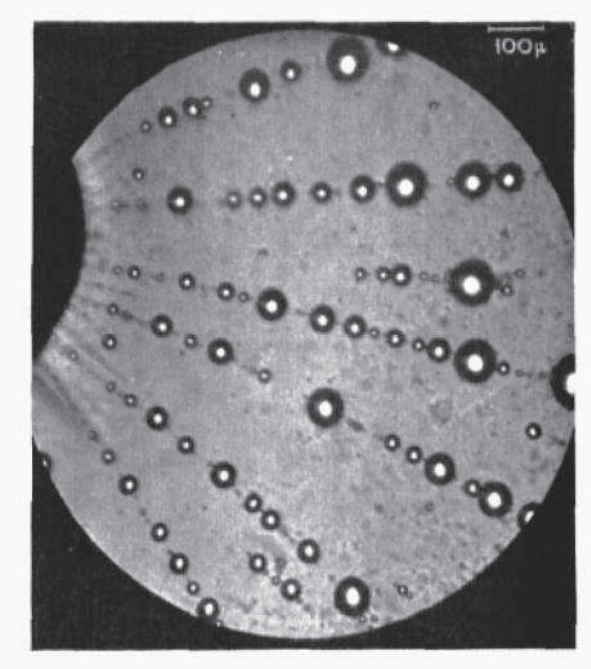

Fig 1.2. Chain formation of water drops in crude oil emulsion between electrodes (Pearce 1954).

Based on this previous research, different influences of DC voltage (Charles & Mason 1960) and pulsed DC voltage (Bailles & Larkai 1981) (Bailes & Stitt 1987) were investigated. The use of AC electric fields to promote the drop coalescence in crude oil emulsion was studied by Taylor and Spenser in 1988 (Taylor & Spenser 1988). They observed conditions where chains of drops form, and other conditions without chain formation, with which drop coalescence appears more efficient. Chemical additives were also studied to break stable emulsions in crude oil (Jones et al. 1978), which lead to research into the combination of electric fields and chemical additives (Dezhi et al. 1999) (Eow et al. 2002). Up to now, available treatments on water emulsion breakdown in crude oil consist of mechanical, thermal, electrostatic, chemical method (Mohammed et al. 1993a; Mohammed et al. 1993b; Mohammed et al. 1994; Chen et al. 1994) or the combinations of the above mentioned methods (Less & Vilagines 2012).

1.2.2 Water emulsion breakup

In the modern petroleum industry, pumped crude oil from an oil field should first go through refinery process to reduce impurities contained inside. These impurities, generally consisting of water, salt, acid gas and other solid contents can cause corrosion, deposition inside the tubes and catalyst poison effects (Fahim et al. 2010). The quantity of impurities may also cause extra transportation cost due to their extra volume when the water-cut in oil reaches more than 50 % (Mhatre et al. 2015) (Silset 2008). When crude oil is extracted from below sea water, foam formation can increase the viscosity of the liquid and cause pollutants (Schramm 1992). Considering all the problems, only a small water-cut of 0.001 % is allowed at the final stage of dehydration (Silset 2008).

The first stage of oil refinery is separation which aims at separating gas, liquid and solid phases inside crude oil body. The separation process is shown on figure below.

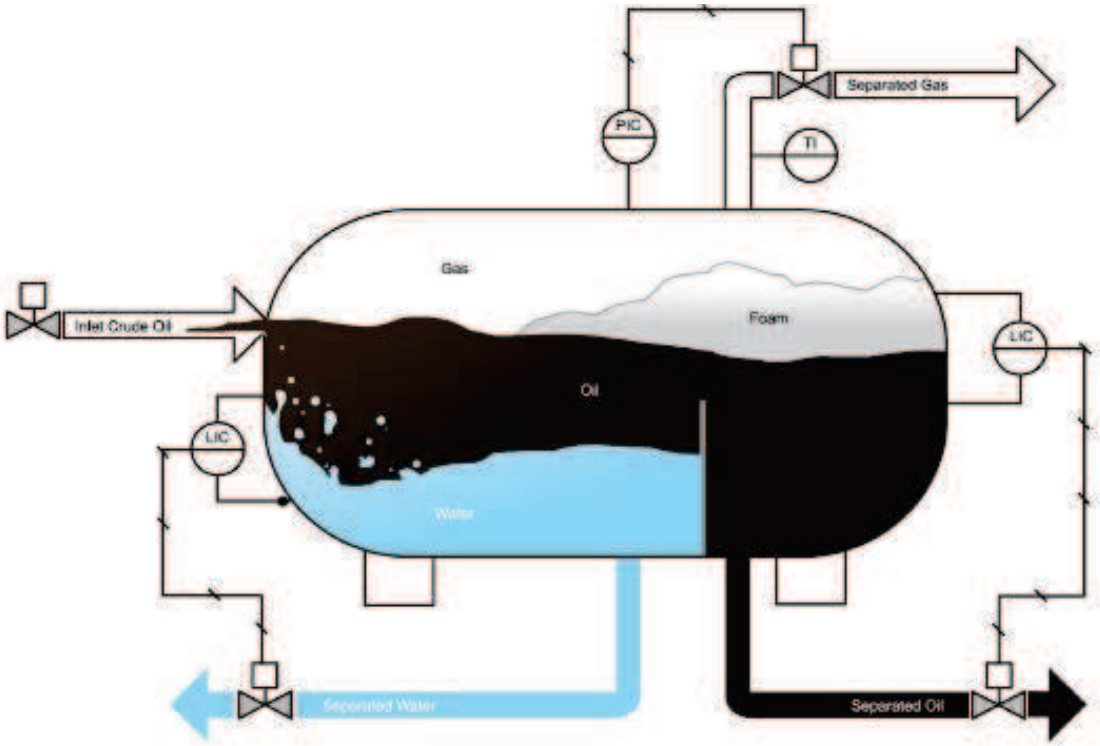

Fig 1.3. Separator of crude oil contents
(http://www.dowcorning.com/content/oilgas/foam-control.aspx?e=Solutions+by+Application).

Fig 1.3 shows a preliminary separation of water (blue), oil (black), gas and foam (clouds like) is achieved with the help of gravitational effect. After this preliminary separation phase, the next step is dehydration which means to remove water droplets emulsion contained in crude oil. This emulsion

is formed at different steps: intense emulsification of water drops in crude oil can be produced both by shear forces which breakup large water drops into smaller ones during oil flow inside tubes (Thompson et al. 1985), and through pressure release valves from the well to the production manifold (Less et al. 2010); also during crude oil refinery, desalting process requires fresh water injection to dissolve salt content. (Manning et al. 1995). To remove this stable water in oil emulsion, the dehydration method is very important. Fine water droplets formed stable emulsion inside crude oil is very difficult to be broken down, and the typical size of the droplets is less than 50 µm in diameter (Atten 1993; Less & Vilagines 2012). The gravitational effect for water – oil phase separation is no longer efficient because, according to Stokes law, the sedimentation speed of water droplets is proportional to the square of the drop diameter, and the finest droplets determine the residence time of the emulsion in the separator (Less & Vilagines 2012; Hellesø et al. 2015). Thus increasing droplet sizes by merging them are priority to accelerate drop sedimentation speed. As oil is a non-conductive medium, the conducting water drops subjected to an electric field are polarized, and the polarity effect of neighboring droplets will drive them to merge together. This merging process under electric fields is called electrocoalescence. As drops merge together, their mass increases and gravitational effect can easily cause them to sediment down.

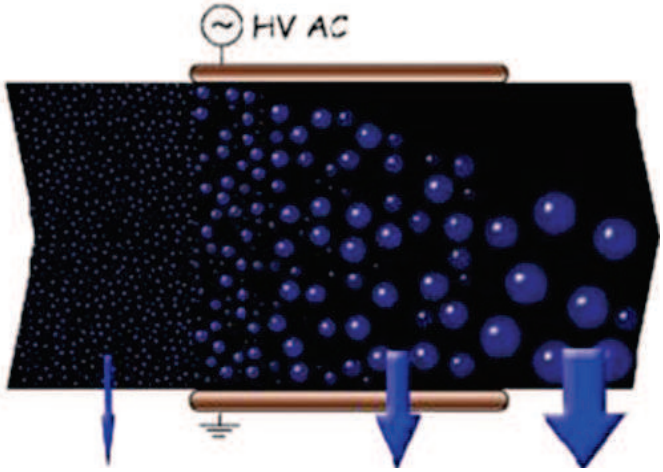

Fig 1.4. Merging droplets increases the settling velocity in crude oil
(https://www.sintef.no/en/projects/compact-separation-by-electrocoalescence-/).

Fig 1.4 shows a global view of electrocoalescence occurring in crude oil medium during dehydration process. In petroleum industry, high electric fields are applied onto the flowing crude oil emulsion to make the dispersed water drops coalesce in order to separate them from bulk phase (Eow et al. 2001).

1.2.3 Interaction of two drops in electric field

For most of the research on drop coalescence, the studies have been focused on the interaction of two drops because in chain formation under electric fields in crude oil, it was found that the coalescence occurred between drop pairs instead of several drops (Galvin 1986). The smaller the distance between the drops was, the faster the coalescence took place. To simulate real crude oil environment, drops sizes should be chosen in the micrometer to tens of micrometer ranges in model oil. The choices of the latter are either oil with good stability in the face of oxidations, or crude oils. Oils exhibit a low conductivity with compared to water. When an outer electric field is applied, the electric force will favor and accelerate coalescence process. When two electrically neutral drops in close vicinity are under electric fields, an induced charge will appear on the surface of the two drops with different polarities (Davis 1964). For this case, more descriptive model is given in (Pedersen et al. 2004).

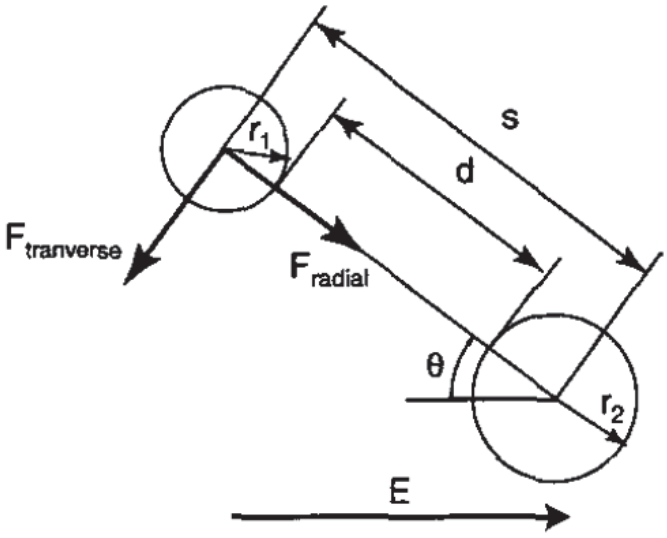

Fig 1.5. Scheme of uneven pair of conductive drops in an insulating medium in a uniform electric field E (Pedersen et al. 2004).

Fig 1.5 shows the diagram of an uneven pair of water drops in an insulating oil medium under a uniform electric field E. The two drops can be simulated as a dipole – dipole configuration and forces acting on the two drops are transversal and radial which are presented as $F_{transverse}$ and F_{radial} on the figure respectively. The r_1 and r_2 are the radius of the two drops with given separated distance d for

polar surface – polar surface and s for center – center. The angle between the center line and the electric field direction is θ.

1.3 First drop coalescence research in gas medium

1.3.1 Colliding drop pair

Drop coalescence studies are not recent, especially in clouds physics. The coalescence is often referred to as merging of two colliding drops into a larger one. The first water drop coalescence phenomena were observed in air. The fact that a liquid body can either coalesce or bounce on another liquid body was observed by Rayleigh in using two fine liquid jets in 1880. He concluded that the scattering of fine jets was caused by the capillary forces which acted on each droplets, and that the force was so high that it made droplets bounce off each other when they collided (Rayleigh 1882).

For drop colliding model in air medium it is the competition between the surface tension which tends to conserve the drop shape, and the kinetic energy which can merge or even split the drop after coalescence. Drop colliding model was first widely used in interest of meteorological studies and droplets were set to collide in atmosphere air condition. Early research on drop coalescence was simulated by numerical method and it was found that collisions between small droplets inside clouds could give a wider range of droplet productions than that issued only from condensation procedures (Mordy 1959). Some years later raindrop size distributions after coalescences were simulated by confining drop concentrations with their initial sizes in a discrete volume (Srivastava 1967). Early experiment of (Adam et al. 1968) used droplets of 60 µm — 500 µm in sizes with 10^{-15}C—10^{-12}C variable electric charges. Some of these droplets were driven by electric field from their trajectories to collide in a normal gravitational zone. By varying velocities of the droplets, different collision behaviors are observed. They reported that when the velocity was less than 2.2m/s, permanent coalescence would occur, when velocity surpassed this value, drop splitting after coalescence would happen constantly. During their experiments, charges on droplets within this impact parameter range did not affect either collision or coalescence process.

Later followed experiments of (Brazier-Smith et al. 1972) in which uneven drop pairs of $r_1 > r_2$ were used with radius varied from 150 µm to 750 µm, to collide in air. They aimed at studying the critical

condition under which the coalescence drop broke up into fragments. x was defined as the perpendicular distance from the center of one drop to the undeflected trajectory of another drop.

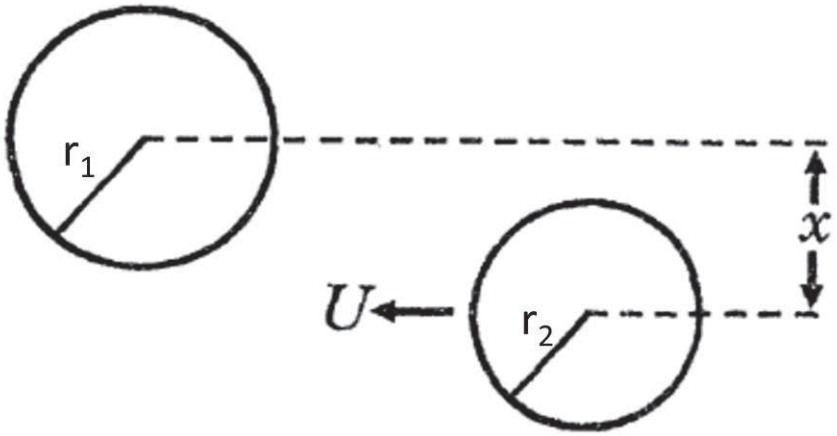

Fig 1.6. Parameters of falling drops pair (Brazier-Smith et al. 1972).

On Fig 1.6 the parameter x is showed between the two drops, and U is the relative velocity of the small drop with radii r_2 to the big drop with radii r_1. Then x is in the range of 0 to $\pm(r_1+r_2)$. x_c is defined as the critical value of x below which the two drops undergo permanent coalescence while above which the coalesced drop will further split. The coalescence efficiency is defined.

$$\in = \left(\frac{x_c}{r_1 + r_2}\right)^2 \tag{1.1}$$

In simulations done by (Martin et al. 1981), it was proved that electric charges on colliding particles could enhance collision efficiencies. The model depicted critical trajectories of charged water drops of 0.02 mm – 0.17 mm in diameters which collided with charged ice crystal plates of 0.1 mm – 1.3 mm in sizes. In 1982 another paper came out with more detailed experiments to explain raindrop formation (Low & List 1982). In their experiments, drop sizes were uneven and the smaller drops were blown to the path of the larger one by compressed air, to perform drop collisions. They had analyzed in detail drop geometric deformations when drops collided in their free fall paths. It was concluded that for a high energy collision, a disk shape deformation of the colliding drop could favor coalescence because this deformation dissipated most of the impact energy of the system. If the colliding energy was much higher, splitting of the coalesced drop could occur. When a low energy collision took place, only an induced wave could travel from bottom to top. The above phenomenon

demonstrated the influence of interfacial dynamics with a scale smaller than the whole drop diameter.

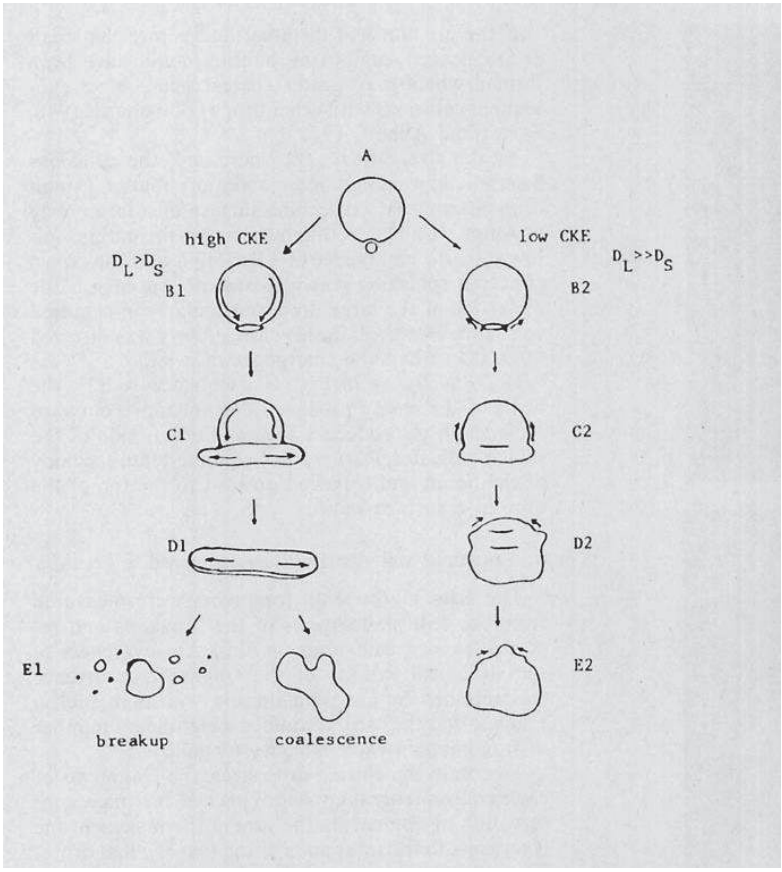

Fig1.7. Scheme of droplet collisions. Left: high energy collision; right: low energy collision. The diameter of the large drop D_L varies from 0.18 cm to 0.46 cm while that of the small drop D_S varies from 0.0395 cm to 0.18 cm. On this figure $D_L >> D_S$ (Low & List 1982).

Fig 1.7 shows drop collisions with different values of the drop kinematic energy. The diagram on the left presented drop collisions with higher kinematic energy, and the out coming result was either coalescence of drops, or splitting of the drop. The diagram on the right described the collisions with lower energy, and generally coalescence took place.

Drop-on-collision in gas is not only used for meteorological study, it is also expanded in other domains. Later another study in hydrocarbon droplet collision appeared with head-on and off-center cases (Jiang et al. 1992). They observed that the phenomenon was different to water droplets collisions. With increasing energy, they had successively permanent coalescence, bouncing, permanent coalescence during which a dimpled disc shape of drop appeared, and droplet splitting,

because high collision energy exceeded surface energy which served to keep the drop in its spherical shape.

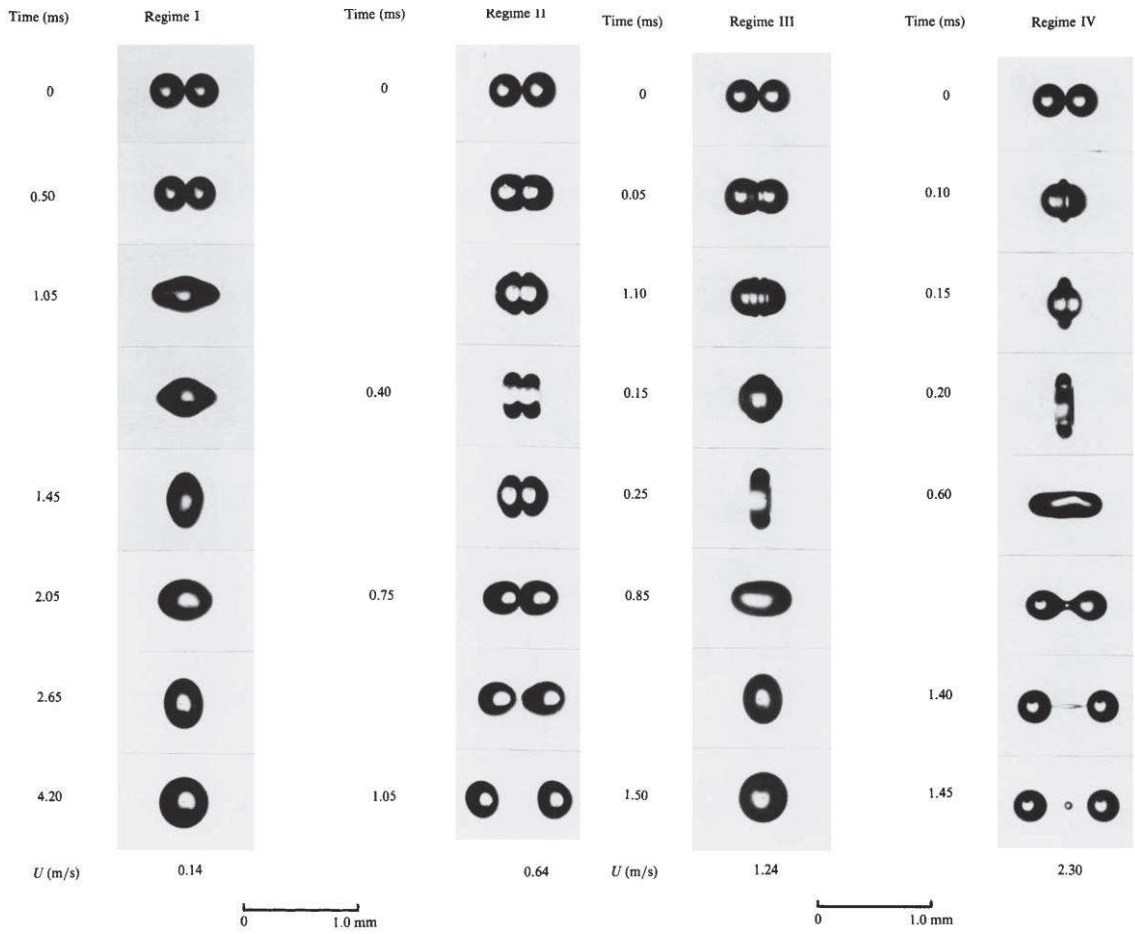

Fig 1.8. From left column to right collision energy increases. The drop diameters are of about 0.35 mm (Jiang et al. 1992).

Also they discussed the phenomenon as a function of Weber number (We) defined below (Jiang et al. 1992).

$$We = \frac{\rho(r_1 + r_2)U^2}{\sigma} \tag{1.2}$$

Here ρ is the liquid density, r_1 and r_2 are the radii of the two colliding drops, U is the relative velocity, σ is the surface tension. In low Weber regimes, permanent coalescence occurred.

Generally in gas for drop coalescence, partial coalescence, bouncing and disintegration, it is the inertia and Weber number which determine the drop behaviors. For drop splitting, viscous

dissipation plays a role and the behavior can be related to Ohnesorge number comparing the viscosity and surface tension effects. A further improvement in the drop collision model was done by (Klimin et al. 1994) and, in their simulations collision efficiencies were calculated for charged drops in an external electric field. Some year's later further investigation was provided on this study. (Qian & Law 1997) enlarged the collision conditions in experiments for both water and hydrocarbon droplets in environments of different gases such as air, nitrogen, helium and ethylene. By varying gas densities via pressure and molecular weight, droplet collisions exhibited different behaviors. It was found that high gas pressure favored drop bouncing, similar to gas viscosity. This was because the air layer trapped between the facing two drops was difficult to be broken up to let contact of two drop surfaces.

More recently, drop collisions in air medium of four drop behavior regimes were simulated and discussed: drop bouncing, coalescence, reflexive separation and stretching separation (Pan & Suga 2005). For the stretching separation case more articles were focused on it. This splitting of merged drops after their collisions was further investigated by (Ko et al. 2007) in simulations and (Brenn & Kolobaric 2006) in both simulations and experiments. The former simulation model was based on mass, momentum and energy conservations before and after drop collisions. In addition energy dissipation which consisted of stretching and reflexive separation regimes in drop bouncing model was added. The simulation model showed the correct number of satellite drops with respect to experimental data. The latter experiments combined with simulations used two streams of monodisperse drops of various liquids and the measurements were done on drop sizes, velocities, dimensions of ligaments and sizes of formed satellites. For the diagram of drop behaviors after collisions, coalescence, bouncing, stretching separation and reflexive separation were studied by (Gotaas, Havelka, Jakobsen & Svendsen 2007) in both experiments and numerical modelling. They defined parameter X as the drops relative position.

$$X = \frac{x}{r_1 + r_2} \tag{1.3}$$

Here the x is defined the same as on Fig 1.6, and r_1 and r_2 are drop radii. The results of collisions were presented as a function of Weber number and initial relative drop positions.

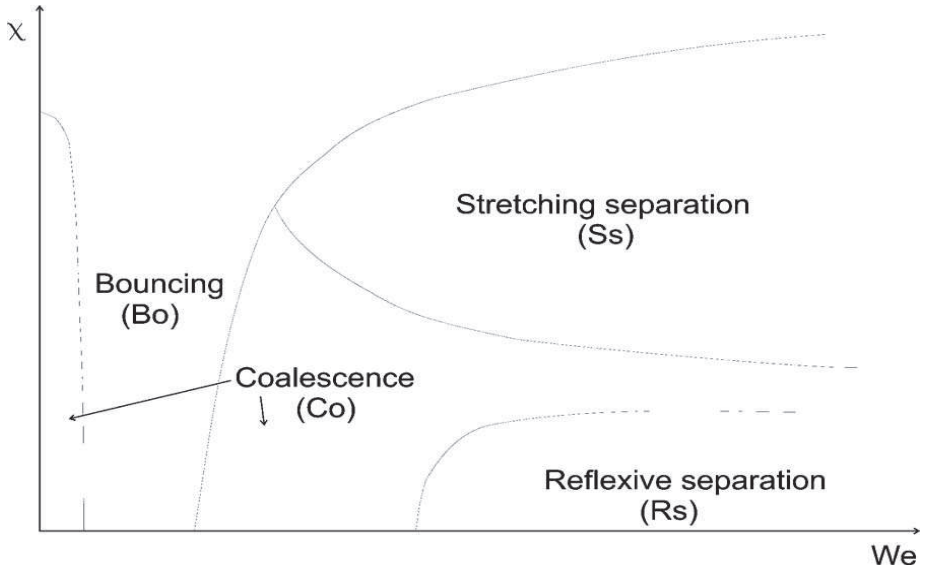

Fig 1.9. A typical collision map for droplet-droplet collisions with respect to Weber number and drops relative position *X*. (Gotaas et al 2007).

The same authors also studied the viscosity effect in drop collisions (Gotaas et al. 2007) and it was found that the borders of the coalescence area were shifted towards high Weber numbers for viscous drop collisions. It was concluded that this shift was due to the dissipation of kinetic energy inside the coalesced high viscous drop. When a portion of kinetic energy is dissipated inside merged drop, the available energy for drop separation is decreased. Thus the separation is expected for higher drop incoming velocities, which are at higher Weber number. Water drop collisions from 0.22 mm to 0.45 mm in diameters were studied by (Rabe et al. 2010) in a spray system. They show that the results obtained for unequal droplet sizes match on a single map, defining the regions of coalescence, reflection and stretching with respect to a new symmetric Weber number taking into account the sum of drop incoming kinetic energy and the sum of surface energy. Head-on collisions of unequal size drops were investigated for both hydrocarbon and water drops, and the relation between Weber number and size ratios were discussed (Tang et al. 2012).

In recent research in cloud physics, coalescence could occur between two colliding drops in air and the efficiency remained high for electrically charged drops (Mölders & Kramm 2014). With small impact energy of two drops in contact, coalescence will occur completely. However increasing impact energy can cause a flattening phenomenon of collided drops. To some extent this high impact energy can split the merged drop because the surface tension of the drop is no longer sufficient to hold the drop. In this way terms of partial coalescence and coalescence efficiency come into use.

Collision and coalescence of two electrically charged drops was simulated very recently (Ghazian et al. 2014). The simulations consisted of two drops with diameters of 0.1 – 0.5 mm colliding in air medium. The boundaries were found by level-set method and the flow was simulated as axisymmetric, incompressible and laminar flow, coupled with electric fields and charge on the interfaces. Also the surface tension of drops was considered as an important parameter. The maximum electric charge that could be carried by a single drop was calculated via the Rayleigh limit, q_{Ray}, under which the drop was not disintegrated:

$$q_{Ray} = 8\pi\sqrt{\varepsilon_0 \sigma r^3} \tag{1.4}$$

Here the ε_0 was the vacuum permittivity, r was the drop radius and σ was the interfacial tension. Results of simulations allow drawing maps of attraction or repulsion of two droplets carrying charges of the same polarity, with respect to the difference of their charge magnitude, or with respect to the head-on collision velocity.

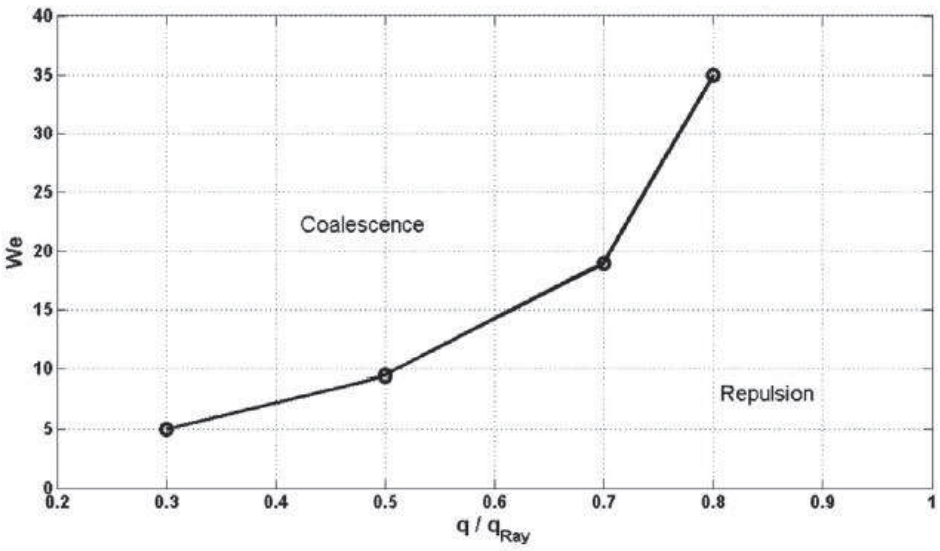

Fig 1.10. Coalescence of two identical drops increased with Weber number with given charge (Ghazian et al. 2014).

With fixed charges in drops, collisions of drops would lead to coalescence with increasing Weber number. Unequal drops could favor the coalescence process because of loss of symmetry in the system. Sometimes, with high kinematic energy, daughter droplets would be produced after coalescence. This model discussed in detail the influence of electric charge contained in pair colliding drops.

1.3.2 Drop interaction with a plane surface

For drop coalescence experiments in air, another configuration is of one drop falling onto a plane surface of the same liquid. This time the kinetic energy is not involved, instead that the Eötvös number which is the ratio of gravity over surface tension, plays a role. The first discovery of spreading liquid drops on the same surface was done by (Mahajan & Katalinie 1931). Later experiments of liquid drop resting on a liquid surface were investigated by varying the two liquid body media (Hazlehurst & Neville 1937). It was said that there existed two kinds of drop formation on another liquid plane: one is of primary drop resting on a planar surface and the other is of splashing from the drop merged with the surface which produces a secondary drop. For the first case, it was found that it took more time for the same or alike liquid bodies to merge, than other body media of very different properties. For the second case some studies were investigated more in details recently by allowing one water drop to fall onto another liquid pool (Manzello & Yang 2002). In the experiments water kinetic energy was involved and the dynamics of splashing after water-planar surface coalescence was studied. The same experiments were done later by adding different pool depth for drop splashing dynamics (Fedorchenko & Wang 2004).

Recent studies involve the notion of thin film formation between two liquid bodies when they are supposed to merge. This thin film layer can either be an air layer or a liquid layer, which plays a crucial role in drop coalescence behavior. When a water drop was initially gently placed on another liquid surface, the air film was not penetrated immediately (Vandewalle et al. 2006). Then by vibrating the liquid surface the air film could be sustained and the drop would rest on the liquid surface for a long time. Another experiment was for droplet bouncing on a high viscosity thin layer inclined surface, it was discussed more in details on the air film surviving which prevented droplets to merge into liquid layer, and the incident normal Weber number (Gilet & Bush 2012). It was said while normal Weber number We was between 2 and 15, droplets would partially immerge with the thin liquid layer and reproduce secondary droplets. When We was smaller than 2, air layer would not be broken and droplets would bounce. When We was larger than 15, the air layer would be broken and droplets would merge entirely with the liquid layer. Thus the air layer between the two liquid facing surfaces dominated the coalescence process.

1.4 Drops coalescence in liquid medium

1.4.1 Shear flow configuration

When two drops are in liquid medium, shear flow can bring them together and the stress can overcome the film drainage force and surface tension to make the drops coalesce. In some other cases the shear stress is so large that it can split the whole drop (Erik Teigen et al. 2011). The latter case is not the case that will be discussed in this thesis. (Howarth 1964) proposed that in a shear flow, the drag force induced by the shear stress was a crucial factor for coalescence, more important than the attraction between the two colliding interfaces which was weak at molecular level. Following their theories, many experiments for droplet coalescence processes have been investigated and they all confirmed the theories above, and provided more details of this coalescence phenomenon. In shear flow the effects of confinement on drop coalescence were tested in experiments (Chen et al. 2009), and it was found that high confinement promoted drop coalescence. In their experiments two water drops of 0.1 – 0.3 mm in diameters, were released into a channel with a certain distance of separation. This channel was filled up with polydimethylsiloxane oil, and between the two plates the shear rate was constant. The confinement was defined as the ratio of the drop diameter to the height of the flux channel. It was found that under low confinement of which $2R/H < 0.085$, the walls had little or no influence. When confinement increased, it promoted drop coalescences. Simulations of the same configuration were first taken by (Shardt et al. 2013), in which they used the lattice Boltzmann method to perform low speed droplet collisions. In their simulations, the fluid was simulated as incompressible flow and both chemical potential and capillary tensions on drop surfaces were considered. The phase field and the molecular collisions were taken into account. For the results, they reported cases of total coalescence and no coalescence of the drops. A critical capillary number was determined, depending on which drop coalescence is observed or not. The capillary number (Ca) is defined below, taking into account the shear stress, the viscous force and the interfacial force.

$$Ca = \frac{\mu \dot{\gamma} R}{\sigma} \tag{1.5}$$

Here μ is the viscosity, R is the radius of the drop, σ is the interfacial tension and $\dot{\gamma}$ is shear flow rate. Thus if the capillary number of the system was lower than a critical capillary number, coalescence of the two drops would occur; if the capillary number was higher than a critical capillary number, no coalescence would take place.

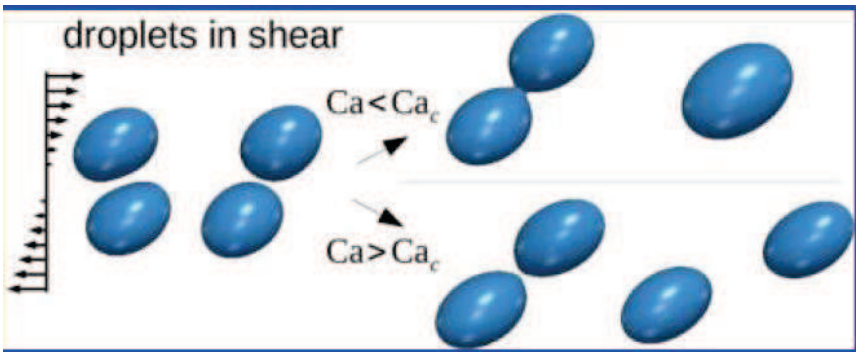

Fig1.11. Droplet coalescences in a shear flow influenced by capillary number (Shardt et al. 2013).

It should be added here that according to (Shardt et al. 2013), another important parameter which influenced the capillary number was interface diffusivity which is related to the chemical potential of the droplet interface. If two contact droplets with a higher diffusivity of their interface meet, the separating film would rupture more easily, leading to interface contact and then coalescence of the drops.

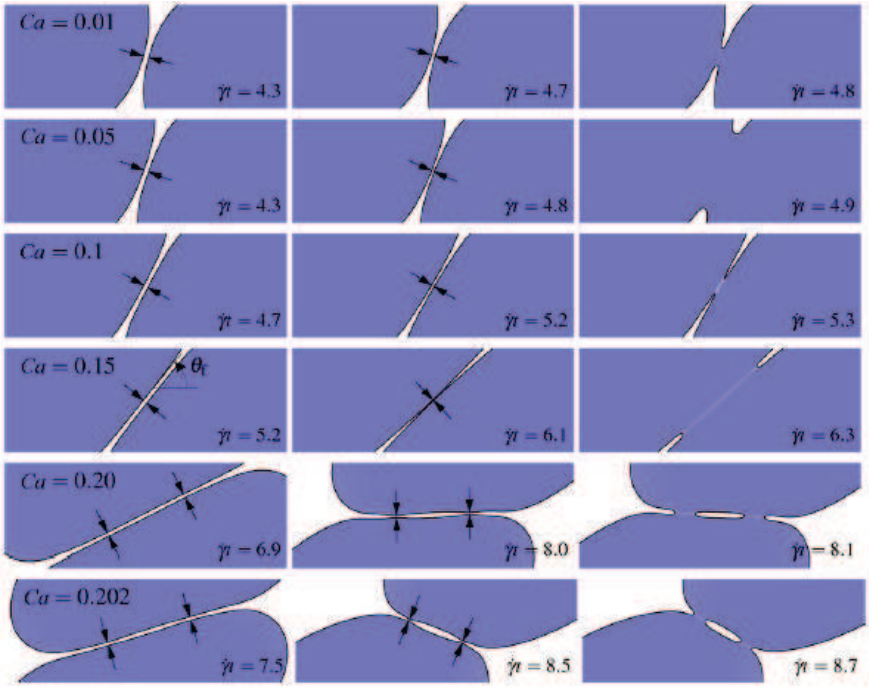

Fig 1.12. Simulations of drop contacting interfaces with different capillary number and approaching durations (Shardt et al. 2014).

Furthermore the same author studied critical conditions of drop coalescences in shear flow (Shardt et al. 2014). In their simulations, the lattice Boltzmann method was adopted, and the chemical potential separated two phases. Simulated drops had the same density and viscosity as the outer

fluid and Reynolds number was fixed to be 1. Under these simulation conditions, the figure above showed drop contacting interface behaviors during the drop coalescence process. The film–thinning time and locations varied with capillary number.

1.4.2 Drop interaction with a plane surface and partial coalescence

For drop coalescence with a liquid surface merging into another immiscible liquid medium, the initial kinetic energy of the falling drop is small and the affecting parameters are gravity, surface tension, viscosity. All the parameters mentioned above can be combined in forms of Eötvös number and Ohnesorge number. The film drainage process is always presented during the approach of the drop to the liquid plan. When external electric fields are applied, an extra parameter, the electric Bond number (B_e), should be added. First experiments were done by (Charles & Mason 1960), and in their experiments the notion of partial coalescence was investigated.

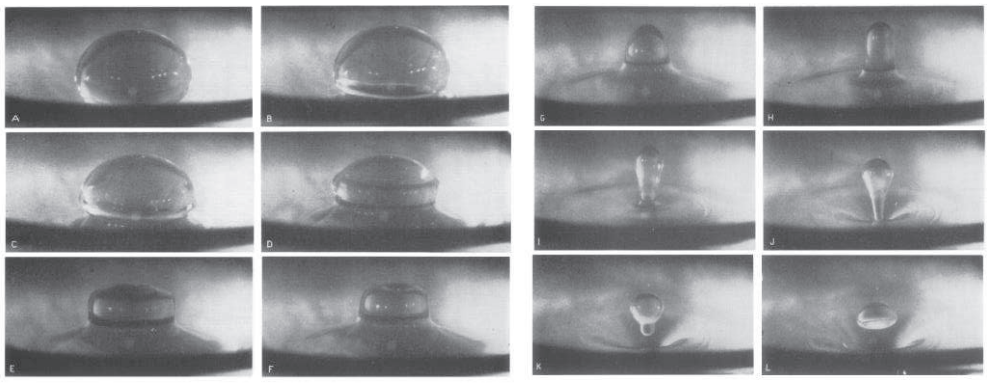

Fig1.13. Illustration of partial coalescence of liquid drop-face bulk in another liquid medium (Charles & Mason 1960).

When a liquid drop is resting on a plane surface of the same liquid and plunged in another immiscible liquid, a thin film layer is formed between the drop and the plane surface. This film layer is further thinned under the gravity effect of the resting drop, until a critical value above which the layer is drilled out and a liquid column is formed connecting the drop and the bulk phase. At the beginning of this column formation, a bulge may be formed and propagate. Under this effect the column may be

broken, forming a satellite droplet. This phenomenon is called partial coalescence. Sometimes the bulge can give multiple satellites formations during the column breaking.

More recently (Aryafar & Kavehpour 2006) studied the partial coalescence process as a function of Ohnesorge number for the same experimental configuration. $Oh=\mu/(R\rho\sigma_{12})^{0.5}$, where R is the radius of the falling drop, μ is the viscosity, ρ is the density of the liquid, σ_{12} is the interfacial tension between the two liquids. In addition, the drop ratio of partial coalescence decreased when Oh approached to 1 and a secondary drop disappeared when Oh was equal to or higher than 1. For one drop falling on another big drop inside crude oil under electric fields, experiments were then compared to numerical simulations to understand the effect of different oil viscosities (Chiesa et al. 2006). Zooming in on coalescence process, drop surface rupture mechanisms were discussed: according to (Priest et al. 2006), the coalescence was caused by surface dynamic instabilities induced by electric field. The used drop diameters were of 0.2 mm and the placement of drops was very narrow.

Later it was again reported that the whole process of this mechanism was driven by the competition of electric strength and surface tension. If the electric strength was weaker than surface tension, drop coalescence could occur; otherwise the drops may retreat after their contact (Jung & Kang 2009). In other experiments done by (Aryafar & Kavehpour 2009) an external constant DC electric field was applied. It was reported that in the high Ohnesorge number region, partial coalescence would occur under DC electric fields while it should otherwise have been suppressed without electric fields. In addition, non-coalescence of an oppositely charged drop with the bulk phase was found above a critical electric fields (Ristenpart et al. 2009) and it was concluded that this non coalescence was caused by fast charge transfer between the drop and the bulk phase, which resulted in same electric potential for the two bodies.

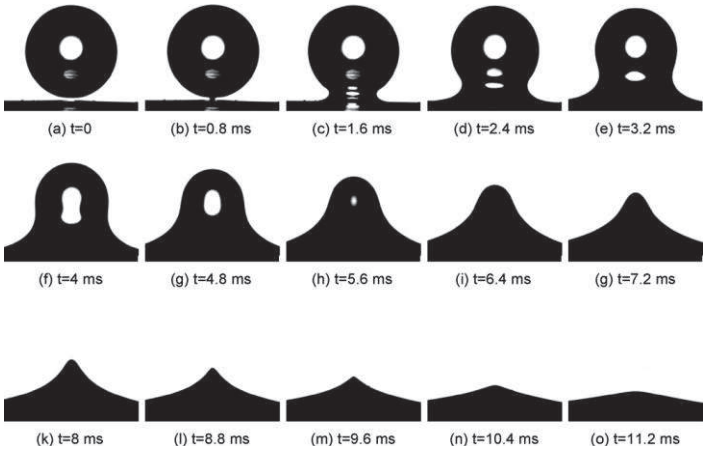

Fig 1.14. Complete coalescence of distilled water drop falling onto a stationary one in sunflower oil medium under electric fields of 56V/mm (Mousavichoubeh et al. 2011).

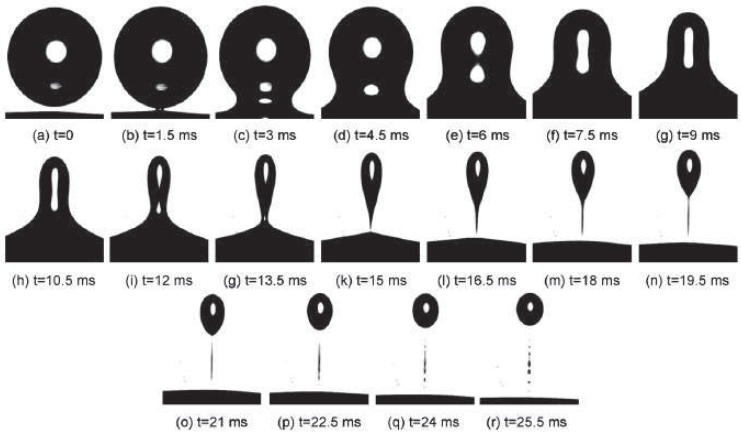

Fig 1.15. Partial coalescence of water drop in oil under electric fields 181V/mm (Mousavichoubeh et al. 2011).

The same experiments were later repeated by (Mousavichoubeh et al. 2011) in which higher electric fields were used. The drops used were of de-ionized water in diameter range of about 576 µm – 1196 µm and the surrounding medium was sunflower oil. They said that the electric fields could increase the film rupture process and when a liquid column was formed between the two contacting drops, the electric fields would detach the draining drop while capillary surface tension tended to pull the drop into the bulk phase and enlarge the column. Thus, competition between capillary force and electric fields took place. If the capillary force exceeded the electric force, the drop would be pumped into the bulk phase. However, if the electric force was higher, the primary drop would not be drained completely and the column became narrower until its breakdown. Thus a secondary drop was formed, training satellites formation through its trail as the breakup of the neck occurred. The same phenomena were also found in other experiments even with oppositely charged drops (Hamlin et al. 2012). When the same experiments were done in crude oil environment, different coalescence behavior was exhibited. There were two series of experiments investigated, one at 40^{o}C and another at 60^{o}C (Hellesø et al. 2015). They found that without electric fields, no coalescence was observed. Under low electric field intensity, coalescence of a falling drop with a stationary one was enhanced. Increasing electric fields would then stop coalescence in experiments at 40^{o}C while it had no effect on the experimental series at 60^{o}C. Under rather high electric fields, a mist of fine charged droplets were injected from the stationary drop at the near contact point, instead of expected coalescence. Further suppression of this secondary drop by pulsatile electric fields was studies by (Mousavi et al. 2014).

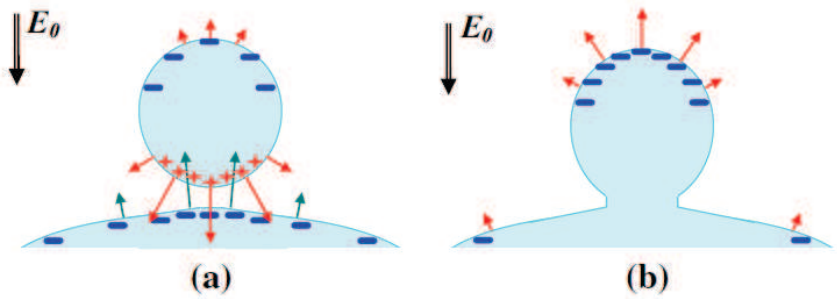

Fig 1.16. Diagram of partial drop coalescence in liquid medium (Hellesø et al. 2015).

If drop coalescence processes are subjected to electric fields, drops can go from total coalescence to partial coalescence or even non coalescence according to electric field strengths (Hellesø et al. 2015). This partial coalescence or non-coalescence is driven by electric force, completely different from the theory of bouncing drops in an air medium. Under electric fields, when the interfaces break down between the two facing drops, a fast electric charges transfer can occur and thus the drop and the bulk body are of the same potential. At this moment a repulsive force tends to extract the drop from the bulk phase, then a secondary drop formed (Hellesø et al. 2015). Fig 1.16 shows an example of partial coalescence occurring between a falling drop and a bulk phase in liquid medium. Electric charge distributions on the two bodies are drawn explicitly. The diagram (a) showed the distribution of electric charges before drop contact to each other. The diagram (b) showed that after a fast transfer of the electric charges, the whole body was in the same potential and at this time the electric force tended to separate the drop from the bulk phase.

The influence of water quality is discussed in (Dong et al. 2002). It is showed that addition of NaCl into water phase can decrease significantly the drops coalescence time, compared to identical configurations with non-ionic aqueous drops. The drop diameters varied from 1.6 mm to 1.9 mm. Five series of experiments were done with different additives (HCl, NaCl, NaOH) which serve to form the drop and plan liquid bulk.

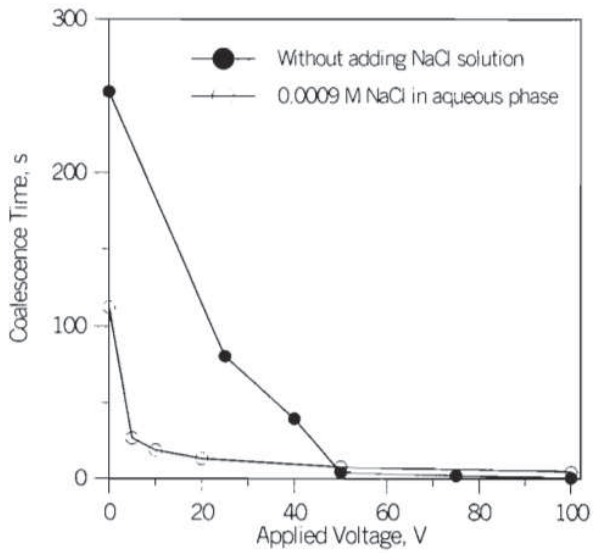

Fig 1.17. Significant decreasing coalescence time by ionization in aqueous drop phase (Dong et al. 2002).

Fig 1.17 shows the drop coalescence trend under electric fields. The ionic drops coalesce much faster than non-ionic drops under the same electric voltage. Moreover it was confirmed about ten years later that in water-oil emulsion, sufficiently high salinity content would favor drop coalescence process (Moradi et al. 2011).

1.4.3 Drop pair coalescence

For drops pair coalescence in liquid medium experiments, in an axisymmetric system, the influencing parameters are gravity, viscosity and surface tension. If external electric fields are applied, an extra factor of electric force is added. For 3D system, where the falling drop direction is perpendicular to the electric field, the influencing parameters are the same as in the axisymmetric system, and one difference is that no gravity factor influences the electrocoalescence process. Film drainage phenomena are present in both cases. For two drop coalescence in an immiscible liquid medium, experiments were done first by (Sartor 1954). In its experiments, two drops with sizes of 0.005 – 0.05 mm diameter were first produced and then fell under a DC electric field.

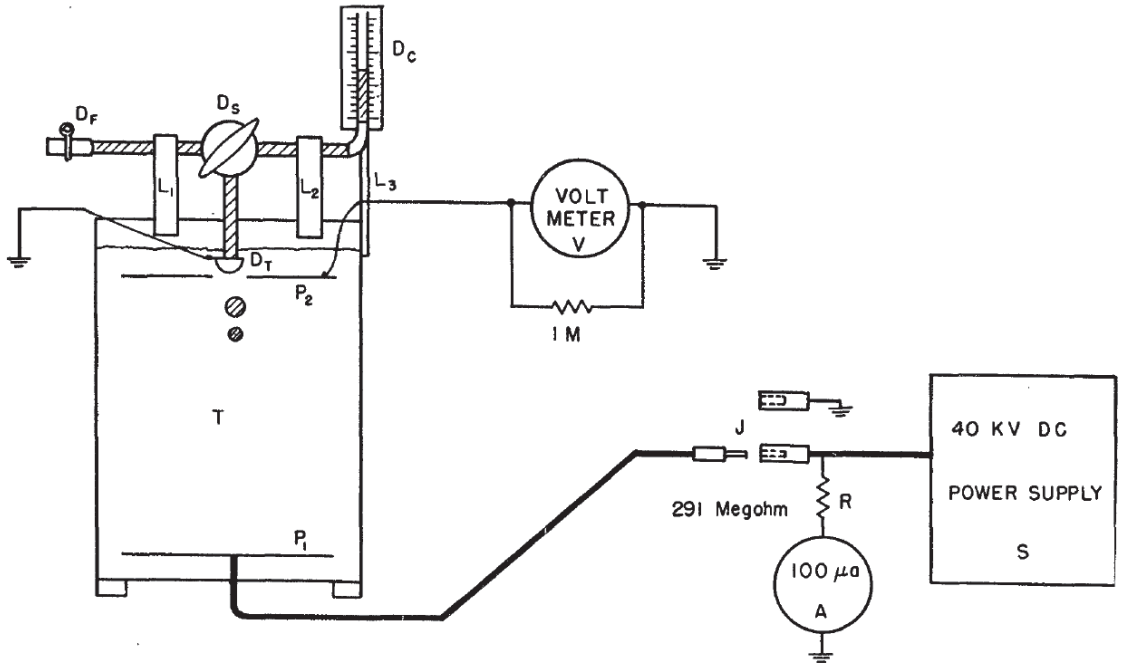

Fig 1.18. Diagram of drop coalescence apparatus (Sartor 1954).

The test cell was made of Plexiglas, 47 cm in height and 30.5 cm^2 of base, and was fulfilled with mineral oil of 0.878 g/ml density. The drops were made of distilled water and the size of the produced drops was controlled by a 'stop cock' which began or stopped the formation of drops at the tip of a capillary tube. The consumed water volume could be read on the capillary tube. The drops pair collision occurred in axisymmetric configuration. It was found that drop coalescence was dominated by the strength of the applied electric field. Earliest experiments for interactions of phase bodies in another liquid medium took place around 1960, where a useful theory of film thinning came about (Shinnar & Church 1960). It was said that when two bubbles came together, a liquid film would prevent the contact of their facing surfaces. Thus the coalescence of the two bubbles took place only if the film layer between them could drain out. Studies on two charged conducting spheres in a uniform electric field were investigated and electrostatic forces acting on the two close facing spheres were calculated accurately (Davis 1964). Later, collision efficiencies between a drop pair falling under gravity in a viscous and incompressible flow field (described using the complete nonlinear and time dependent Navier – Stokes equations), were studied by (Shafrir & Gal-Chen 1971).

For drop coalescence without electric fields, approaching time of two close drops was calculated and presented in (Chesters 1991) (Abid & Chesters 1994) (Chesters 1975) for different cases. For drops of relatively small size (d < 1mm) with a large distance between them, different models were applied:

rigid spheres; deformable particles with immobile interface; deformable particles with partial mobile surfaces and with fully mobile surfaces.

This drop pair coalescence research is picked up in the 21th century first by (Lundgaard et al. 2002) for research into crude oil emulsions. Later studies on the effects of external electric fields and electrode geometry during electrocoalescence of a drops pair have been investigated (Eow & Ghadiri 2003). The viscosity effect of the surrounding medium on the coalescence process was discussed (Chiesa et al. 2006; Chiesa et al. 2005; Pedersen 2008).

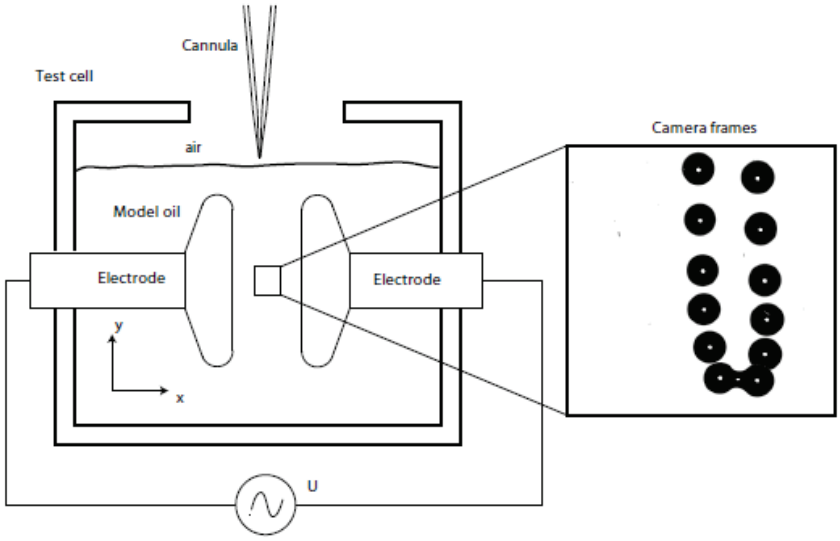

Fig 1.19. Two falling water drops inside synthetic oil under electric fields (Pedersen 2008).

Fig 1.19 shows experiments done by injecting a pair of water drops falling side-by-side into synthetic oil Nytro 10X under electric fields. The two water drops moved towards each other and coalesced under electric fields. It was found that when the two drops were more than one radius apart, the system could be modelled using a dipole approximation. When the distance was less than one drop radius, the film thinning effect was added and the dipole approximation was no more valid.

Drop coalescence processes in liquid medium are different from that in air because of the influence of momentum and the dynamic viscosity of the surrounding fluid. When the two drops collide in air, they coalescence or bounce off depending mainly on the kinematic energies possessed by the drops, and the air layer does not strongly reduce the initial momentum of the drops. For drops approaching each other inside an immiscible liquid medium, the liquid layer can reduce the approach velocities due to viscosity, and in most cases drop coalescence occurs.

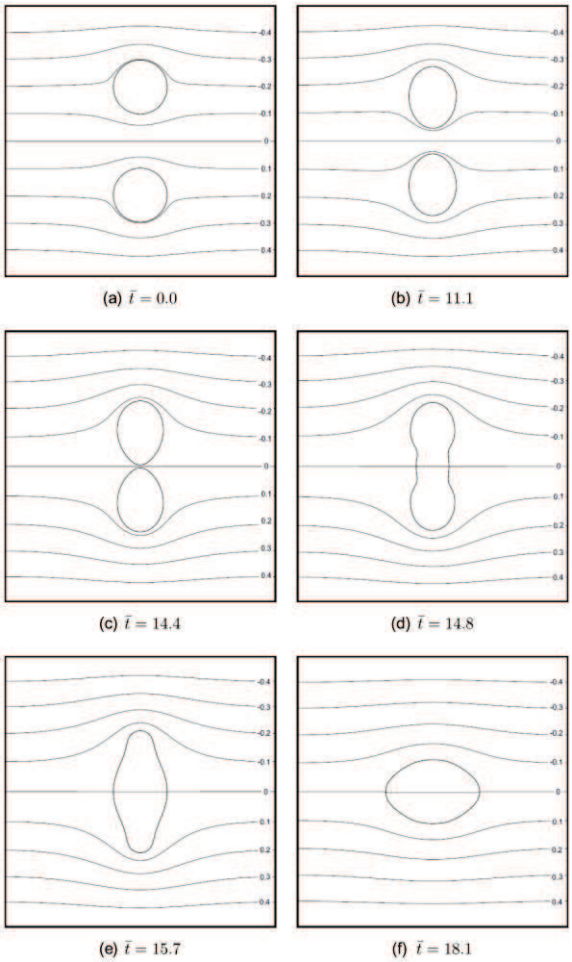

Fig 1.20. Simulation of droplet deformations and coalescence under electric fields (Bjørklund 2009).

Numerical modelling of the electrocoalescence of a droplet pair has formed an increasing subject of research for the last ten years. (Bjørklund 2009) did simulations for electrically induced droplet coalescence, investigating drop deformations before and after contact. The two fluids were considered to be incompressible fluids and the boundaries were found by the level-set method, shown on Fig 1.20. Before coalescence the two drops approach each other and the deformations of droplet shapes occur in the center line ''face to face''. During the approaching movement, the deformations were more and more pronounced until interface broke up, leading to coalescence. Just after the coalescence, as shown in (e), the drop was not a spherical shape. Then capillary force of the interface pushed the two extremities towards the center and helped this coalesced drop to return a spherical shape. This simulation is consistent with experimental work done by (Guo & He 2014). In simulations done by (Lin et al. 2012), two incompressible immiscible binary liquids were considered with Neumann boundary conditions, using the free energy electro-hydrodynamic model. The effects of viscosity compared to electric forces were investigated.

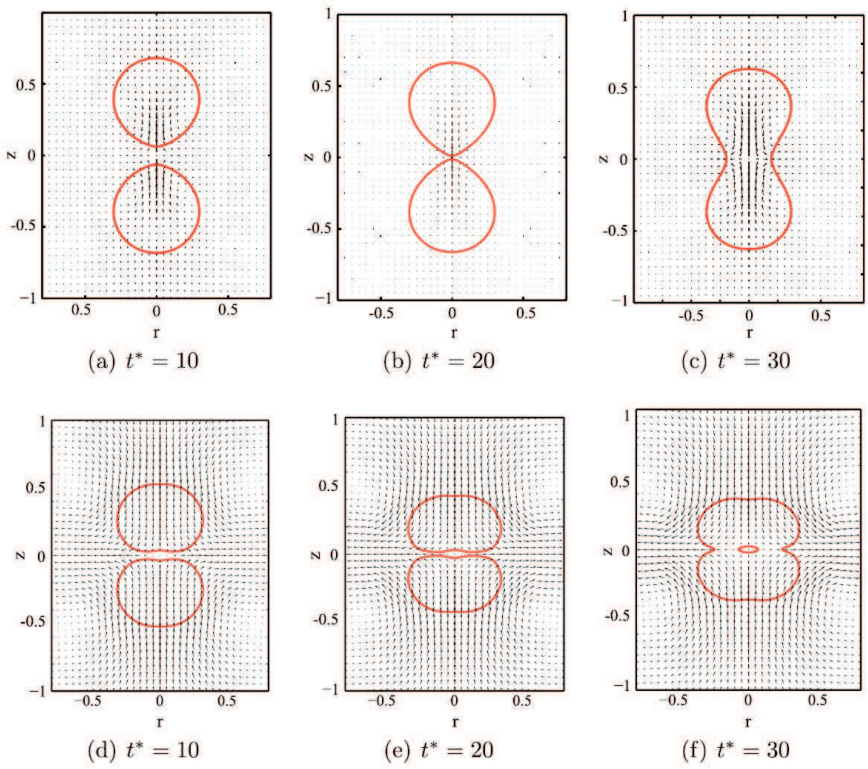

Fig 1.21. Coalescence process simulation of two drops under different viscosity medium (Lin et al. 2012).

It was demonstrated that with a lower viscosity of the medium, the drop deformed itself into a shape with a higher curvature on their central line face to face (fig a-c), while under an environment of a higher viscosity, the two drops plated their faces when they approached each other (fig d-f). The viscosity value of the film layer between the two drops could modify the drop interface deformation. From this diagram it could be thought that for drop coalescences without electric fields, the viscosity effect was predominant, and the drop interfaces deformations were similar to the Fig 1.21. d-f. For drop coalescence under electric fields, generally the electric force could overcome the viscosity effects, and then the drop dynamics could be simulated by Fig 1.21. a-c.

(Mohammadi et al. 2014) did experiments of drop pair electrocoalescence. The water drops contained 3.0 wt% NaCl , and the bulk medium was transformer transparent oil.

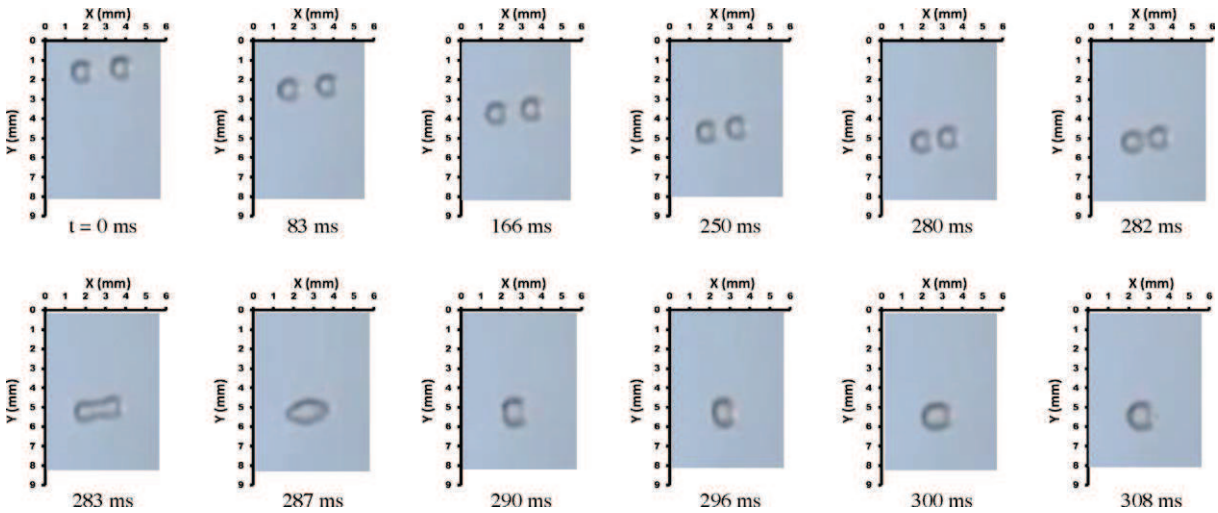

Fig 1.22. Two falling water drops in oil under electric field with strength of 2.8 kV/cm (Mohammadi et al. 2014).

The two drops were released from parallel micro syringes with a diameter of about 1.25 mm and electric field was perpendicular to their motion. They observed that when electric field was switched on, the two drops began to approach each other under a dipole-dipole system. After collision, the interfaces of two drops broke up and the two drops merged together immediately, forming a cylindrical liquid column. Then under push of capillary force, this cylinder came into spherical form through oscillations. More experiments were performed with a skew angle between the drops and it was found that more time was needed for coalescence process due to the skew angle. With large skew angles and moderate electric fields the drops would first aligned with electric fields and then coalesce. This experiment was compared with simulations done by the same author (Mohammadi et al. 2012). Moreover investigations of waveform effect on electrocoalescence process was added in their numerical research (Mohammadi et al. 2013). In recent study, electric field intensities and drop deformations in coalescence processes were analyzed in details (Guo & He 2014). It was said that a low electric field would favor coalescence while a very high electric field made drops collide and repel from each other.

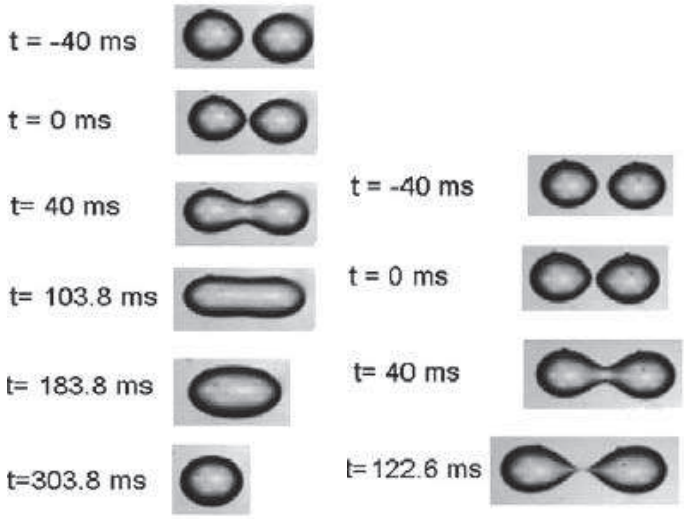

Fig1.23. Two water-ethanol drops in oil under electric field. The field strength for the left series is 193 kV/m and for the right series is 200 kV/m (Guo & He 2014).

Fig 1.23 shows drop coalescence on the left photo and non-coalescence on the right photo. It is showed that even when the beginning of coalescence has occurred, the electric force can separate again the drops pair. As relatively large droplets were used, of about 1.72mm to 1.80mm in diameter range, deformation of drop shape along electric field was also observed, and the duration of the bridge formed between the two colliding drops was discussed as it was longer with a moderate electric field. It should be noticed that here drops were distilled water mixed with alcohol in order to compare its density to that of surrounding white oil.

1.4.4 Influence of surfactants on moving droplets

For a water drop with free surfactants falling inside oil medium, fluid friction may cause inner fluid circulation within the drop, and thus the falling velocities of the drops increase. This phenomenon is depicted by Hadamard-Rybczynski equation, shown below.

$$U_{HR} = \frac{2}{3}\frac{r^2 g(\rho_w - \rho_o)}{\mu_o}\frac{\mu_o + \mu_w}{2\mu_o + 3\mu_w} \tag{1.6}$$

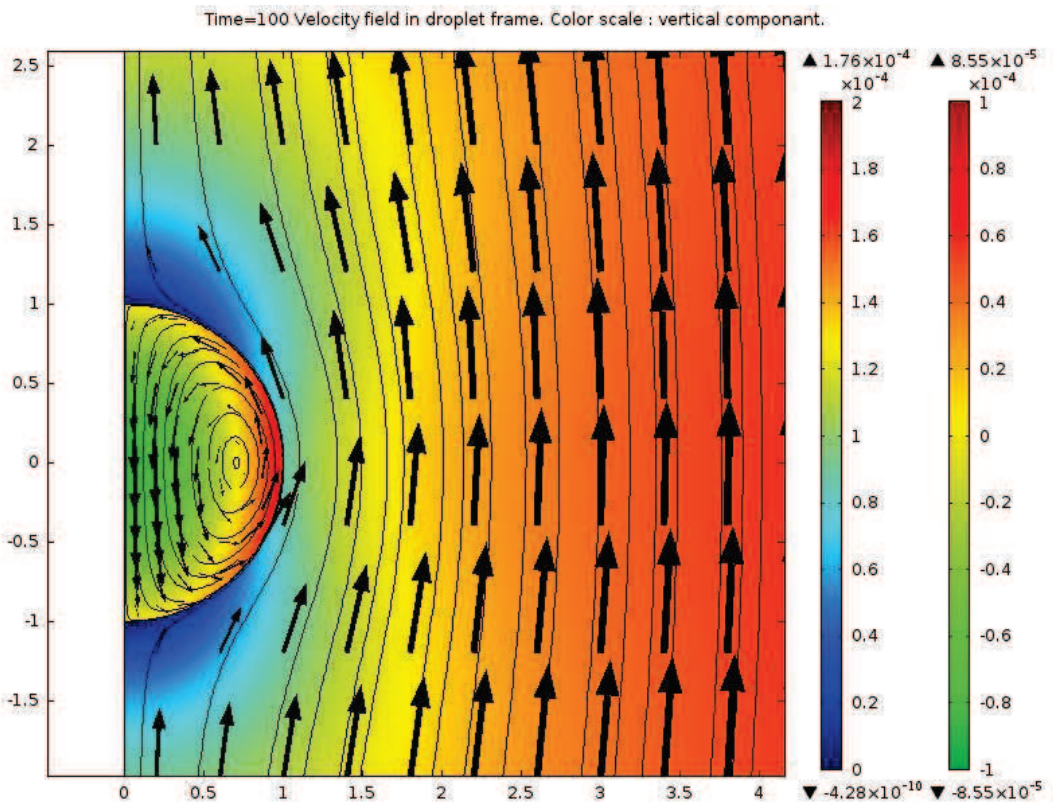

Fig 1.24 Water drop falling in a viscous liquid. Simulation using Comsol Multiphysics. Navier-Stokes equations are solved in the two liquids, with mobile interface. Results are drawn in a frame moving with the drop (drop radius R = 50µm, water viscosity μ_w = 1 mPa.s outer fluid viscosity μ_o = 10 mPa.s, surface tension σ = 25mN/m). Velocities are non dimensionnalized by $U_{cap} = (\sigma/\rho_w/R)^{1/2}$. $U_{stockes}/ U_{cap} = 1.3\ 10^{-4}$ and $U_{HR}/U_{cap} = 1.9\ 10^{-4}$.

Fig 1.24 shows the outer fluid flow lines with inner drop circulation. When surfactants are added into fluid medium, they will accumulate at the water-oil interface and decrease interfacial tension. While the drop falls within the oil medium, friction will sweep the surfactants towards the drop rear face, leading to gradient of interfacial tension $\nabla_s\sigma$ (Pawar & Stebe 1996) (Milliken et al. 1993). Then this gradient induces a Marangoni force which tends to redistribute the surfactants over the drop surface (Teigen & Munkejord 2010). When a stable state is reached, the Marangoni force is equal to friction force and the drops can be simulated as solid spheres whose motion can be described by the Stokes equation (Hamlin & Ristenpart 2012).

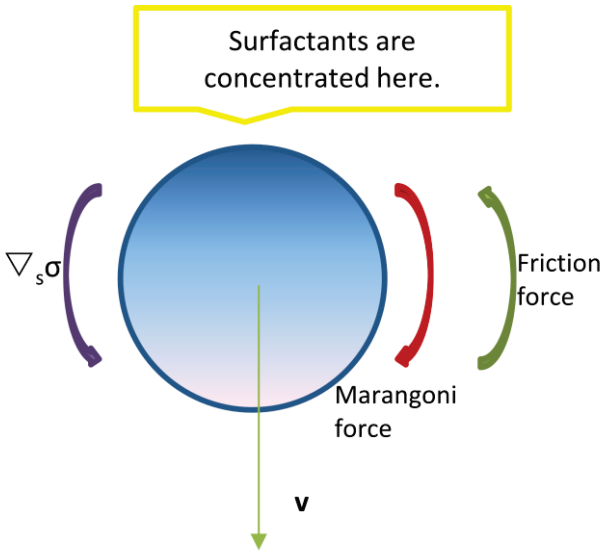

Fig 1.25. Surfactants are concentrated on the rear of the falling drop, and the Marangoni force equals to the friction force.

In experiments, falling drops are of diameters D = 0.14 mm, the inertial force and interfacial tension variation are so small that they could not modify the spherical shape of drops (Levan & Holbrook 1989). This assumption of spherical shape of drops is consistent with experimental observations.

Surfactants can also influence on a micrometer scale the ‘’approaching process’’ of a drop pair and modify the coalescence efficiencies ((Zhang et al. 2012).

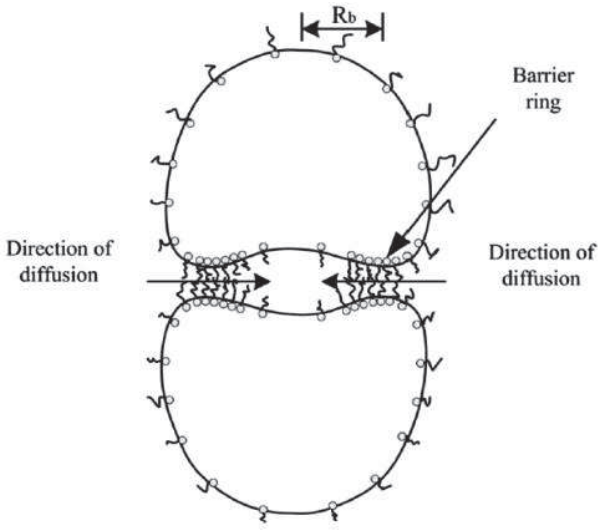

Fig 1.26. Contact of two surfactant covered drops (Zhang et al. 2012).

It is shown from Fig 1.26 that while two drops were approaching each other, surfactants located between the interfaces would be swept to the fronts of two drops and thus formed a 'barrier ring' which would prevent the two interfaces from coming into contact with each other. In addition effects of surfactants on drop deformation subjected in an electric field was simulated by (Teigen & Munkejord 2010). Navier-Stokes equation was applied to solve both fluid equations and the interface was tracked using the level-set method. Leaky-dielectric model was adopted to simulate effects of electric fields. Surfactants were considered to be non-soluble and could move along drop interface. It showed that surfactant effects depended on characteristics of the contacting two fluids and the inner drop circulation which could influence surfactant distributions on drop surface, could favor or decrease drop deformations. Later with the same method it was added that insoluble surfactant could give a solid cover over the falling drop in a liquid medium, while soluble surfactant could give a mobilize drop interface (Erik Teigen et al. 2011). Following the previous research, both experiments and simulations were investigated in studying a water drop covered by surfactant Span 80, falling inside model oil Marcol 52 (Ervik et al. 2014).

1.5 Conclusion

Crude oil contains a variable amount of water, and their separation is highly needed. Such separation concerns just as much high water-cut mixture, to reduce extra transportation cost, than low water-cut mixture, prior to refinery processes. Water-in-crude-oil emulsions are difficult and long to breakup because of the very small size of water droplets, in the micrometers to tens of micrometers range.

To increase the sedimentation rate, thanks to the difference of density between water and oil, the coalescence of small droplets in larger ones is desirable. That can be done on water-in-crude oil flows in electocoalescers, through the assistance of applied AC or DC electric fields, to obtain droplets in the millimeter range.

Coalescence of droplet was studied for long time in air: water drop in meteorological field or more recently hydrocarbons droplets in sprays. The studies of colliding drop pairs enlighten the influence of surface tension and the associated Weber number as the main parameter influencing the coalescence or separation behaviors. The influence of external electric field has been taken into account in some papers, but through the electrophoresis effect on electrically charged droplets. For

colliding droplets, good agreements are generally observed between experiments and models when inertia and surface tension effects are dominant. However difficulties remain in the description of the surface effects more locally, such as the one involved in bouncing.

Droplets behavior is different in another liquid, mainly because there is a strong influence of the viscosity of the bulk phase, and of gravity. Different studies have been published for configurations of drop falling on larger one or on a plane surface under electric field. Phenomena as partial coalescence or bouncing have been discussed, involving the viscosity of the liquid bulk and the electrostatic pressure applying on the interfaces. Drop pair coalescence was studied experimentally only in very few papers since year 2000, notably in very recent ones, published after the beginning of the PHD.

Existing experiments have some common characteristics: quite large droplets are generated and observed (not far under the millimeter scale), only few cases of interactions of droplets pair are reported, always in configuration of side-by-side fall in transverse electric fields (that is perpendicular to the gravity). Thus, the observed phenomena are fully 3D. On the other side, numerical models have been developed but rarely compared systematically to experimental data.

In this context, G2Elab works in collaboration with SINTEF energy research on ElectroCoalescence (EC) projects for more than ten years. The present PHD is a part of ECIII project “Fundamental understanding of **e**lectrocoalescence in heavy crude oils”. Among the conclusions of the previous project (ECII), it was stated that experimental data on the electrocoalescence of small droplets will be useful to improve the understanding of the dynamics of water-oil interfaces and to validate numerical models. The aim of the research project, proposed in Grenoble, concerned initially experiments on droplets pair in oil flows. As a first step the present PHD will focus on pairs of small droplets falling in stagnant fluid, under electric field aligned with the gravity and the droplets pair axis. The choice of this configuration aims at providing simple experimental data to compare with models, thanks to the axial symmetry. The difficulty remains on generating and controlling the injection of very small droplets, up to one order of magnitude smaller than in existing experimental data.

Chapter 2. Experimental set-up and measurements

2.1 Introduction

The goal of the thesis is to study coalescence of two drops under electric fields. The drop pair is of micrometer scale and aligned with electric field lines while falling inside model oil. For this study a dual drop injection system combined with high tension application system is needed. The background light is chosen as conventional light, and the test cell filled with model mineral oil is transparent. Camera visualizations are needed for different angles for the drop coalescence process. A waveform generator is used for dual drop injection process and a high tension connecting electrode is needed for introducing electric fields. The physical measurements consist of liquid temperature, oil-water interfacial tension, densities, viscosities and related uncertainties. This chapter is divided into four parts, and they are respectively drop injection methods, experimental set-up, physical measurements with uncertainties and oil properties.

2.2 Existing drop injection methods

In drop injection experiments, different techniques have been developed such as piezoelectric injection (Harris et al. 2015), ultrasonic injection (Lévin & Agneray 1999), thermal bubble injection (Chen et al. 1997), electrohydrodynamic (EHD) injection (Chen & Basaran 2002). These techniques will be presented briefly hereafter. However it can first be mentioned that in most cases the obtained droplet diameter depends on the nozzle size and the most often only droplet diameters of millimeter scale can be obtained. Electrohydrodynamic drop injection technique appears to be the

only one allowing us to obtain droplet sizes independent of the nozzle size. Moreover the injected droplets are much smaller than the nozzle tip diameter (Raisin et al. 2013). For the desired experiments on drop electrocoalescence in model oil, the drop diameters are required to be of the order of tens of micrometer. Such drops scale can only be achieved by using EHD injection method.

2.2.1 Drop injection in air

Injecting liquids into surrounding environment has long been a research subject and there are mainly two categories of injection methods: continuous streaming technique and drop-on-demand technique. For the continuous streaming, droplets obtained are mainly due to capillary breakup of a single jet. For the drop-on-demand technique, a drop is injected by a single actuation, and this actuation is either by stimulating the liquid formed meniscus at the orifice, or by pushing liquid medium through a container. Early drops injection techniques involved injecting droplets into air, mostly in meteorological studies.

For drop injection into air, up to now, there have been many techniques for injection processes such as thermal method, pneumatic method, acoustic method, ultrasonic method and finally electrohydrodynamic method, often named as EHD method. In thermal drop-on-demand method, heat is transferred to a thin film resistor at the bottom of ink reservoir and this leads to an augmentation in temperature in this reservoir. This would by consequence cause the growth of a vapor bubble, the growth of which pushes a small amount of ink to be ejected from the nozzle of the reservoir (Chen et al. 1997). This method is often known as ‘’thermal bubble’’ and this is a train ejection, not a single droplet extraction. Thus the diameter of a single drop cannot be exact. Another drop actuation method is called spark bubble and this depends mainly on bubble dynamics and during the growth of which a liquid column is ejected from nozzle. This method is also used in ink jet printing technology, and the advantage of spark bubble is that it favors a large droplet with smaller satellites. Control of drop size can be achieved (Dadvand et al. 2008a). However, both thermal and spark bubble method have the possibility to alter chemical compositions of the fluid in its reservoir due to heating (Lee 2002).

For the pneumatic method, a drop ejected from the nozzle depends on the variation of gas pressure which is introduced via a pneumatic generator to push the liquid meniscus in an ‘‘in-out’’ sequence. The gas pressure pulse is sinusoidal and it is out of phase with the meniscus oscillation. When a jet

from the meniscus is pushed out of the nozzle, the jet could be broken when it retracted back to the meniscus, leaving a formed drop.

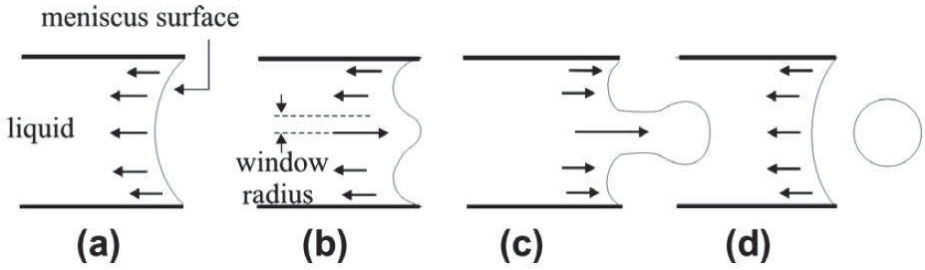

Fig 2.1. Process of single drop formation by pneumatic method (Amirzadeh & Chandra 2010a).

Drops with diameters much smaller than the nozzle size can be produced, but the pneumatic generator requires adjusting the liquid viscosity range to the nozzle size, to inject droplets of a given size (Amirzadeh & Chandra 2010a). For this pneumatic generator, applications are varying from deposition of molten metal droplets (Cheng et al. 2005) to recent research into the evaluation of pneumatic methods in biochemical use, which aims at producing drops of pesticide aqueous solution for crop plants and weeds (Basi et al. 2012). Recently piezoelectric droplet-on-demand generators have come onto the market and are stable with good repeatability of drop production. This method is similar to the pneumatic method because it uses pressure to push out a liquid meniscus. With the application of an electric pulse, a pressure is induced onto the piezoelectric buzzer which then presses the fluid chamber to push out a precise quantity of liquid through the nozzle (Harris et al. 2015).

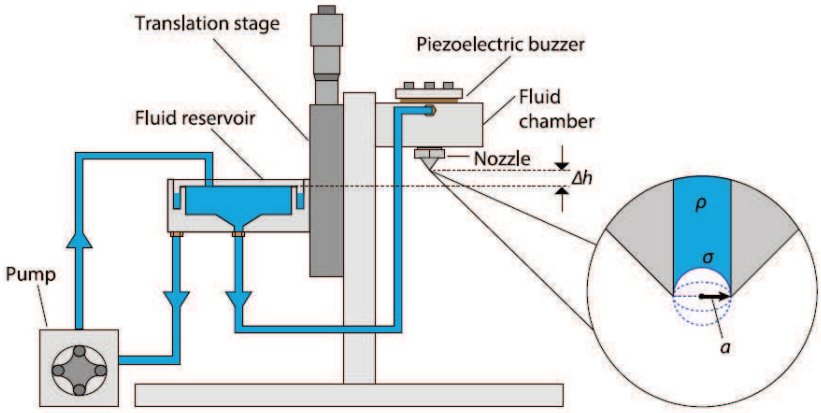

Fig 2.2. Piezoelectric droplet-on-demand generator (Harris et al. 2015).

This generator is reported to be able to give good production of water droplets with sizes of 0.5-1.4 mm in diameter. Further decreasing the droplet sizes to around 0.15 mm would be difficult with this technique. Thus other experiment set-ups should be considered.

The acoustic drop-on-demand method, which was first discovered by (Mem & Loomis 1927) for oil drop injection into air, was developed in many research domains both scientific and industrial, such as in picoliter drug transfer (Ellson 2002) and ink jet printing (Krause 1973). The acoustic energy is focused near the liquid surface to achieve drop injections without any physical contact. The drop volume can be controlled by the applied acoustic energy, frequency and the used liquid property (Arrondo & Alonso 2007). During acoustic drop injection process, propagation and reflection of acoustic waves plays a crucial role (Bogy & Talke 1984).

For the ultrasonic drop-on-demand technique, an ultrasonic pressure wave is generated by a transducer and focused through lenses onto the liquid-air interface at the nozzle tip (Lee 2002)(Lee 2002). Then this focused ultrasonic wave will interact with capillary wave of liquid-air interface to give a full drop injection process. With this ultrasonic injection method, both individual drop injection and a continuous jet could be achieved. Experiments were done by (Meacham & Vara 2005) who used nozzle diameters from 5 µm to 10 µm to study water drop ejections into air dynamics and the ejected droplets were of a diameter of 7.2 µm with a nozzle size of 5.93 µm. The drawback of this ultrasonic method is that it can cause nearby equipment to vibrate while ejecting droplets (Lévin & Agneray 1999).

Finally we come to the electrohydrodynamic (EHD) method which consists in applying electrostatic pressure to the liquid meniscus, in order to deform and extract a droplet from it. This technique is often used in inkjet printing because it is easy to reduce and control droplet sizes. In the experiments of (Rahman et al. 2011), they had a minimum droplet size of 40 µm in drop train production. Table 2.1 is given to sum up produced droplets by different drop injection methods.

Up to now, experiments for droplet sizes evolution from one given nozzle is rarely reported. It is only noted that the two unique drop-on-demand techniques which can give droplet sizes smaller and independent of nozzle sizes are the ultrasonic and EHD methods (Lee 2002). However the ultrasonic technique could cause equipment to vibrate. Thus it appears to us that the best drop-on-demand method is EHD injection, on one hand because the contamination of chemical compositions of liquids can be avoided, on the other hand because the droplet size can be reduced largely, due to its

independence of the nozzle size. Thus studies and improvements will be focused on EHD injection experiment set-ups.

	D_{int} (mm)	d/D_{int}	Diameter range (mm)	Method
(Dadvand et al. 2008b)	1, 3, 6, 8	23.5 %	1.41	Spark bubble
(Amirzadeh & Chandra	0.25, 0.45, 0.80	--	0.075—0.200	Pneumatic
(Harris et al. 2015)	0.5 – 1.4	1	0.5 – 1.4	Piezoelectric
(Ellson 2002)	0.35	2.8 %	0.1	acoustic
(Meacham & Vara 2005)	0.00593	121.4 %	0.0072	ultrasonic
(Raisin et al. 2013)	0.46	8.7 % -- 34.8 %	0.04 – 0.16	

Table 2.1. Produced droplet sizes by different injection methods.

2.2.2 Droplet injection in liquids

2.2.2.1 Injection in microchannels

Drop injection into liquids has been the subject of much research in different domains. In microfluidics, small drop injection into other immiscible liquids with successful control of drop diameters over a wide range were done by (Nisisako et al. 2002). Pushing one liquid medium flowing through a channel forth to meet another liquid which goes inside a perpendicular channel at a variable given space, can cut the former liquid body into drops under drag force. Using this method, droplets of 100 – 380 µm which are of a size smaller than the given channel, have been produced. Some people have done experiments on drop coalescence in microfluidic channels (Jose & Cubaud 2011) (Tan et al. 2006), however the boundary conditions can influence drop shapes and motion during coalescence process.

2.2.2.2 *Injection of single droplet*

In other cases the drop injection techniques are mostly discussed in electrocoalescence experiments. The investigation of this research is mainly focused on petroleum use and improvement of actual techniques. The drop injection method is to hold a glass cannula with tip size of 0.03 – 3.1 mm in diameter, immersed into model oil. The water in the glass cannula is distilled with 3.5 wt% NaCl and the formed water drop at the tip of the cannula is 0.2 – 0.5 mm in diameter. To detach the water drop, the glass cannula is pulled upwards and the water drop falls off at the oil-air interface (Pedersen 2008).

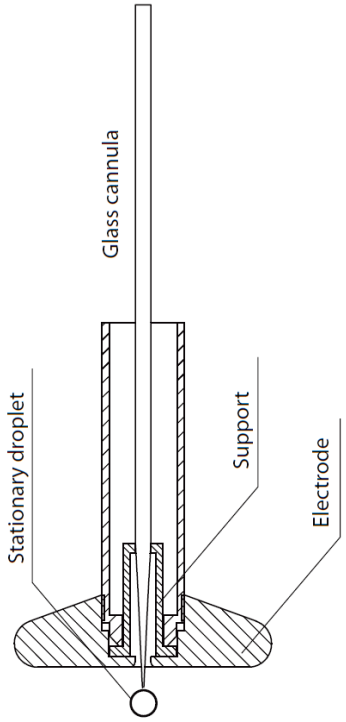

Fig 2.3. Experimental set-up for drop injection into model oil by (Pedersen 2008).

Later this method of injecting water drops into model oils is used for further experiments on drop coalescence under electric fields. Globally there are two types of experiments: one injected water drop falling onto a stationary bigger one and two drops falling side-by-side. In the former case, the research has been led by (Ingebrigtsen et al. 2005) in the early years with a test cell filled with crude oil and images visualized by infrared camera. With the same experimental configurations, other research has been performed to complete drop coalescence parameters in more details.

(Mousavichoubeh et al. 2011) did experiments with falling drop size of about 0.98 mm in diameter. (Chiesa et al. 2006) did experiments with drop sizes 0.17 – 0.35 mm of the falling one onto a stationary big drop of 4 mm in diameter, and the viscosity effects of surrounding model oil on water drops coalescence were investigated. (Hellesø et al. 2015) performed drop coalescence with drop diameters of 0.7 mm of the falling one and 4 mm of the bottom stationary one. In their experiments on drop coalescence, the test cell was filled up with crude oil and visualization was done by using a near-infrared camera. The experiment configuration and set-up is shown on Fig 2.4.

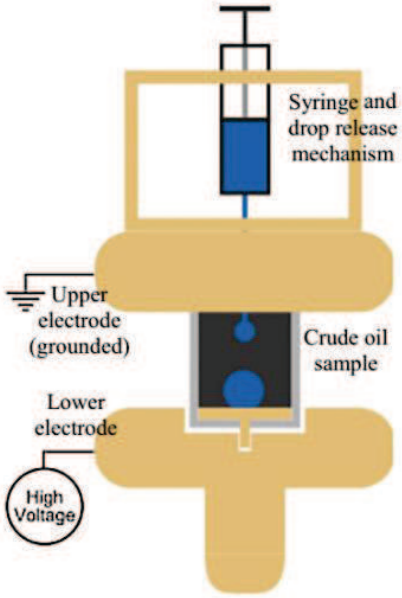

Fig 2.4. Drop coalescence experiments in crude oil using near-infrared camera for visualization (Hellesø et al. 2015).

It is noticed that all the experiments above have large drop diameters for electrocoalescence research, and the coalesced drops are uneven.

2.2.2.3 Injection of drop pair

To simulate falling drops inside crude oil environment, two water drops falling side-by-side were released and submitted to a transverse electric field. Two falling droplets were first examined by (Mohammadi et al. 2014) and the two electrodes were oriented left – right. As with previous experiments, two micro-syringes were used for producing electrically uncharged water droplets with 3.0 wt% NaCl added while transparent transformer oil filled the test cell. When the two water drops

fell into the electrode zone, an electric field was applied. The goal of this research was to study droplet moving times with their different initial positions when injected into model oil. It should be noticed here that average size of injected water droplets is 1.25mm.

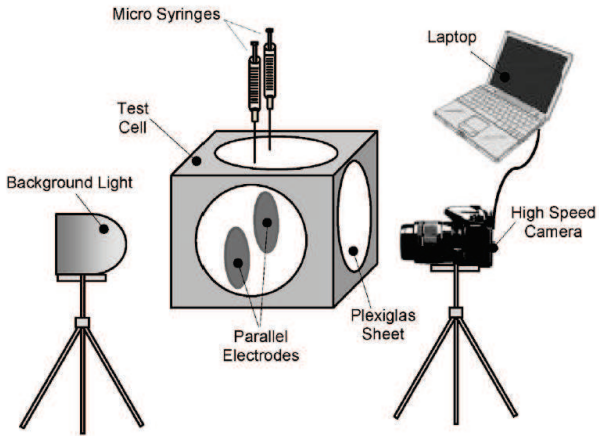

Fig 2.5. Drop coalescence experimental set – up (syring injection) for droplet diameters of 1.25 mm (Mohammadi et al. 2014).

This coalescence of two falling drops was also examined by (Guo & He 2014) especially for investigating coalescence dynamics. In their research, two big drops of water mixed with alcohol of about 1.72 mm to 1.80 mm were produced by syringe injection. The experimental set-up was more or less the same as previous studies with two electrodes mounted parallel connected to high voltage, immersed in oil medium.

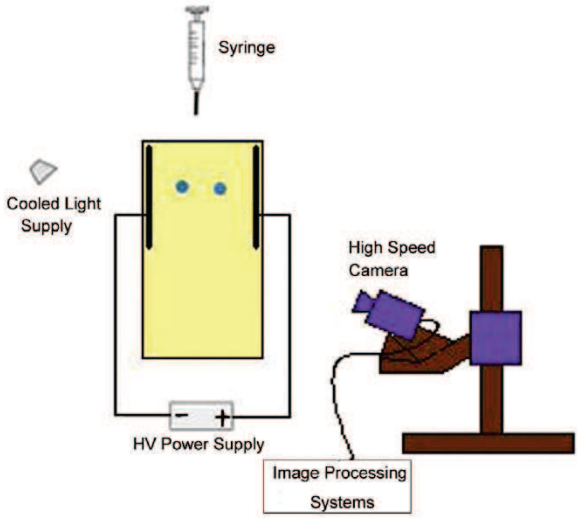

Fig 2.6. Drop coalescence experimental set – up (syring injection) for alcohol contained water drops of diameter range from 1.72 mm to 1.80 mm (Guo & He 2014).

As it was mentioned before, the water droplets in crude oil have a diameter range smaller than 0.05 mm. Thus a further reduction in drop diameters should be considered. Moreover, this system of two drops side-by-side was not axially symmetric, which could complicate the calculations of drop coalescence process. Consequently these drop injection methods were not suitable for experiments of small drop electrocoalescence in axisymmetric system.

2.2.2.4 Electrohydrodynamic (EHD) injection method

To inject liquid drops into another immiscible liquid without constraint on the size of the injecting nozzle, up to now there are not so many existing methods. A leading research of injecting drops independent of nozzle sizes was done by (Chen & Basaran 2002) using piezoelectric transducers. Further improvement of this injection technique was done by (Raisin 2011) in which water drops were injected into polybutene oil with the help of multi-step electric pulses. This injection is called Electrohydrodynamic (EHD) because the whole drop formation process is based on water meniscus dynamics. In experiments, one grounded needle is fixed at the top cover of the test cell with its tip immersed into model oil. The needle is filled with tap water and the water meniscus is anchored on the inner diameter of the needle. Below the needle a high voltage electrode is placed. The test cell configuration is shown below.

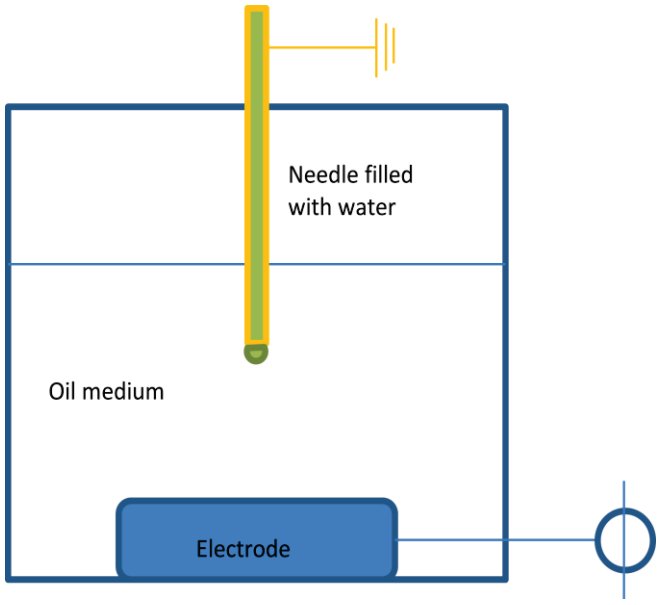

Fig 2.7. Principle of experimental design for drop injection.

The application of high voltage on the bottom electrode can induce the upper water meniscus to deform and then detach water drops from the hanging needle. The advantage of this technique is that the injected drop diameters were independent of the needle inner diameter, and could vary over a large range. Thus this EHD injection method is chosen for further experiments of two falling drops in axisymmetric configuration.

2.3 Experimental set-up

2.3.1 Experimental apparatuses

For the EHD drop injection set-up, the connection of the different devices is presented on Fig 2.8. They include: a PC sending and receiving signals through standard I/O ports or a special card (video), a waveform generator (Agilent 33500B series, or Wavetek 395), a high voltage amplifier (Trek 20/20C), an oscilloscope (Tektronix DPO 4034), two Dalsa Falcon 1.4M100 XDR cameras and a fast camera (AOS S-MOTION 1683). Two supplementary Bosch Dinion CDD cameras are directly linked to video screens for live reading of water meniscus and injected droplet position in the cell.

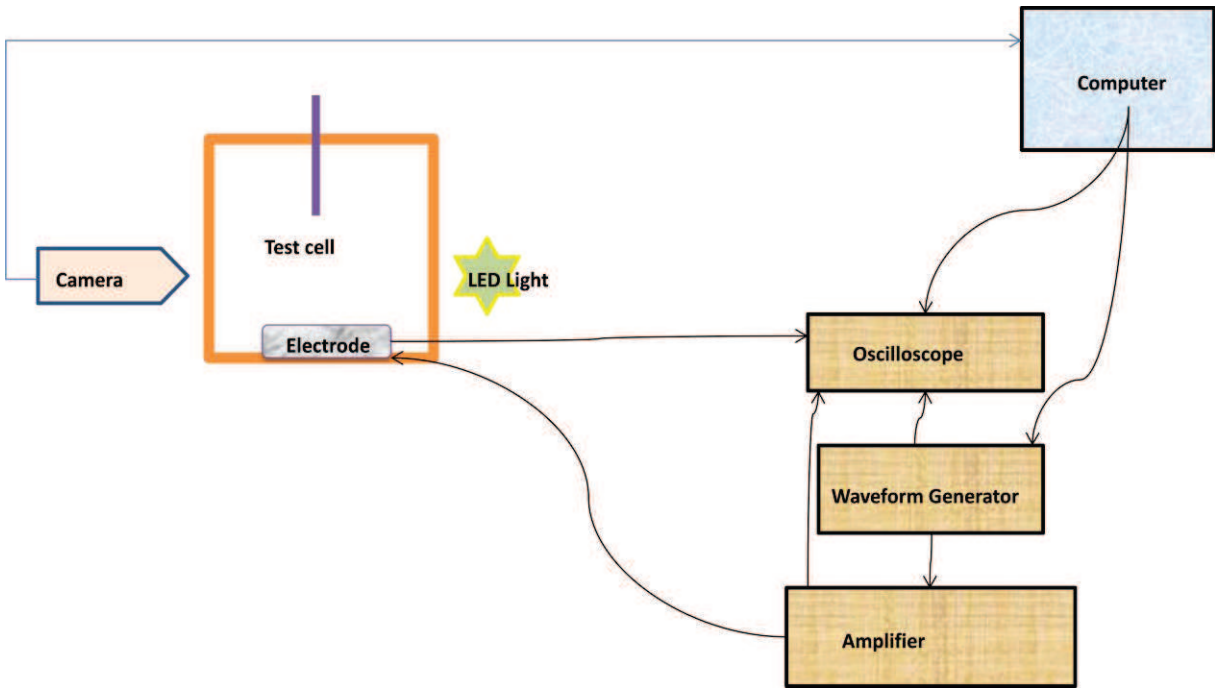

Fig 2.8. Diagram of electric devices.

The signals generated by in-house developed software are sent from the computer to the waveform generator. The waveform, in the range: -10V to 10V, is sent to the amplifier to be increased 2000 times (output range -20kV to 20 kV). The software in the computer has a pulse delay function which can allow passages of successive triggers with defined precise time interval. A sequence of four successive triggers is possible. The first two triggers destined to create waveforms while the last two triggers are used to apply the sinusoidal or DC voltage on the electrode. With the help of trigger delays, two Dalsa cameras can be turned on at the third or the forth trigger according to needs. All the signals from the cameras, the waveform generator, the amplifier and the triggers sent from the computer are observed on the oscilloscope to verify whether any anomalies happen through the procedure. Fig 2.9 is a schema illustrating a typical example.

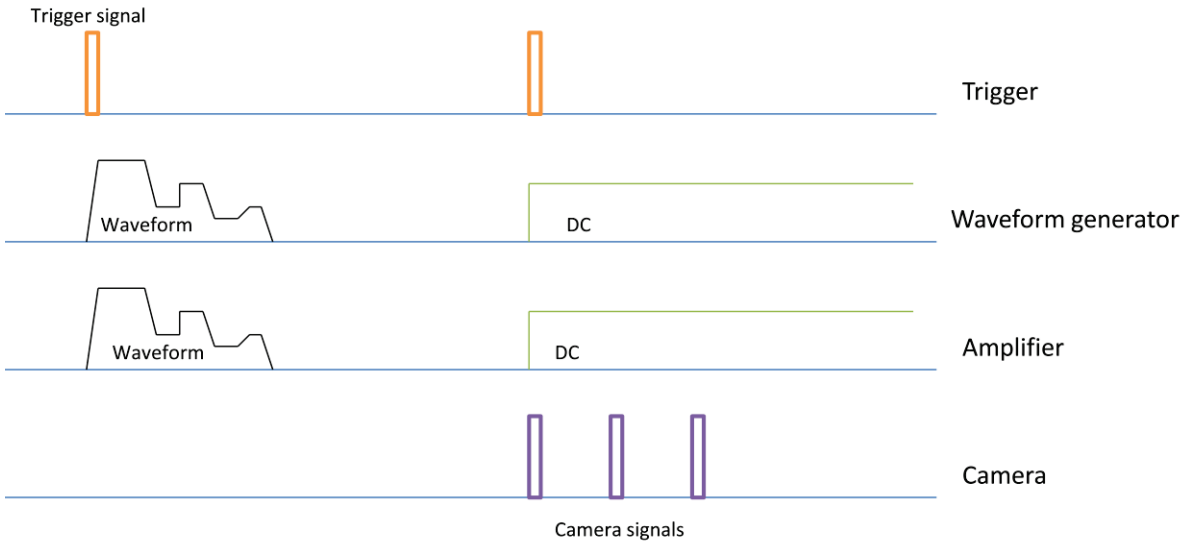

Fig 2.9. Scheme of different signals from the electric devices recorded by the oscilloscope.

In some experiments the verification via the oscilloscope of the triggers sent by the computer may be changed. The signals of another Dalsa camera may need to be verified, and thus on the figure above the connection between the computer and the oscilloscope should be changed for the connection between the horizontally placed Dalsa Camera and the oscilloscope. The amplifier connects to the test cell, and the length of the connection wire is about 3 m. The test cell is a Plexiglas recipient filled with model oils. First experiments were made in a cubic cell, but a second octagonal cell was designed, allowing the use of five cameras and three light sources, placed around the test cell, along the axes of symmetry.

2.3.2 EHD injection set-up

The first test cell set-up, hereafter called EHD injection set-up, was used for first sets of single drop injection. This first test cell is cubic, with 0.5 mm thick Plexiglas walls and of 9 cm inner length on each side. A grounded needle is placed approximately 1.5 cm above the bottom electrode. The inner diameter of the needle is 0.46 mm.

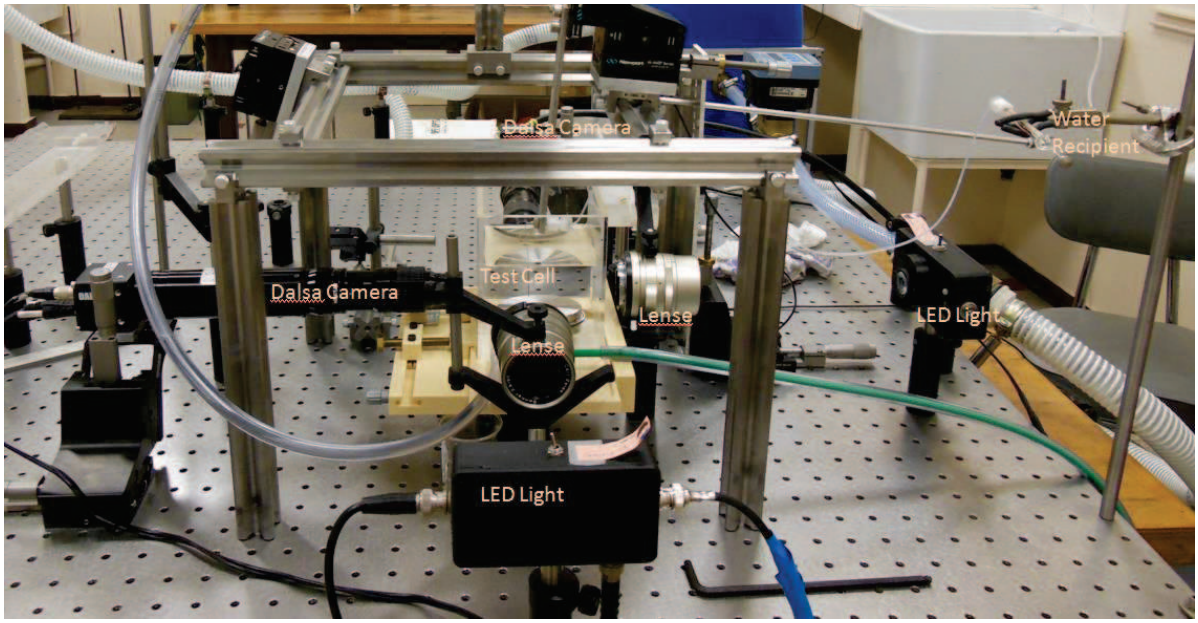

Fig 2.10. EHD injection set-up of test cell.

Fig 2.10 shows the test cell of EHD injection set-up. Here only two Dalsa cameras were mounted along two perpendicular symmetry axes to visualize drop injection dynamics. One camera serves to survey the meniscus shape and the other to take photographic images of drop injection procedure. The light sources were LED lights, and two lenses just behind each source were used to focus the lights. Due to the good reproducibility of the drop injection processes (Raisin 2011), the second Dalsa camera takes one photo for each injection series with a variable delay (fixed as a multiple of a 200 µs time step) and a shutter speed of 40 µs synchronized with a strobe light. All the images are then combined together to give a full series of drop injection dynamics. It is impossible to trigger the camera to take a full sequence of drop injection because the maximum frame rate of the camera is 100 fps. The whole drop injection process is approximately 1.3 ms, and the time interval between two frames of the Dalsa camera is too large to capture the injection dynamics. To survey the drop electrocoalescence process in model oil, the test cell is replaced by an octagonal test cell and a fast camera (AOS S-Motion) of up to 16000 fps is used. In experiments the configuration of the AOS camera uses a spatial resolution of 250*200 pixels, with 8000 fps.

2.3.2.1 Needle form and water recipient connections

The forms of needles used in both the EHD injection and the drop coalescence set-ups have the same shape. The tip of the needle is blunt to make sure the water meniscus can anchor on its inner diameter without bordering out. The only difference between the injection needles is the diameter value. For the EHD injection set-up the needle has an inner diameter of D = 0.46 mm, while the needle used for drop coalescence was D = 0.72 mm inner diameter. The outer diameter of the needle used in this latter set-up is D_{ext} = 1.057 mm which is often used for calibrations purposes.

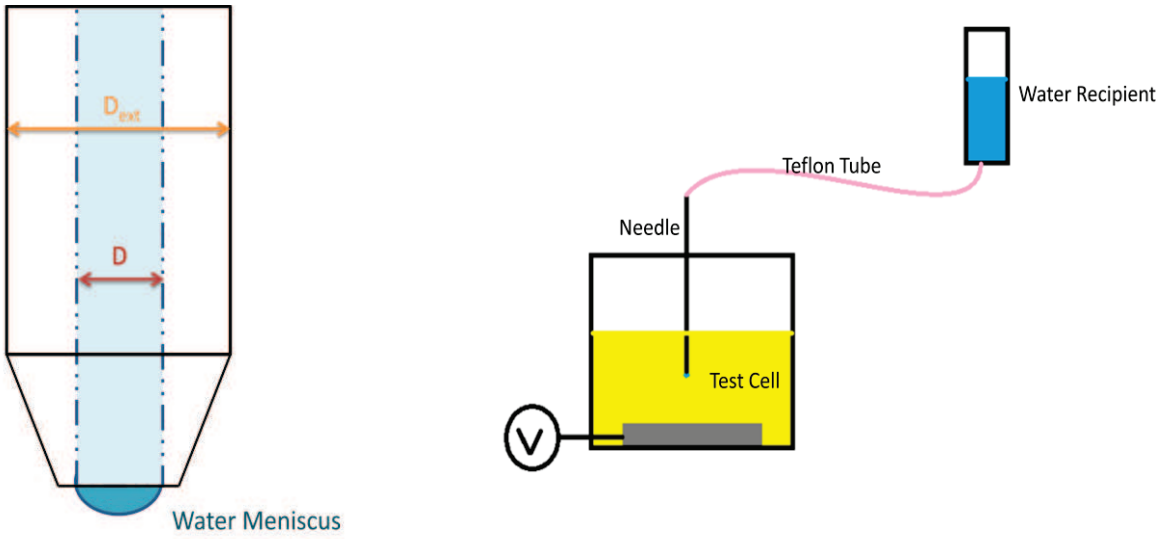

Fig 2.11. Diagram of the needle used for drop injection (the diagram to the left) and the connection of the test cell with the water recipient (the diagram to the right).

The left hand schematic on Fig 2.11 shows the type of needle used throughout the experiments, while the right hand schematic shows the water supply system during drop injection. The needle immersed into the model oil is filled with water, and a meniscus is anchored on its tip. This needle is connected to the water recipient through a Teflon tube with an inner diameter of 0.8 mm and length of about 0.5 m. The water recipient serves to supply water during drop injection, by just adding some water drops inside the recipient.

2.3.3 Test cell set-up

Test cell set-ups are very important because they can influence drop injection. With different test cell configurations, the obtained results may differ from one to another. Thus it is important to specify the test cell used in each set-up in order to explicitly indicate experimental parameters. For drop coalescence experiments, the test cell was an octagonal Plexiglas cell measuring 4.8 cm on each inner side. This test cell design allows visualizations along four axes perpendicular to its sides, as illustrated on Fig 2.8 and Fig 2.12.

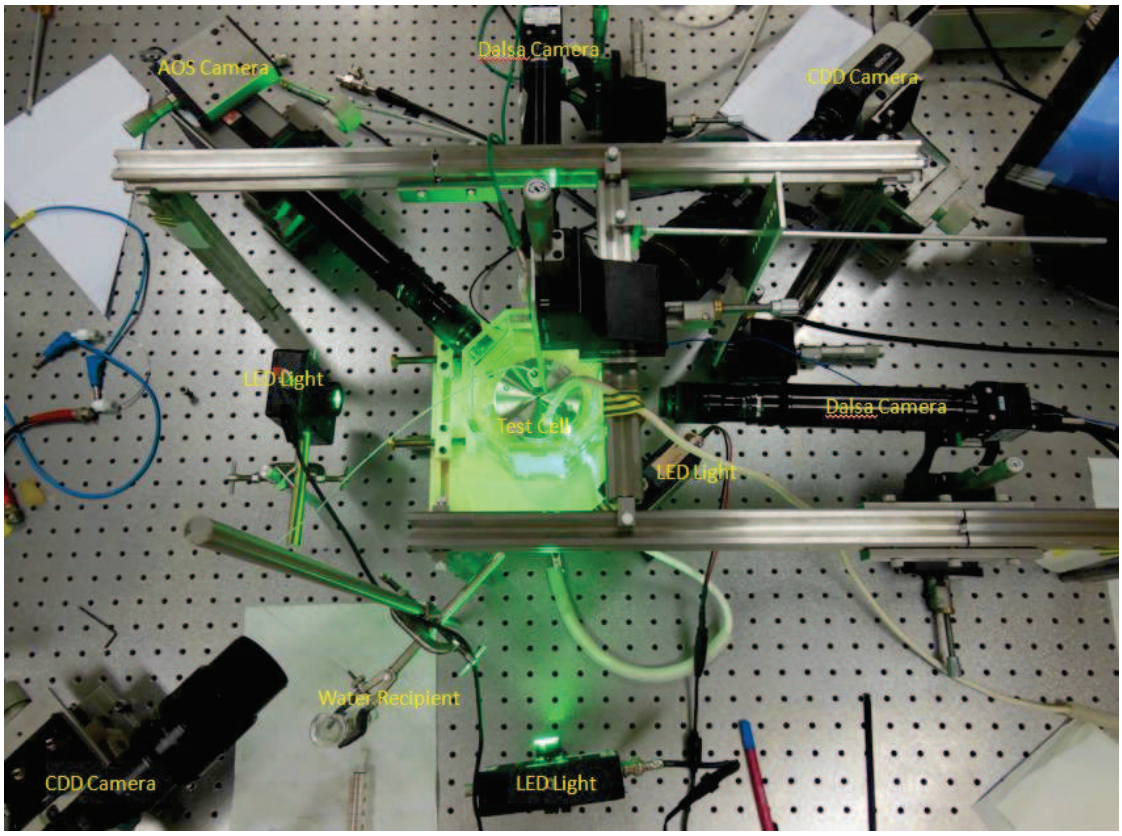

Fig 2.12. Test cell configurations of drop coalescence set-up.

The two Dalsa cameras take images of drop falls and the AOS camera should be triggered manually to record videos immediately prior to coalescence. The two Dinion CDD cameras are mounted face to face because they do not need specific flights for visualization, and ambient light is good enough for them to record ‘‘in vivo’’. One CDD camera serves to give an idea about where the drops are located in the test cell, while the other CDD surveys the water meniscus form for drop injection. Three green LED lights serve to illumination for the Dalsa cameras and the AOS camera.

When zooming in on the test cell, the electrode connected to the high voltage is placed between the needle and the bottom grounded metallic plate. The electrode is 0.5 cm in thickness, and the distance between the needle tip and the upper surface of the electrode was 0.8 mm. The distance between the lower surface and the bottom metallic plate surface was 1.5 cm. The hanging needle was 1.057 mm outer diameter, 0.72 mm inner diameter. Generally the outer diameter was used for calibration of the cameras.

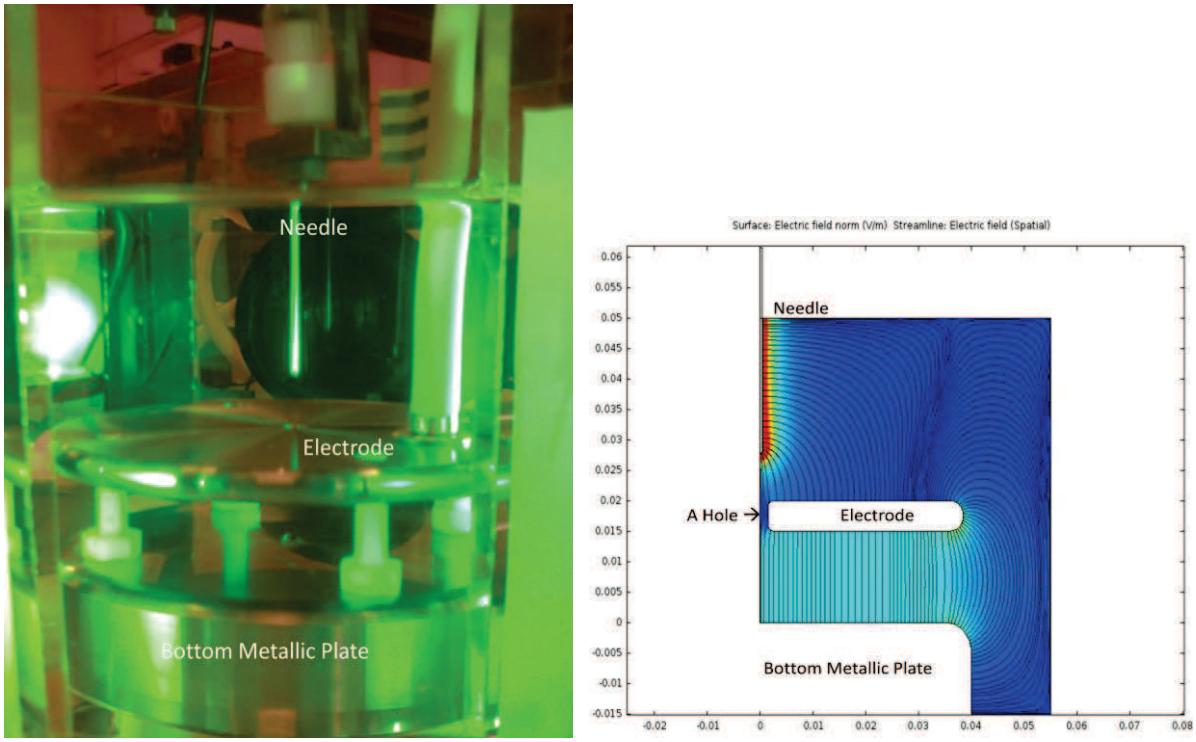

Fig 2.13. Drop coalescence setup test cell viewed under LED illumination (left) and axisymmetric view of the cell drawn by COMSOL (right). Electric field norm is drawn in color when electrode is set to a high voltage while bottom and needle are grounded.

Fig 2.13 shows the test cell configuration of the drop coalescence set-up as a real photo graph and for electric field simulations. The latter uses an equivalent axisymmetric configuration and 1kV voltage is applied on the electrode. The calculated electric field is drawn on one meridian half plane (axis of symmetry on the left). The electrode was held by Nylon screws on the bottom metallic plate, and it has a small hole at the middle of the disc. This hole is 5 mm in diameter and is drilled on the electrode of 80 mm diameter. This hole can be seen clearer on the right hand photo graph of Fig 2.13. This set-up will be called hereafter the ‘’drop coalescence set-up’’.

2.4 Measurement uncertainties

2.4.1 Uncertainty on visual estimation of drop diameter

2.4.1.1 Dalsa Falcon 1.4M100 XDR Camera visualizations

Dalsa Falcon 1.4M100 XDR Cameras were used in both experiments of EHD injection and drop coalescence. The former used software ImageJ to measure drop diameters while the latter used Spotlight for drop falling velocity calculations.

For the experiments of EHD drop injection, one injected drop and the needle tip were taken on the same photo. The needle tip serves to set the scale in the photo graph, in order to measure the drop diameter. The meniscus anchored on the needle tip is clear in shape, and thus the inner diameter length can be measured in pixels. The inner needle diameter is already known, and this then can help to convert pixels to millimeters.

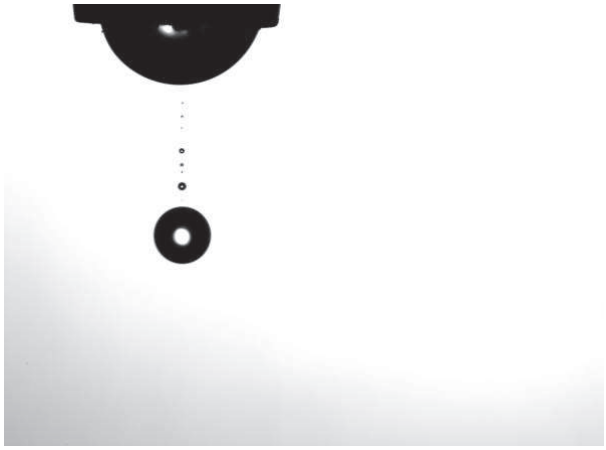

Fig 2.14. Drop injected in EHD injection set-up (25/04/2013, MSP5 1.3ms).

The image taken by the Dalsa camera on Fig 2.14 is composed of 1392*1024 pixels. It shows an injected droplet of quite large diameter (about 250 microns). For increased accuracy, we zoom in on the drop image and use a pixel – counting software. The measurements of drop diameter were done at different angles across the drop, which can be seen on the window next to the drop (Fig 2.15). The values of the diameter were measured in pixels, shown on the last column named 'Length'. The values are not integers because the software ImageJ has a subpixel resolution of the starting and the end points of the yellow line segment.

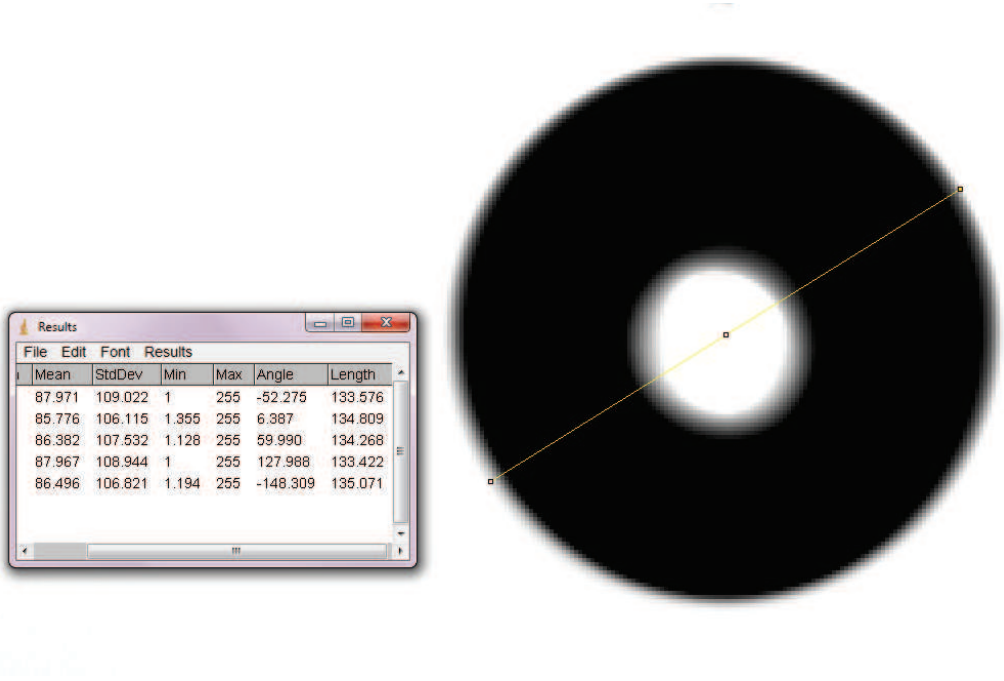

Fig 2.15. Measurements of drop diameter by using ImageJ software, according to measurements at different angles (seen 'Length' on the window), the uncertainties done by experimenter is $\pm$ 1 pixel.

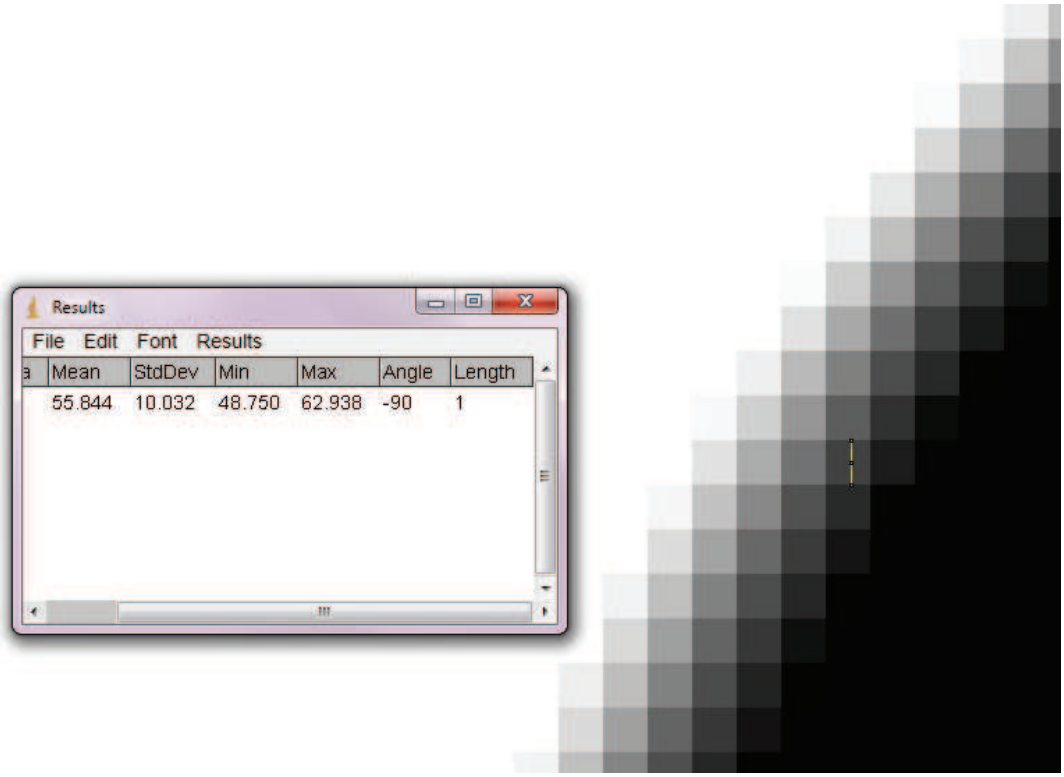

Fig 2.16. Further zoom in on the boundary of the drop.

Further zooming in around the boundary of the drop (Fig 2.16) shows that the gray levels of the neighboring pixels are not smoothed (Gray level is uniform on one pixel, whose length is measured as '1' by the software). During all the measurements of length using ImageJ, the starting point and the end point of the yellow line segment should be fixed manually. The uncertainty of the diameter measurement is estimated to be $\Delta n = \pm 1$ pixel, with n the measured diameter of the drop in pixels. For the uncertainties of the calibration, the length of the inner needle diameter was also estimated to within ± 1 pixel.

At the moment of calibration, the length in pixels of the needle inner diameter x was set as reference and was measured manually. Thus this involved also one pixel of uncertainty. The real needle inner diameter is $2R_{cap}$ which is a fixed value in millimeters, n is the number of pixels across the drop and D is the real drop diameter in millimeters.

$$\frac{x}{2R_{cap}} = \frac{n}{D} \tag{2.1}$$

The combined standard uncertainty is computed by summation in quadrature (Bell 2001), assuming that the origins of the different individual uncertainties are independent. The summation in quadrature is applied on the uncertainty values when the combination is a sum or a difference and on the fractional uncertainties when the combination is a product or division. The combined uncertainty on drop diameter D calculated using equation (2.1) is:

$$\frac{\Delta D}{D} = \sqrt{\left(\frac{\Delta n}{n}\right)^2 + \left(\frac{\Delta x}{x}\right)^2} \tag{2.2}$$

The droplet diameter D is 3 to 15 time smaller the needle diameter. Then inside the square root the second term is much smaller than the first one and can be neglected. Thus the uncertainties can only take account of the uncertainties of the drop diameters measured in pixels.

$$\frac{\Delta D}{D} \approx \frac{\Delta n}{n} \tag{2.3}$$

For a drop with 134 pixels diameter, the relative uncertainty of drop diameter is $\Delta D/D = 1/134 = 0.75$ %. The relative uncertainty is small and thus, in single drop injection experiments done in the EHD injection setup, drop diameters were estimated using this method.

For experiments done in the drop coalescence setup, the Dalsa Cameras are placed lower and the needle tip is largely out of the camera vision field. It should be noted that the cameras are turned at 90° to get the largest recording length in the direction of the drop falling path. The vision field of the Dalsa camera is 1392*1024 pixels. Thus the two drops are aligned horizontally on all photos. The calibrations are done by lowering the needle into the camera field of vision. Two photos were taken through the needle descending process and the distance between the two can be read on the mechanical micro-screw holding the needle. This calibration will then be verified by measuring the outer diameter of the needle. The real value of the needle outer diameter is D_{ext} = 1.057 mm. This calibration uncertainty can also be neglected compared to the measured drop diameter uncertainties (in pixels).

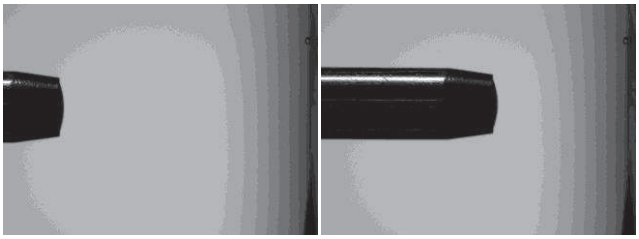

Fig 2.17. Move of the needle in Dalsa Camera vision field for distance calibration (03/06/2015).

After the calibration has been done, the measurements were carried out using Spotlight software, because this software can follow drop falling paths from a set of successive images. As a second example, a very small single droplet, with diameter d smaller than 70 microns, injected in the drop coalescence setup is shown on Fig 2.18.

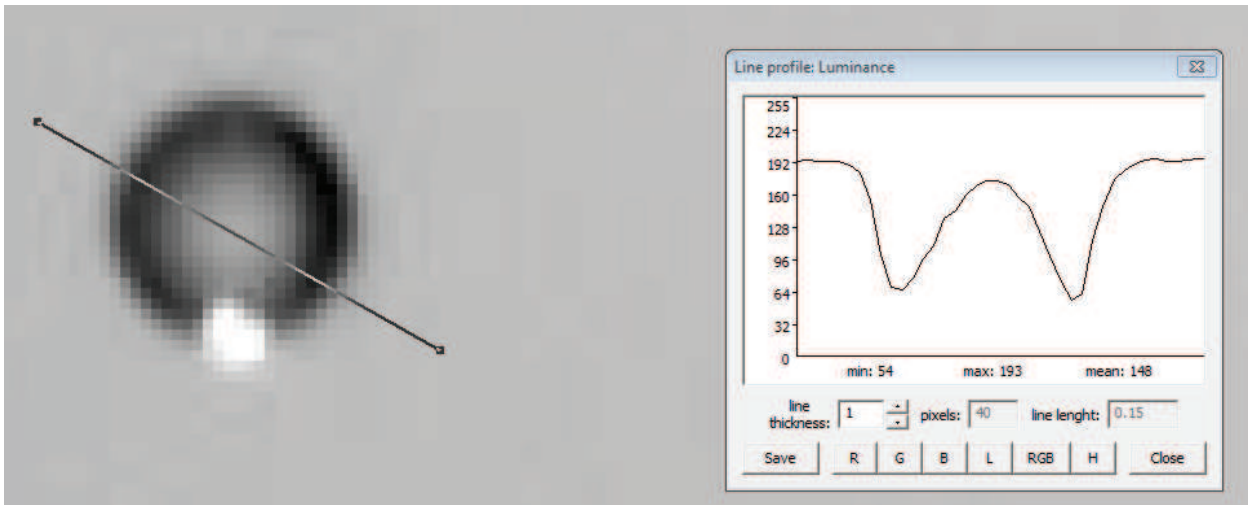

Fig 2.18. Measurements of the gray values though the drop (26/05/2015, –MSP4 injection, -5250 V).

The image is taken with a stronger zoom-in, so that the drop diameter D is only about 20 pixels on the image. A line is drawn across the drop as a probe of measurement of gray levels. On the right of Fig 2.18 is the measurement window with the gray value curve presented as 'line profile luminance', 'pixels' gives the number of pixels on the line and 'line length' gives the value after converting pixels into millimeters by the calibration process. On Fig 2.18 the boundaries of the drops appear very fuzzy. One straight line cut the drop into two parts, and the variations of gray values were measured along this line. The maximum gray value was located out of the drop and the minimum values were situated on the boundary of the drops. At the center of the drop, the gray value is high because the drop was a bit transparent to background light. The boundary location was determined at the average gray value between these maximum and minimum. For the measurement it is important to avoid the reflection light spot on the drop (white spot on the image).

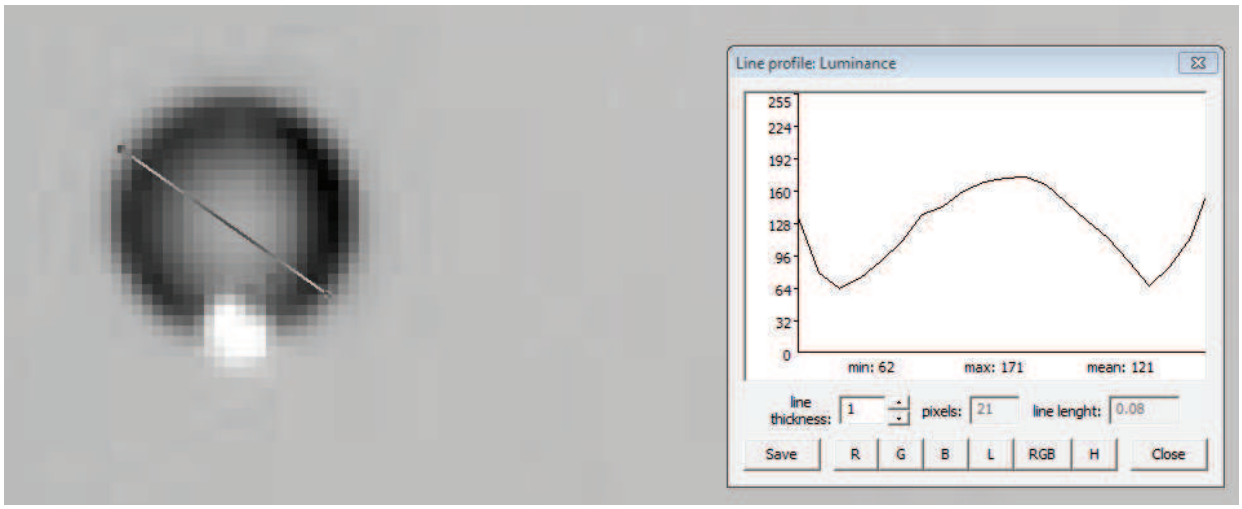

Fig 2.19. Measurements of drop diameters (26/05/2015, –MSP4 injection, -5250 V).

On Fig 2.19 the line of measurement is shortened with two extremities locating on the drop boundary. The uncertainty of the drop is estimated to be 1 pixel, and the relative uncertainty of the drop on the figure above is 1/21 ≈ 4.8 %. Through calibration process of that set of images, the scale is 303.33 pixels/mm, and the real droplet diameter is 0.069 mm.

2.4.1.2 AOS S-MOTION 1683 Camera visualization

The AOS camera has a fast motion which helps to visualize meniscus dynamics through drop injection process and drop coalescence moments when two falling drops approach each other. The AOS

Camera was also turned 90° to have the maximum number of pixels along the drop path. The vertical positions of the AOS camera are different depending on experiments. In single drop injection experiments, this camera was used to observe the meniscus dynamics. Thus the vision field was placed at the height of the needle tip, and the calibration of the images used the diameter of the needle. In drop coalescence experiments, the AOS camera only took photos in the zone where the drop coalescence would occur, with a strong zoom in. The calibration of AOS was done by taking first, one photo of the needle tip. The diameter of the needle was used for calibrations. For both cases the AOS Camera was speeded up of 8000 fps with a 4 µs shutter speed. This reduced the spatial resolution to 250*200 pixels. One example of single drop injection, identical to the case on Fig 2.18 and Fig 2.19 is shown below (Fig 2.20).

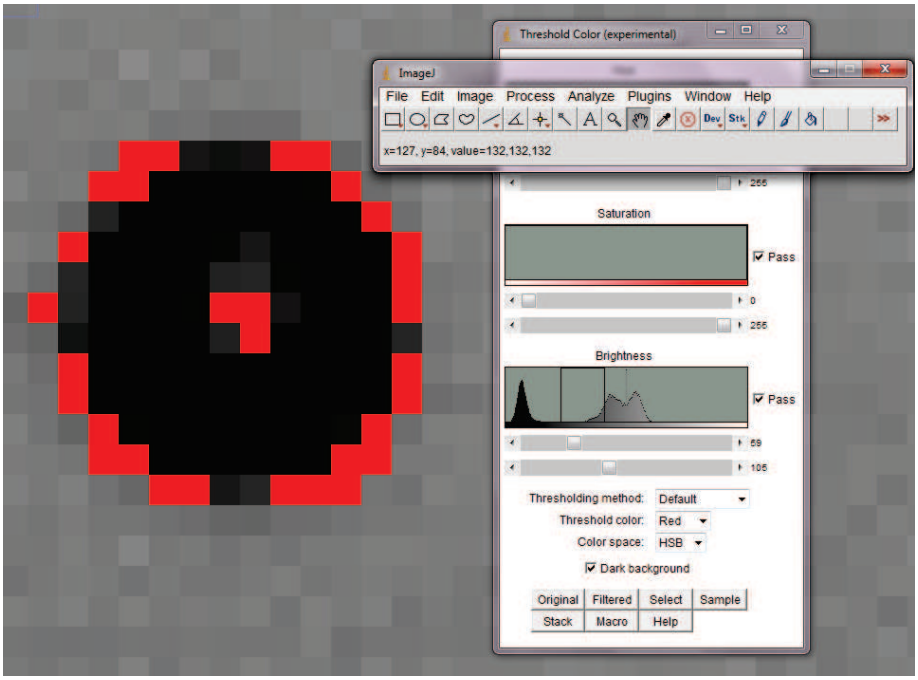

Fig 2.20. Visualization of injected drops by using AOS camera (26/05/2015, –MSP4 injection, -5250 V).

Fig 2.20 shows the photo taken by the AOS camera during drop injection process, and the drop contour was drawn using ImageJ. Despite this software having subpixel accuracy, it cannot define drop boundaries within pixel resolutions. To overcome this problem, newly developed software AMILab by (Trujillo-Pino et al. 2013) is used for measurements. Once the drop boundary was determined within pixel uncertainties and was drawn on the image, the diameter of the drop could be measured using ImageJ.

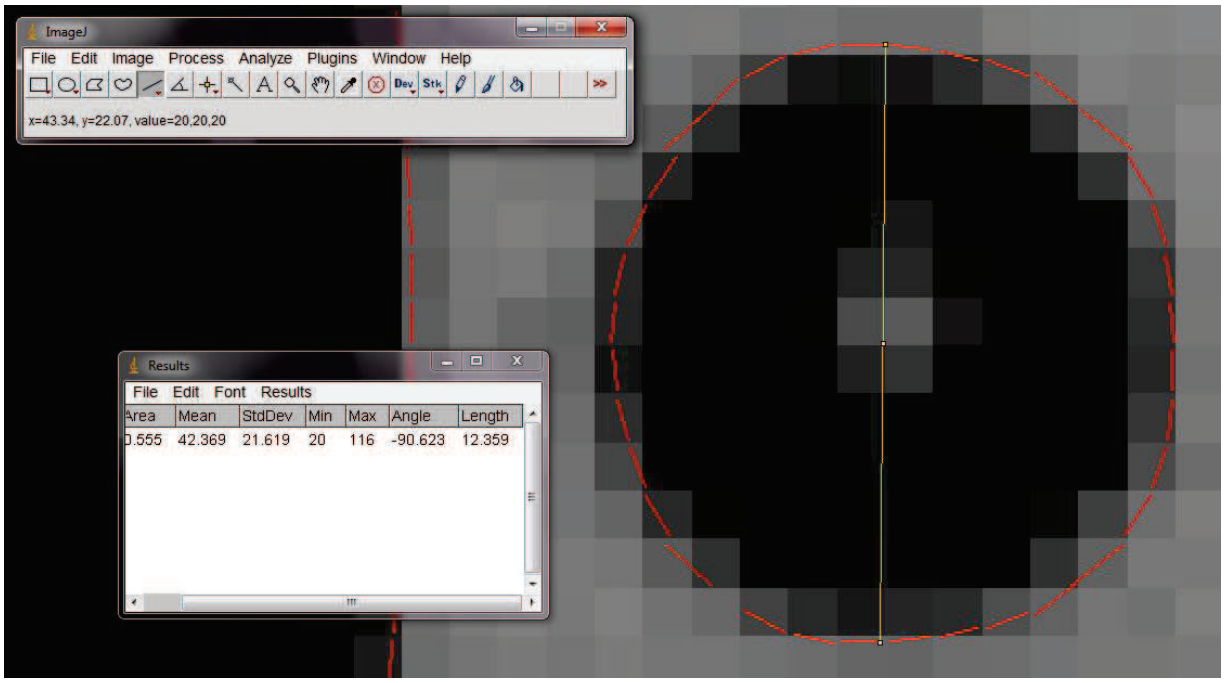

Fig 2.21. Diameters are measured by ImageJ with the help of subpixel resolution given by AMILab, of photo taken by AOS Camera (26/05/2015, –MSP4 injection, -5250 V).

On Fig 2.21 the drop boundaries in red line were drawn by AMILab software. For subpixel boundary (drawn in red), the threshold was set to 80, and the diameter of the drop was measured by ImageJ to be 12.359 pixels. For photos taken by AOS camera, the calibration was found equal to 153 pixels/mm by measurement of the needle diameter on the same photo. Thus the real diameter of the drop is of 0.0808 mm. The drop diameter was also calculated through its falling velocity, and the method is described in Chapter 4. The resultant drop diameter is 0.0798 mm. The two measurements are both around 0.08 mm as measured on Fig 2.19 by Spotlight software. The drop diameter measurements performed using Spotlight software give fewer significant digits.

2.4.2 Uncertainty on transient high applied voltage

2.4.2.1 Waveform Generator

The electric devices used in experiments have calibration uncertainties. The most important electric device is the waveform generator which determines the transient value of voltage during the pulse trains, and the return to zero after the pulse. During the drop injection process, the water bridge between formed drop and the meniscus should be cut after the shutdown of voltage to ensure

electric neutrality of injected droplets (Raisin 2011). Thus a possible offset zero is very important to ensure that when the pulse is finished, there is no tension applied on the electrode which might potentially influence the water meniscus on the needle tip. The functions of the Wavetek 395 are not sure to work well and it had a small deviation of 0.1V for the offset value. This deviation is amplified, 2000 times and at the exit of the amplifier, the deviation could reach to 200V. One conclusion was to change it for a newly fabricated waveform generator for a better accuracy.

The offset value helps to modify a waveform location compared to the grounded value 0. For the generator Agilent 33500B Series, the 0 offset has a small derivation to the grounded value. Checked on the oscilloscope, this value is of +140 µV above the ground. This value is not due to the accuracy of the oscilloscope because the latter has an uncertainty much smaller than that value, of about 3.8 µV. Thus for this +140 µV amplified by the amplifier 20/20C, it gives 0.28 V at the exit of the amplifier.

2.4.2.2 Trek amplifier

The high voltage amplifier Trek 20/20C connects directly to the electrode in the test cell. According to the commercial information, the offset of the amplifier is less than $\pm$ 2V. This value is good given that the electrode well returned to zero after application of high voltage. The slew rate of the amplifier is defined as the slope of the transient voltage: dV/dt. According to the manufacturer, the amplifier allows a maximum slew rate greater than 450 V/µs (Anon n.d.). This amplifier can generally give accurate values of electric fields following the created electric signals in waveform generator. Fig 2.22 is one photo taken from the screen of the oscilloscope. The dark blue curve is the wave form created on the waveform generator, and the green curve is the output signal of the amplifier already divided by a factor of 2000. In this case, the other two curves of the light blue one and the purple one are the outputs of the two Dalsa cameras. When this photo was taken, the two cameras were not triggered up. In other experiments one of the light blue curve or the purple curve follows the signals sent from the computer to see whether triggers were generated correctly. On the oscilloscope, the dark blue line is of 2.00 V scale while the green curve is of 1.00 V. Clearly the two curves are of the same shapes, and the output of the amplifier follows the input signal well.

However limitations of the amplifier dynamics have been reached when trying to generate pulses with high amplitude and fast changes of polarity. Fig 2.23 shows the pulse shape MSP10 returned by the amplifier and compared to initial signal.

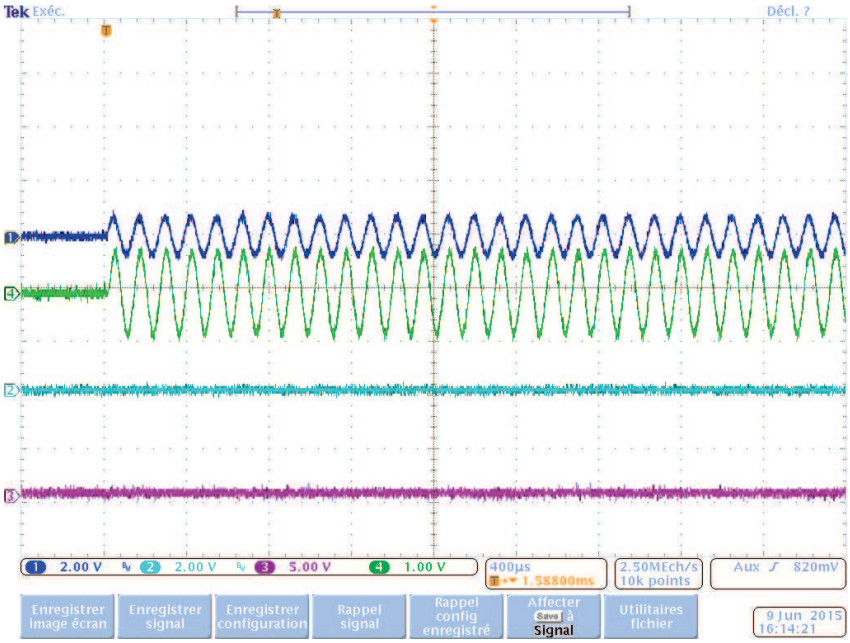

Fig 2.22. Verification of sinusoidal signals by the oscilloscope Tektronix DPO 4034. The blue curve is the input signal generated by the house developed software in the computer and the green curve is the output signal from the amplifier Trek 20/20C, already divided by a factor of 2000.

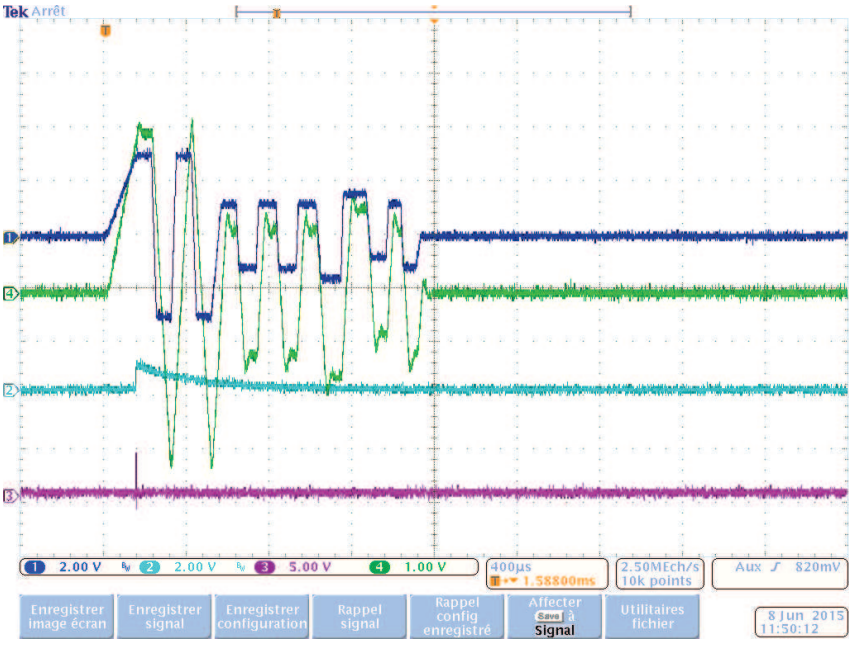

Fig 2.23. Screen image of oscilloscope Tektronix DPO 4034 which survey the signals of all outputs.

The blue line is the signal output of wave generator Agilent 33500B Series. The green line is the signal returned by the amplifier. The two other lines show the signals of the two Dalsa cameras, and they are not used in this photograph. The deformations of the light blue line and the purple one are merely noise. It is obvious that the amplifier has deformed the input signal into a form of a bigger oscillation while the offset of the signal stays close to 0 volt. The major part of this defection is probably due to the length of the electric wire which connects the amplifier to the electrode in the test cell. This wire had a capacity of an order of magnitude 100 pF/m, and a length of about three meters. Thus the total capacity between the amplifier and the test cell is estimated to be $C = 3*10^{-10}$ F. This wire cannot be reduced to help approach the amplifier to the test cell because of spatial constrains. The electric wire acts as a capacitor and it slows down the changes of voltage. To put it in calculations, two points are taken marked with quadrilaterals and pentagons on the figure below. The peak to peak voltage of the blue curve is identical to the green curve, of about 12 kV. The total duration of the MSP10 pulse is 1.52 ms and according to the pulse shape, the horizontal distance of the blue curve (pentagon mark to next pentagon mark on the figure) is 24.1 µs. That of the green curve revealed from the figure (quadrilateral to next quadrilateral) is 100 µs. For the blue curve, the peak to peak voltage divided by the time used is 12 kV / 24.1 µs = 498 V/µs. This value of slew rate should be allowed by the amplifier theoretically. However in reality the amplifier follows the green curve. For the green curve, the slope is 12 kV/ 100 µs = 120 V/µs, much smaller than the maximum slew rate indicated by the manufacturer.

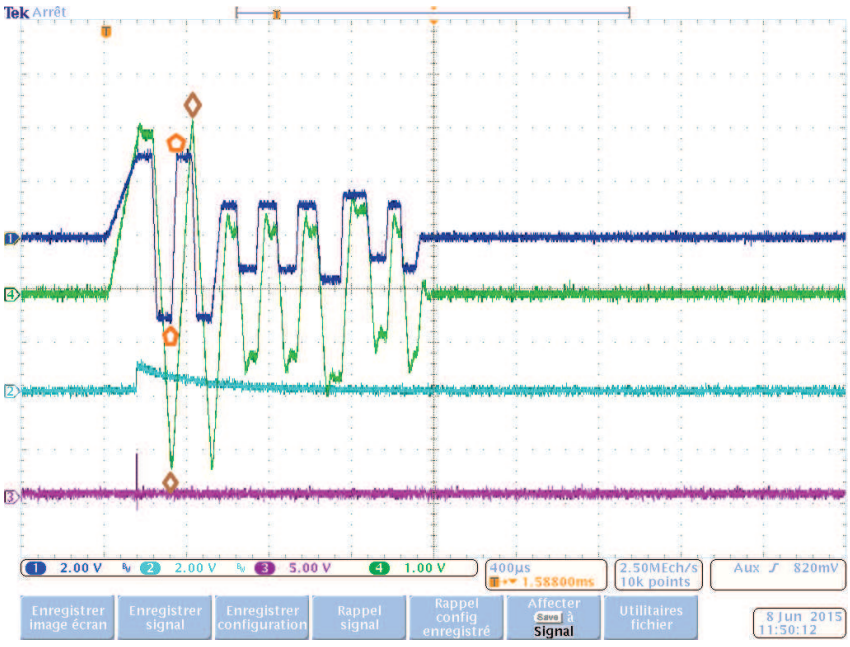

Fig 2.24. Screen image of MSP10 with two marked points shown by oscilloscope Tektronix DPO 4034 which survey the signals of all outputs.

The limiting current of Trek 20/20C is 20 mA. Using this value, the equation of current with an addition of capacitor can be written as follows.

$$i = C\frac{dV}{dt} \tag{2.4}$$

Here C is the capacity, i is the limit current, and V is the voltage. dV/dt is the slew rate. Taking the slope of the green curve, dV/dt = 120 V/µs, with i = 20 mA, then the calculated capacitor is $C = 1.67*10^{-10}$ F. The capacitor has the same order of magnitude as the electric wire between the amplifier and the electrode. It is confirmed that this deformation of the pulse shape may be due to the electric wire which connects the amplifier to the electrode in the test cell.

2.4.3 Uncertainty on mechanical position

The position of the needle with respect to the HV electrode has an influence on the electric field. For the EHD injection setup, the height of the needle is measured by a ruler with 1 mm uncertainty on 15 mm of total height. The relative uncertainty is 6.7 %. In the drop coalescence setup, the needle position is surveyed by a CDD camera and the distance can be measured on the screen with a magnification factor of about 30. The exact scale is given by measuring on the screen the outer diameter b' of the needle (b' = 3 cm), and comparing with the real needle diameter b = 1.057 mm. Then the height H of the needle over the HV electrode can be calculated for the distance H' on screen:

$$\frac{b}{b'} = \frac{H}{H'} \tag{2.5}$$

$$H = \frac{b}{b'}H' \tag{2.6}$$

Equation (2.6) gives relative uncertainty of δH/H.

$$\frac{\delta H}{H} = \sqrt{\left(\frac{\delta b'}{b'}\right)^2 + \left(\frac{\delta H'}{H'}\right)^2} \tag{2.7}$$

The second term under the square root is much smaller than the first one, because of the small needle diameter and the calculated uncertainty is:

$$\delta H/H \approx \delta b'/b' \approx 3\ \%.$$

2.5 Oil properties

2.5.1 Model oils and measured characteristics

Liquids used for experiments such as EHD injection and drop coalescence, consist of distilled water, tap water mixed with 35 wt% NaCl, Marcol 52, Marcol 52 mixed with 0.001 wt% Span 80 and Primol 352. These different liquids were used in different experiments according to their properties. Distilled water is used for EHD injection experiments; however, for drop coalescence experiments tap water mixed with 3.5 wt% NaCl took the place of the former one, aimed at approaching the real water in crude oil conditions. Marcol 52 and Primol 352 are oils for medical and other food control or cosmetic uses; they are both products from crude oil refineries, transparent oils. Marcol 52 oil is used in EHD injection experiments and drop coalescence experiments while mixed with 0.001 wt% Span 80. The latter is a trading name of sorbitan monooleate, a nonionic surfactant often used as a w/o emulsifier or as an o/w emulsifier in cosmetics or food preparation. Its formula is $C_{24}H_{44}O_6$ and specific weight is 429 g/mol (Benmekhbi et al. 2014). Marcol is a mixture of saturated hydrocarbons and its advantage compared to other model oils lies in its components stability to oxidation. Such properties assure that water-oil interfacial tension change is not due to any possible molecular chemical structure change caused by oxidation since this oil content generally stayed in test cell for weeks once filled up. Primol 352 exhibits the same properties as Marcol 52, the difference is that Primol 352 is more stable while with a higher viscosity (Anon n.d.). During the PHD Primol was only used in EHD injection experiments.

2.5.1.1 Interfacial tension measurements

Interfacial tension is the force on the interface between two immiscible phases which holds a liquid medium in its proper environment. This interfacial tension is often referred to as capillary tension which is generally discussed in the domain of fluid mechanics as it plays an important role in fluid movements, especially in liquid column breakups and droplet formations. The movements of a liquid drop in its surrounding space or the deformation of its own shape depend on many parameters,

including its interfacial tension with respect to the surrounding medium. This interfacial tension between different liquid mediums, including liquid – air interface, can be measured in different experiments. The most used are Pendant drop formation and the Du Noüy Ring method. For our experiments, this interfacial tension is measured for oils such as Marcol 52, Primol 352 or Marcol 52 mixed with Span 80.

The Du Noüy Ring method and Pendent Drop method were used to measure water-oil interfacial tension.

The Du Noüy Ring method

The Du Noüy Ring method uses a platinum ring initially immersed below the interface separating the two immiscible liquids (here in water, the heaviest fluid). Slowly lifting this ring from the interface into the upper liquid permits the measurement of the net fluid force coming from attached liquid meniscus on the ring. This maximum lifting force just before the rupture of the liquid meniscus is directly related to the interfacial tension. This Noüy Ring method is used for measurements in pure Marcol 52, and for pure Primol 352 with distilled water, and the tensiometer used is KRUSS School Tensiometer K6. This tensiometer has a correction coefficient only under conditions of measured interfacial tension smaller than 25 mN/m and with a density difference between the two liquids of more than 1 g/ml. Thus for our experiments, no correction term needed to be considered. For pure Marcol 52 with distilled water, the measurements were performed from five minutes (the time for preparation of the liquids) to 240 hours (about ten days). During the waiting time before making the measure, the beaker containing Marcol 52 is covered by a reversed beaker as shown on Fig 2.25, in order to prevent dusts falling into the oil. It should be mentioned that the Marcol 52 oil is taken from the bottle, and is not directly the oil used in the test cell.

On Fig 2.26, it shows that the values measured decrease from 43 mN/m, for immediate measurement, to 21.8 mN/m at the end of 240 hours. The interfacial tension of pure Marcol 52 and distilled water decreases with time to a quite stable value around 22 mN/m while at the beginning the interfacial tension decreased very fast. One point of σ=20.5 mN/m at the end of 72h24min is largely out of the tendency curve, probably due to some accidental pollution (dust particles) of the interface.

Fig 2.25. Marcol 52 pure in beaker is covered by another reversed beaker to avoid contamination by dusts.

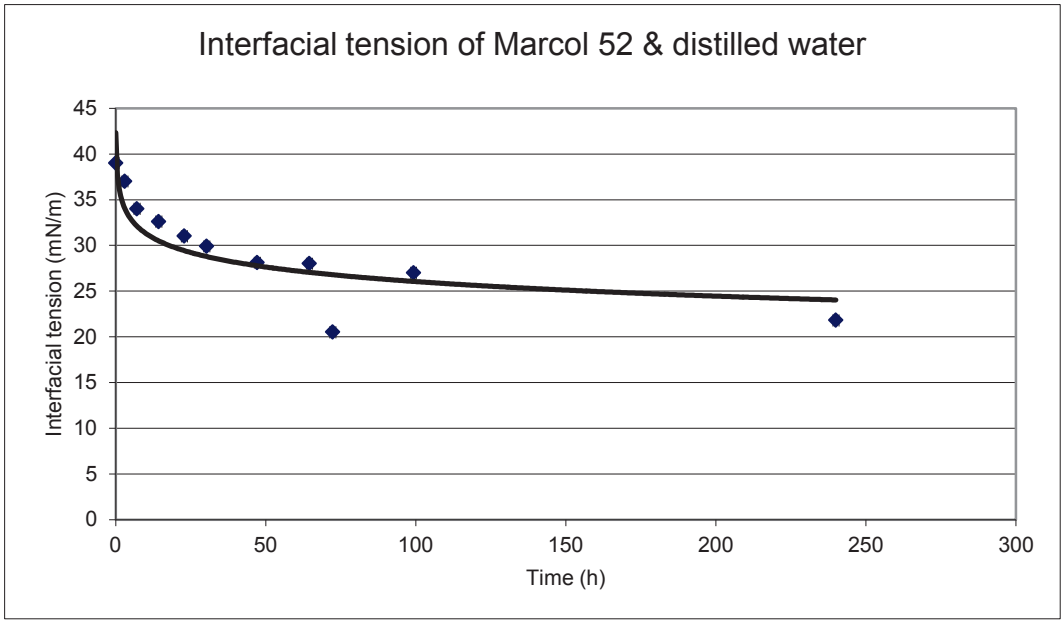

Fig 2.26. Interfacial tension measurements of Marcol 52 with distilled water (Du Noüy ring method).

The Pendant Drop method

The Pendent Drop method was used to measure the interfacial tension of Marcol 52 with different additives. Two kinds of measurements were done: one of 3.5 wt% NaCl contained tap water with pure Marcol 52, another of the same salt water with 0.001 wt% Span80 addition in Marcol 52. The tensiometer used for measurements was KRÜSS Drop Shape Analyzer – DSA30s model. During

measurements, a glass cuvette is filled up with oil and a metallic needle with plate tip is plunged into the oil medium. This needle connects to a syringe filled with salt water.

Fig 2.27. Photo of KRÜSS Drop Shape Analyzer -- DSA30S model (http://www.kruss.de/products/contact-angle/dsa30/drop-shape-analyzer-dsa30/).

By dosing the syringe slowly, water content exits from the needle tip and forms a drop. Combined with gravity, this spherical drop slowly deforms into a pear shape, and the analysis of the interfacial tension is based on the water drop shape viewed by a camera placed behind (http://www.kruss.de/services/education-theory/glossary/pendant-drop/).

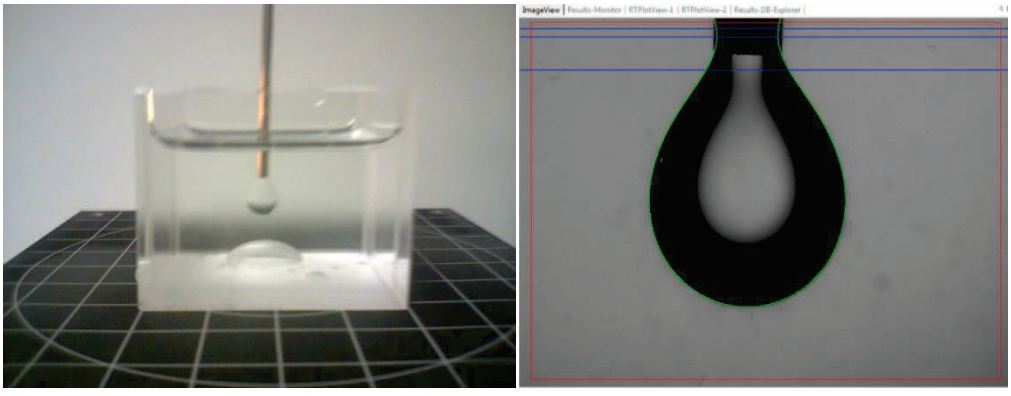

(1) (2)

Fig 2.28. (1) Pear form of drop shape hanging on the needle tip; (2) Hanging drop captured on the screen of analyze.

The calibration of the image depends on the outer diameter of the needle used and the shape parameter calculated by the software should reach more than 0.5 to begin measurements. Generally the measurements end upon detachment of the hanging drop. Due to the accumulation of surfactants on the drop surface the interfacial tension decreased further until a point where it could no longer sustain the drop hanging on the needle tip under gravity effect.

Sum up of all the results with Marcol 52

The results of interfacial tension (IFT) measurements are summed up below. The measurements are of Marcol 52 & tap water by the Du Noüy Ring method, Marcol 52 & 3.5 wt% NaCl solution, 0.001 wt% Span80 in Marcol 52 & 3.5 wt% NaCl solution, 0.0025 wt% Span80 in Marcol 52 & 3.5 wt% NaCl solution and 0.010 wt% Span80 in Marcol 52 & 3.5 wt% NaCl solution.

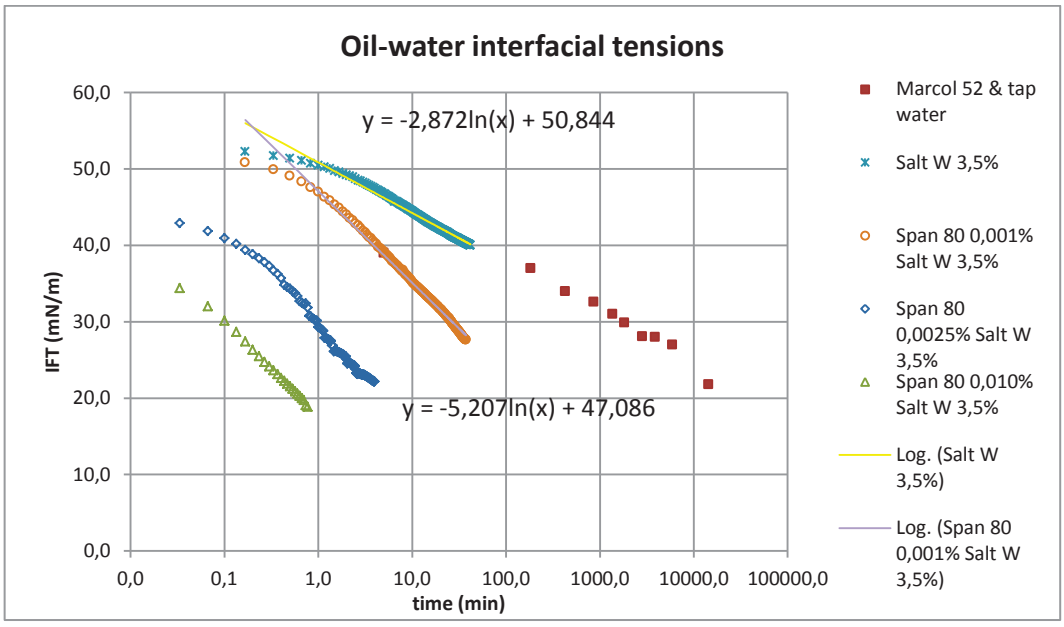

Fig 2.29. Interfacial tension measurements of Marcol 52 with different additives.

The curves of surface tension on Fig 2.29 decrease with increasing time, and the more Span80 is added, the lower the interfacial tension is. The curve of 0.010 wt% Span80 has the shortest duration because the hanging drop detached rapidly under the weak capillary tension which cannot hold the weight for longer. The curves are fitted by logarithm trend lines. The decrease in interfacial tension is caused by surfactant concentration deposition on a liquid drop interface with another immiscible

liquid (von Szyszkowski 1908). The equation between the surfactant concentration on the liquid interface and interfacial tension is shown below (Ervik 2016).

$$\sigma(\Gamma) = \sigma_0 \left[1 + \beta \ln\left(1 - \frac{\Gamma}{\Gamma_\infty}\right)\right] \tag{2.8}$$

Here $\beta = R_{gas}T\Gamma_\infty/\sigma_0$, R_{gas} is the constant of ideal gas, T temperature in Kelvin and Γ_∞ the maximum surface concentration of surfactant on drop interface. In equation (2.8) σ_0 is the interfacial tension without surfactant and Γ should be the equilibrium interfacial concentration for a given bulk concentration.. We use this equation although Γ is in fact in our case a transient value that increases with the hanging time of the droplet. The equation (2.8) can be rewritten as follows.

$$\frac{\Gamma}{\Gamma_\infty} = 1 - \exp\left[\frac{\sigma(\Gamma) - \sigma_0}{R_{gas}T\Gamma_\infty}\right] \tag{2.9}$$

For the calculations, T = 295 K and σ_0 is taken as the first value for all interfacial tension measurement series. The value $\Gamma_\infty = 4.18*10^{-6}$ mol/m^2 is taken from (Benmekhbi et al. 2014) at the interface between brine (salted water) and a Primol-decane mixture (Γ_∞ = 4.82 to 5.55*10^{-6} mol/m^2). It might be a little different with Marcol, but in the same range of magnitude. The graphs are then drawn on Fig 2.30.

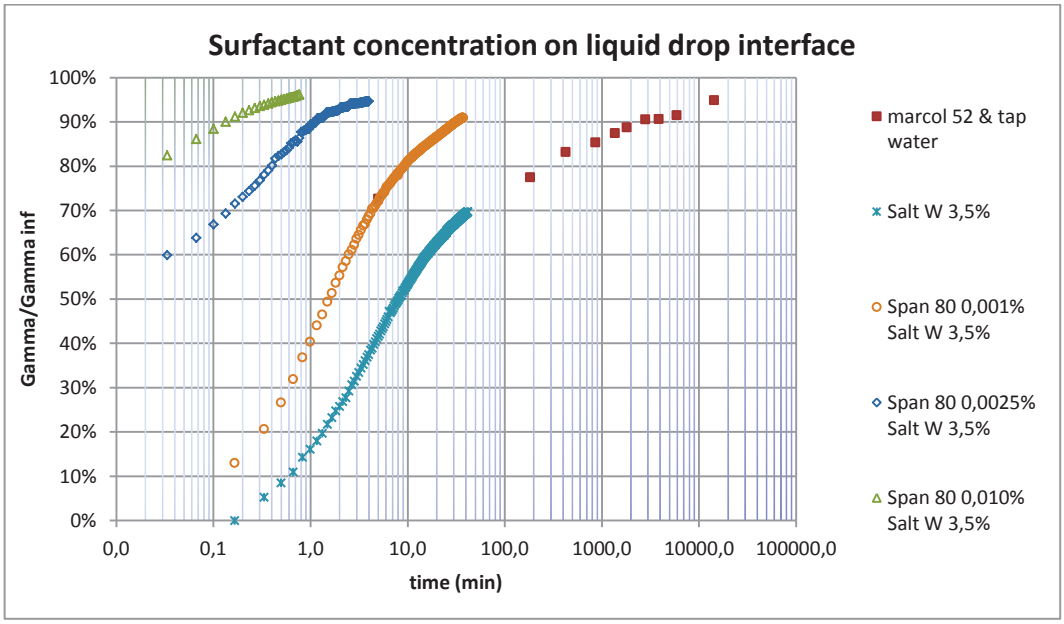

Fig 2.30. Surfactant concentration on liquid drop interface for Marcol 52 with different quantities of Span80.

On Fig 2.30 it is shown that the surfactant concentrations deposited on the liquid drop interface increase towards 100 %. High concentration of Span80 in liquid bulk deposits faster on an immiscible liquid drop interface. In experiments only two curves are used: Marcol 52 & 3.5 wt% NaCl solution and 0.001 wt% Span80 in Marcol 52 & 3.5 wt% NaCl solution.

As the interfacial tension decreases logarithmically, the uncertainties of the interfacial tension over a certain time interval can be calculated by using trend line equations. The trend lines have following forms.

$$y = A - Bln(x) \tag{2.10}$$

Here A and B are constants, x is a variable and y describes the interfacial tension. Then the uncertainty of y can be calculated as:

$$\delta y = \delta A + \delta(Blnx) = \delta(Blnx) = \frac{B\delta x}{x} \tag{2.11}$$

The relative uncertainty of y is written as:

$$\frac{\delta y}{y} = \frac{\frac{B\delta x}{x}}{(A - Blnx)} = \frac{\delta x}{x\left(\frac{A}{B} - lnx\right)} \tag{2.12}$$

With y replaced by σ, x is replaced by t, A and B are replaced by the coefficients on fig 2.31. During experiments of drop injection or drop coalescence, before experiments of the day were carried out, one large water drop was pushed through to refresh the meniscus which stayed inside oil medium overnight. Between each drop injection the interval time was estimated to be 1.5 minutes. During drop injection, extracted drops could only partly refresh the meniscus. Considering all above parameters, the estimated interfacial tension of the water-oil meniscus occurs at t = 3 minutes with uncertainties corresponding to $\pm$ δt = 2 minutes of time durations. The uncertainties can then be expressed as a function of time. Starting from equation (2.10), the uncertainty can be calculated in a simpler way. For 3.5 wt% NaCl solution & Marcol 52, A = 50.844, B = 2.872, t = 3 min and δt = 2 min.

$$\frac{\delta\sigma}{\sigma} = 3.4\%$$

The interfacial tension (after 2 mn) is σ = 48 mN/m ± 3.4 %.

For 3.5 wt% NaCl solution & 0.001 wt% Span80 in Marcol 52, A = 47.086, B = 5.207, t = 3 min and δt = 2 min.

$$\frac{\delta\sigma}{\sigma} = 6.7\%$$

The interfacial tension (after 2 mn) is σ = 42 mN/m ± 6.7 %.

Interfacial tension with Primol 352

The Du Noüy ring method is used for interfacial tension measurements of Primol 352 – distilled water. Primol 352 exhibits a more stable interfacial tension trend compared to Marcol 52. Primol 352 has interfacial tension decreases from 43.2 mN/m at the beginning, to about 36.2 mN/m.

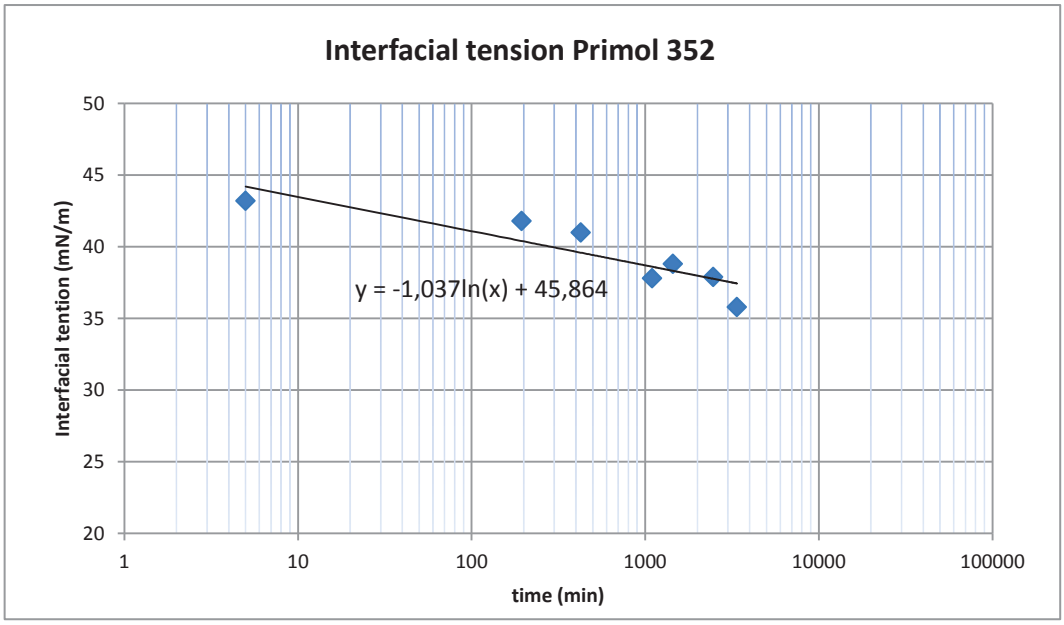

Fig 2.31. Interfacial tension measurements of Primol 352 with distilled water (DoD excel Primol 352).

From Fig 2.31 the interfacial tension of Primol 352 after 2mn is estimated to be 43 mN/m ± 1 mN/m (rough estimate from Fig 2.31).

2.5.1.2 Temperature measurements

The temperatures of the test oils are measured by EXTECH instruments 3 Channel Temperature Datalogger, Model SD200. The measured range is -50.0 – 1300.0 °C. The resolution of the apparatus is 0.1 °C.

2.5.1.3 Viscosity & density measurements

The densities and viscosities of the Marcol 52 with 0.001 wt% Span 80 in the test cell were measured with increasing temperatures. The viscosity of the oil was measured with a HAAKE Falling Ball Viscometer C. This viscometer serves to measure viscosities of transparent Newtonian liquids, and it comprises a temperature control bath filled with an appropriate liquid, and two cylindrical tubes, one inside the other. A nickel iron alloy ball of density ρ_R = 8.157 g/cm^3 is placed inside the inner cylinder which should be later filled with the liquid to be measured. Between the inner and the outer cylinder wall the thermal bath liquid circulates to fix the temperature of the inner liquid. The viscosity value relates directly to the time of the ball falling a defined distance marked on the cylindrical tube:

$$\mu = t * (\rho_R - \rho_o) * k \tag{2.13}$$

The μ is the dynamic viscosity, k is the ball constant given by the manufacturers with k = 0.0685, ρ_R is the density of the metallic ball given as 8.157 g/cm^3, ρ_o is the oil density at the bath temperature, and t is the ball drop time measured in seconds. Before each measurement it should take at least 15 minutes after the test temperature was achieved, to wait for the stabilization of the thermal transfer between the inner cylinder tube and the outer circulating fluid. The reproducibility of the machine is 0.5 % according to the manufacturers.

The oil density values are measured by Fischer hydrometer of CAT.No.11-555-D with measurement range of 0.820 – 0.890 g/ml, and increment of 0.0005 g/ml. This is a glass tube which floats inside the test liquid if the density of the latter is in the range of hydrometer measurements. The graduations are marked on the glass tube and the oil surface height read on the glass tube corresponds to the value of the oil density. This hydrometer floats in the oil medium in a large recipient and the entire recipient is immersed into the temperature controlled bath. Table 2.1 shows the decrease in both liquid density and dynamic viscosity when the temperature increases. These variations are linear.

Temperature T (°C)	ρ_o (kg/m^3)	μ_o (Pa.s)
17	830.0	13.43*10^{-3}
20	829.0	12.01*10^{-3}
23	828.0	10.72*10^{-3}
26	827.0	9.63*10^{-3}
29	826.0	8.75*10^{-3}

Table 2.1. Measured oil viscosity values and densities with increasing temperature.

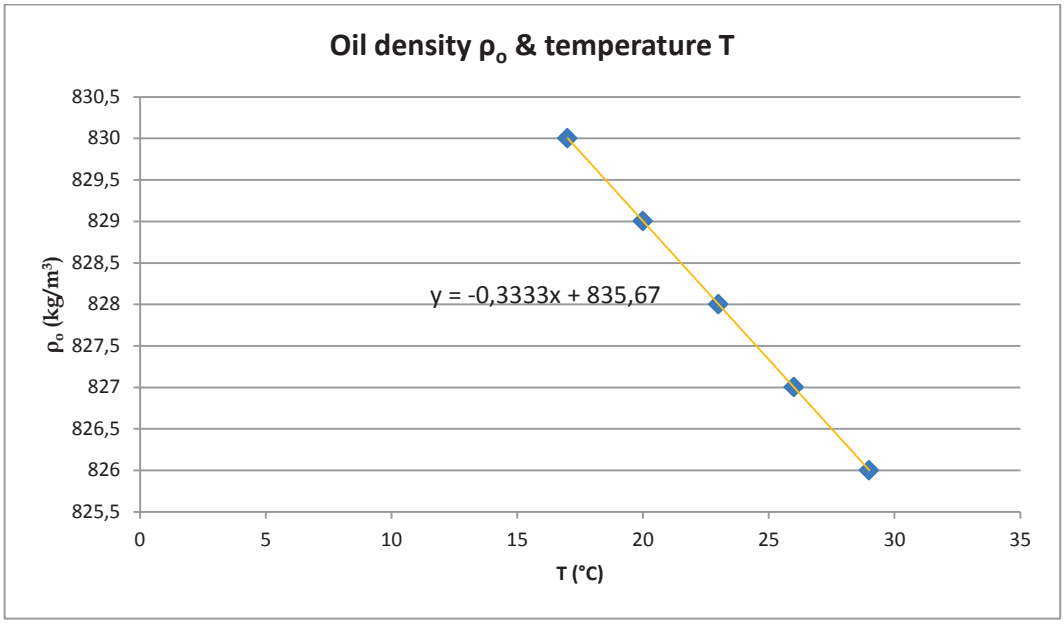

Fig 2.32. Graph of oil density ρ_o with increasing temperature T.

Fig 2.32 shows the oil density ρ_o as a function of temperature T. The trend line added is a linear function with a slope of $d\rho_o/dT$ = -0.3333 kgm^{-3}°C^{-1}. In experiments, oil temperature increases due to heating from the LED lights, and the augmentation is estimated to be 2 °C between the beginning and the end of experiments. For experiments done in winter the temperature is estimated to be 21 °C ± 1 °C, in spring and autumn the temperature is 23 °C ± 1 °C, and in summer the temperature is 25 °C ± 1 °C. Then the corresponding oil densities are: ρ_o (21 °C) = 828.67 kg/m^3 ± 0.33 kg/m^3, ρ_o (23 °C) = 828.00 kg/m^3 ± 0.33 kg/m^3, ρ_o (25 °C) = 827.34 kg/m^3 ± 0.33 kg/m^3, ρ_o (27 °C) = 826.67 kg/m^3 ± 0.33 kg/m^3.

The viscosity of the oil μ_o decrease with augmentation of the temperature T, and the graph is drawn on Fig 2.33.

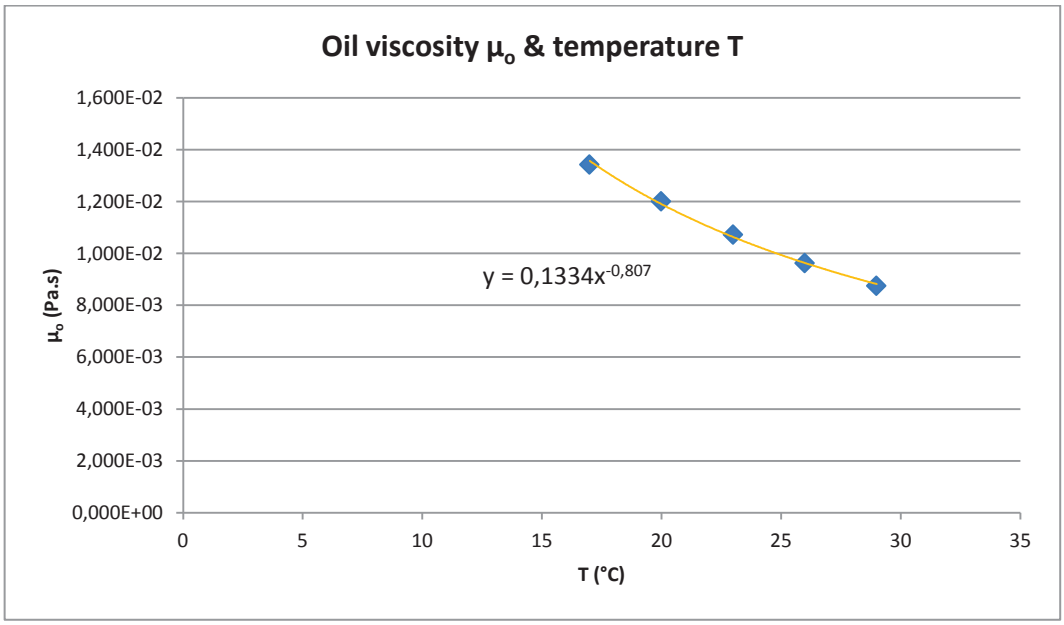

Fig 2.33. Oil viscosity μ decrease with increasing temperature T.

The relative uncertainty is calculated below.

$$\frac{\delta\mu_o}{\mu_o} = \frac{0.807\delta T}{T} \tag{2.14}$$

With uncertainty of δT = 1°C, the relative uncertainty for 21 °C is $\delta\mu_o/\mu_o$ = 3.8 %; for 23 °C = 3.5 %; for 25 °C = 3.2 %. The viscosities can be expressed as μ_o (21 °C) = 11.43*10^{-3} Pa.s ± 3.8 %; μ_o (23 °C) = 10.62*10^{-3} Pa.s ± 3.5 %; μ_o (25 °C) = 9.93*10^{-3} Pa.s ± 3.2 %, μ_o (27 °C) = 9.33*10^{-3} Pa.s ± 2.9 %.

2.5.1.4 Conductivity and relaxation time

The capacity and the conductivity of the oil are measured with a high sensibility resistivimeter IRLAB – LDTRP2 model. Both capacitance C and conductance G were measured in the test cell. The capacity value was measured with a very good repeatability C = 45.8 pF. With air the value was C_0 = 22.3 pF. That gives the relative permittivity, $\varepsilon_r = C/C_0$ = 2.1, which is the classical value for white oils, and the relative permittivity of water is taken equal to the classical value of 80.1. The conductance value G was a more fluctuating value, measured between 10^{-14} and 4.10^{-14} Ω^{-1}. It corresponds to oil conductivity $\sigma = \varepsilon/\tau$ between 0.4 and 1.5 10^{-14} S/m. The discharge time of the oil can be calculated directly as:

$$\tau = \frac{C}{G} \tag{2.15}$$

The calculated time is τ = 1000-5000 s. Thus the wandering free charge can stay a very long time inside the oil medium and influence the falling drops.

2.5.1.5 Summation of results

The liquids mentioned above all have their own properties such as capillary time, viscous time, interfacial tension, viscosity and density. Thus to define electric pulse duration for EHD injection, or to calculate Stokes velocities while two drops are falling in oil medium, these characteristics are very important to understand.

	T (°C)	ρ (kg/m^3)	σ (mN/m) (after 2 mn)	μ (Pa.s)
Water (taken from document)	20	1002.7	70	1.002 *10^{-3}
	25	1001.5		0.890 *10^{-3}
3.5 wt% NaCl solution (taken from document)	20	1029.1		1.070 *10^{-3}
	25	1027.6		0.955 *10^{-3}
3.5 wt% NaCl solution & Marcol	21	830	48 ± 3.4%	0.012 (taken from document)
3.5 wt% NaCl solution & 0.001 wt% Span80 in Marcol 52	21	828.7 ± 0.3	42 ± 6.7 %	11.43*10^{-3} ± 3.8 %
	23	828.0 ± 0.3		10.62*10^{-3} ± 3.5 %
	25	827.3 ± 0.3		9.93*10^{-3} ± 3.2 %
	27	826.7 ± 0.3		9.33*10^{-3} ± 2.9 %
Distilled water & Primol 352	21	863	43 ± 1	0.193 (taken from document)

Table 2.2. Different measured characteristics of used oils, parts of the values taken from documents are from (Copin-Montégut 2002) and the web ''ExxonMobil''.

Table 2.2 gives a summation of all the parameters that need to be used in later calculations or experiments. As it was illustrated before, the interfacial tension curves of distilled water & Marcol 52 matched the curve of 3.5 wt% NaCl solution & Marcol 52. Thus it is considered that for short time durations of interfacial tension measurements, the interfacial tension values revealed in the latter case are also valid for the former. In the next chapter, the high viscosity influence of Primol 352 will be illustrated in experiments.

2.5.2 Derived characteristics

2.5.2.1 Capillary time t_{cap}

Equation of t_{cap}

During the drop injection process, the dynamics of the liquid-liquid interface are affected by electric force, surface tension and surrounding liquid viscosity. With respect to inertia, surface tension has its characteristic time, which is called surface energy time scale. This time characterizes the dynamics of the liquid body under the effect of surface tension (Hsiao et al. 1988). Moreover when a fluid is flowing as a cylindrical column, disturbances propagating on its surface, called capillary waves, tend to break it up and the breakup time is of the order of the capillary time. The capillary time is calculated as follows (Vicent et al. 2013):

$$t_{cap} = \sqrt{\frac{\rho_w R_{cap}^3}{\sigma}} \tag{2.16}$$

In the case of drop injection experiments, the t_{cap} is capillary time, ρ is viscosity of the water, R_{cap} is the inner radius of the needle and σ is interfacial tension. This capillary time gives an idea of the life time of the water column generated by stretching the initial water meniscus, and this may give a rough estimation of the starting value of the electric pulse duration range.

Uncertainty calculations of t_{cap}

The relative uncertainty of t_{cap} can be expressed as a function of relative uncertainties of water density, inner radius of the needle and the interfacial tension respectively.

$$\frac{\delta t_{cap}}{t_{cap}} = \frac{1}{2}\sqrt{\left(\frac{\delta \rho_w}{\rho_w}\right)^2 + \left(\frac{3\delta R_{cap}}{R_{cap}}\right)^2 + \left(\frac{\delta \sigma}{\sigma}\right)^2} \quad (2.17)$$

By comparing the relative uncertainties of the water density, the inner radius R_{cap} and the interface tension, it is found that the relative uncertainty of t_{cap} depends mainly on the last:

$$\frac{\delta t_{cap}}{t_{cap}} = \frac{\delta \sigma}{2\sigma} \quad (2.18)$$

Here the interfacial tension varies with different model oils used in experiments.

2.5.2.2 Viscous time t_μ

Equation of t_μ

All fluids have a different viscosity and this parameter influences fluid dynamic behaviors under external forces. Thus for liquid thread breakup the viscosity also plays an important role (McKinley 2005). With high viscosity fluids , a liquid column or liquid bridge may increase the life time before break-up (Furbank & Morris 2007). The viscous time is an important factor used (as is the capillary time) in most cases of liquid thread breakup studies. In liquid-liquid configurations it may involve the viscosities of the two fluids:

$$t_\mu = \frac{\rho_w R_{cap}^2}{\mu_o + \mu_w} \quad (2.19)$$

For water drop injection in oil, ρ_w is water density, R_{cap} is the inner radius of needle, μ_o is the viscosity of oil. Generally this viscous time is the upper limit of pulse duration.

Uncertainty calculations of t_μ

As used previously, the relative uncertainties on the water density and the needle inner radius are considered to be much smaller than the relative uncertainty on the viscosities, due to the possible

variations of temperature. Moreover, the viscosity of water μ_w and its associated uncertainty is much smaller than the corresponding values for oil. Then the relative uncertainty on the viscous time can by simplified to be:

$$\frac{\delta t_\mu}{t_\mu} = \frac{\delta \mu_o}{\mu_o + \mu_w} \tag{2.20}$$

Here the viscosities vary with different oils used in experiments.

2.5.2.3 Reynolds number Re

The Reynolds number is a dimensionless parameter which compares the importance between inertial and viscous forces in fluid mechanics. It is represented as the ratio of momentum force to viscous force.

$$Re = \frac{\rho_o U L}{\mu_o} \tag{2.21}$$

In the case of our experiments, here ρ_o is the oil density, U is a characteristic velocity of the falling drop, L is the characteristic length which corresponds to diameters of droplets (McKinley & Renardy 2011), and μ_o is the oil viscosity. In experiments of falling drops inside a stagnant oil medium, one example will be taken as a water drop of diameter D = 0.14 mm falling inside Marcol 52 with its terminal velocity U = 0.28 mm/s. Then the calculated Reynolds number is Re = 0.003. This number is very small and it means that the experiments are completely within the classical Stokes regimes (Brennen 2005).

2.5.2.4 Weber number We

The Weber number is also a dimensionless parameter often used in fluid mechanics, and it compares the fluid disruptive hydrodynamic forces to surface tension forces (Pilch & Erdman 1987) (Anon n.d.).

$$We = \frac{\rho_o U^2 L}{\sigma} \tag{2.22}$$

Here, the ρ_o is the oil density, U is the velocity of falling drops, L is the characteristic length and σ is the surface tension.

2.5.2.5 Ohnesorge number Oh

The Ohnesorge number is a dimensionless parameter which relates the internal viscosity dissipation to surface energy. It can also be written as the square root of Weber number divided by the Reynolds number (Li 2008). This can also be referred to as the viscous number because it characterizes viscous effects on drop dynamics (Pilch & Erdman 1987). Oh number is widely used in describing drop ejection mechanisms, and this number is independent of liquid motion (Lefebvre 1988).

$$Oh = \frac{\mu_o}{\sqrt{\rho_o \sigma L}} = \frac{\sqrt{We}}{Re} \tag{2.23}$$

Here, μ_o is the viscosity of the fluid, ρ_o is the density, σ is the surface tension and L is the characteristic length (Mundo et al. 1995). A low Oh number means that the dynamics of droplet deformation is mainly controlled by the surface tension, while a high Oh number denotes the dominant effect of viscous dissipation (Li 2008).

2.5.2.6 Eötvös number

For a drop falling inside another immiscible liquid, the drop shape should be determined because its shape can possibly be modified due to the resultant effects of body force, viscosity force and capillary force. This determination involves Eötvös number calculations, which is a dimensionless number and shows the relative importance of the surface tension force and gravity force on the moving drop. If the Eötvös number is relatively low, the surface tension force is stronger than the gravity force and the deformation of the drop is small. With a relative high Eötvös number, the drop can have a more important deformation of its shape, even breakup in liquid surroundings (Fakhari & Rahimian 2009; Clift et al. 2005). The expression for the Eötvös number is written as:

$$Eo = \frac{\Delta\rho g r^2}{\sigma} \tag{2.24}$$

The estimation of the Eötvös number values is done by assuming one given falling salt water droplet inside 0.001 wt% Span80 contained in Marcol 52 at 23 °C. The density difference $\Delta\rho = \rho_w - \rho_o$ = 196 kg/m^3, acceleration g = 9.8 m/s^2, drop radius r = 0.07 mm (D = 0.14 mm for drop diameter) and surface tension σ = 42 mN/m. These numerical numbers are just shown as an example not far from values taken from experiments. The result is Eo ≈ 10^{-4}. To be more precise, this value should be combined with previously calculated Reynolds number Re = 10^{-3} on Table 2.3 to confirm that the free falling drops are well in spherical shape.

2.5.2.7 Electric capillary number

When the droplet is subjected to an electric field stress, the electrocapillary number should be introduced to determine whether the drop is subsequently deformed. The electrocapillary number is the balance between electric pressure and capillary pressure (Bird et al. 2009).

$$\varepsilon_c = \frac{\varepsilon_r \varepsilon_0 E^2 r}{\sigma} \tag{2.25}$$

Here ε_c is the electrocapillary number, ε_r is the relative permittivity of the medium and ε_0 is the permittivity of the void. E is the electric fields, r is the drop radius and σ is the surface tension of the drop. The transitions of the drop shape occur at $\varepsilon_c \approx 1$ (Bird et al. 2009).

For an estimation of falling drop shapes under electric fields in experiments, we assume a drop with diameter D = 0.14 mm (with D = 2r) falling in 0.001 wt% Span80 in Marcol 52 subjected to a field strength of E = 60 kV/m. Combining Table 2.2 for relative parameter values, the calculated electrocapillary number is $\varepsilon_c \approx 10^{-4}$ F/m. Thus the falling drops remain almost spherical under electric fields.

2.5.2.8 Summation of results

To sum up all the characteristics calculated above, a table is drawn up below. The calculated values are of theoretical values, thus the uncertainties are not revealed here. It should be noted that for experiments in tap water & Marcol 52 and distilled water & Primol 352, the needle used had an inner radius of 0.23 mm. For experiments in 3.5 wt% NaCl solution & Marcol 52 and 3.5 wt% NaCl solution & 0.001 wt% Span80 in Marcol 52, the inner radius of the needle was 0.36 mm. Other values are taken as in the example combined with Table 2.2. For the Reynolds number calculated for distilled water and Primol 352, we assume a water drop with diameter of D = 0.14 mm falling inside the oil medium. The terminal velocity is calculated based on the principles in section 3.5, and the result is U_t = 7.57*10^{-3} mm/s.

	T (°C)	R_{cap} (mm)	t_{cap} (ms)	t_μ (ms)	Re	Oh
Tap water & Marcol 52	21	0.23	0.504 ± 1.7 %	4.08	0.0015	0.13
3.5 wt% NaCl solution & Marcol 52	23	0.36	1.000 ± 1.7 %	10.2	0.0017	0.10
3.5 wt% NaCl solution & 0.001 wt% Span80 in Marcol 52	21	0.36	1.069 ± 3.4 %	10.7 ± 3.5 %	0.0019	0.10
	23			11.4 ± 3.2 %	0.0022	0.095
	25		1.068 ± 3.4 %	12.2 ± 2.9 %	0.0025	0.089
	27			12.9 ± 2.6 %	0.0029	0.084
Distilled water & Primol 352	21	0.23	0.533 ± 1.2 %	0.273	5*10^{-6}	2.09
Tap water & polybutene	---	0.23	0.785	4.76	---	0.16

Table 2.3. Calculated characteristics numbers of different used oils. The calculations of Reynolds number are based on drop diameter D = 0.14 mm, and the intermediate value of drop terminal velocity is calculated using Stokes equation from the given drop diameter and the corresponding different oil viscosities according to different cases.

From Table 2.3 it is seen that all cases have a very low Reynolds number. This means that a water drop of D = 0.14 mm falling in the oil medium is always in Stokes regime. The capillary time t_{cap} is smaller than the viscous time t_{μ} for all the cases using Marcol 52, and for Primol 352 on the contrary the capillary time t_{cap} is higher than the viscous time t_{μ}. These values are in accordance with Ohnesorge number calculations. For cases using Marcol 52 the Oh number is small, which means for water phase inside the oil it is the surface tension that dominates the water dynamics. On the contrary, the Oh number for Primol 352 is high, thus the viscous force is dominant with respect to surface tension on the dynamics of water body.

2.6 Conclusion

This chapter is dedicated to describe the experimental set-ups, to discuss related uncertainties and to present oil properties. This can give readers a global view of the whole experimental design and process, and let them become familiar with the model oils.

The electric devices ensure that relatively small uncertainties are related to the choices of apparatuses. On the other hand, main sources of uncertainty results on image processing of the visualizations of very small droplets with limited spatial resolution, on the effect of temperature on oil characteristics (mainly the viscosity) and on large range transient variations of interfacial tension between the model oils and water.

The summation of different oils properties in tables and the presentation of characteristic times and non-dimensional parameters aim to simplify the comparisons of different cases.

Chapter 3. Single drop injection in model oils

3.1 Introduction

For drop coalescence experiments, water droplets need to be successfully injected into model oil. As mentioned before, to simulate real crude oil emulsions, droplets of microscale dimension are required to perform electrocoalescence studies. To inject such small water droplets into oil medium, three factors should be considered: first, the size should be as much as possible independent of nozzle size; second, a large and continuous range of available drop diameters are required; third, injected droplets are expected to free fall in the oil medium. In most existing drop injection systems for single drop or drop pair injection, the drop diameter range depends on the nozzle orifice used. Moreover in drop coalescence experiments drops of millimeter scale were mainly used (Guo & He 2014) (Mousavichoubeh et al. 2011) (Hellesø et al. 2015). It appears that only the EHD technique, in which electric pulses are applied to a water meniscus anchored at needle tip, allows the injection droplets of diameter smaller than the nozzle size (Chen & Basaran 2002). Thus the development of this technique is necessary to give a wider range of drop diameters with improved control. This chapter presents the use and improvement of EHD injection technique and the corresponding experimental data. During EHD injection many Multistage Pulses (MSP_i) are tested and each of them is signed a number i (i=1,2,3…). These numbers are only an index with no significant meaning.

3.2 Electrohydrodynamic (EHD) drop injection principles

3.2.1 Geometry

EHD drop injection is based on the electrostatic force applied across a liquid meniscus to cause its dynamic motion leading to break-up of the liquid thread into droplets. In a test cell, a grounded needle hanging from the top is filled with water with the meniscus anchored on its inner orifice. At the bottom of this test cell a metallic electrode is connected to high voltage. This test cell is filled up with model oil and the hanging needle is merged into the oil (Fig 3.1).

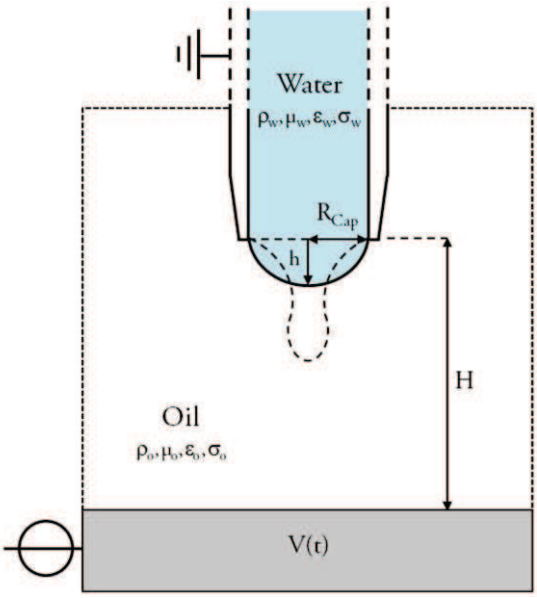

Fig 3.1. EHD injection principle (Raisin 2011).

R_{cap} is the inner needle radius and h the height of the initial meniscus. H is the distance between the needle tip and the electrode upper surface. ρ_w, μ_w, ε_w and $\sigma_{w/o}$ are the density, viscosity, permittivity and surface tension of water/oil interface, while ρ_o, μ_o, ε_o are the same parameters for the surrounding oil. Since the oil has different permittivity and conductivity than water, while applying a high voltage V(t) with a certain pulse shape onto the bottom electrode, the electric force will induce charge on the surface of the water meniscus, and deform it without exercising much influence on the surrounding oil. The Multistage pulse(Raisin 2011) was chosen, and during applications of the pulses on the electrode, the water meniscus is stretched as illustrated by the dashed lines on Fig 3.1. With sufficient amplitude of the applied voltage, the stretched drop detaches from the initial

meniscus. This break off from the water body is generally named necking breakdown, or water ligament cut off. It should be noticed that the shutdown of the high voltage pulse should be earlier than the water necking breakdown to ensure the electrical neutrality of the injected drop. The surface charge induced by the electric field on the meniscus should have enough time to evacuate through the water necking to the grounded needle after the high voltage cut off. Thus it is considered that the method can allow the injection of electrically neutral droplets into oil. However, despite this precaution, we will see hereafter that small droplets generally remain slightly charged.

3.2.2 Injected drop size requirements

To simulate drop coalescence in model oil, injected drops should have diameters in the same range as in crude oil emulsions. For the drop sizes in crude oil emulsions, several experiments were done to determine water drop diameters. Analyzing water in oil emulsion with the help of optical techniques, authors reported that in crude oils the drop sizes were mainly between 20 µm and 33 µm (Less & Vilagines 2013). (Aichele et al. 2007) did experiments using the NMR (Nuclear Magnetic resonance) technique to characterize the droplet size distributions inside crude oil and they found distributions varying between 19 µm and 59 µm. Another experiment confirmed that the droplet sizes were in microscale range, the drop sizes being observed in the very narrow range 13 – 15 µm (Rodionova et al. 2014). However with so small diameters the falling velocities in oil would be very slow.

We can take the example of one droplet of diameter D = 0.05 mm (50 microns) to calculate the falling velocity. The drop is supposed to be falling in Marcol 52 oil with 0.001 wt% Span80, and the oil characteristics are given in Table 2.2 with assumed temperature of 23 °C. Under these experimental conditions, the Reynolds number based on the droplet diameter, falling velocity and oil characteristics will be very low (to be verified later), the surfactants deposited on drop surface can block the surface velocity and the drop is considered to be a rigid sphere. Thus the falling drop is in the Stokes regime. When the drop reaches steady state, its terminal velocity can be deduced from the force balance:

$$\Delta m\boldsymbol{g} - 6\pi\mu r\boldsymbol{U} = 0 \tag{3.1}$$

The Δm is the difference between the water mass and the oil mass, $\Delta m = m_w - m_o$. The falling drop is considered to be a sphere of radius r, thus the mass can be replaced by other terms and:

$$\boldsymbol{U}_{Stokes} = \frac{2}{9}\frac{\Delta\rho r^2 \boldsymbol{g}}{\mu} \tag{3.2}$$

Then the final drop falling velocity is U ≈ 0.03 mm/s. This velocity is too small and can be easily influenced by other parameters inside oil bulk such as convection fluxes. Through simulations, if the test wall is only 0.1 °C warmer than the bulk oil content, (for example due to heating by LED light source in experiments), oil velocities of U = 0.03 mm/s can be observed under free convection effects. Fig 3.2 shows two photos taken in experimental conditions (the cameras were rotated of 90 ° as mentioned before and gravity is from left to right).

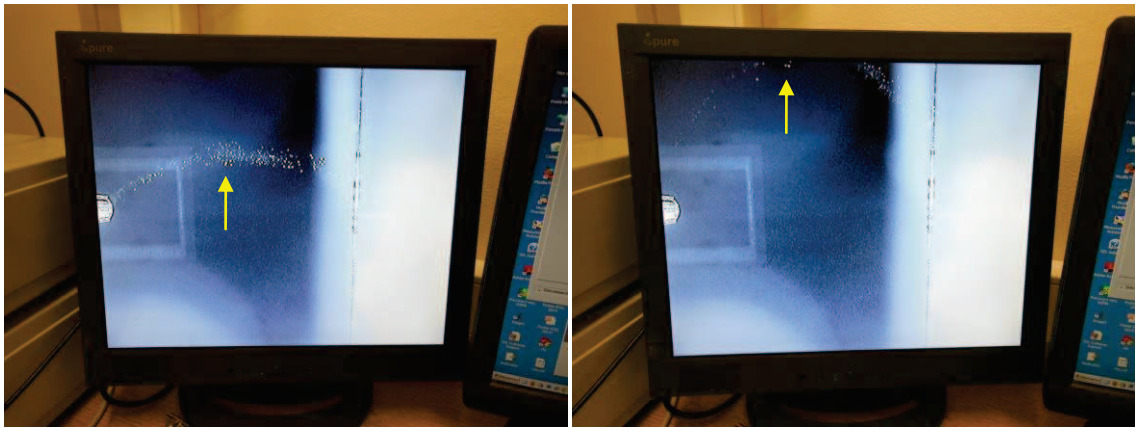

Fig 3.2. Photos taken as illustrations of convection flux inside test cell: particles exiting at the needle tip are displaced by oil movement (05/05/2015).

The two images of Fig 3.2 show the fine particle trace issuing from the needle tip, which marked convection flux inside the test cell. The particles formed an arc when they fell down from the needle tip to the electrode, and their motion can be noticed between the left and right images. The time interval between the two images was 4 min. On the images one point near the middle of the distance between the needle tip and the electrode was taken as reference to give a rough calculation of the maximum displacement. With respect to the 1mm diameter of the needle, the displacement of the particles can be estimated close to 5 mm. The corresponding oil flux reaches 0.02 mm/s, the same order of magnitude than as in previous simulations.

If the diameter of the drop is changed to D = 0.14 mm, the calculated velocity becomes U ≈ 0.2 mm/s. This range of drop diameter seems then more convenient to perform further experiments of drop coalescence in oil medium, because the falling velocity will not be so widely influenced by convection flux inside the test cell.

3.3 Previous experiments on EHD injection

3.3.1 Drop injection in polybutene oil

The Drop-on-demand technique of EHD injection was previously proposed and tested by (Raisin 2011) in polybutene oil. The liquid used to form drops was tap water, and the interfacial tension was measured, using the Du Noüy Ring tensiometer as being close to σ = 0.021 mN/m. The distance between the needle tip and the electrode was H = 20 mm and the inner radius of the needle R_{cap} = 0.23 mm. Several multi stage pulse (MSP) shapes were tested and the best one, named MSP_6 on Fig 3.3, was chosen so that the injected drop diameters obtained with this pulse shape vary linearly over a wide range of applied high voltage.

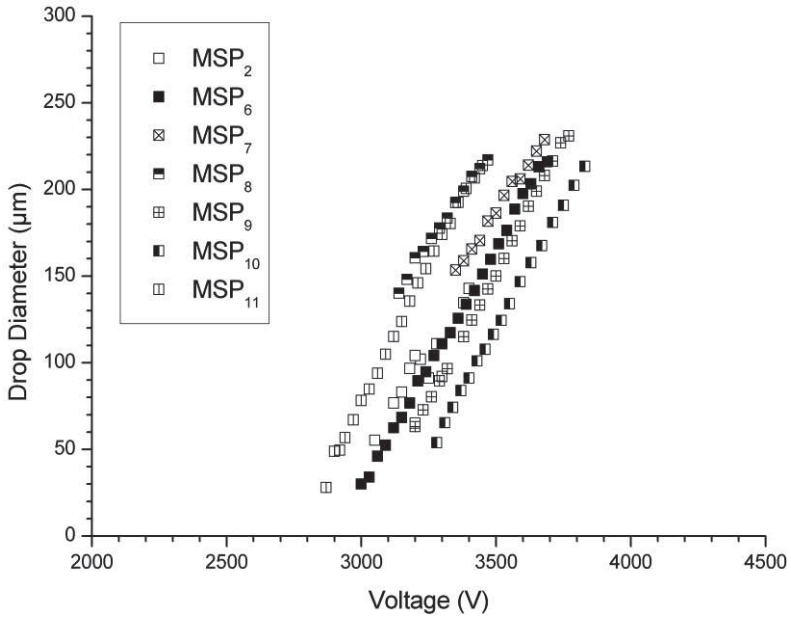

Fig 3.3. Injected drop diameters vs maximum applied voltage: results obtained with different pulse shapes in polybutene oil by (Raisin 2011).

The best pulse is indicated by black squares on Fig 3.3, and this pulse shape is later named as MSP_j. The adjusted meniscus height was of h/R_{cap} = 0.75. The beginning of the curve started at about 3.0 kV with the injected drop diameter of 0.03 mm. The injection of the largest droplet was observed at 3.7 kV and the corresponding drop diameter was 0.22 mm. To obtain an injected drop diameter of 0.1 mm the applied voltage was found equal to 3.3 kV. As described on Fig 3.4, the shape of the MSP_j

pulse consists of three plateaus and the total duration was 1.76 ms. To simplify the notation, the pulse shape is divided into three parts indicated as: Part 1, Part 2 and Part 3.

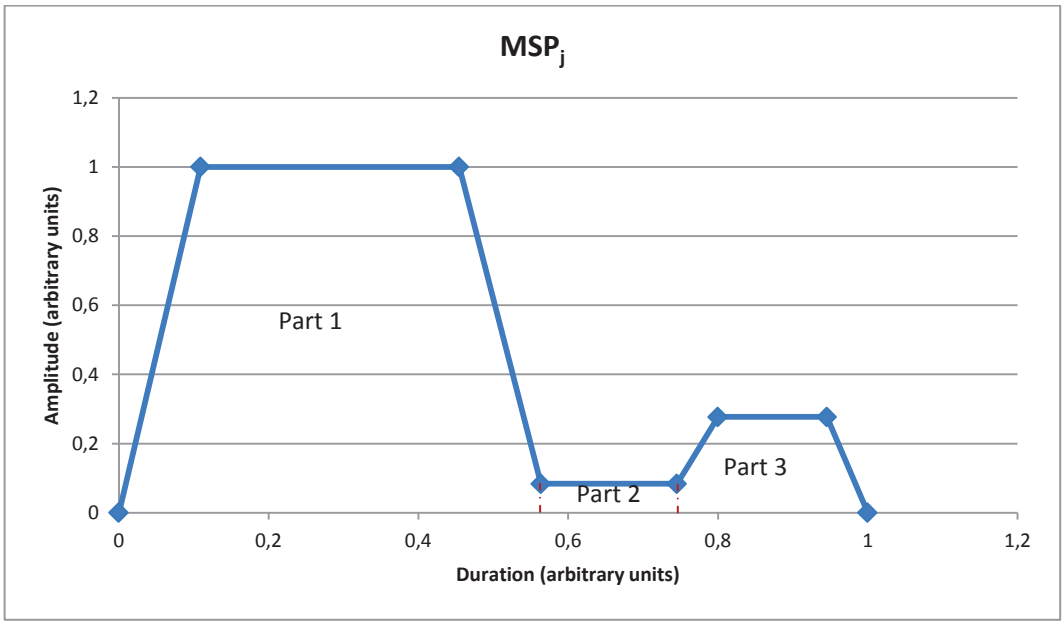

Fig 3.4. Multistage pulse shape used by (Raisin 2011) to perform EHD water drop injection into polybutene oil.

Part 1 deforms the meniscus into a blunt-tip shape, which is due to the fast shrinking of the sides compared to the tip displacement (Wright et al. 1995). Part 2 forces the meniscus, especially the locality of highest curvature which is away from the axis, to retract itself due to inertial effects as the voltage amplitude decreases. At this stage a cone will be formed at the tip of the meniscus due to the ''push'' force of the mass located away from the axis during the step before. Then Part 3 is applied which will enforce the highest curvature at the cone tip and drag this quantity of mass downwards. At the end of the pulse, a quantity of mass is connected to the meniscus via a thin necking. Due to the inertial and capillary forces, the necking will break off and thus the quantity of mass forms a drop and falls. A good drop injection needs a suitable pulse shape and any excessive pulse deformation can give charged jets. For example, the prolongation of Part 1 will give lateral jets while a strong increasing of Part 3 will favor axial jets (Raisin, 2011). A series of good drop injections is illustrated on Fig 3.5.

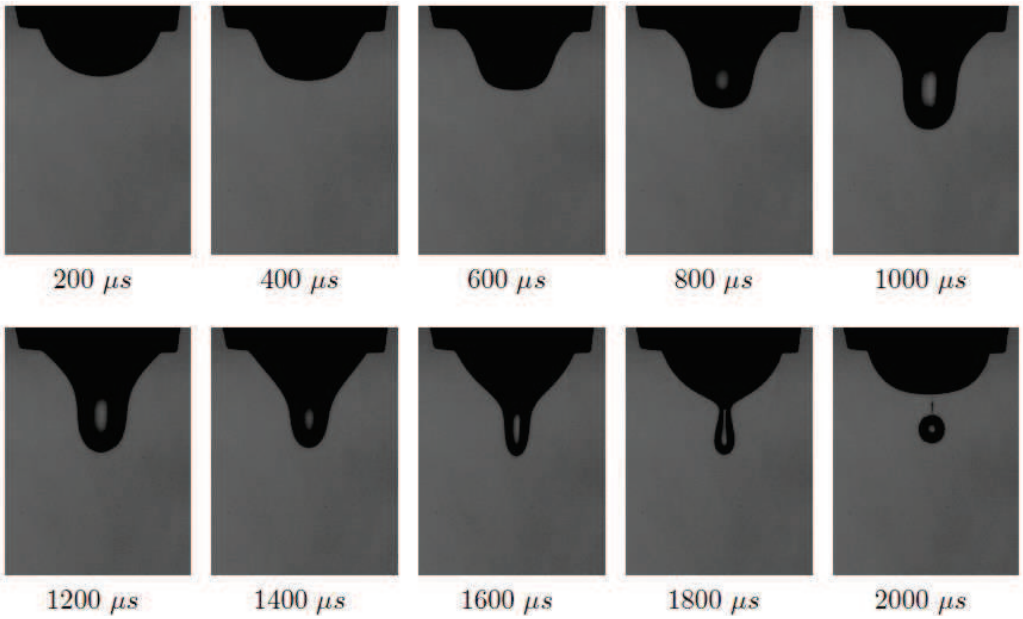

Fig 3.5. Injection process of tap water into polybutene oil using a Multistage pulse shape MSP_j with V = 3150V, h/R_{cap} = 0.75, σ = 21mN/m, total pulse duration 1750 µs (Raisin 2011).

Fig 3.5 shows meniscus dynamics under electric pulse were taken by (Raisin 2011) at different instants to give an overview of the drop injection process. From 0 to 900 µs the processes correspond to blunt-tip formation of Part 1. From 900 µs to 1350 µs the retraction of the meniscus takes place over the small influence of Part 2. The rest, until 1750 µs, corresponds to Part 3, which gave a short drag force on the tip of the meniscus. The pulse was shut down at 1750 µs, thus the breakup of the water necking was driven only by the capillary force. Some conclusions were drawn from former experiments:

- First, as the electric voltage was returned to zero before the breakup of the water thread which connected the tip head to the rest of the initial meniscus, the drop formed and ejected was supposed to be electrically neutral because the induced charge in the tip head had enough time to evacuate to the grounded needle. All through the experiments the tap water which has a high conductivity was used, and the relaxation time of charge in the drop through the necking was estimated around 0.15 µs (Raisin, 2011).
- Second, the efficiency of the Multi-stage pulse seemed to rely on the ratio between the second and third part of the pulse shape.
- Third, with a higher value of h/R_{cap}, the drops injected were of bigger diameters with the same voltage amplitude.

3.3.2 Active parameters

For water drop injection by MSP_j into polybutene oil, the theoretically required lowest voltage needed to be applied on the electrode was calculated (Raisin 2011). Since the Eötvös number is small (Eo=$(\rho_w - \rho_o) g R_{cap}^2/\sigma < 0.005$), the gravitational effects can be neglected and the meniscus can be considered as a hemispherical shape. To deform the meniscus, the electrostatic pressure must overcome the capillary pressure (Raisin 2011).

$$p_E > p_{cap} \Rightarrow \frac{1}{2} \in_r \in_0 E^2 > \frac{2\sigma}{R_{cap}} \tag{3.3}$$

Here, p_E, p_{cap}, R_{cap} and σ are respectively electrostatic pressure, capillary pressure, radius of the metallic needle and the interfacial tension. An approximation of threshold field intensity allowing deforming the meniscus at its axial tip, the highest electric field region, is calculated as E_{Max} (Coelho & Debeau 1971):

$$E_{Max} = \frac{2V}{R_{cap} \ln(\frac{4H}{R_{cap}})} \tag{3.4}$$

In this calculation, the form of the meniscus is supposed to be hyperboloid and have the same radius of curvature as the metallic needle. Then the electric potential necessary for quasi-static deformation and injection of a charged drop is written as:

$$V_{low} = \sqrt{\frac{\sigma R_{cap}}{\in_r \in_0}} \ln(\frac{4H}{R_{cap}}) \tag{3.5}$$

This estimation is a rough calculation because the real applied voltage would be higher than V_{low} due to the short duration of the pulse. That means that a large quantity of energy is given to the meniscus for the injection in a limited time (Raisin 2011). The numerical calculation results are summed up and shown in the next section.

Uncertainty on V_{low}

For uncertainty calculations, the R_{cap}, ε_r and ε_0 are assumed to be constant. Then V_{low} depends only on σ and H.

$$\frac{\delta V_{low}}{V_{low}} = \sqrt{\left(\frac{\delta\sigma}{2\sigma}\right)^2 + \left(\frac{\frac{1}{H}\delta H}{\ln\left(\frac{4H}{R_{cap}}\right)}\right)^2} \tag{3.6}$$

The uncertainty on V_{low} is not calculated for polybutene oil here. It is used for the calculations of the new oils in our experiments.

3.3.2.1 Pulse energy parameter

A number representative of the pulse energy is defined as the area of the non-dimensional pulse shape multiplied by the applied voltage squared over the pulse duration (Raisin 2011). It takes into account the pulse shape when comparing different cases.

$$W = \int_0^{tmax} V^2 dt \tag{3.7}$$

Here V is the voltage applied for drop injection and t_{max} is the pulse maximum duration. This allowed us to plot diameters of injected drops as a function of applied pulse energies and helped, in comparing different pulse shapes.

3.4 Improvement of EHD injection parameters for new model oils

3.4.1 Electric field in EHD injection set-up

For experiments done in EHD injection setups, the electric fields inside the test cell are calculated using COMSOL Multiphysics software. The conditions are chosen as the application of 1 kV voltage on the electrode, while the distance between the needle and the electrode is H = 15 mm.

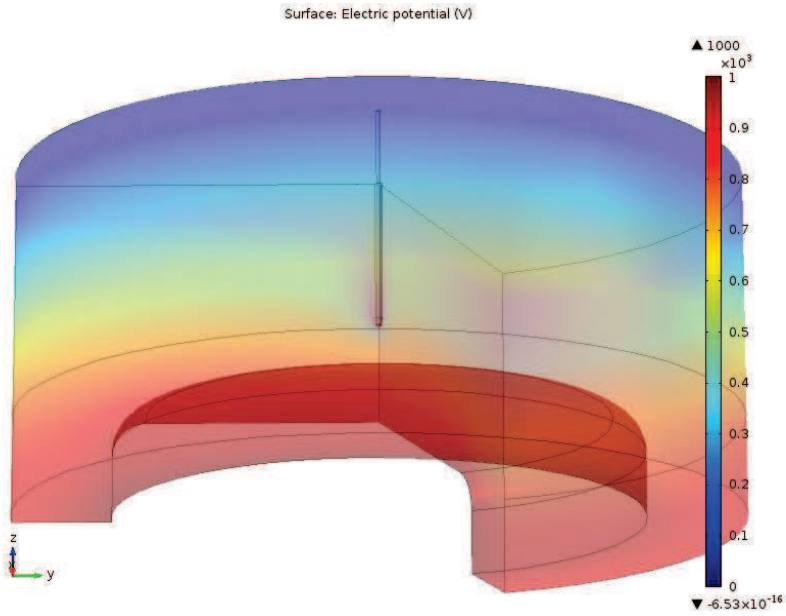

Fig 3.6. Electric potential simulated by COMSOL inside HED injection setups with H = 15 mm. Electric potential varies from 0 (ground - dark blue) to 1kV (high voltage electrode- red color).

As expressed by equation 3.4, the high curvature of the tip of the needle hanging from the top generates the highest electric fields. Electric field intensity has been drawn on Fig 3.7 along the vertical axis passing from the bottom electrode to the needle.

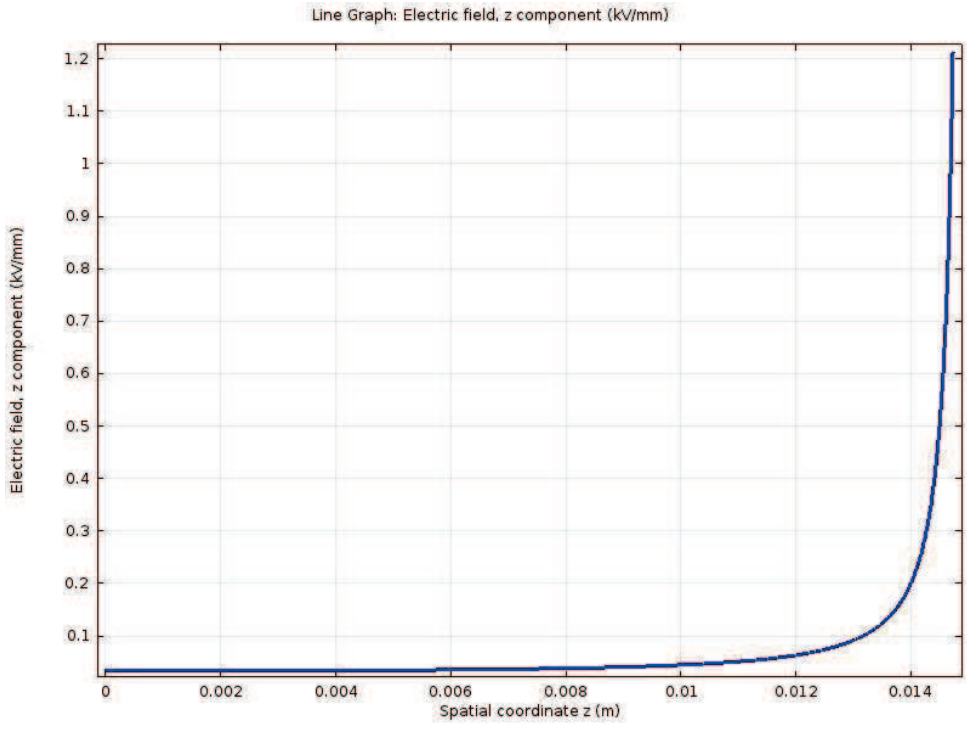

a)

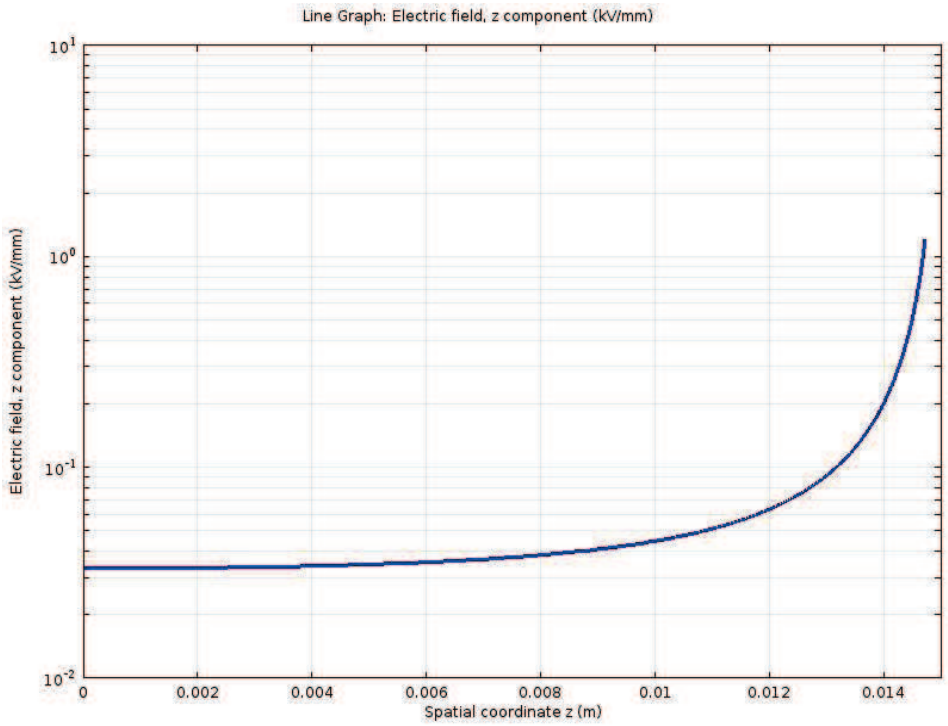

b)

Fig 3.7. Electric fields intensity in vertical axis z(m) passing through the needle with H = 15 mm, V = 1kV applied on the electrode. (a) Electric fields in function of z; (b) electric fields in function of z in logarithm scale.

The axis z(m) takes positive direction upwards from the upper surface of the electrode, and beyond the distance of 0.012 m the electric field intensity increased abruptly. Equation 3.4 gives a maximum electric field at the needle tip of 1.1 kV/mm, but the numerical simulation is very sensitive to the oil level above the needle tip (here 2.2 cm) and the condition applied at the free surface (here grounded, as the needle).

3.4.2 Definition of new multistage pulses

Marcol 52 and Primol 352 have interfacial tension higher than polybutene oil, and the direct application of MSP_j did not give any water drop injection in these new oils. Thus new pulse shapes must be defined to have successful drop injection. To overcome the high interfacial tension, elongation of the first plateau and increase of the second plateau based on MSP_j should be considered. New pulse shapes were tested and compared and, as an example, one of them (MSP6)

mainly used hereafter, is drawn in comparison with MSP_j on the graph of Fig 3.8. In experiments the duration of the pulse is of an order of three times the t_{cap} and the amplitude is of order of V_{low}.

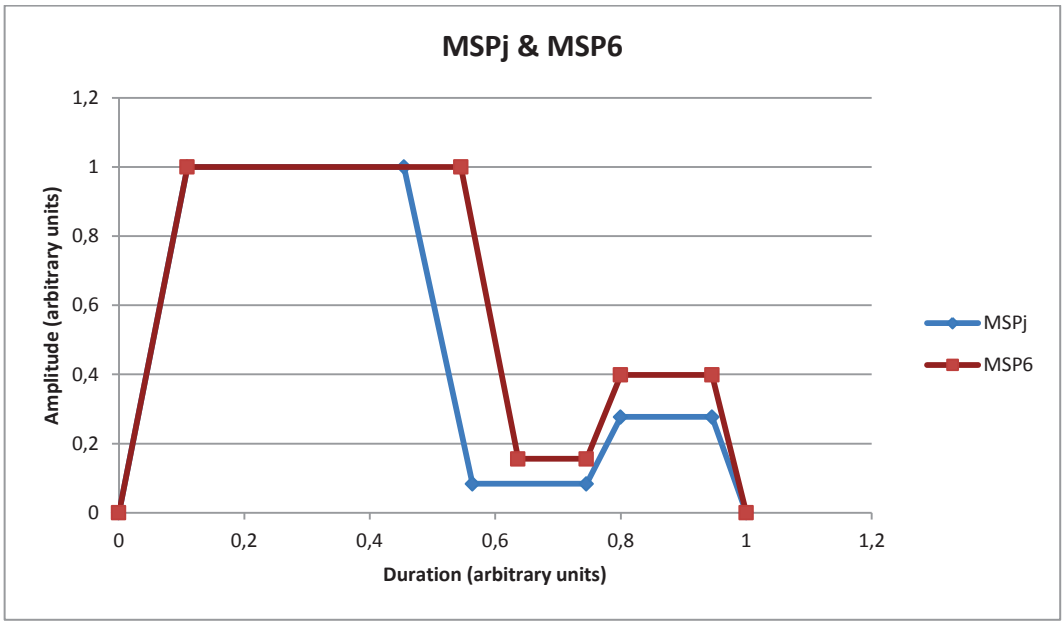

Fig 3.8. Comparison of MSP_j with new defined pulse shape MSP6 (29/05/2015).

On Fig 3.8 the area of MSP6 is larger than that of MSP_j, which means the quantity of energy given by MSP6 is bigger, as the pulse shape area relates directly to the quantity of electric energy. This extra energy serves to overcome the bigger interfacial tension in Marcol 52 or Primol 352. The durations of the pulse shape is in arbitrary units and it needs to be fixed by observations in drop injection experiments. Through experiments it is observed that, in addition to former conclusions, the relative duration of Part 1, on the total duration, also plays a crucial role in drop injection. An insufficient duration of Part 1, with higher voltage, will lead to long necking under inertia effect, which often results in big satellite formations (Tjahjadi et al. 1992).

3.4.3 Drop injection in Marcol 52

Previous EHD drop injection was performed in polybutene oil which was a type of unsaturated organic medium. This oil may be oxidized, which can modify its interfacial tension with water. In the present study, polybutene oil has been changed for Marcol 52 and Primol 352, both saturated hydrocarbon mixtures, to ensure that no oxidation could take place in these organic liquids. However, compared to polybutene oil, surface tension with water is significantly higher. Thus droplet injection

conditions should be again put in question. The Marcol 52 oil is a transparent mineral oil, and its characteristics have been presented in Table 2.2 and 2.3. The calculation of the Ohnesorge number of Marcol 52 showed that the capillary force dominates the meniscus dynamics compared to the viscosity effect. The calculations of capillary time and viscous time gave a global idea about the pulse durations for EHD drop injection. However this range is too large and more precision is needed to better define a convenient pulse shape. Thus experiments are needed to test pulse durations in order to find a best suitable pulse shape.

3.4.3.1 Summation of characteristics of drop injection in Marcol 52

To sum up the characteristics of drop injection in Marcol 52 with two types of oil corresponding to Fig 3.11: the 'old oil' and the 'new oil', Table 3.2 is drawn with all the parameters and calculated values. The temperature is estimated to be 21 °C ± 1 °C, and the injection was done with tap water. The values of viscosity and density of oil are taken as the values of Marcol 52 with Span 80 addition on Table 2.2.

	Polybutene	Marcol01 (old oil)	Marcol02 (new oil)
T	21°C ± 2 °C	21 °C ± 1 °C	21 °C ± 1 °C
ε_r	2.3	2.1	2.1
σ (mN/m)	21	25 to 48 (*)	48 ± 3.4 %
μ_o (Pa.s)	$10.2*10^{-3}$	$11.4*10^{-3}$ ± 3.8 %	$11.4*10^{-3}$ ± 3.8 %
ρ_o (kg/m^3)	824	828.7 ± 0.33	828.7 ± 0.33
R_{cap} (mm)	0.23	0.23	0.23
H (mm)	20	15	15
V_{low} (kV)	2.85	3.1 to 4.3 (*)	4.29 ± 2.1 %
t_{cap} (ms)	0.77	0.66 to 0.51 (*)	0.504 ± 1.7 %
t_μ (ms)	4.76	4.26 ± 3.5 %	4.26 ± 3.5 %

Table 3.2. Calculated parameters of drop injection in Marcol 52 and comparison with polybutene (*) during the injection in "old" oil, the interface is cleaned progressively by successive ejections of droplets : thus the surface tension is varying between the value obtained after 5 days with respect to measurements summarized in formula 2.8 and the value obtained after only 3 minutes. During the experiment reported on Fig 3.11 the

surface tension is supposed to increase from the beginning (extraction of the smallest droplets) to the end (extraction of the largest droplets).

3.4.3.2 Pulse duration tests

To fix pulse duration, experiments were done in EHD injection set-ups into model oil (Marcol 52) with H = 15 mm. The needle was the same as used for polybutene oil and the inner radius was of R_{cap} = 0.23 mm. Experiments were done with a fixed pulse shape named MSP6 by varying the pulse total durations by 1.25 ms, 1.30 ms, 1.37 ms and 1.5 ms. The diameter values were determined by visualizations with the help of ImageJ.

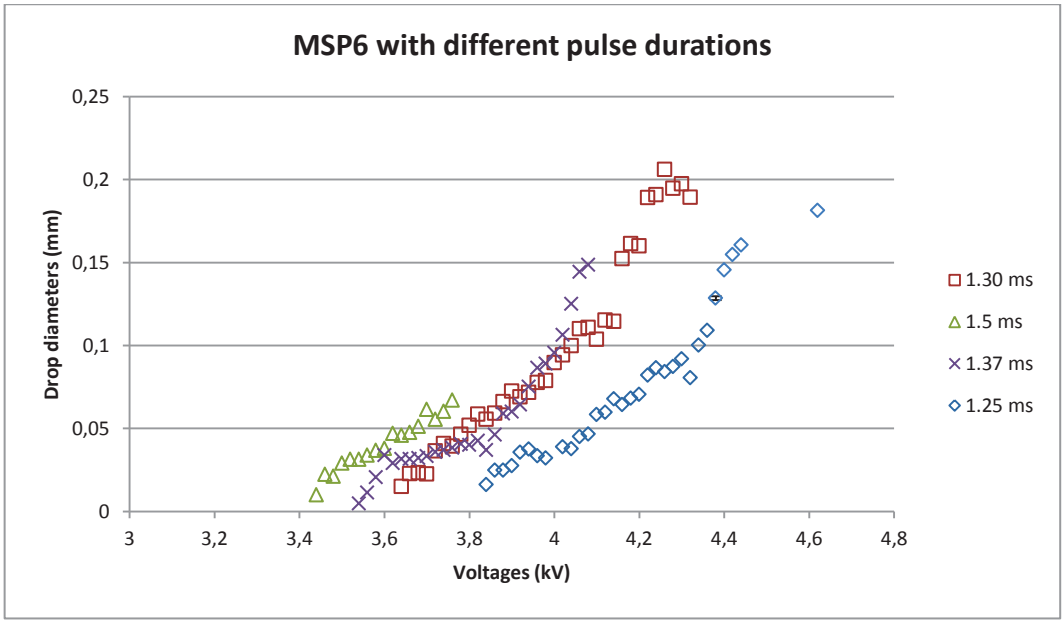

Fig 3.9. Single drop injection performed in EHD injection set-ups by MSP6 with tested different pulse durations. The temperature is taken of 21 °C ± 1 °C and H = 15 mm.

From Fig 3.9 it can be seen that the best curves are those of 1.25 ms and 1.30 ms as pulse durations because they have the largest drop diameter ranges compared to other curves. The smallest drop injected in the experiments was 0.005 mm in diameter and the largest one a little larger than 0.2 mm. The injection of larger drops was marked by jet production, either lateral or axial. Thus it can be concluded that large pulse durations of a pulse shape with two plateaus can favor jetting during drop injection. The uncertainty of drop diameter is only drawn for one point so as not to render the curves unreadable. The calibrations of the images for the four series are the same, and the scale is 831 pixels/mm. The uncertainty of the drop diameter is ±1 pixel which was already discussed in

Section 2.4.1. This value corresponds to 0.0012 mm, and the uncertainty bar is ΔD = ± 0.0012 mm. This error is not larger than the marker point.

The curves are further drawn as a function of applied pulse energies on Fig 3.10.

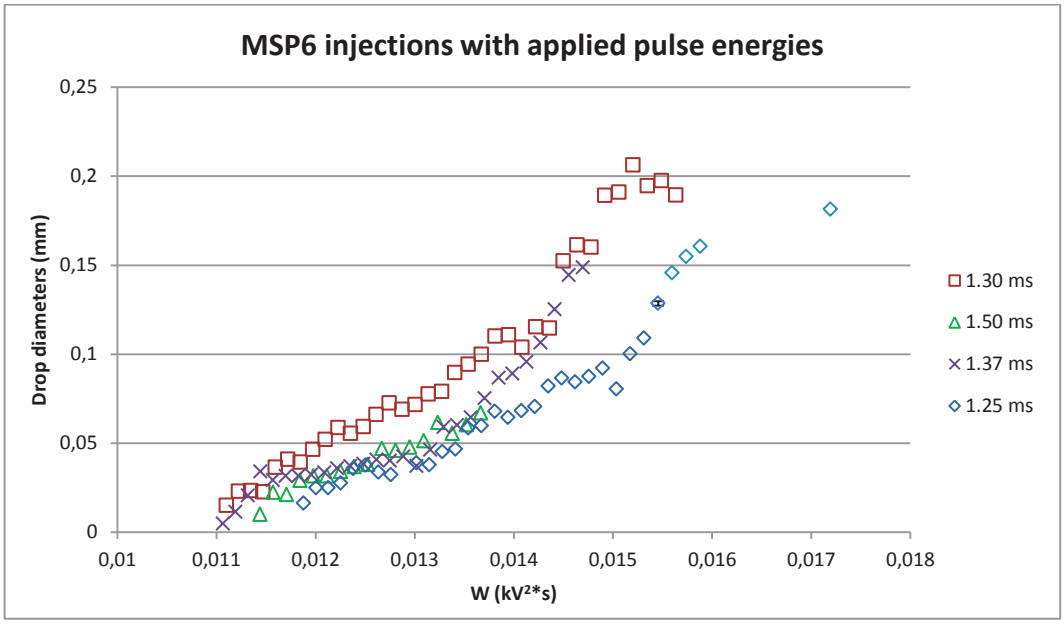

Fig 3.10. Injection by MSP6 versus pulse energy parameter W. The temperature is taken of 21 °C ± 1 °C and H = 15 mm.

On Fig 3.10 the curves are grouped together for small drop diameters but for larger droplets it seems that the efficiency is better for intermediate duration of 1.30 ms. For drop injection, the pulse duration is fixed at 1.30 ms which gives the largest drop diameter range on the figure. This value is located between the t_{cap} and t_{μ} calculated for Marcol 52 on Table 2.3.

3.4.3.3 Effects of oil interfacial tension on drop injection

The oil interfacial tension changes may affect drop injection processes and drop diameters. The injection experiments were done in the EHD injection setup. Two series of experiments were done and their results are compared on Fig 3.11. Since the error bars are no larger than the size of markers, on the following graphs the error bars will be omitted. Fig 3.11 shows the drop injection data using the MSP6 pulse of 1.3 ms duration. The series of droplet injection were carried out in Marcol 52 with different ageing. The 'old oil' refers to the Marcol 52 which rested in the test cell for five or six days

while the 'new oil' means the Marcol 52 was just poured into the test cell from the container. For these two oils the only significant change seems to be the interfacial tension.

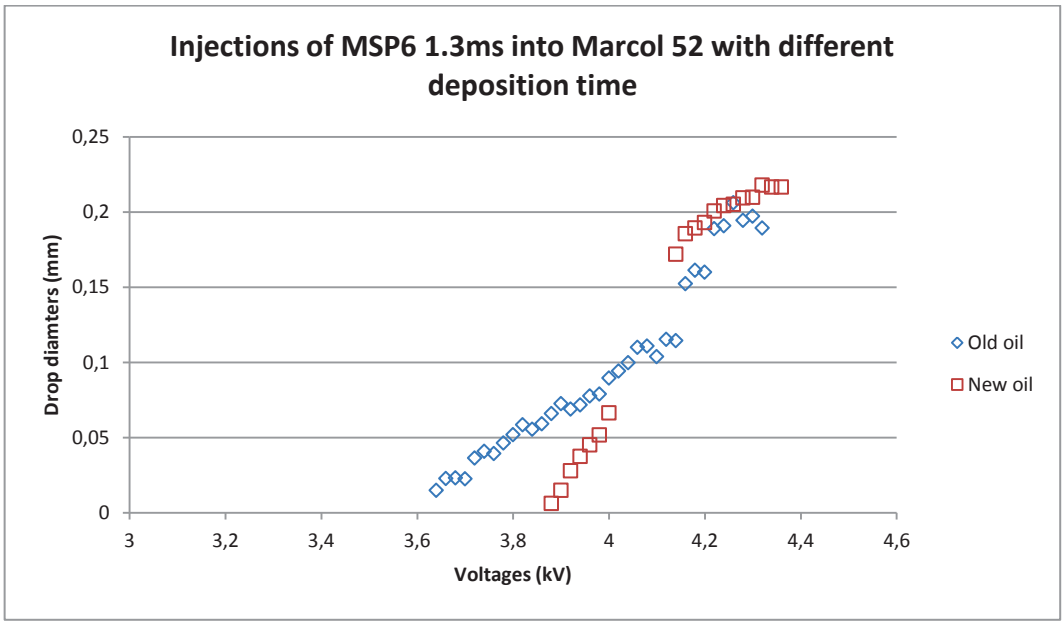

Fig 3.11. Drop injection were performed by MSP6 of 1.3 ms into Marcol 52 with different ageing. The temperature is taken of 21 °C ± 1 °C, H = 15 mm and the interfacial tension is σ = 48 mN/m ± 3.4 % for the new oil, but can vary between 25 and 48 mN/m for the old oil.

Studying these two curves, the trend of the 'old oil' is not as smooth as the 'new oil', and it starts at a lower voltage value. This is because the surfactants or impurities present in the 'old oil' lowered the surface tension on the water meniscus, which could favor drop injection. For the 'new oil', an obvious gap occurred in the middle of the curve (no injection of single droplet observed between 4 and 4.1 kV), which is not as evident for the 'old oil'. This gap in the curve is caused by the non-breakup of the water necking, the drop beginning to form is completely absorbed by the meniscus. The reason of such a meniscus dynamic relates to the oil-water interfacial tension. Above this voltage the two curves combine. This phenomenon may be due to the meniscus refreshment by successive drop injection which drains parts of total surfactants on the interface until the drained meniscus reached the same state as the meniscus of 'new oil'. To conclude, a low interfacial tension favors water necking breakup which leads to drop injection as seen in 'old oil' series. This change of interfacial tension seems not to affect the injected drop diameter range. This lowing of interfacial tension is supposed to come from the particle pollution such as falling dusts or impurities in oil.

Table 3.3 shows the characteristics of injections. The uncertainty on V_{min} is taken as the intersection of the curve with the abscise Voltage (kV). On Fig 3.11, the absolute uncertainty viewed from the

graph is estimated to 0.02 kV, thus the relative uncertainty is of 0.02/3.6 = 0.5 %. This uncertainty on V_{min} combined with the uncertainty on V_{low} gives 2.6 % of relative uncertainty on V_{min}/V_{low}. The same estimation is made for the other ratios.

h/R_{cap} = 0.75	MSP_j	MSP6	MSP6
t (ms)	1.76	1.30	1.30
V_{min} (kV)	3	3.62	3.88 ± 0.02
$V_{0.1mm}$ (kV)	3.3	4.01	4.01
V_{max} (kV)	3.7	4.30	4.32
t_{cap} (ms)	0.77	0.66 to 0.51 (*)	0.504 ± 1.7 %
t/t_{cap}	2.30	2.58 ± 1.7 %	2.58 ± 1.7 %
V_{low} (kV)	2.85	3.1 to 4.3 (*)	4.29 ± 2.1 %
V_{min}/V_{low}	1.05	1.17 to 0.844 (*)	0.905 ± 2.6 %
$V_{0.1mm}/V_{low}$	1.16	1.30 to 0.935 (*)	0.935 ± 2.6 %
V_{max}/V_{low}	1.30	1.39 to 1.00 (*)	1.01 ± 2.6 %
figures	Fig 3.3.	Fig 3.11	Fig 3.11

Table 3.3. Results of droplets injection with different pulse shapes and oil age

(*) during the injection in “old oil”, the interface is cleaned progressively by successive ejections of droplets : thus the surface tension is varying between the value obtained after 5 days with respect to measurements summarized in formula 2.8 and the value obtained after only 3 minutes. During the experiment reported on Figure 3.11 the surface tension is supposed to increase from the beginning (extraction of the smallest droplets) to the end (extraction of the largest droplets).

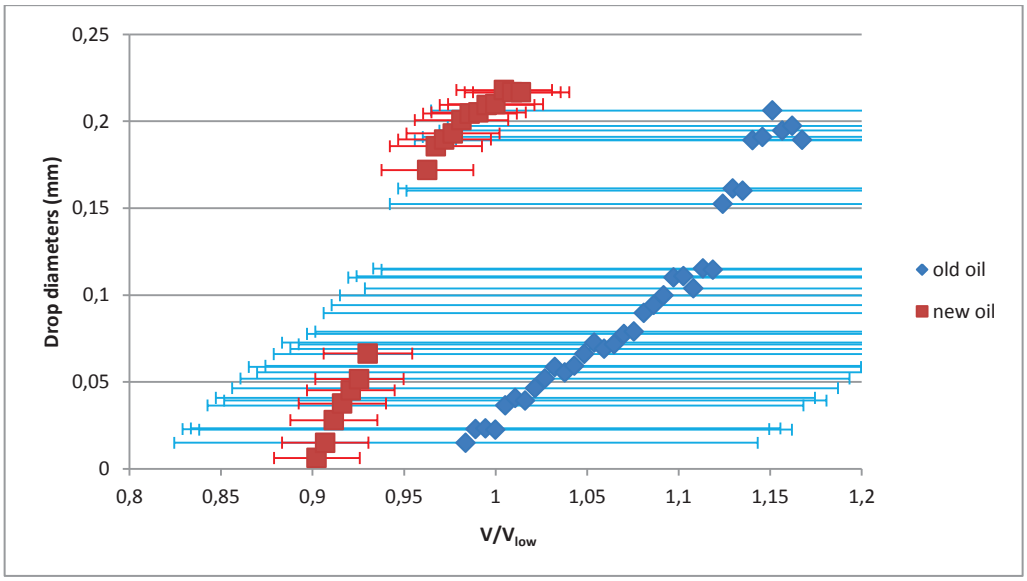

Fig 3.12. Drop injections were performed by MSP6 of 1.3 ms into Marcol 52 with different deposition time, drawn with horizontal axis V/V_{low}. Error bars are drawn from results of table 3.3: For new oil it gives 2.6%. For old oil surface tension is varying and V_{low} is taken as 3.7 kV +/- ΔV_{low} = 0.6 kV. "Error bars" are drawn using as an uncertainty $\Delta V_{low}/V_{low}$ = 16.2 %.

On Fig 3.12 it is shown that if the variation of surface tension during the successive injections for old oil is seen as an uncertainty on the parameter and is then used to draw large error bars, the data obtained for old oil and new oil are located within those errors bars.

3.4.3.4 Complete results for drop injection in Marcol 52

Many experiments were carried out by adjusting pulse shape adaptation to the Marcol 52 model oil, in the EHD injection set-up for a needle of R_{cap} = 0.23 mm. Some selected results are presented below to show the global trend of the curves and the problems generally encountered during drop injection.

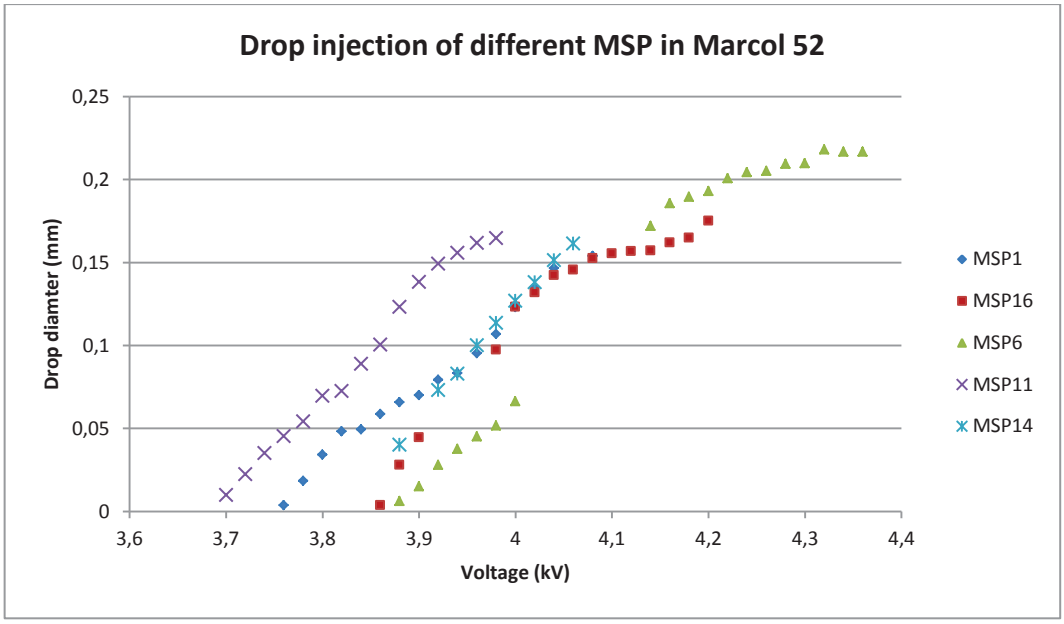

Fig 3.13. Drop injections were performed by different MSP into Marcol 52. The temperature is taken of 21 °C ± 1 °C and H = 15 mm.

The curves on Fig 3.13 go from 0.004 mm to more than 0.220 mm in drop diameter. To see more in detail, most of the curves have shorter drop diameter ranges, such as MSP14, MSP4, MSP11 and MSP1. Only MSP6 was able to get drops larger than 0.220 mm in diameter value. However the MSP6 failed to inject drops from 0.07 mm to 0.15 mm in diameter. Such a gap in the curves also affects

MSP14 and MSP4, thus the two continuous curves are MSP1 and MSP11. On the other hand, these two pulses generate a smaller range of drop diameters. Another observation is that the curves do not have the same behavior: one curve is almost linear and others have slight undulations. These different curve trends are probably to be related to the MSP pulse forms which directly affect meniscus dynamics during drop injection. For a given pulse shape, the ratio between the areas under the first plateau and under the rest of the curve lead to different meniscus movement which relates to masses of the injected drops.

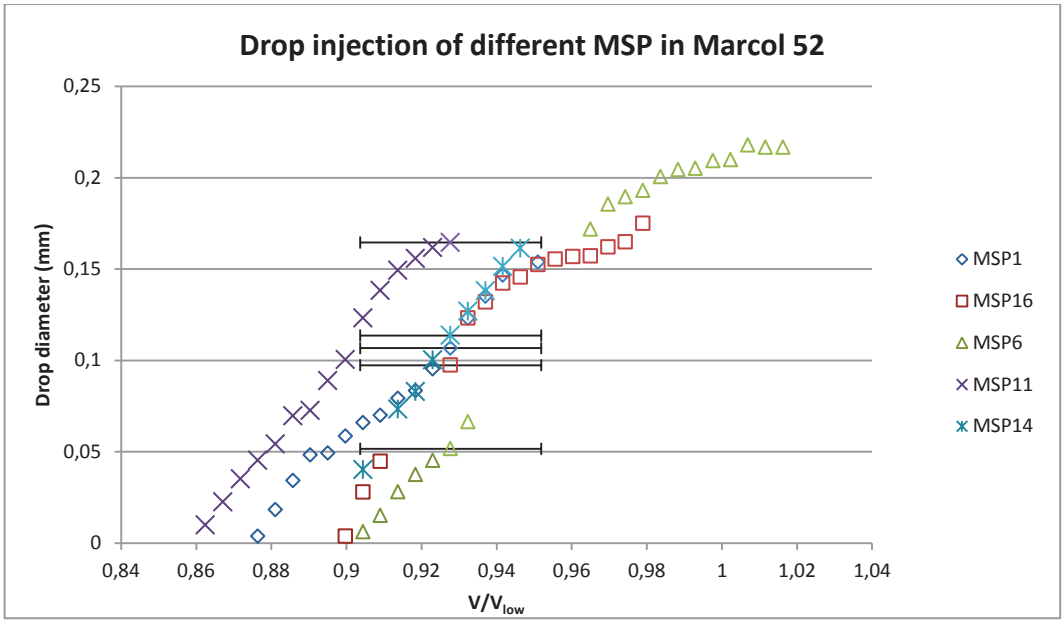

Fig 3.14. Drop injection as function of V/V_{low} for different MSP.

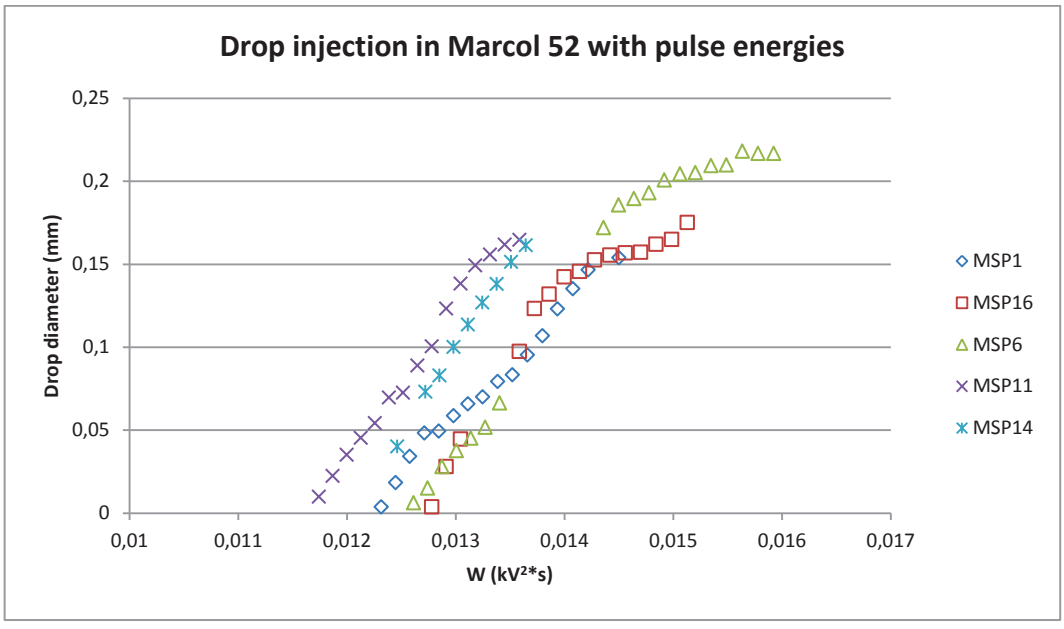

Fig 3.15. Drop injection into Marcol 52 with different MSPs, versus pulse energy parameter. The temperature is taken as 21 °C ± 1 °C and H = 15 mm.

Fig 3.14 shows drop injection with different MSPs, and the error bars are based on the uncertainty of calculated value of V_{low}. Fig 3.15 shows drop diameters as function of pulse energies W.

On Fig 3.16 the curves are drawn as a function of pulse energy parameter $W/(t_{cap}*V_{low}^2)$ so as to give a non-dimensional aspect.

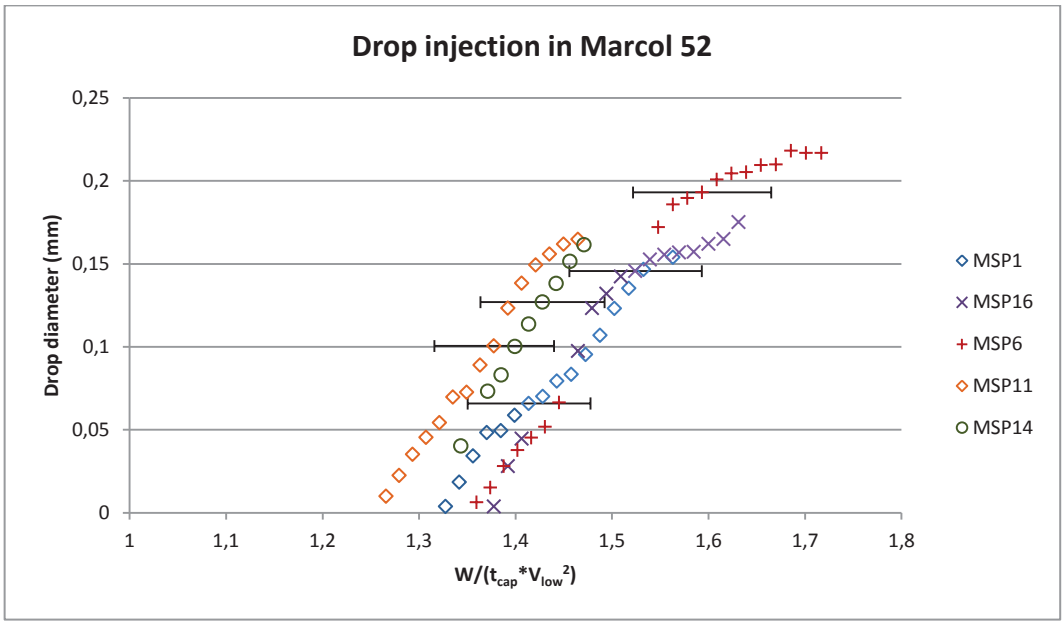

Fig 3.16. Drop injection in Marcol 52 with non-dimensional pulse energy parameter.

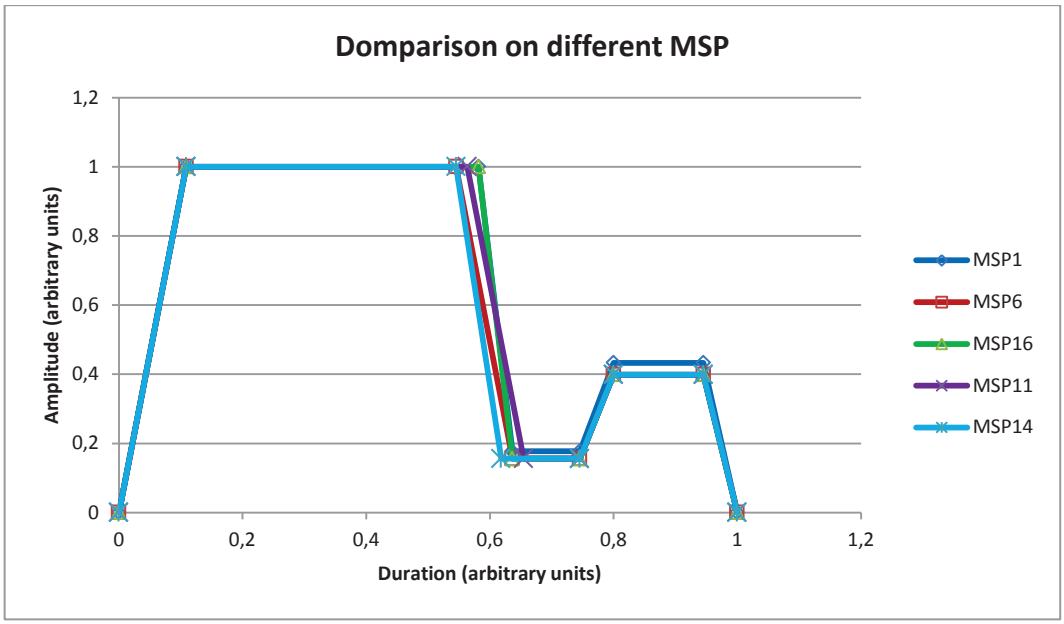

Fig 3.17. Comparison of different MSP used in drop injection.

The uncertainties of the value points on Fig 3.16 are based on uncertainties on t_{cap} and V_{low}. The error bars can almost cover all the values. It is shown that the curve behaviors of different drop injection based on different MSPs differ from one to the other. Meanwhile the used MSPs are similar in pulse shapes, as shown on Fig 3.17. This can be concluded that slight change in drop injection process can lead to big difference in meniscus dynamics, and thus give different drop injection.

3.4.4 Improvements of pulse shapes for drop injection

3.4.4.1 Improvements of drop injection pulse shapes

During the experiments of droplet injection in Marcol 52 presented above, gaps in the injected drop diameter curves are observed which is due to meniscus dynamics. Moreover, for large drop diameters, the pulse shapes tested are not so convenient to use because of jets and satellite production. Thus to better control meniscus dynamics in drop injection, improvement of pulse shapes is necessary. The needle was changed for R_{cap} = 0.36 mm to facilitate larger drop injection. The improvements of pulse shapes are focused on two points: first, to obtain larger drops with better smooth curves without any gaps inside, without producing jets; second, reduce or even eliminate satellite production after main drop injection. This leads to a new Multi-stage pulse shape with five distinct parts. That is, a new plateau is added at the end of a normal MSP pulse shape. This pulse shape is named MSP4.

The advantage of the pulse shape shown on Fig 3.18 compared to normal pulses is that it removes the gaps present on other curves. This effect is mainly due to adding Part 5 which serves to reapply a little force onto meniscus apex while the latter is dragged under the force of Part 3. This helps to prevent a long necking which would result in large satellite formation. This new pulse shape can give a larger range of drop diameter injection. The important thing in this pulse shape is that Part 5 should not be higher than Part 3. Otherwise, this would give axial jets during injection. This pulse shape especially favors droplet injection in viscous liquid medium to get small size droplets, which would otherwise not be possible due to large necking formation.

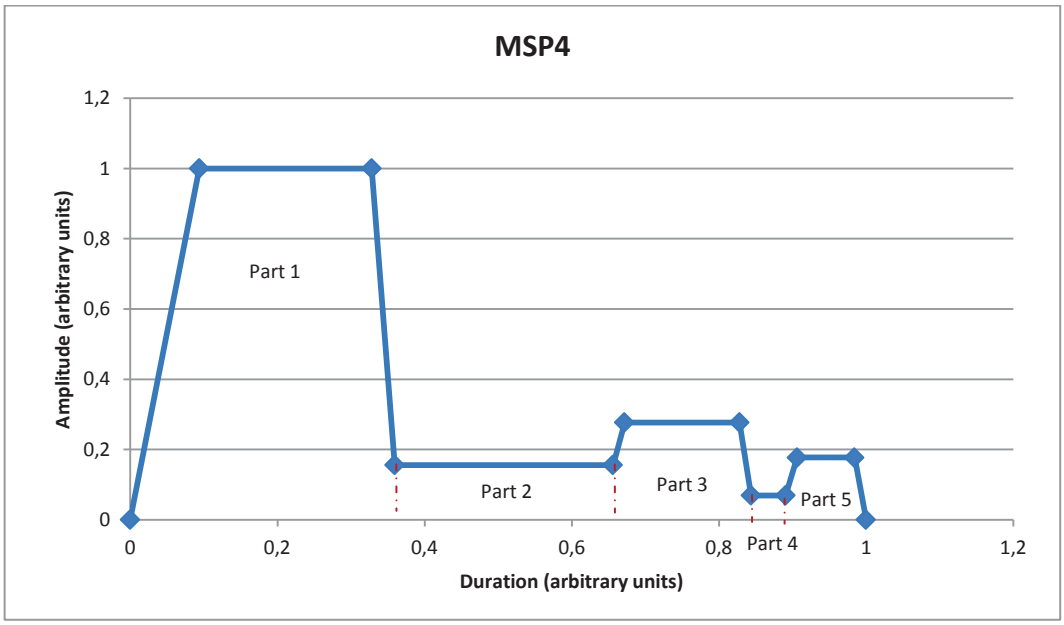

Fig 3.18. New MSP4 pulse shape for EHD drop injection.

As will be discussed hereafter, among other attempts to suppress the generation of electrically charged droplets, this pulse shape (MSP4) was modified to get MSP_{inv}. For this inversed pulse, the voltage of Part 1 is kept positive, while the voltage of later parts is negative. This inversion of voltage polarity aims at neutralizing charge injection.

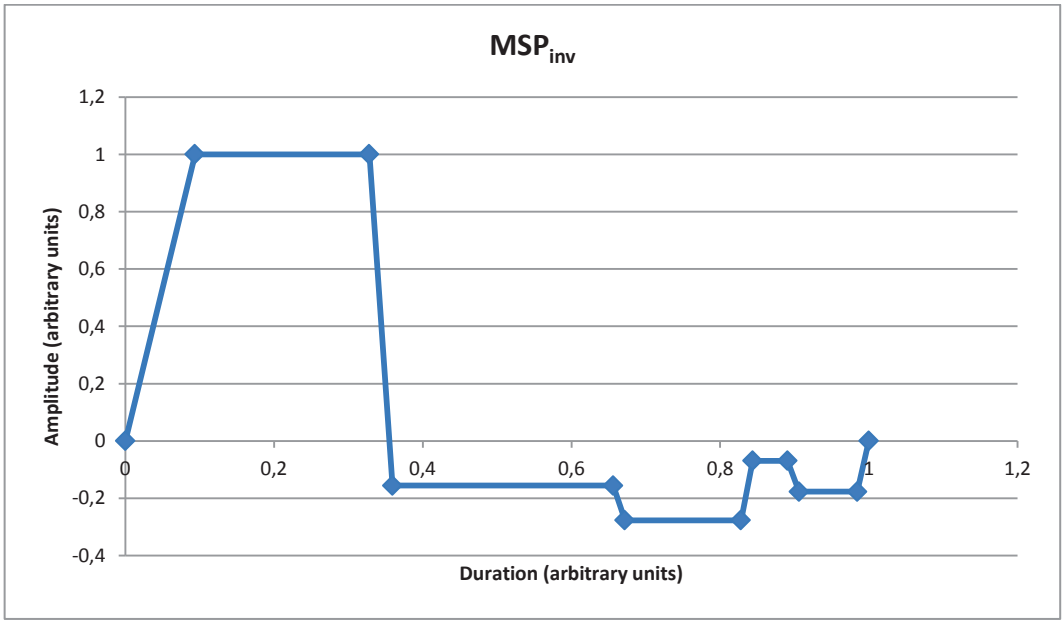

Fig 3.19. New MSPinv pulse shape for EHD drop injection.

3.4.4.2 EHD drop injection with improved pulse shape

The drop injection was performed in EHD injection setups, with a straight needle of R_{cap} = 0.36 mm hanging above the electrode. The distance between the needle and the electrode is H = 18 mm. To drain the electric charges possibly injected into oil during successive drop injections, a grounded metallic plate was added just below the oil free surface. The drop injections were done with different additives to compare their effects. One series was performed by injecting tap water drops into Marcol 52, and this is named 'tap water'. The second curve was done with the same drop injection, but adding 3.5 wt% NaCl to the tap water. The third injection series involved injecting 3.5 wt% NaCl solution into Marcol 52 with 0.001 wt% Span 80. These three curves are drawn on the same graph below.

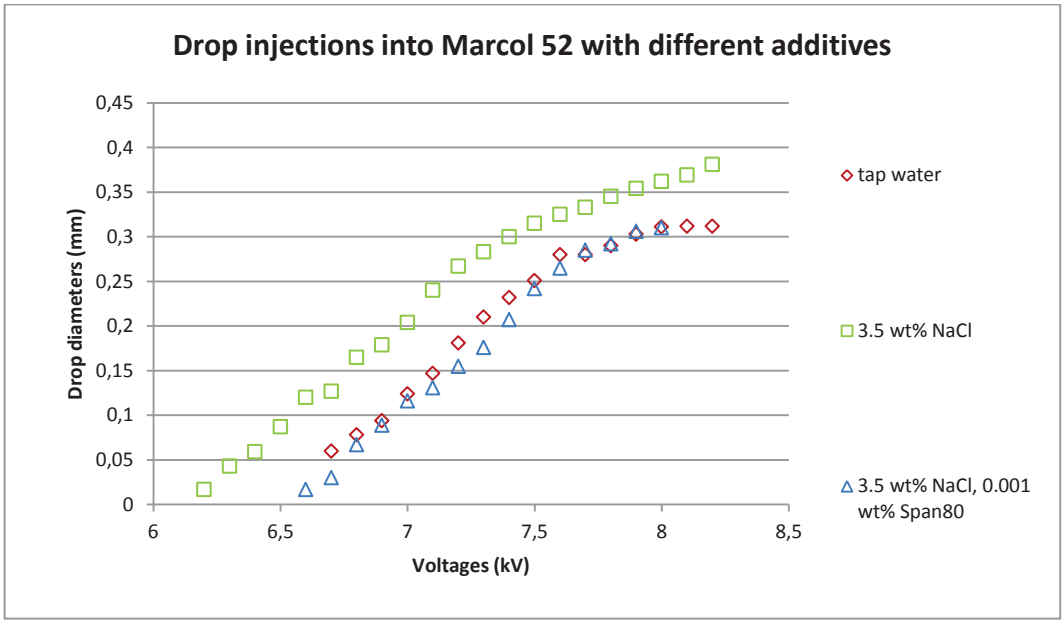

Fig 3.20. Drop injection are performed in EHD injection set-ups with different additives, and the oil free surface is covered by a grounded metallic plate (23 °C).

At the first view on Fig 3.20, the drop diameter curves are smooth and no gap appears inside them. The drop diameters have a continuous increase from less than 20 micrometers (60 micrometers with tap water) to 0.32 mm or 0.38 mm. The injections are stable between 0.10 mm and 0.15 mm for the three curves, which is good for later drop coalescence experiments. During drop injection, the sizes of formed satellites are very small, even eliminated. This means that the water necking which connects the main drop to the bulk meniscus is cut perfectly under capillary forces. This satellite elimination phenomenon relates to the effect of the third plateau addition. The displacement of the

green curve may be due to some pollution of the oil medium by falling dust, which decreased the w/o interfacial tension.

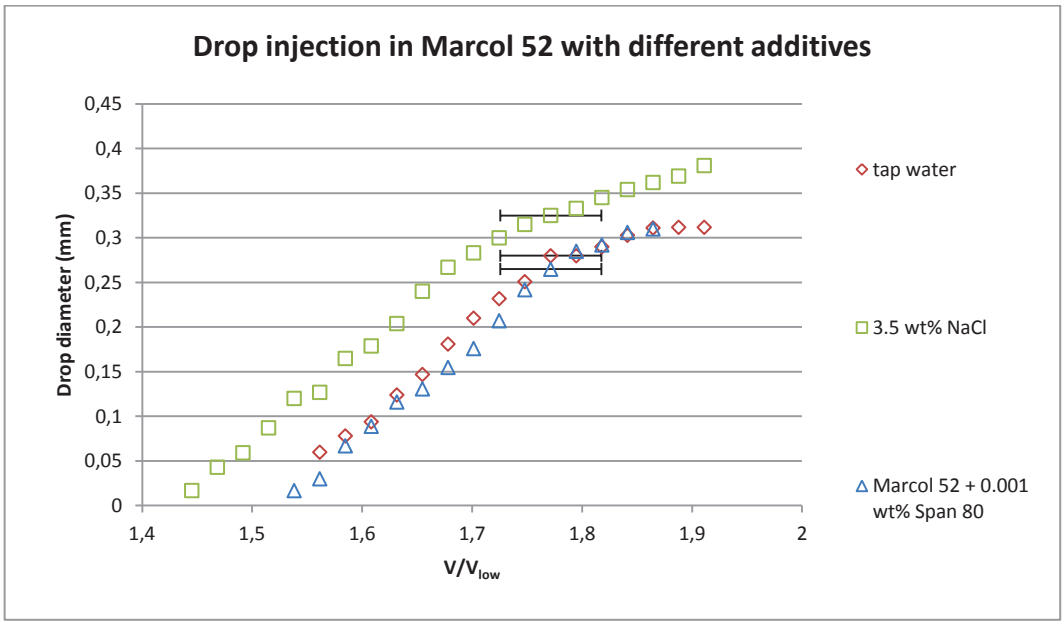

Fig 3.21. Drop injection in Marcol 52 with different additives drawn on V/V_{low}.

Fig 3.21 shows drop injection with improved pulse shape MSP4. Overall, the improved pulse form with three plateaus can give good drop injection, and experiments hereafter are based on this pulse shape.

3.5 Calculation of drop diameter based on falling velocity

Regime determination

For electrocoalescence experiments, cameras need to be placed at the potential drop coalescence region, far from the needle tip. Drop sizes can be revealed by two methods: either directly from the camera vision field or through calculations based on the drop falling velocities. Generally the second method is adopted because later electric charge of drops could be calculated using the same method. When one water drop is falling inside the oil medium, the first thing is to determine the regime of the

oil flow. As shown on Table 2.3, the Reynolds number is much smaller than 1, which denotes laminar flow in the Stokes regime.

Surface mobility discussions

When a liquid drop is falling inside an immiscible liquid, surfactants on the drop surface will be swept toward the rear point on the drop by viscous stress and lead to an interfacial tension gradient (Pawar & Stebe 1996) (Milliken et al. 1993). As a result Maragoni stress grows in opposition to the viscous stress to the point where the fluid velocity vanishes along the drop surface, fixing the surfactant distribution (Teigen & Munkejord 2010). In experiments, falling drops are of diameter D = 0.14 mm, the inertial force and interfacial tension variations are so small that they will not modify the spherical shape of drops (Levan & Holbrook 1989). This assumption of spherical shape of drops is consistent with experimental observations on the videos.

Falling drop velocities are accessible by camera records, and with given parameters of test oil, this velocity is in accordance with the Stokes Law rather than the Hadamard – Rybczynski model. The latter model depicts a moving drop surface when it is falling inside oil medium, while the former describes a solid sphere behaviour (Hamlin & Ristenpart 2012). From this phenomenon it is concluded that, as shown by (Levan 1981), the interfacial tension gradient on the drop surface could form a cap over the water drop surface and block the circulations of the liquid inside the water drop.

3.5.1 Calculation of drop diameter from measured falling velocity

When a water drop reached its terminal falling velocity inside oil medium, the total forces acting on the water drop equals zero. It combines gravity force, buoyancy force and Stokes' drag force, as shown on Fig 3.22.

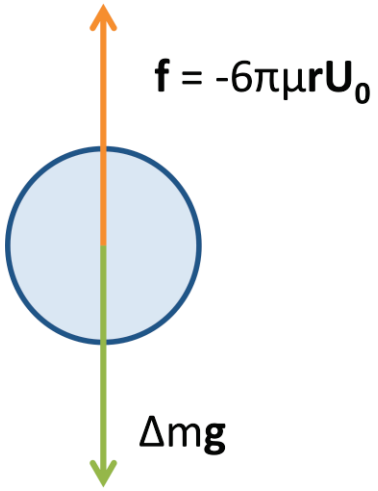

Fig 3.22. Forces acting on falling water drop inside oil medium.

The Stokes drag force is written $\mathbf{f} = -6\pi\mu_o r\mathbf{U}_0$, where r is the radius of the drop and $\mathbf{U}_0$ the terminal falling velocity of the drop without electric field. The balance equation can be written as follows:

$$-\Delta m\boldsymbol{g} + 6\pi\mu_o r\boldsymbol{U}_0 = 0 \tag{3.8}$$

Δm is the difference between the mass of the water drop and the mass of the equivalent oil drop.

$$\Delta m = V\Delta\rho = \frac{4}{3}\pi r^3\Delta\rho \tag{3.9}$$

Here Δρ is the difference in densities of water and oil, with $\Delta\rho = \rho_w - \rho_o$. Combining the equations leads to the following expression for D (=2r).

$$D = 6\sqrt{\frac{\mu_o U_0}{2(\rho_w - \rho_o)g}} \tag{3.10}$$

This calculated drop diameter will replace the visual revealed diameter. For the calculations of the drop diameters, there are also uncertainties involved in the equation. This should be discussed to determine the relative uncertainty of the drop diameter value.

3.5.2 Uncertainty on drop diameter

For the uncertainty calculation of drop diameter based on equation (3.10), the variables are respectively μ_o, U_0, and $\Delta\rho$. The uncertainty equations can be written as below (Bell 2001).

$$\frac{\delta D}{D} = \frac{1}{2}\sqrt{\left(\frac{\delta\mu_o}{\mu_o}\right)^2 + \left(\frac{\delta U_0}{U_0}\right)^2 + \left(\frac{\delta(\rho_w - \rho_o)}{\rho_w - \rho_o}\right)^2} \tag{3.11}$$

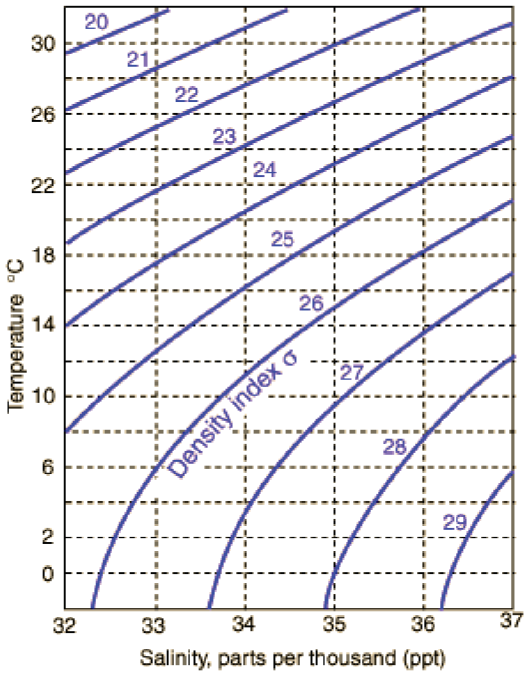

Fig 3.23. Density of seawater (ρ_w = (1000+σ)kg/m^3) from (http://hyperphysics.phy-astr.gsu.edu/hbase/chemical/seawater.html.).

On Fig 3.23, for 3.5 wt% NaCl solution the density varies from 1024.5 kg/m^3 to 1023 kg/m^3 between 21 °C and 27 °C. With the same temperatures, the density of oil varies as expressed in chapter 2 between 828. 7 and 826.7 kg/m^3 with +/- 0.3 kg/m^3 uncertainty from the oil density measurement. The difference of densities is then respectively 195.8 and 196.7 kg/m^3. Finally, by linearizing, the variation of density difference due to a temperature uncertainty of 1°C is 0.15 kg/m^3 and the total relative uncertainty $\frac{\delta(\rho_w-\rho_o)}{\rho_w-\rho_o} = 0.23\%$ is very small and can often be neglected facing to other terms.

$$\frac{\delta\mu_o}{\mu_o} = \frac{0.807\delta T}{T} \tag{3.12}$$

The uncertainties of drop falling velocities rely on image quality. During experiments Dalsa cameras survey drop falling journeys at 100 fps. The calibration of images gave 0.0033 mm/pixels. For a drop of 0.15 mm in diameter this gives 50 pixels in length. The uncertainty is of $\pm$ 1/50 = $\pm$ 2 %. There are two ways to track the falling drop using Spotlight software: center tracking and threshold tracking. The center tracking follows the drop center through image steps. The threshold tracking locates drop boundary in downwards direction. No matter which tracking method is used, the uncertainty of drop location is 1 pixel, which corresponds to 0.0033 mm after calibration. The time interval between two successive photos is 0.1 s, and the relative uncertainty is the division of drop location uncertainty over the time interval between two successive photos.

$$\delta U = \frac{\delta x}{\delta t} \tag{3.13}$$

Here δx is the uncertainty on the drop position δt is the time interval between two successive photos. The uncertainty of the velocity calculated from 2 successive photos is δU = 0.0033 mm / 0.1 s = 0.033 mm/s. The uncertainty decreases in inverse proportion of the time interval, or of the step of a time-averaging process. The graph drawn below presents drop falling velocities and distance as a function of time.

On Fig 3.24 the amplitude of the oscillations of the falling velocities is about 0.033 mm/s (shown by blue curve), which corresponds well with the calculated uncertainties. A moving average over 20 successive values can be applied and it can be seen that the resulting fluctuations are smaller. The values of velocity uncertainties are taken as averages. The drop falling velocity is almost constant which suggests that the different forces are balanced. Considering all the equations above, the uncertainties of drop diameters can have a simpler form at different oil temperatures, with reference to Table 2.2.

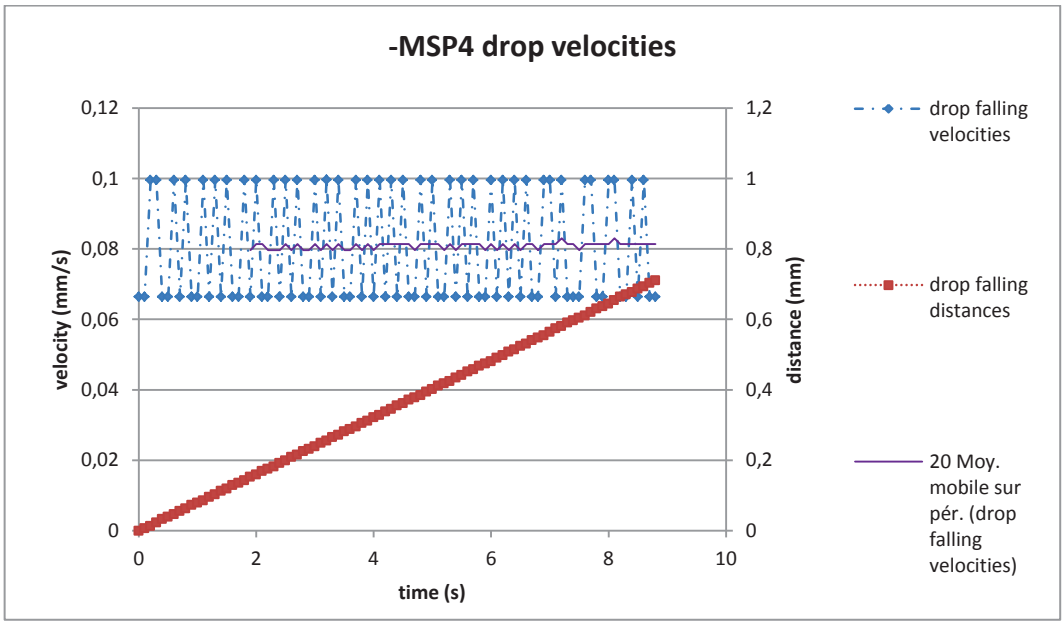

Fig 3.24. Drop falling velocities and distance in drop coalescence set-up. The purple curve is the average drop falling velocity over 2 seconds (26/05/2015, -MSP4, -5300V).

For example at 21 °C ± 1°C, $\delta\mu_o/\mu_o$ = 3.8 %, drop falling velocity over 2 seconds, then the uncertainties of the drop diameter can be written as:

$$\frac{\delta D}{D} = \frac{1}{2}\sqrt{0.038^2 + \left(\frac{1.65 * 10^{-6}}{U_0}\right)^2} \tag{3.14}$$

For a falling velocity of 0.1 mm/s the relative uncertainty on the velocity is 1.65 $10^{-6}/10^{-4}$ = 0.0165 and it gives a relative uncertainly on the diameter of 2 %. This uncertainty is smaller than those obtained by direct visualization for small droplets, and is mainly due to the oil density variation. With a shorter averaging time on the velocity, the second term in equation (3.14) increases, as the total uncertainty: for example with an averaging on 1 second instead of 2, the relative uncertainty on the velocity becomes 3.3 $10^{-6}/10^{-4}$ = 0.033 and the relative uncertainly on the diameter increases to 2.5 %.

At 23 °C and 25°C the main changes concern the viscosity relative uncertainty with respectively $\delta\mu_o/\mu_o$ = 3.5 % and 3.2 %, with a small influence on the total relative uncertainty. However the relative uncertainty is smaller for larger drop diameter, through the increasing term of falling velocity. Section 3.5.4 will show the calculated drop diameters with error bars.

3.5.3 Comparison of drop sizes obtained from visualization and calculation

When drops are injected and falling in model oil, the sizes of the drops should be determined. One example is illustrated by 3.5 wt% NaCl contained water drop injected in Marcol 52 with 0.001 wt% Span80, with –MSP4 pulse shape in the drop coalescence setup.

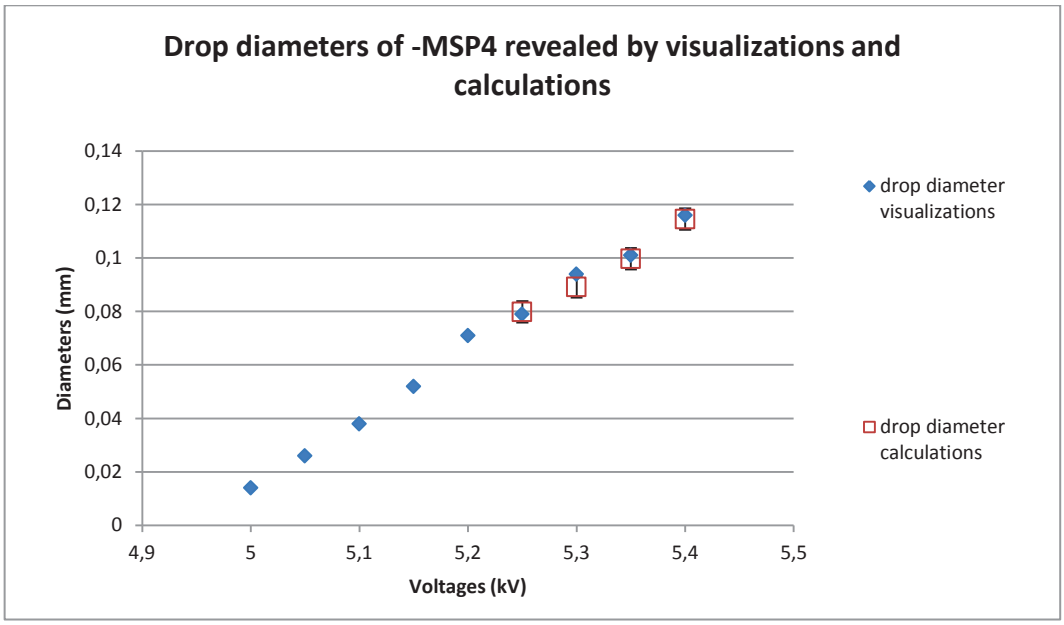

Fig 3.25. Single drop injection were performed by –MSP4 into Marcol 52 + 0.001 wt% Span 80 in drop coalescence set-up (26/05/2015).

On Fig 3.25 two series of drop diameters were drawn. One series in blue are the drop diameters taken from visualization and the series in red was taken from calculations from drop falling velocities. Since it was shown before that error bars of drop diameters were not larger than the markers for visualization data, only the error bars associated with the calculated drop diameter uncertainties are presented on the figure above. For small drops no calculations of drop diameter are available because it was not possible to detect these drops with the Dalsa camera. For larger drops they fell well into the camera detection range and motion was recorded. Both diameters through visualizations and calculations coincide well. The error bars are no larger than markers of calculated drop diameters, thus for following figures the error bars of drop diameters will not be presented.

3.6 Electric charge of generated droplets

3.6.1 Electric charge: first observations

The electric charge of water drops was first observed by applying a DC field on the electrode while injected water drops were falling inside oil medium. At the instant of DC application, the motion of the water drops changed immediately. Moreover, these changes of motion vary with the polarity of the DC field. One may conclude that the injected water droplets are electrically charged. However according to previous experiments described in section 3.3.1, the water droplets were assumed to be electrically neutral after their injection in the oil, because the voltage was always shut down sufficiently before the complete separation from the grounded meniscus. Moreover during drop injection no jets were produced, as verified by AOS camera at 5000 fps with 4 µs shutter speed. A possible reason is that wandering electric space charge was trapped in the oil medium. The electric relaxation time of the model oil was measured in section 2.5.1.4 in the range τ = 1000-5000s, thus the trapped space charge could not be evacuated efficiently. Consequently the changes remain inside oil medium and affect injected water drops.

Different methods were tested to evacuate the electric space charge from the model oil, and the objective of all them was to increase the surface contact of the model oil with grounded metallic parts. A grounded metal mesh was deposited along the wall of the test cell or a grounded metal plate covered the free surface in direct contact with the oil. Even in association with the application of a small DC voltage, no solution was found sufficiently efficient in suppressing the phenomenon. Thus it was decided to improve the understanding and control of the electric charge of the injected droplets. All the experiments reported hereafter have been carried out with the drop coalescence set up. The test cell includes an intermediate electrode, at which the high voltage is applied, while the needle and the bottom electrode are grounded. A hole was drilled in the intermediate electrode. The idea was to separate the generation of droplets to the upper part of the cell, and their analysis to the lower part, in a more uniform electric field. In fact, because of the low falling velocity of the droplets, it was quite difficult to observe with a good repeatability the interaction of droplet pairs after their passage through the hole and it was decided to carry out all analyses in the upper side. The main consequence is that the electric field is not absolutely uniform, because of the needle-electrode configuration. The distance between the needle tip and the electrode is H = 8 mm. The height z = 0 corresponds to the upper surface of the bottom metallic plate, and the intermediate electrode is located between z = 0.015 m and z = 0.02m.

The result of a numerical simulation is presented in figures 3.24 and 3.25 for a DC voltage of 1 kV applied on the electrode.

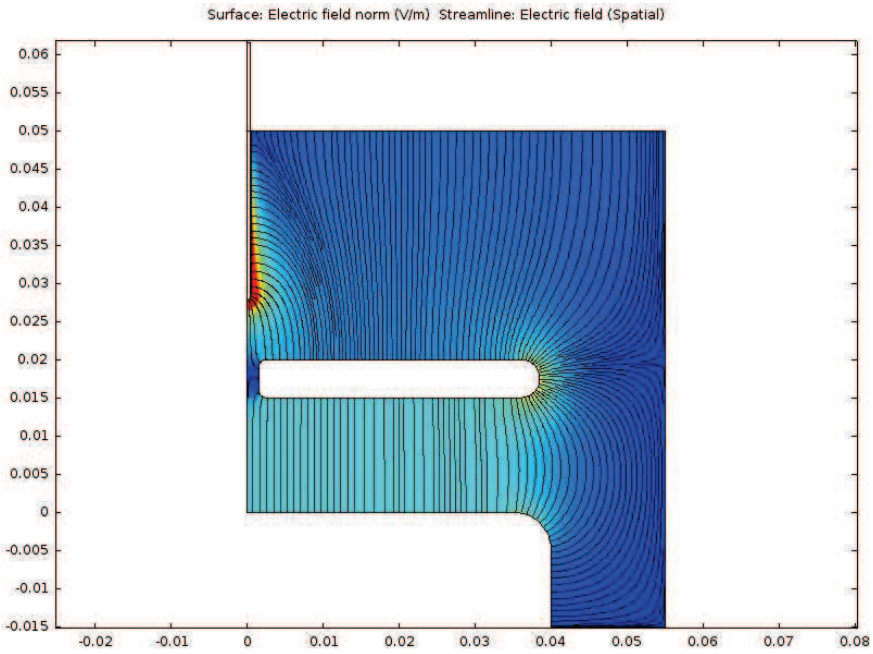

Fig 3.26. Norm of electric field and streamlines inside drop coalescence set up. Applied voltage is 1 kV DC on the intermediate electrode, the needle and bottom electrode are grounded. At the oil free surface, a no charge condition is applied there.

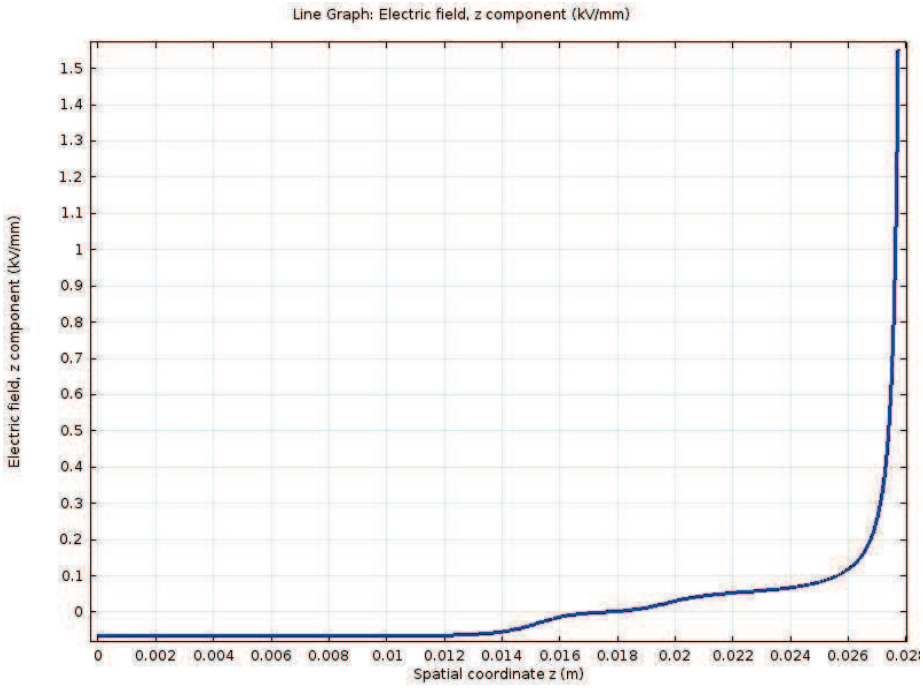

a)

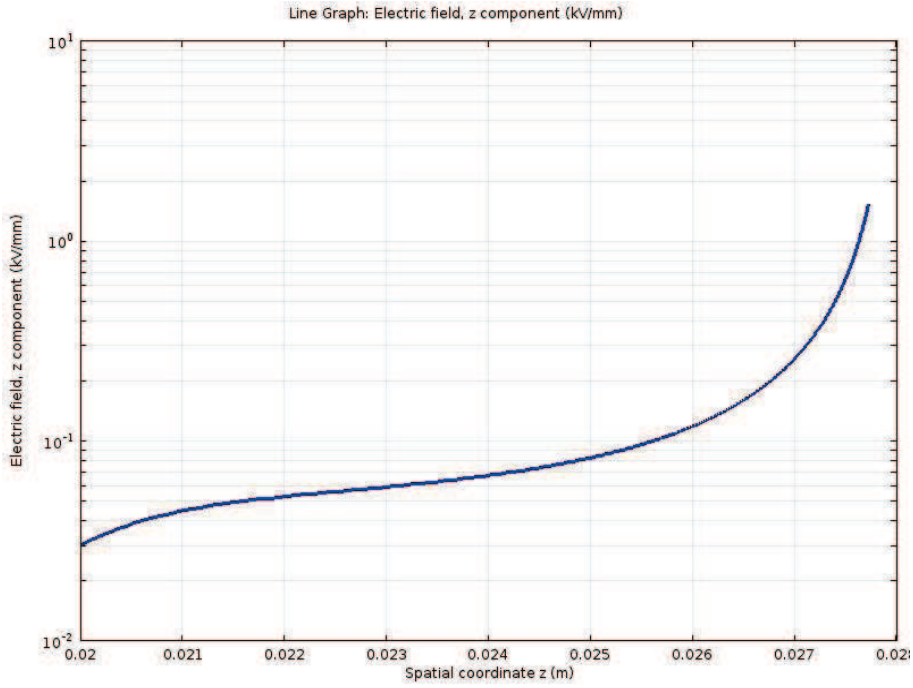

b)

Fig 3.27. Electric field vertical component for 1 kV DC voltage applied on the intermediate electrode in drop coalescence set up. a) linear scale (one can observe the change of sign when passing the hole in the intermediate electrode) b) semi-log scale (the electric field intensity is drawn only on the upper side).

The vertical electric field is drawn along the axis of symmetry on Fig 3.26. On Fig 3.27 a), it can be seen that the sign of the electric field vertical component changes when passing the hole. On the upper side, the electric field intensity increased rapidly when approaching the needle tip.

3.6.2 Droplet charge measurement

3.6.2.1 Principles of calculation

To determine the charge contained in water drops, a DC field was applied on the electrode during free fall of the injected drops. Since the drops are charged, this electric field will change the forces acting on the drops and then modify their motion. A Dalsa camera was placed along the path of the falling drops and when the drop entered the camera field of vision, the DC field was turned on. The velocities were revealed with the help of Spotlight software. A droplet without applied electric field, is subjected to only gravity force, buoyancy force and viscous force. However, when an electric field

is applied, the supplementary electric force will influence this droplet to modify its falling motion. Neglecting the possible dielectrophoresis effect, this can be illustrated as:

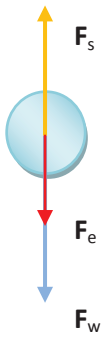

Fig 3.28. Forces acting on falling water drop inside oil medium.

For the calculation of the forces, the upwards direction of the vertical axis is taken as positive direction. The forces of gravity and buoyancy combine to give:

$$\boldsymbol{F}_w = \Delta m \boldsymbol{g} \tag{3.15}$$

Here the Δm is the difference between the mass of the water drop and the equivalent oil mass. The viscous force can be calculated in Stokes regime as:

$$\boldsymbol{F}_s = -6\pi\mu_o r \boldsymbol{U} \tag{3.16}$$

Where μ_o is the dynamic viscosity of the oil, r is the radius of the droplet and U is the stabilized falling velocity of the drop under electric field.

The force balance is:

$$\boldsymbol{F}_w + \boldsymbol{F}_e + \boldsymbol{F}_s + \boldsymbol{F}_{dep} = 0 \tag{3.17}$$

With $\mathbf{F}_e = q\mathbf{E}$ and $\mathbf{F}_{dep}$ is the dielectrophoresis force which depends on electric field gradient.

$$\boldsymbol{F}_{dep} + \boldsymbol{F}_e = -\Delta m\boldsymbol{g} + 6\pi\mu_o r\boldsymbol{U} \tag{3.18}$$

The dielectrophoresis force is not strong, and it can be calculated as following (Benselama et al. 2006).

$$\boldsymbol{F}_{dep} = 2\pi\varepsilon_2 r^3 K\overrightarrow{grad}\boldsymbol{E}^2 \tag{3.19}$$

$$K = \frac{1}{3}\frac{\varepsilon_1 - \varepsilon_2}{\varepsilon_2 + (\varepsilon_1 - \varepsilon_2)/3} \tag{3.20}$$

Here ε_1 is the permittivity of the water drop and ε_2 is the permittivity of the model oil. For the values of the permittivity refer to table 2.2. K is the polarizability factor of the drop. The form of the drop is assumed to be spherical. For the calculations, the factor K is taken equal to 1.

For an experiment in the drop coalescence set up for a drop of diameter D = $7.82*10^{-5}$ m with an applied DC voltage V = +1000V on the electrode, the calculated force is: $F_{dep} + F_e = -3.28 * 10^{-10}$ N, with $F_{dep} = 1.25 * 10^{-11}$ N. The percentage of the dielectrophoresis force over total force is 4 %. Thus the dielectrophoretic force can be neglected to first order.

$$\boldsymbol{F}_e = -\Delta m\boldsymbol{g} + 6\pi\mu_o r\boldsymbol{U} \tag{3.21}$$

Combined with equation (3.9), the equation becomes as follows:

$$q = \frac{6\pi\mu_o r(U - U_0)}{E} \tag{3.22}$$

The electric field and drop velocities are aligned vectors and the sign of the calculated result gives the polarity of the charge.

3.6.2.2 Drop charge uncertainties

Starting from equation (3.22), with r = D/2, the relative uncertainty of r is δr/r = δD/D. D is the diameter of the drops.

$$\frac{\delta q}{q} = \sqrt{\left(\frac{\delta \mu_o}{\mu_o}\right)^2 + \left(\frac{\delta D}{D}\right)^2 + \left(\frac{\delta (U - U_0)}{U - U_0}\right)^2 + \left(\frac{\delta E}{E}\right)^2} \tag{3.23}$$

The uncertainties of U_0 and U depend on image quality, and $\delta U_0 = \delta U = 1.65*10^{-6}$ m/s. The parameter $\delta D/D$ was calculated previously and the expression depends on temperature. In the expression for $\delta D/D$, the used drop velocity is the value without electric field, and it is changed for U_0 in calculations of drop charge uncertainty. The drop charge uncertainties can be simplified and written (for example at 21 °C) as:

$$\frac{\delta q}{q} = \sqrt{\left(\frac{\delta \mu_o}{\mu_o}\right)^2 + \frac{1}{4}\left(\left(\frac{\delta \mu_o}{\mu_o}\right)^2 + \left(\frac{\delta U_0}{U_0}\right)^2 + \left(\frac{\delta (\rho_w - \rho_o)}{\rho_w - \rho_o}\right)^2\right) + 2\left(\frac{\delta U_0}{U - U_0}\right)^2 + \left(\frac{\delta E}{E}\right)^2} \tag{3.24}$$

$$\frac{\delta q}{q} = \sqrt{\frac{5}{4}\left(\frac{\delta \mu_o}{\mu_o}\right)^2 + \frac{1}{4}\left(\frac{\delta U_0}{U_0}\right)^2 + 2\left(\frac{\delta U_0}{U - U_0}\right)^2 + \left(\frac{\delta E}{E}\right)^2} \tag{3.25}$$

For equation (3.25), the term $\delta U_0/(U-U_0)$ can diverge if the drop falling velocity under electric fields does not change much comparing to its free fall velocity. This case often happens for droplets with very small charges. The term of $\delta E/E$ depends on the voltage applied to the electrode. Noting y as the distance between the drop (or the middle point of a drop pair) and the electrode a curve fitting on the electric field obtained by numerical simulation and drawn on Figure 3.27a gives the following expression for a voltage V applied at the electrode:

$$E(y) = (0.0145y^6 - 0.207y^5 + 1.13y^4 - 2.27y^3 - 0.475y^2 + 13y + 22) * V/1000 \tag{3.26}$$

The term $\delta E/E$ depends on the vertical distance y between the droplet position and the bottom electrode, and can be expressed as follows:

$$\frac{\delta E}{E} = \frac{E(y + \delta y) - E(y)}{E} \tag{3.27}$$

As mentioned previously the calibration is 0.0033 mm/pixels. The uncertainty of the position of the droplet is 1 pixel which corresponds to 0.0033 mm but the bottom of the electrode is not so clear

and its position can vary by +/- 5 pixels. The corresponding uncertainty on y is close to δy = +/- 0.2 mm. Using the equation (3.25) and (3.26) the relative uncertainty δE/E is found equal to 0.5%.

3.6.2.3 Experimental methods for revealing electric charge of injected drops

The Dalsa registered drop falling velocities are drawn on the figure below and the changing velocities under DC field is obvious.

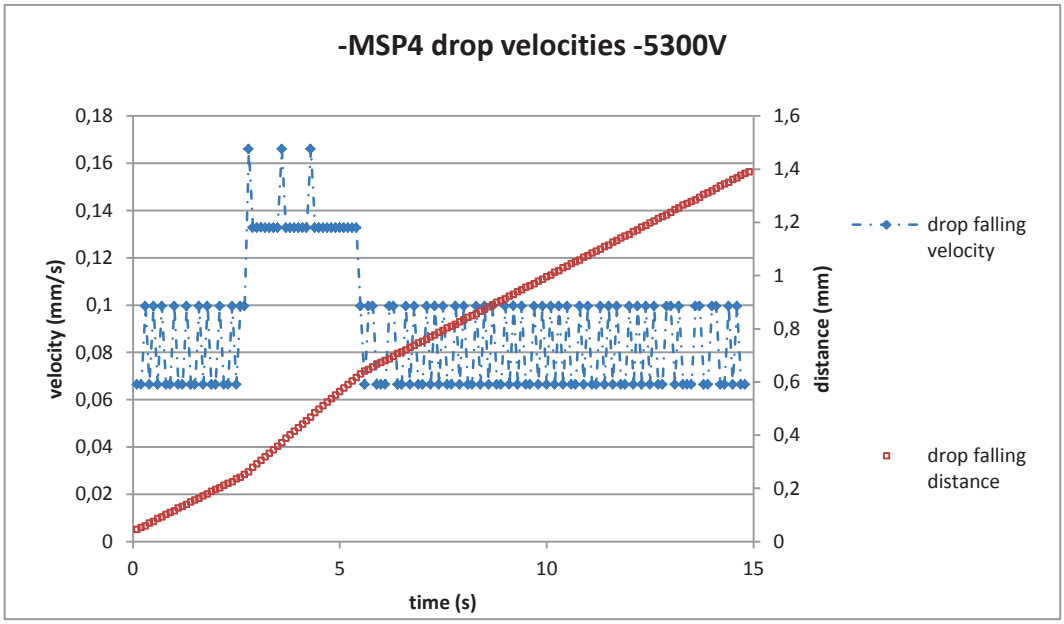

Fig 3.29. The falling velocities were calculated of one drop injected by –MSP4 at -5300V, into Marcol 52 + 0.001 wt% Span80, DC = 1 kV (23 °C ± 1 °C, 26/05/2015).

Fig 3.29 shows one example of changes to drop velocities during DC application. The DC voltage was applied for 3 seconds after 3 seconds free fall inside Dalsa camera vision field. The positions of the falling drop were obtained from Spotlight software and the velocities can be calculated.

As already described chapter 3.5.2, the duration of record without and with electric field allows averaging the velocity on a duration of 2s and the uncertainty on resulting velocity is 1.65 10^{-6} m/s. The drop falling velocity without DC field is estimated to be 0.081 mm/s and during DC field it is estimated to be 0.132 mm/s. This method for drop falling velocity calculations is used for all experiments hereafter. At 23 °C ± 1 °C, δD/D = 2 %, and δq/q = 6.4 %.

3.6.3 Results of experiments

Drop injection was performed in the drop coalescence setup, using water containing 3.5 wt% NaCl and Marcol 52with 0.001 wt% Span80. Multistage pulses applied are MSP4 and MSP_{inv} with negative polarity of DC voltage (noted hereafter -MSP4 and $-MSP_{inv}$). The drop diameters and contained charge are drawn on the figure below. Once the drops had been injected, a DC = 1 kV was applied on the electrode to change drop falling velocities, and reveal drop charge.

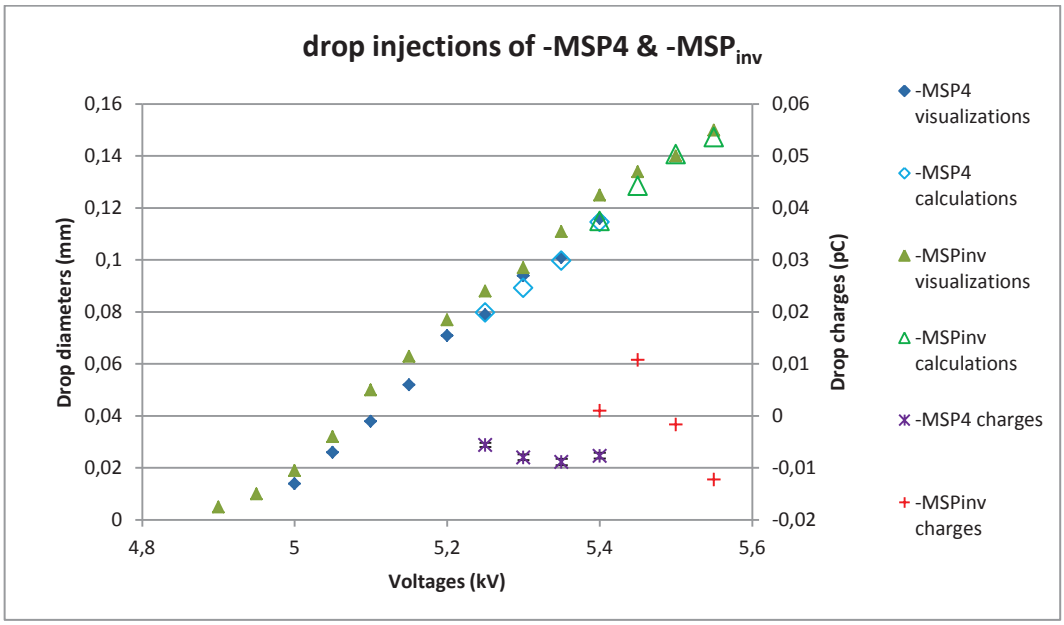

Fig 3.30. Drop diameters injected into Marcol 52 + 0.001 wt% Span 80 by -MSP4, $-MSP_{inv}$ pulse shapes, with drop coalescence set-up (26/05/2015, 23°C ± 1 °C). The error bars on drop contained charge are taken for the calculated largest uncertainty of one point, 7%.

Fig 3.30 shows two series of drop injection: -MSP4 and $-MSP_{inv}$. The curves consist of visual drop diameters, calculated drop diameters and electric charge of drops. Since the uncertainties of calculated drop diameters are no larger than the size of the marks, the error bars are not drawn here. On the figure all the series of drop diameters coincide well. The charge of droplets generated with -MSP4 are all negative. That is coherent with the idea that positive space charge is injected around the needle tip during the negative pulse, and, remaining after the voltage shutdown, can induce the opposite polarity on the meniscus and detached droplet. Thus the polarity of the injected drop is in accordance with that of applied voltage on the electrode.

For the drop falling velocities, in some cases the drop did not change its motion during applications of DC. One example is shown below for $-MSP_{inv}$ injection at -5.40 kV with DC = +1 kV.

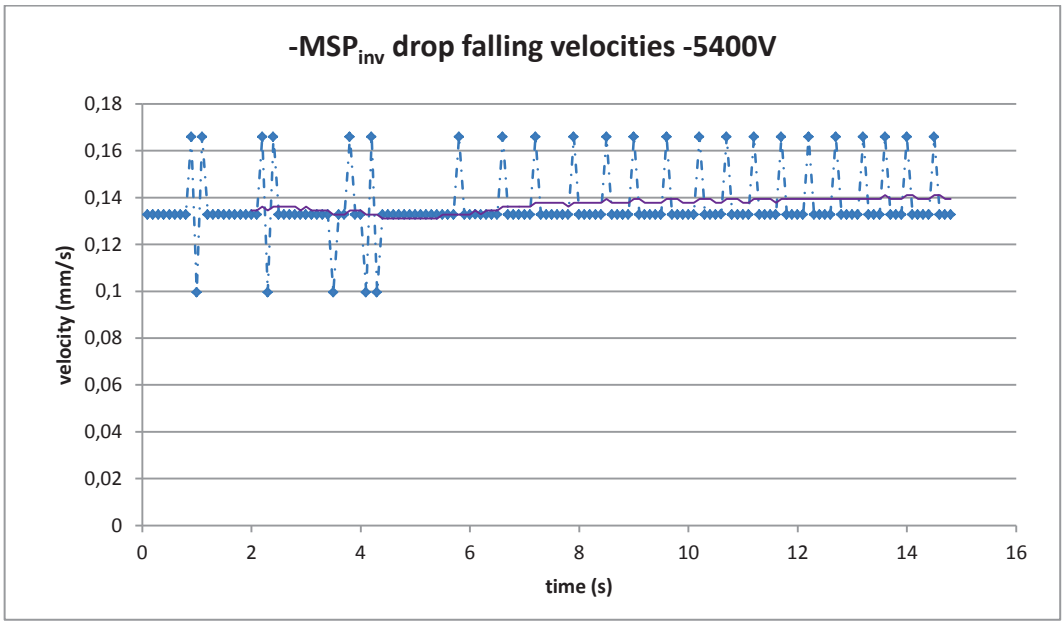

Fig 3.31. Drop falling velocities without and under DC fields for -MSP$_{inv}$ injection at -5.40 kV with DC = +1 kV (26/05/2015, 23°C ± 1 °C).

In experiments when the drop fell into Dalsa camera vision field, three seconds later a DC field was applied on the electrode with a finite duration of three seconds. Generally it is expected to see drop motion changing as on Fig 3.29. However no obvious drop velocity changing was observed Fig 3.31. In this case the drop charge uncertainty is difficult to calculate because the third term in equation (3.25) diverges.

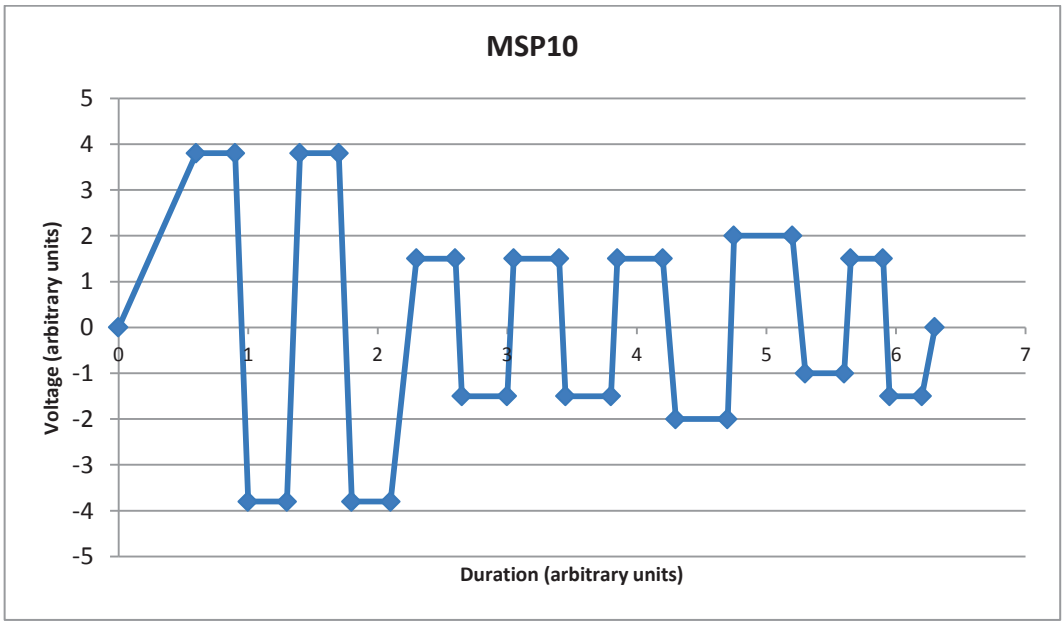

Fig 3.32. Pulse shape of MSP10.

As it was shown that water drops are electrically charged, modifications of pulse shapes have been tested trying to minimize the droplet charge. The last pulse shape proposed, named MSP10 is drawn Fig 3.32.

The MSP10 proposal aims at neutralizing injected charge around the needle tip via alternating polarity. Drop injection was also performed applying the MSP10 pulse, with a duration of 1.5 ms for a water meniscus height h/R_{cap} = 0.75. The injected drop diameters can increase up to more than 0.3 mm. The drops with large diameters are not needed in experiments, thus only one limited range of drop diameters are presented on Fig 3.33.

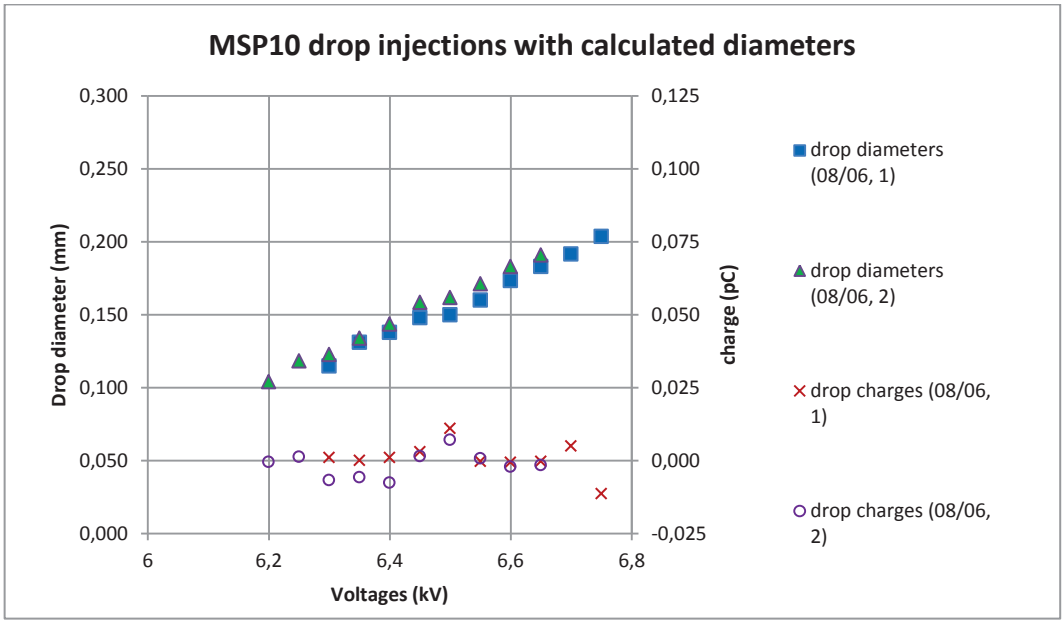

Fig 3.33. Drop diameters injected into Marcol 52 + 0.001 wt% Span 80 by MSP10 pulse shape, with drop coalescence set-up (08/06/2015, 25 °C ± 1 °C).

Fig 3.33 presents two series of drop injection by MSP10 performed the same day. The drop diameters are taken from calculations from the falling velocity. Since the visual diameters are in good agreement with calculated diameters, the former are not drawn on the figure. It is the same for diameter uncertainties because the error bars are no larger than markers. The two series of data are in good agreement, which shows the good repeatability of drop injection. The charges of the drops are small, thus the calculated charge uncertainty is large.

3.6.4 Summation of the characteristics of drop injection using different pulses

	Marcol (-MSP4)	Marcol (-MSP_{inv})	Marcol (MSP10)
T	23 °C ± 1 °C	23 °C ± 1 °C	25 °C ± 1 °C
ε_r	2.1	2.1	2.1
σ (mN/m)	42 ± 6.7 %	42 ± 6.7 %	42 ± 6.7 %
μ_o (Pa.s)	$10.6*10^{-3}$ ± 3.5 %	$10.6*10^{-3}$ ± 3.5 %	$9.93*10^{-3}$ ± 3.2 %
ρ_o (kg/m^3)	828.0 ±0.33	828.0 ±0.33	827.3 ±0.33
R_{cap} (mm)	0.36	0.36	0.36
H (mm)	8	8	8
V_{low} (kV)	4.05 ± 3.4 %	4.05 ± 3.4 %	4.05 ± 3.4 %
t_{cap} (ms)	1.07 ± 3.4 %	1.07 ± 3.4 %	1.07 ± 3.4 %
t_μ (ms)	11.3 ± 3.2 %	11.3 ± 3.2 %	12.1 ± 2.9 %
h/R_{cap} = 0.75	-MSP4	-MSP_{inv}	MSP10
t (ms)	1.5	1.5	1.5
V_{min} (kV)	5.00	4.90	6.25
$V_{0.1mm}$ (kV)	5.35	5.30	6.25
V_{max} (kV)	5.40	5.55	7.90
t/t_{cap}	1.41 ±3.4 %	1.41 ±3.4 %	1.41 ±3.4 %
V_{min}/V_{low}	1.24 ± 3.4 %	1.21 ± 3.4 %	1.54 ± 3.4 %
$V_{0.1mm}/V_{low}$	1.32 ± 3.4 %	1.31 ± 3.4 %	1.54 ± 3.4 %
V_{max}/V_{low}	1.33 ± 3.4 %	1.37 ± 3.4 %	1.92 ± 3.4 %
figure	Fig 3.30	Fig 3.30	Fig 3.33

Table 3.5. The characteristics of drop injection performed into 0.001 wt% Span80 in Marcol 52 model oil with drops made of 3.5 wt% NaCl solution.

The different characteristics of the drop injection presented above will be summed up and showed in a table. The experiments were -MSP4, -MSP_{inv} and MSP10. The injections were performed in Marcol 52 model oil with 0.001 wt% Span80 and water containing 3.5 wt% NaCl solution. On Table 3.5 the maximum voltages for -MSP4 and -MSP_{inv} are in the same range, and only MSP10 can reach a much higher voltage. The pulse shape of MSP10 is special and the injected drop charge is mostly neutralized. Thus until a high voltage the injected drops are not obviously charged.

3.7 Different phenomena observed during drop injection

3.7.1 Influence of meniscus height

During drop injection there are many parameters which could influence the injection process. One important factor is meniscus height h/R_{cap} which influences directly injected drop diameters. The following graph represents the relation between the meniscus heights h/R_{cap} and the diameter of injected drops. Two series of experiments were done by MSP4 at 5400V and MSP10 at -6350V with different meniscus height. All the experiments were performed in the drop coalescence set-up.

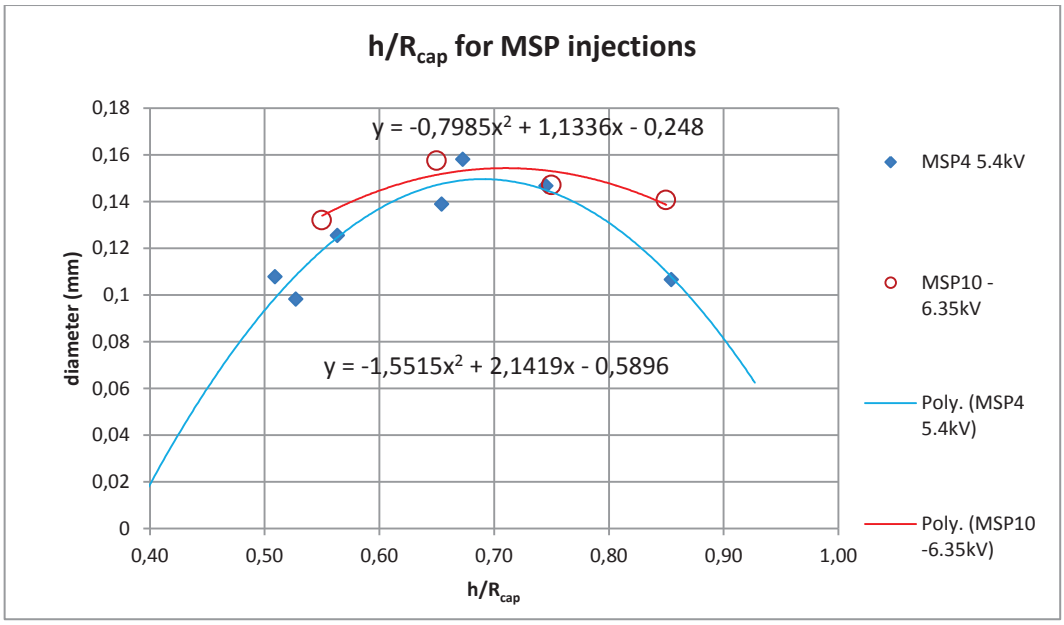

Fig 3.34. Injected drop diameters vary in function of h/R_{cap} for MSP4 5400V (26/05/2015) and MSP10 -6350V (12/06/2015).

The drop diameters on Fig 3.34 are taken from calculation. By fixing injection voltage and pulse shapes, meniscus height h/R_{cap} varied from about 0.5 to 0.85. The two series MSP4 and MSP10 are fitted with a polynomial trend line of order 2. The maximum value of the trend line can be calculated as 2.1419/(2*1.5515) = 0.6903 for MSP4 and 1.1336/(2*0.7985) = 0.7098 for MSP10. The value of h/R_{cap} chosen for experiments is 0.75, not far from the maximum value.

3.7.2 Jets formed during meniscus stretching

During drop injection, jets can be formed on the meniscus at different instants of meniscus dynamics and under different forms according to liquid properties. The jets are charged fine water droplets caused by excessively high electric forces at local points. There are two types of jet: off-axis jets which are formed on blunt-tips of the meniscus shape and on-axis jets which are produced at the final step of the drop injection process. The figure below shows off-axis jets on the blunt-tip meniscus.

Fig 3.35. Jets off-axis produced from blunt-tip salted water meniscus for injection into Marcol 52 + 0.001 wt% Span 80 with MSP4, -5450V, h/R_{cap} = 0.75 (26/05/2015).

On Fig 3.35 the white arrow indicates the jets region. The jets are caused by local reinforcement of electric fields due to stronger curvature. Dynamic inception of the jets may be due to impurities initially deposited on the meniscus, locally lowering the interfacial tension. The on-axis jets are either injection of charged fine droplets, or in the form of long necking. Fig 3.36 shows the on-axis jets at the final drop injection step.

(a) (b)

Fig 3.36. Jets at low voltage of injection into Marcol 52 with MSP5, 1.3 ms, relative meniscus height of h/R_{cap}=0.78 and voltage 3.76 kV for (a) and 3.78 kV for (b).

In this case jets at low voltage as in the figure above take the appearance of a needle sitting on the relatively flat meniscus. The jets are caused by the latter where the injection is mainly based on electrical force, and not the inertial dynamics of the meniscus. Generally the drops could be detached before the end of the electric pulse and be charged directly. Other on-axis jets take the form of long necking at high voltage, as shown on Fig 3.37.

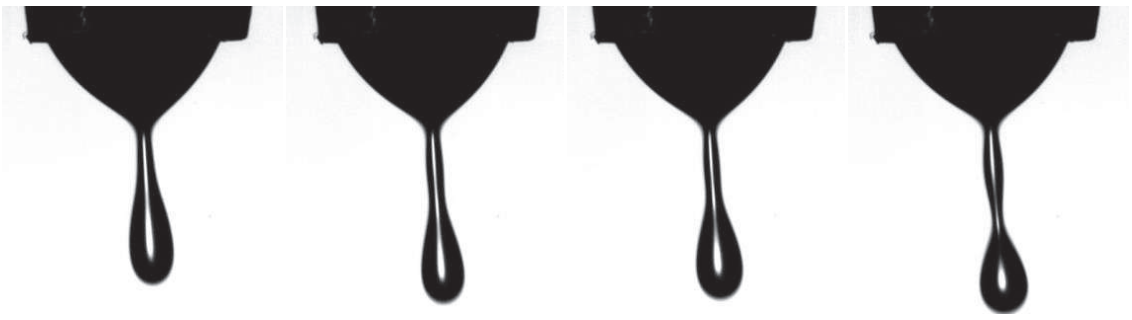

(a) (b) (c) (d)

Fig 3.37. Jets formation at high voltage (a) 4220V; (b) 4240V; (c) 4260V; (d) 4280V.

Fig 3.37 shows an example of injection into Marcol 52 with MSP3 1.3 ms, relative meniscus height h/R_{cap}=0.78 and voltage (a) 4.22 kV; (b) 4.24 kV; (c) 4.26 kV; (d) 4.28 kV. This long necking results in

big satellite formation. During drop injection, under some conditions the injected drop diameters converged with increasing voltage (as shown on Fig 6.2 in Appendix). The increasing voltage caused long necking and increasing satellite sizes, instead of main drop sizes.

3.7.3 Failure of neck breaking

As said in chapter 3.4.3, a gap in the droplet diameter versus applied voltage curves is sometimes observed. This could be related to the fact that the dynamics of stretched meniscus fails sometimes in detaching a droplet. This failure seems due to very small differences in the sequence, as illustrated in the example shown hereafter. The example shown on Fig 3.38 corresponds to the result of the application of MSP10 pulse with a 6.8 kV maximum voltage.

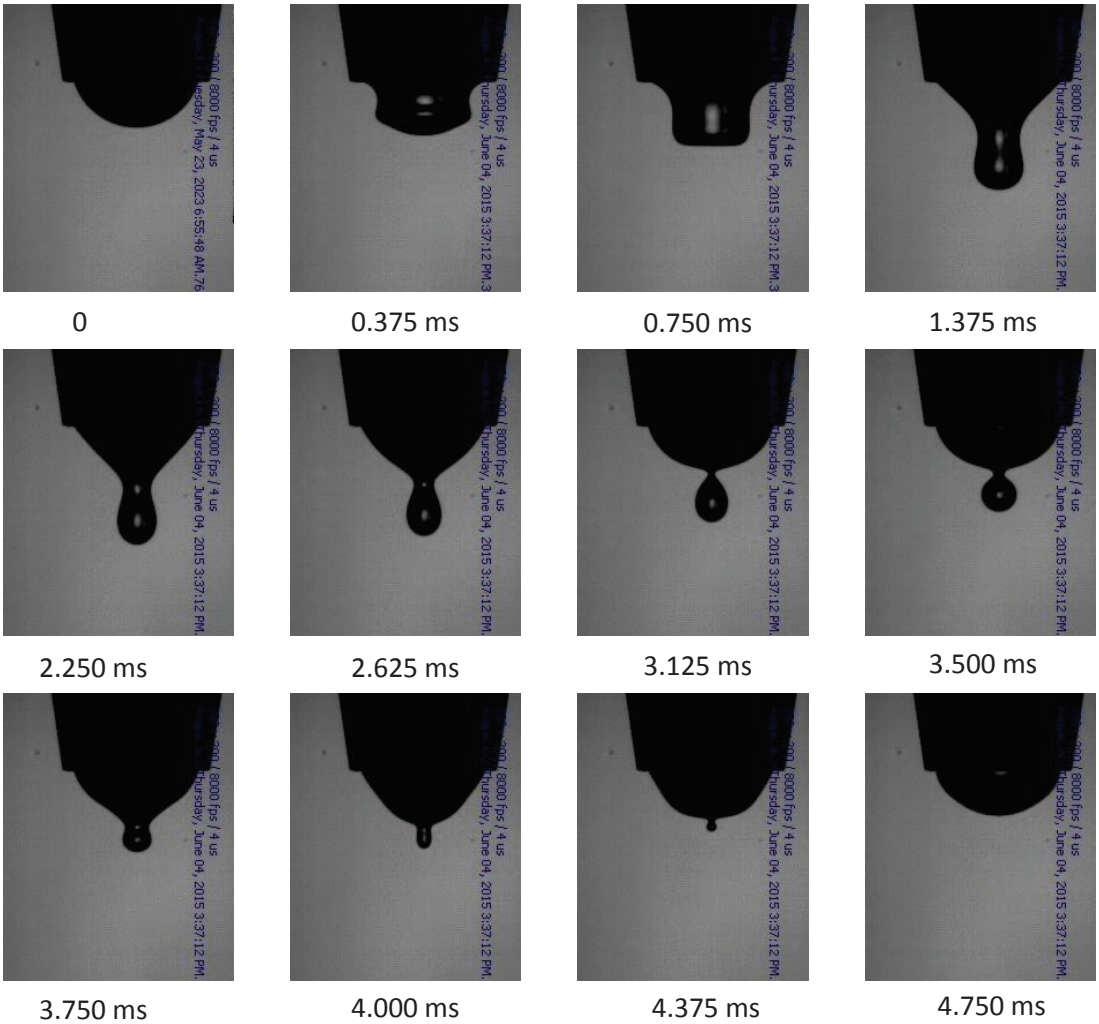

Fig 3.38. Injection performed with MSP10 6.8 kV (04/06/2015) case A.

The sequence on Fig 3.38 is called case A, and it shows that the water thread was not cut off and the formed drop was completely reabsorbed by the attached meniscus. The same experiment was repeated and the results were found completely different. This experiment, called case B, is shown on Fig 3.39.

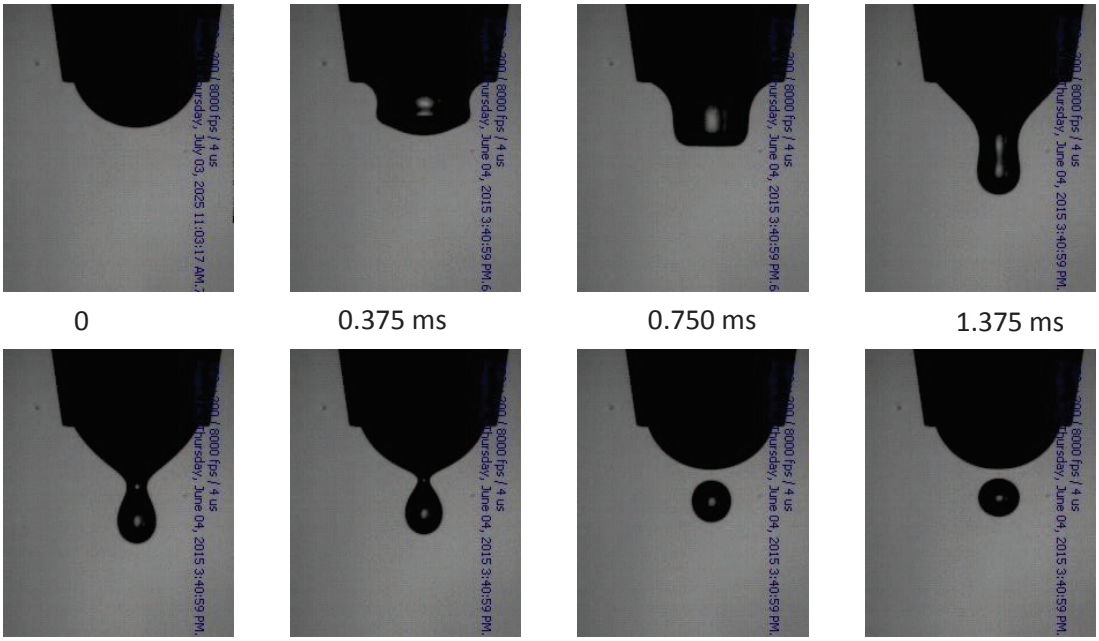

Fig 3.39. Injection performed with MSP10 6800V (04/06/2015) case B.

Comparing the two sequences, no clear differences can be seen up to the 6th pictures. This is illustrated more in detail by drawing on Fig 3.40 the contour obtained from image processing in the two cases, just before the retraction in case A and drop separation in case B. Only small differences can be observed in the curvature and neck diameter, leading to completely different behaviors. More in depth analysis will be needed to understand all the physics of such bifurcations.

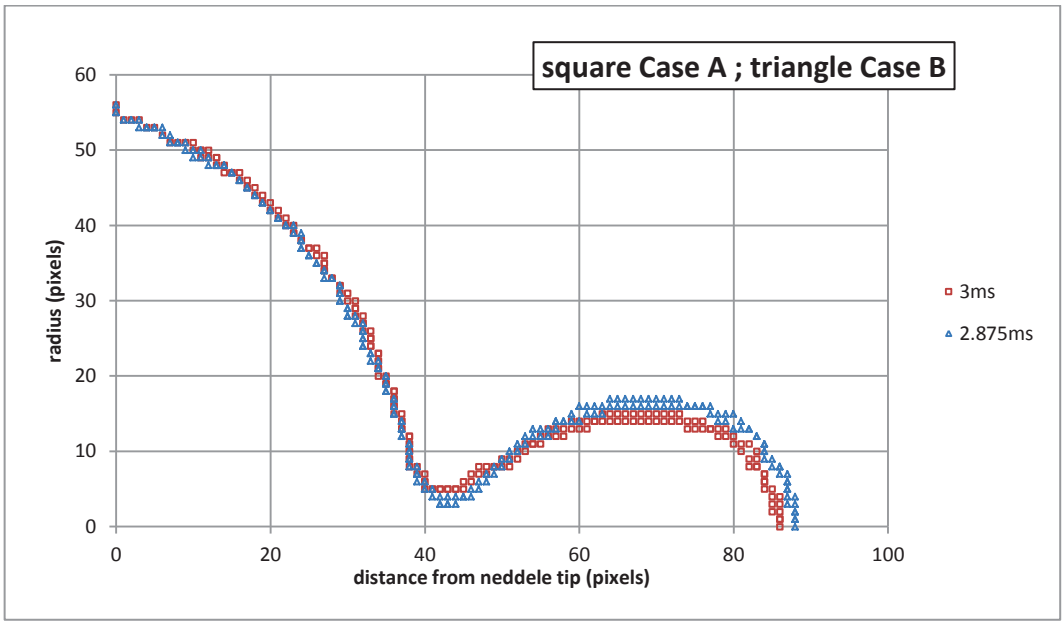

Fig 3.40. Water thread cutting points are illustrated for both injection of case A and case B for MSP10 at 6800V.

3.8 Conclusion

In this chapter, EHD single drop injections are investigated in details. For such injections, oil viscosity, interfacial tension, meniscus height and pulse shape were found influencing the meniscus dynamics and the resulting droplets. Starting from the results obtained by Raisin (2011) with Polybutene oil, improvements of injection parameter were needed to control the generation of droplets in Marcol 52 and Primol 352 model oils.

Application of DC electric field enlightened the fact that droplets injected by EHD method are electrically charged. First this observation led us to propose further improvements of the applied electric pulses to reduce the droplet charge. Secondly, since it was not possible to obtain droplets completely electrically neutral, it was needed to characterize with the highest possible accuracy the droplets size and charge. To improve such accuracy, a method based on the measurement of falling velocity is proposed, in addition to the direct measurements from images. The analysis of their associated uncertainties is also discussed. It should be recalled that for the EHD injections the best MSP pulse shapes are MSP4, MSP_{inv} and MSP10, and they are the pulses used in following chapters.

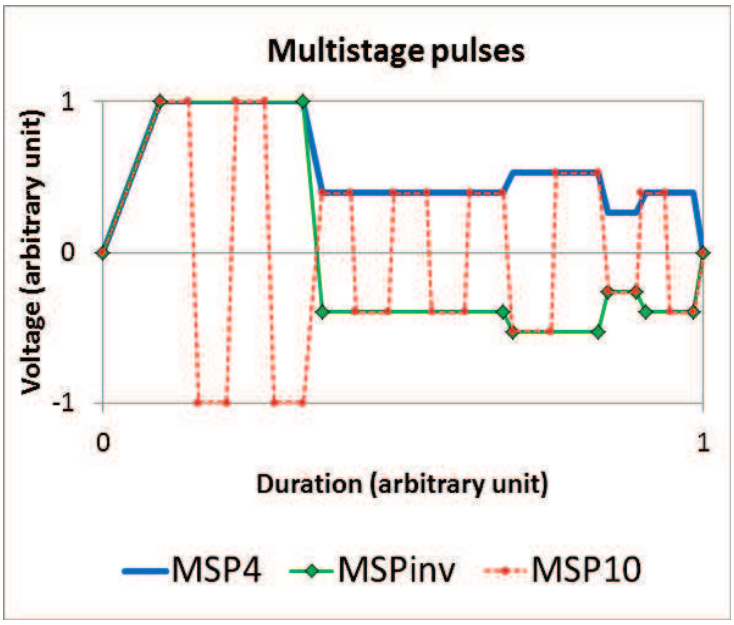

Fig 3.41. Used pulse shapes MSP4, MSP_{inv} and MSP10 for following chapters.

Chapter 4. Dual drop injection in model oil

4.1 Introduction

The drop coalescence study requires the injection of drop pairs in model oils. In previous experiments drop pairs were produced by pushing two syringes (Mohammadi et al. 2014) (Ingebrigtsen et al. 2005) (Guo & He 2014). For such drops, the diameter range is of millimetre scale. However our experiments on drop coalescence require drop diameters of smaller scale to simulate real crude oil water emulsion conditions. For this reason the EHD drop injection technique was adopted. Dual drop injection from two parallel needles was tested by (Raisin 2011). In this chapter, dual drop injection from a single needle is proposed. The analysis of the drops pair falling velocity should take into account strong hydrodynamic coupling effect obtained at very low Reynolds number. The electric charge of the two drops can then be deduced from the falling velocity.

4.2 Previous dual drop injection from parallel needles

The EHD drop injection technique allows injecting droplets with variable diameter smaller than nozzle size. This drop injection method was first used by (Raisin 2011) for drop electrocoalescence experiments. In his studies two parallel needles were mounted with identical heights and meniscus shapes. By applying a multistage electric pulse, two equal drops were produced successfully. However, the motions of the two drops are off-axis as illustrated on Fig 4.1.

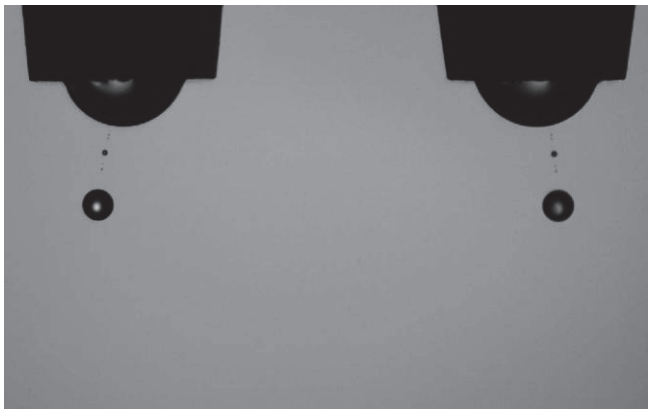

Fig 4.1. Dual drops injection from parallel needles (Raisin 2011).

This phenomenon is due to the modification of the surrounding electric fields caused by the presence of the other needle. As the two drops fall with divergent trajectories and with initial large relative distance, it is quite difficult to bring them close and induce coalescence. Moreover, for this configuration of dual drop injection, the injecting process is very difficult to control because slight difference between meniscus height or needle position can significantly influence the injected drop size.

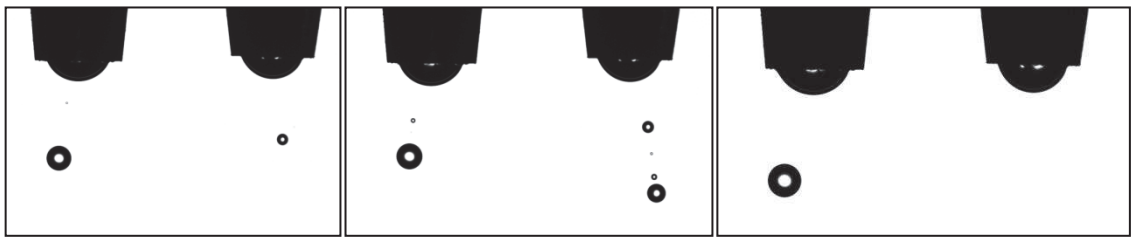

(a) (b) (c)

Fig 4.2. Dual drop injection performed using pulse MSP1 with 1.3 ms duration. (a), uneven drops. (smaller droplet associated with satellites extracted from the right needle. (c) the drop formed at the right needle is quickly absorbed by the meniscus.

Fig 4.2 illustrates some examples of different types of failure in generating a pair of similar droplets. Uneven droplets, generation of large satellites or failure in detaching one of the two droplets are often observed, and appear very sensitive to initial conditions. Thus a new drop injection method should be thought of for more stable and repeatable drop production to perform drop coalescence experiments.

4.3 Dual drop injection from single needle

The new dual drop injection method aims at injecting a pair of drops from the same needle, hanging straight above the bottom electrode. The injected drop pair then falls along the vertical axis in model oil and remain aligned with the electric field. This system is axisymmetric and this drop injection method shows a better repeatability than that using two parallel needles. The falling drops approach each other before they reach the bottom of the test cell, to allow coalescence. The experiments of dual drop injection were performed both in EHD injection setup and in drop coalescence setup. The oil used was Marcol 52 with 0.001 wt% Span80, and injected drops were made of tap water with 3.5 wt% NaCl.

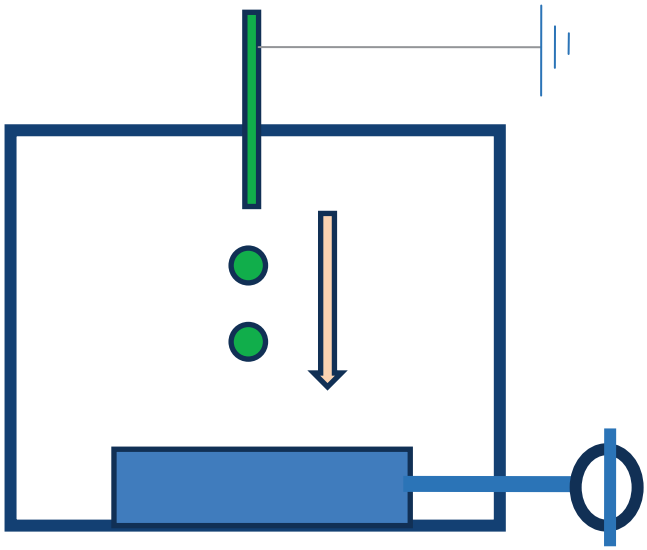

Fig 4.3. Dual drop injection principle.

Fig 4.3 shows the principle of dual drop injection in EHD injection setup. The needle is grounded and the electrode below is connected to high voltage. All are immersed in model oil and the two drop extracted from the needle fall, their axis remaining aligned with the electric field. On their way down, before they reach the electrode, a DC field or AC field may be applied to induce drop electrocoalescence.

4.3.1 Parameters influence on dual drop injection

For dual drop injection, the first important factor influencing the injection process is the distance between the first injected drop and the needle tip during the second drop injection. As it is known that a single drop exposed to high voltage fields may disintegrate (Taylor 1964), it is important to ensure a sufficient distance between the first drop and the meniscus apex to give no split of the former and good injection of the second droplet. To give an idea about this distance, a simulation was done using COMSOL software.

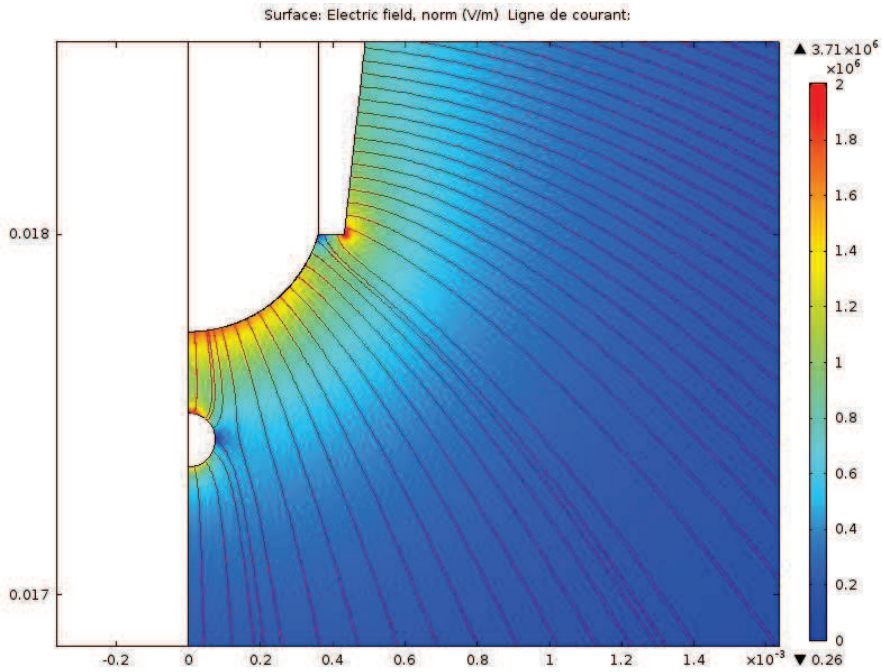

Fig 4.4. 3D numerical simulation of electric fields faced by the first injected drop around the needle tip.

Fig 4.4 shows the electric field intensity and streamlines around the meniscus hanging at the needle tip and a first injected drop. With the presence of the drop, the electric fields at the needle tip will be modified. Also the first drop will be exposed to a very high electric field during the second drop injection if it remains in the close vicinity of the needle tip and in the reinforced electric field. The critical value of the uniform electric field has been calculated by (Taylor 1964) as:

$$E_c = 0.648\left(\frac{\sigma}{\varepsilon_0 \varepsilon_r \mathrm{D}}\right)^{0.5} \tag{4.1}$$

Here σ is the interfacial tension, ε_0 is the permittivity of free space and ε_r the relative permittivity of the medium. D is the water droplet diameter. The electric field intensities were obtained by

numerical simulation for both the first drop and the meniscus apex prior to the second drop injection. For the calculations, the first injected drop diameter is assumed to be D = 0.15 mm, and the constant applied voltage on the electrode is 7.0 kV. The distance between the needle tip and the electrode is H = 18 mm. The permittivity of used oil is given in Table 2.2.

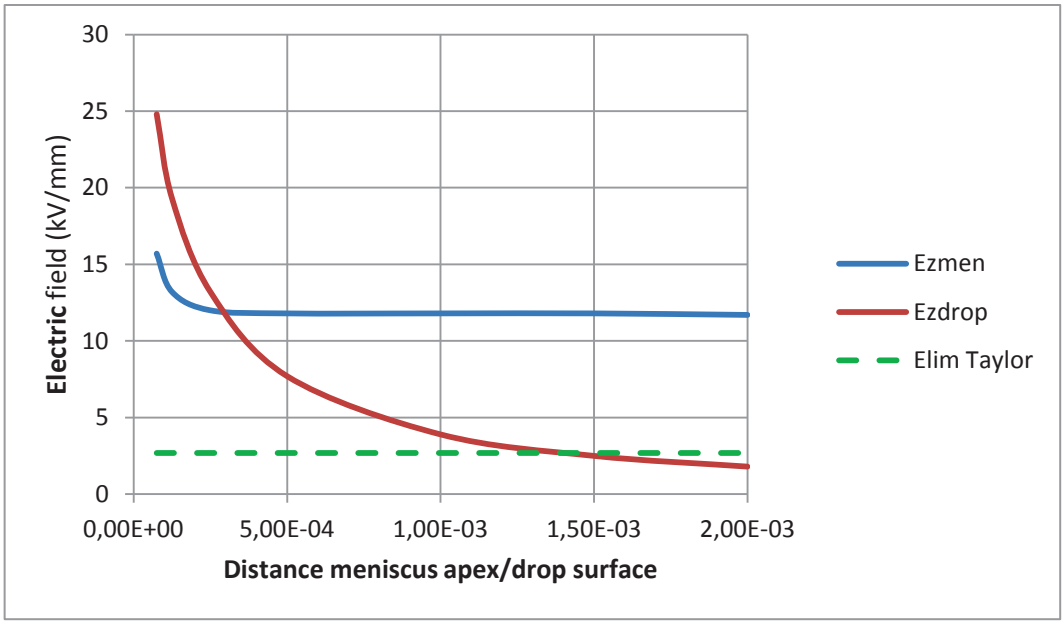

Fig 4.5. Maximum electric field calculated at water meniscus and at the first drop apex during the second drop injection.

Fig 4.5 shows the steady maximum electric field calculated at the apex of the water meniscus and of the first drop. The distance is between the meniscus apex and the drop surface, and it begins at 0.075 mm which corresponds to one half of the first drop radius. When the drop is very close to the meniscus, the electric field intensity on the drop surface is stronger than that on the meniscus. On the contrary when the distance is quite large (about 10 times the diameter) the electric field on the droplet surface is smaller than Taylor limit. It should be noticed that the voltage applied on the electrode is fixed to extract one droplet and not to make the meniscus fully disintegrate. On the other hand the Taylor critical electric field does not take into account the dynamics of the surface deformation for short duration pulses. The intersection of the two curves indicates only an order of magnitude of the minimum distance that should be ensured between the first injected drop and the needle tip, and it corresponds to a little less than twice the droplet diameter.

Fig 4.6 illustrates a real behavior of the first droplet, when located too close to the meniscus apex when the second pulse is applied. . The photographs were taken during drop injection by MSP4 pulse with 1.5 ms duration and -8.5 kV voltage amplitude in EHD injection setup (H = 18 mm). The video

was made using the AOS camera with 200*373 pixels for spatial resolution and 5000 fps frame rate and a 4 µs shutter speed. Oil temperature was 25 °C ± 1 °C.

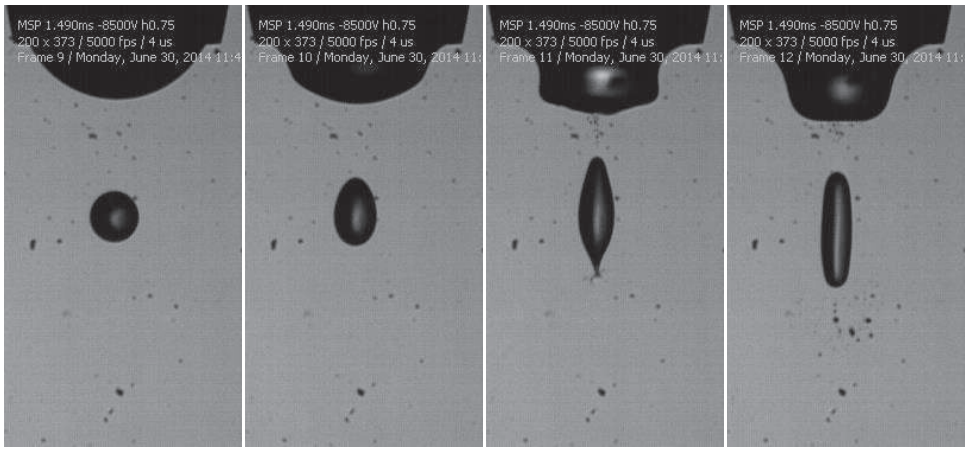

0 0.2 ms 0.4 ms 0.6 ms

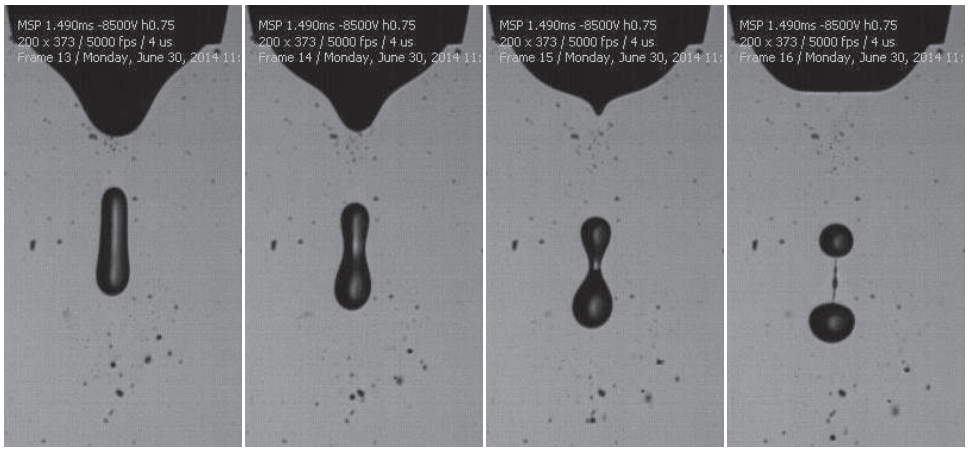

0.8 ms 1.0 ms 1.2 ms 1.4 ms

Fig 4.6. First drop was split during application of the second electric pulse (30/06/2014, 25 °C ± 1 °C).

The series of frames taken from the high speed video illustrated the splitting process of the first injected drop during the second pulse and the influence on the meniscus cancelling the second drop injection. To make the two droplets meet during their descent down in cell, the best method consists in generating a second droplet a little larger than the first one. The processes were recorded using the Dalsa camera at 100 fps frame rate.

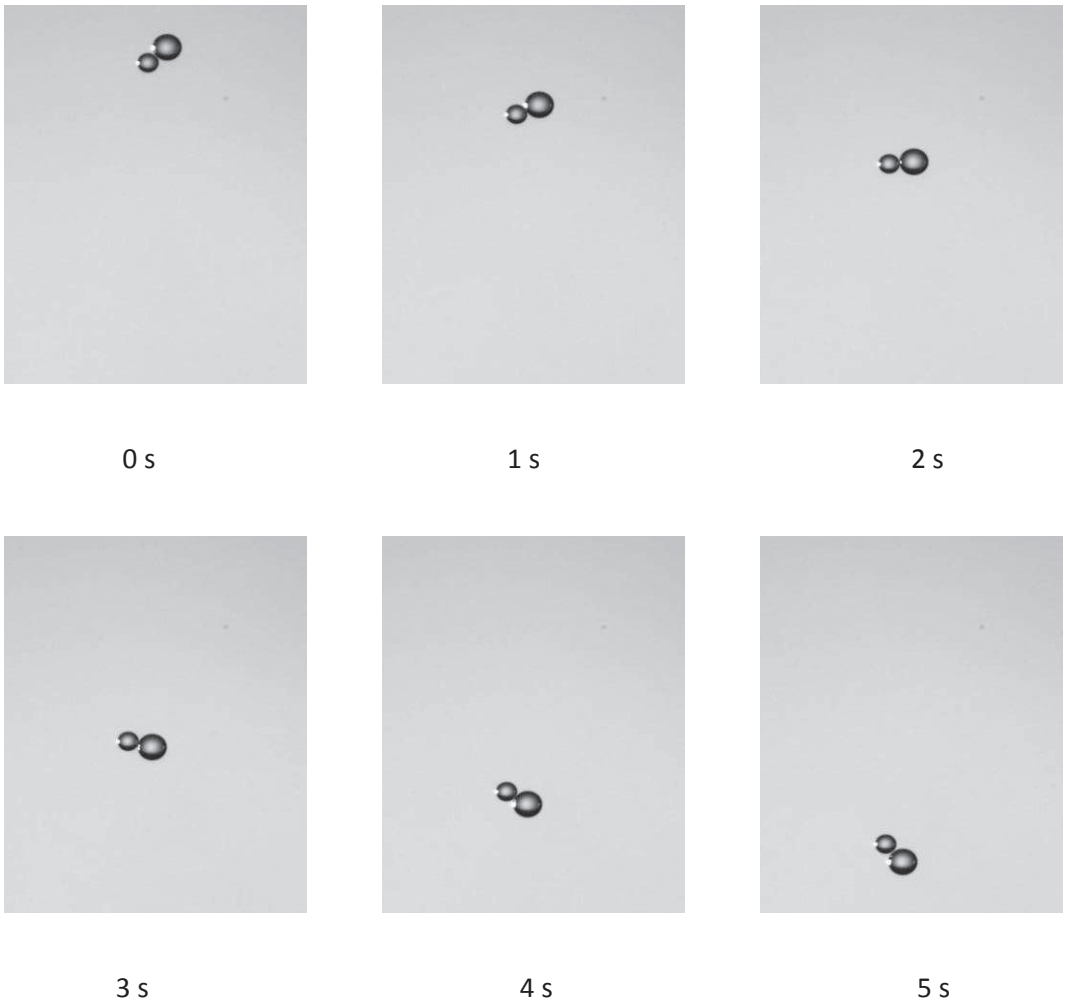

Fig 4.7. Falling two drops without DC fields (injected by MSP10 – MSP10 at +6060V and +6200V). (08/06/2015, 25 °C ± 1 °C).

The photos on Fig 4.7 show an example that when two drops are falling in oil medium without electric field application, they can pass by each other closely without coalescing. The time interval between the successive two photos is 1 second. The drops were injected by MSP10 at +6060V and +6200V respectively, and the diameter values are 0.11 mm and 0.15 mm. The weight difference causes the second drop to catch up on the first one and bypasses it in the absence of electric field. This phenomenon of non–coalescence is due to the separation effect of thin oil film which locates between the drops pair facing poles.

4.3.2 Diameter range of droplet pairs

On the optimal conditions for dual drop injection were found, a series of injections were performed to test the widest range of drop diameters. The experiments were done in the EHD injection setup containing Marcol 52 with 0.001 wt% Span80. The water contained 3.5 wt% NaCl and the distance between the needle tip and the electrode was H = 18 mm. The needle inner radius was R_{cap} = 0.36 mm. For this injection series a metallic cover was placed on the top of the test cell. The applied electric pulse for drop injection was of MSP4 at identical voltage for the two drop injections. Between the two successive pulses, a time delay of 600 ms was applied so that the first injected drop was far enough to have a sufficiently small influence on the second injection.

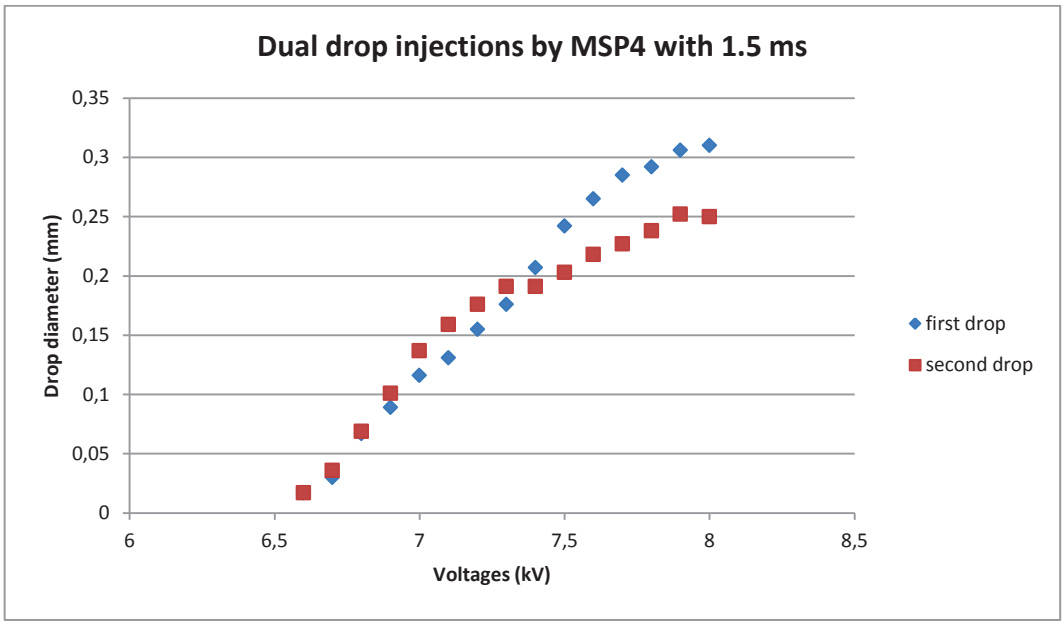

Fig 4.8. Dual drop injection with identical MSP pulse shapes (02/07/2014, T = 25 °C ± 1 °C).

Fig 4.8 shows that the drop diameter range is from about 25 µm to 300 µm. For small drops the diameters obtained are identical. With increasing voltage, a discrepancy occurs between the sizes of the two drops injected which enlarges with voltage. At intermediate diameters, the second drop is a little larger than the first one, while for the higher voltage the second droplet is clearly smaller than the first one.

As it was shown previously the meniscus heights could influence injected drop sizes. Our analyses are that this difference in drop size is due to the difference in meniscus heights for the two drop injection. When the first injected drop is of a small size, the meniscus height is not modified significantly. When the first injected drop enlarges, the meniscus height is then reduced because of the extraction of the

corresponding volume of water. As shown on Fig 3.34 the injected drop diameter is not a monotonic function of the meniscus height and it can explain that a small reduction of this height increases slightly the droplet size while a larger one decreases it. The curve stopped at 8 kV because jets were produced.

4.4 Determinations of diameter and charge of the two falling droplets

For small droplet size and falling velocity, the Reynolds number is very low, of the order of 10^{-3}, and the interaction between the two drops is fully symmetric. The strong coupling of the two drops is called reflection, as described by (Batchelor 1982).

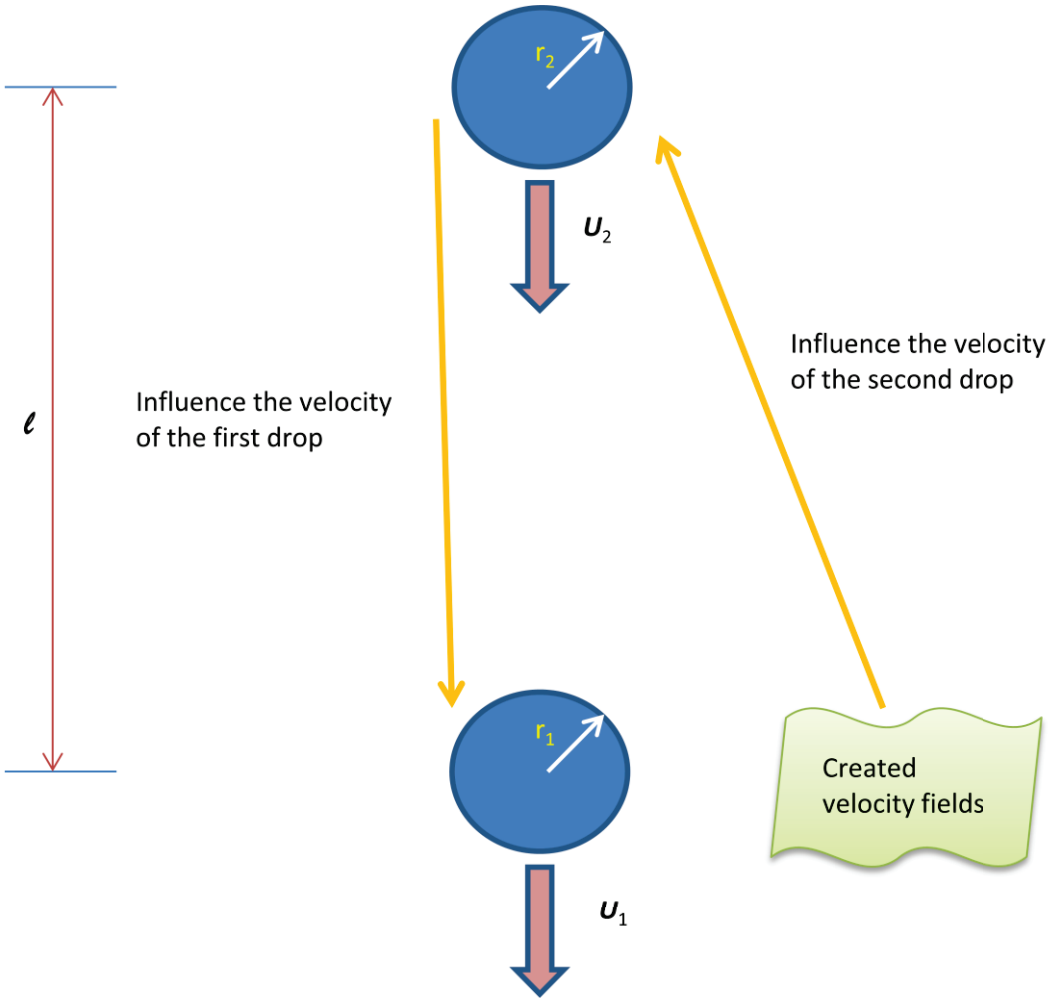

Fig 4.9. Diagram of the coupling of the two falling drops.

On the Fig 4.9 the two drops are falling with different velocities $\boldsymbol{U}_1$ and $\boldsymbol{U}_2$ inside oil medium. Their velocities are mutually influenced.

4.4.1 Drop diameter corrections

For a drops pair falling inside oil medium, the diameters and forces acting on the two drops can be calculated through their falling velocities. However these parameters do not connect to each other through a simple law because of the strong coupling effect between the two drops. Thus more developed calculations were adopted based on principles described in (Batchelor 1982) and (Jeffrey & Onishi 1984). For drop diameter calculations, in experiments on falling drops pairs only translations of the two drops should be considered as there is no rotational effect on these two drops. Thus the velocity of the two drops can be depicted as following.

$$\boldsymbol{U}_1 = M_{11}\boldsymbol{F}_1 + M_{12}\boldsymbol{F}_2 \tag{4.2}$$

$$\boldsymbol{U}_2 = M_{21}\boldsymbol{F}_1 + M_{22}\boldsymbol{F}_2 \tag{4.3}$$

With $\boldsymbol{U_m}$ the velocity of the drops m (m = 1, 2) (bold characters denotes a vector), M_{mn} the mobility tensors (Batchelor 1982) and $\boldsymbol{F_n}$ the exterior forces exerted on the drop n (n=1, 2).

The mobility tensors can be decomposed along axial (with respect to the axis joining the two drop centers) and perpendicular directions by involving the mobility coefficients X_{mn} and Y_{mn} respectively which gives the mobility tensor M_{mn} another form.

$$M_{mn} = \frac{1}{3\pi\mu_o(r_m + r_n)}\left[X_{mn}\frac{\boldsymbol{l}*\boldsymbol{l}}{l^2} + Y_{mn}\left(\boldsymbol{I} - \frac{\boldsymbol{l}*\boldsymbol{l}}{l^2}\right)\right] \tag{4.4}$$

In the above formula, **I** is the identity matrix; r is the radius of the drops and $\boldsymbol{l}$ the distance between the drops center to center (bold character $\boldsymbol{l}$ denotes the vector form and $\boldsymbol{l}*\boldsymbol{l}$ is then a tensor). Thus $\boldsymbol{U}_1$ and $\boldsymbol{U}_2$ can be rewritten in the more developed forms.

$$\boldsymbol{U}_1 = \frac{1}{6\pi\mu_o r_1}\left[X_{11}\frac{\boldsymbol{l}*\boldsymbol{l}}{l^2} + Y_{11}\left(\boldsymbol{I} - \frac{\boldsymbol{l}*\boldsymbol{l}}{l^2}\right)\right]\boldsymbol{F}_1 + \frac{1}{3\pi\mu_o(r_1+r_2)}\left[X_{12}\frac{\boldsymbol{l}*\boldsymbol{l}}{l^2} + Y_{12}\left(\boldsymbol{I} - \frac{\boldsymbol{l}*\boldsymbol{l}}{l^2}\right)\right]\boldsymbol{F}_2 \quad (4.5)$$

$$\boldsymbol{U}_2 = \frac{1}{6\pi\mu_o r_2}\left[X_{22}\frac{\boldsymbol{l}*\boldsymbol{l}}{l^2} + Y_{22}\left(\boldsymbol{I} - \frac{\boldsymbol{l}*\boldsymbol{l}}{l^2}\right)\right]\boldsymbol{F}_2 + \frac{1}{3\pi\mu_o(r_1+r_2)}\left[X_{21}\frac{\boldsymbol{l}*\boldsymbol{l}}{l^2} + Y_{21}\left(\boldsymbol{I} - \frac{\boldsymbol{l}*\boldsymbol{l}}{l^2}\right)\right]\boldsymbol{F}_1 \quad (4.6)$$

In the experiments of dual drop injection, the two injected drops fall one after another in an axisymmetric fashion. This implies that firstly there is no force acting perpendicular to the drop motion, and thus the parameter $Y_{mn} = 0$. Secondly, according to symmetrical properties of the system, these mobility coefficients have symmetries $X_{mn} = X_{nm}$ and $X_{mm} = X_{nn}$. Thirdly, as the system is axisymmetric, there is only one component (z axis) and the vectors $\boldsymbol{U}_m$ and $\boldsymbol{F}_n$ are projected along this z axis. Thus they are described by scalars U_m and F_n. Summing up all the above conditions, the equations of drop velocities can be much simplified.

$$U_1 = \frac{1}{6\pi\mu_o r_1}X_{11}F_1 + \frac{1}{3\pi\mu_o(r_1+r_2)}X_{12}F_2 \quad (4.7)$$

$$U_2 = \frac{1}{6\pi\mu_o r_2}X_{11}F_2 + \frac{1}{3\pi\mu_o(r_1+r_2)}X_{12}F_1 \quad (4.8)$$

U_1 and U_2 are velocities of the two droplets that can be taken directly from the Dalsa cameras in experiments. r_1 and r_2 are drop diameters which are firstly calculated as single drops falling freely inside oil medium, by using Stokes equation (3.2). Then the forces F_1 and F_2 can be calculated as:

$$F_1 = 6\pi\mu_o \frac{r_1 X_{11}U_1 - \frac{2r_1r_2}{r_1+r_2}X_{12}U_2}{X_{11}^2 - \frac{4r_1r_2}{(r_1+r_2)^2}X_{12}^2} \quad (4.9)$$

$$F_2 = 6\pi\mu_o \frac{r_2 X_{11}U_2 - \frac{2r_1r_2}{r_1+r_2}X_{12}U_1}{X_{11}^2 - \frac{4r_1r_2}{(r_1+r_2)^2}X_{12}^2} \quad (4.10)$$

Introducing two non-dimensional parameters λ and s, with $\lambda = r_2/r_1$ and $s = 2\,l\,/(r_1+r_2)$, with l the drop center to center distance, the mobility coefficients are given by (Batchelor 1982) as:

$$X_{11} = 1 - \frac{60\lambda^3}{(1+\lambda)^4 s^4} + \frac{32\lambda^3(15-4\lambda^2)}{(1+\lambda)^6 s^6} - \frac{192\lambda^3(5-22\lambda^2+3\lambda^4)}{(1+\lambda)^8 s^8} + O(s^{-10}) \tag{4.11}$$

$$X_{12} = \frac{3}{2s} - \frac{2(1+\lambda^2)}{(1+\lambda)^2 s^3} + \frac{1200\lambda^3}{(1+\lambda)^6 s^7} + O(s^{-9}) \tag{4.12}$$

For a simplified model when the two drops are sufficiently far from each other (typically s > 4), the terms of the equations (4.11) and (4.12) can be limited to O (s^{-4}). If the two drops are much closer, all the terms in the equations will be considered. For very close droplets (typically s < 3) the terms in equations (4.11), (4.12) are decreasing only very slowly with the increasing exponent of (1/s) and the accuracy of the relation between velocities and forces is degraded.

When the forces acting on the drops are calculated through equation (4.9) and (4.10), the values of drop radii r_1 and r_2 can be obtained using a technique of successive approximation. For free fall drops inside oil medium, the forces are balanced.

$$\boldsymbol{F}_1 = \Delta m_1 \boldsymbol{g} \tag{4.13}$$

$$\boldsymbol{F}_2 = \Delta m_2 \boldsymbol{g} \tag{4.14}$$

The difference of mass Δm is written below.

$$\Delta m_1 = \frac{4}{3}\pi r_1^3(\rho_w - \rho_o) \tag{4.15}$$

$$\Delta m_2 = \frac{4}{3}\pi r_2^3(\rho_w - \rho_o) \tag{4.16}$$

Then, combining equations (4.13), (4.14), (4.15) and (4.16), the radius of the drops can be calculated again.

$$r_1 = \sqrt[3]{\frac{3F_1}{4\pi(\rho_w - \rho_o)g}} \tag{4.17}$$

$$r_2 = \sqrt[3]{\frac{3F_2}{4\pi(\rho_w - \rho_o)g}} \tag{4.18}$$

These values of drop radius can then be substituted into equations (4.9) and (4.10) to calculate the corrected forces acting on the two drops. In this method of successive approximations, the initial radii can be given by the method without interaction (equation 3.4). It was observed that generally one or two iterations are sufficient to get a pretty good convergence of the results (radii, velocities and forces). Moreover at the second iteration, the convergence can be improved by applying Newton's method.

4.4.2 Drop charge calculations

To determine the electric charge of water drops, an application of DC field on the electrode is programmed during the free fall journey of the drops. The drop descents are recorded by the Dalsa camera. When the falling drops pair is subjected to the electric field, the motion is modified due to the contained electric charge. The drops change their velocities within 0.1 seconds and they readjusted immediately to an equilibrium state. For this system the positive direction is upwards along the vertical axis z and the applied electric fields lines are parallel to the drop center-center lines. The forces acting on the two falling drops can be calculated using the complete method suggested by (Davis 1964).

$$F_z(1) = 4\pi\varepsilon r_1^2 E^2 F_1' + E(F_3' q_2 + F_4' q_1) + \frac{1}{4\pi\varepsilon r_1^2}(F_5' q_2^2 + F_6' q_1 q_2 + F_7' q_1^2) + E q_1 \tag{4.19}$$

$$F_z(2) = 4\pi\varepsilon r_2^2 E^2 F_1 + E(F_3 q_1 + F_4 q_2) + \frac{1}{4\pi\varepsilon r_2^2}(F_5 q_1^2 + F_6 q_1 q_2 + F_7 q_2^2) + E q_2 \tag{4.20}$$

Here ε is the permittivity of the medium with $\varepsilon = \varepsilon_0\varepsilon_r$, q_1 and q_2 are the electric charges carried by the two drops, E the electric field intensity. F_1 to F_7 in equation (4.20) are coefficients given in (Davis 1964) which can be noted as F_j. It should be noticed that the coefficients F_j' in equation (4.19) and F_j in equation (4.20) are not the same because the system described is not symmetric, and the coefficients F_j depend on the drop ratio $1/\lambda = r_1/r_2$ and the ratio of drop ''inter-distance'' on drop radius $(l - r_1 - r_2)/r_i$ with r_i the drop radius of either the first drop or the second one according to

calculations of F_j. The calculations of F_j involve a series of summations at different drop ''inter-distances'', thus a simplified model is used.

The third terms in equation (4.19) and (4.20), $F_{z3}(1) = \frac{1}{4\pi\varepsilon r_1^2}(F_5' q_2^2 + F_6' q_1 q_2 + F_7' q_1^2)$ and F_{z3} (2) = $\frac{1}{4\pi\varepsilon r_2^2}(F_5 q_1^2 + F_6 q_1 q_2 + F_7 q_2^2)$, represent the electrostatic interaction between the two charged droplets. For a simplified form the charges are considered as concentrated at the drop centers, and the resulting force, opposing for to the two drops, can be written as:

$$F_{es} = \frac{1}{4\pi\varepsilon_0\varepsilon_r}\frac{q_1 q_2}{l^2} \tag{4.21}$$

For the first drop the attraction force is positive and the repulsion is negative. It is the contrary for the second drop.

$$F_{es}(1) = -F_{es} \tag{4.22}$$

$$F_{es}(2) = F_{es} \tag{4.23}$$

Here $F_{es}(1)$ and $F_{es}(2)$ are the electrostatic forces acting on the first drop and the second drop respectively.

The dipole-dipole interaction force corresponds to the first term in equation (4.19) and (4.20), $F_{z1}(1) = 4\pi\varepsilon r_1^2 E^2 F_1'$and $F_{z1}(2) = 4\pi\varepsilon r_2^2 E^2 F_1$, and the equations are taken from (Atten 1993). In experiments to reveal drop charge, the distance between the two drops is larger than the smallest drop radius, and no coalescence process occurs in these cases. Thus the equation is taken for large separations without deviation angle between drop center-center lines and the electric field:

$$F_{dd}(1) = 24\pi\varepsilon_0\varepsilon_r r_1^3 E^2\left(\frac{r_2^3}{l^4}\right) \tag{4.24}$$

$$F_{dd}(2) = 24\pi\varepsilon_0\varepsilon_r r_2^3 E^2\left(\frac{r_1^3}{l^4}\right) \tag{4.25}$$

The dipole-dipole forces are attractive, thus the force on the first drop is positive and that on the second drop is negative.

$$F_{dd}(1) = 24\pi\varepsilon_0\varepsilon_r r_1^3 r_2^3 E^2 \left(\frac{1}{l^4}\right) \tag{4.26}$$

$$F_{dd}(2) = -F_{dd}(1) \tag{4.27}$$

The Coulomb force involving the external electric field E corresponds to the second term combined with the fourth term in equation (4.19) and (4.20), $F_{z24}(1) = E(F_3' q_2 + F_4' Q q_1) + E q_1$ and $F_{z24}(2) = E(F_3 q_1 + F_4 q_2) + E q_2$, and its simplified form when the charges are considered as concentrated at the drops center is:

$$F_c(1) = E q_1 \tag{4.28}$$

$$F_c(2) = E q_2 \tag{4.29}$$

The dielectrophoresis force F_{dep} described in equation (3.19) is considered always to be upwards because the up hanging needle has a much larger curvature than the electrode below. It is not taken into account in the Davis paper where the electric field E is uniform. The hydrodynamic coupling forces, dealing with viscous effects, F_1 and F_2 are calculated by equation (4.9) and (4.10).

The last term is the drop weight minus buoyancy force, which is presented as the difference between the drop weight and the replaced quantity of oil weight.

$$F_w(1) = \frac{4}{3}\pi r_1^3(\rho_w - \rho_o)g \tag{4.30}$$

$$F_w(2) = \frac{4}{3}\pi r_2^3(\rho_w - \rho_o)g \tag{4.31}$$

The total forces acting on the two drops are balanced as follows:

$$F_z(1) + F_{dep}(1) + F_1 + F_w(1) = 0 \tag{4.32}$$

$$F_z(2) + F_{dep}(2) + F_2 + F_w(2) = 0 \quad (4.33)$$

And in simplified model:

$$F_{dd}(1) + F_{es}(1) + F_{dep}(1) + F_1 + F_c(1) + F_w(1) = 0 \quad (4.34)$$

$$F_{dd}(2) + F_{es}(2) + F_{dep}(2) + F_2 + F_c(2) + F_w(2) = 0 \quad (4.35)$$

With equation (4.34) and (4.35), the drop charge can be calculated as well as the relative uncertainties on drop charge using the same method as described in section 3.5.2. It should be noticed again that the calculations are fully valid for relatively large drop distance (non-dimensional parameter s > 4) and less accurate when the distance decreases (s < 3). The differences between the forces given in (Davis 1964) and that of the simplified model is calculated and drawn on Fig 4.10 for the example of a drops pair at variable distance. The condition is taken for $r_1 = r_2$. The electric field applied is E = -0.125kV/mm (i.e. -1kVDC for H = 8mm). The charge on the drops are assumed to be q_1 = 0.01 pC and q_2 = -0.02 pC.

On Fig 4.10 the red solid curve is the first term F_{z1} in equation (4.20) and the red dashed line is the value F_{dd} of the dipole-dipole model of equation (4.27). The green solid line is the second term combined with the fourth term F_{z24} in equation (4.20) and the green dashed line is the value F_c of the Coulomb force model of equation (4.29). The blue solid line is the third term F_{z3} in equation (4.20) and the blue dashed line is F_{es} from the electrostatic force model of equation (4.23). The purple solid line is the sum of all the forces F_z calculated in equation (4.20) and the dashed purple line is the sum of the forces in simplified models. It is shown on the graph that when the distance between the two drops becomes smaller than 2 to 3 times the drop radius, the differences between the model given in (Davis 1964) and the simplified models of forces increase. Fig 4.11 quantifies the error made by using simplified models: a little more than 5% when the distance equals two times the radius (s = 4) , less than 2% when it exceeds 4 times the radius.

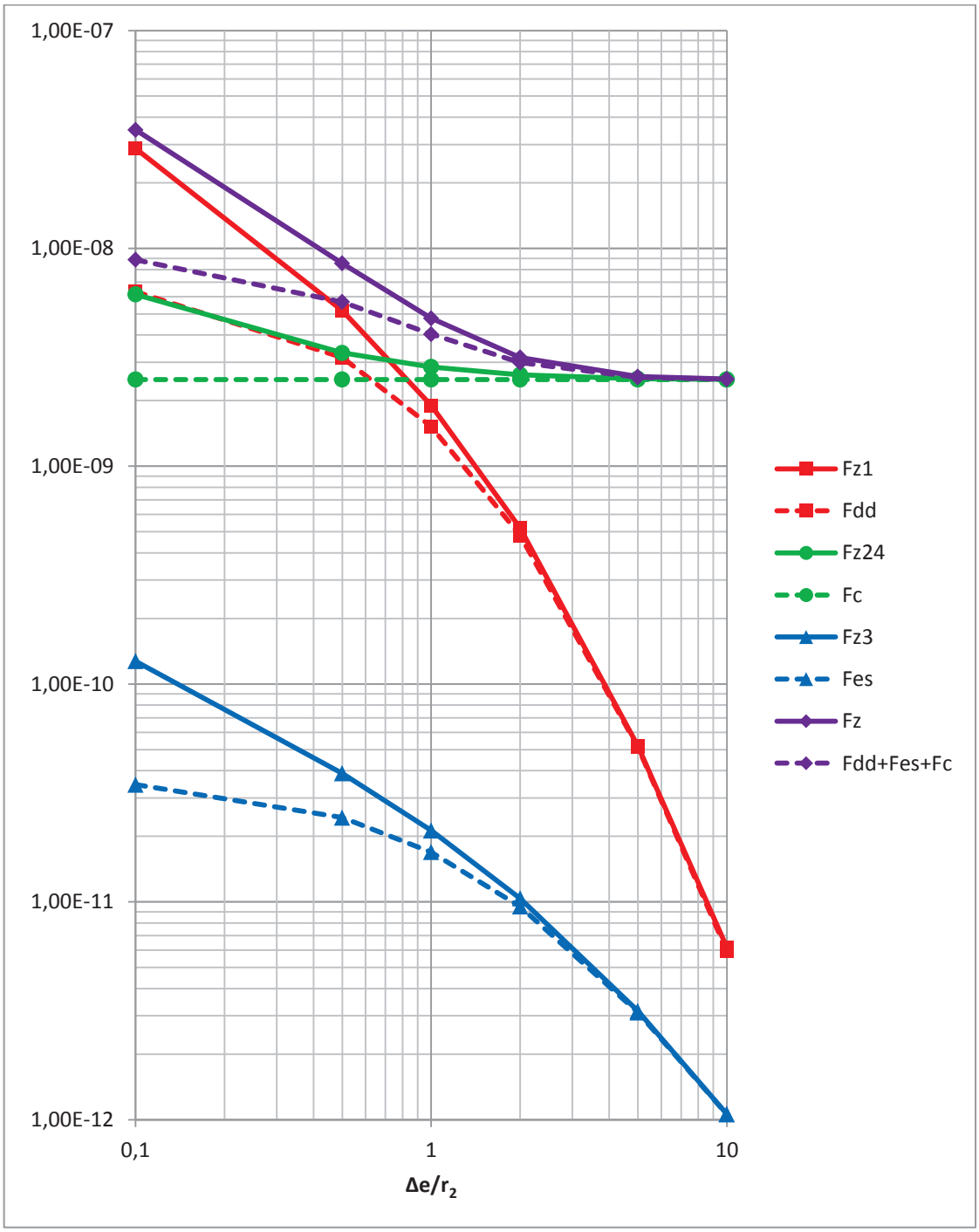

Fig 4.10. Different part of electric forces on drop 2 are calculated (full lines) and compared with their simplified models (dotted lines).

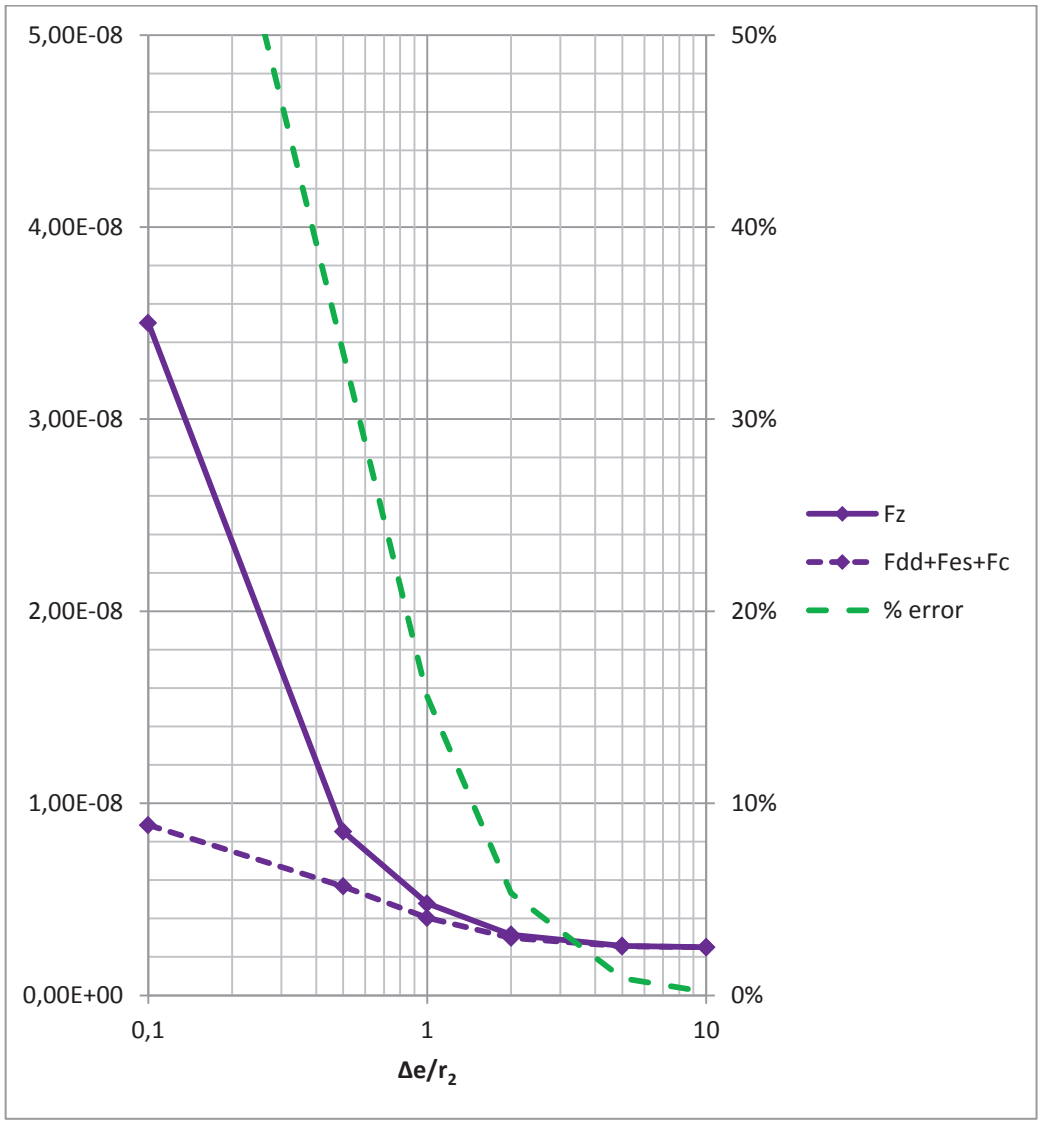

Fig 4.11. Relative error with inter drop distances.

4.5 Experimental results

Experiments of drops pair falling in model oil medium was performed in the drop coalescence setup with the water drop containing 3.5 wt% NaCl and Marcol 52 with 0.001 wt% Span80. Dalsa cameras were placed at the half way point between the needle and the electrode to register drop falling trajectories. With a 2-second delay after the two drops entered the camera vision field, a DC field of short duration was applied between the electrodes. During the application of the external electric fields, the motion of the drops changed. When the DC field was shut down, the two drops returned to falling velocities close to the initial ones, only affected by the increasing drop interaction due to

the fact that the droplets are closer to each other. Different cases were studied for drops pairs generated with different injection pulses.

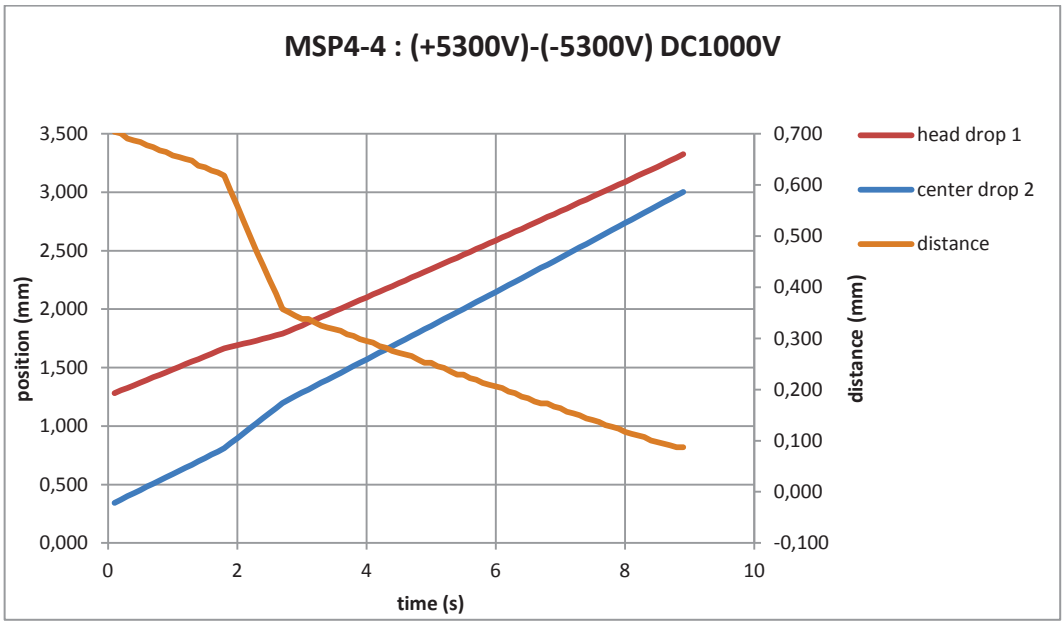

a)

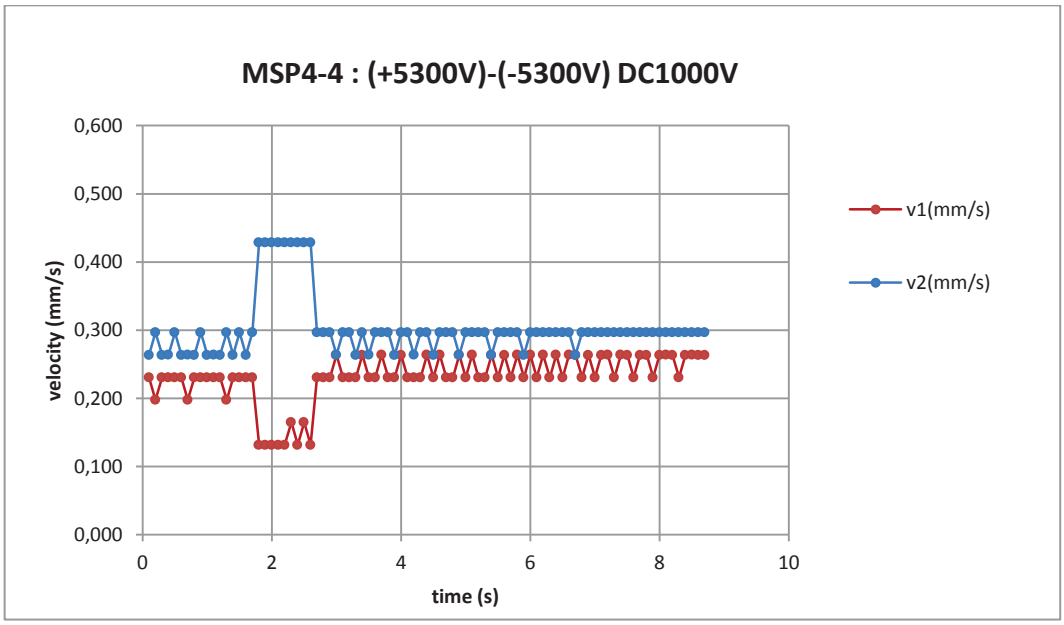

b)

Fig 4.12. Drop falling positions a) and velocities b) with dual injection MSP4 – MSP4 at +5300V and -5300V respectively, DC=1kV(29/05/2015, 23 °C ± 1 °C).Duration of application of DC voltage is 1 second. Velocities and position are positives from top to bottom. The position 0 corresponds to the upper entry of the video screen.

The calculations of velocities can be explained from the graph drawn on Fig 4.12. The positions of the drops are obtained using the Spotlight software applied to a set of successive images, and drop velocities are calculated from those position values.

$$v_n = \frac{x_{n+1} - x_n}{t_{n+1} - t_n} \tag{4.36}$$

Here x_n is the drop position at time t_n. The time step is 0.1 seconds and the change of drop velocities under DC fields began at 1.8 s and ended at 2.7 s, which corresponds more or less to the DC duration of 1 second. After 9 seconds the acquisitions stopped in that experiment. From the graph it can be seen that there are many quantification noises on the velocity curves. This is due to the uncertainties of the drop positions revealed by visual imaging. For drop velocity trends, one can observe three successive phases. In the first phase which starts from the beginning to 1.7 s, the drop velocity is steady, which means all the forces acting on it are in equilibrium. This is the drop free falling velocity in oil medium without DC application. The second phase began from 1.8 s to 2.6 s when the falling drop is subjected to an electric field generated with the DC voltage +1000V. The velocities changed within 0.1 s and droplets appear again falling in steady state. The shutdown of this DC field began at 2.7 second and the drop velocities changed again. The positions of the first drop and the second drop are also drawn on the graph and the yellow curve is the distance between the two drops. With the application of the DC field, the first drop decelerated while the second drop accelerated, which gives the sign of the electric charge of the two droplets: there the electric field is negative from electrode (+1 kVDC voltage) to the needle (grounded): a positive charge tends to oppose the Coulomb force to the motion (falling from needle to the bottom) and to slow down the droplet. The estimated drop diameters are D_1 = 0.137 mm and D_2 = 0.157 mm. The electric charges of the two drops are respectively q_1 = 0.033 pC and q_2 = -0.055 pC.

Fig 4.13 shows dual drop injection of MSP4 – $MSP_{inverse}$ at +5300V and -5300V respectively. The estimated drop diameters are D_1 = 0.115 mm and D_2 = 0.120 mm. The electric charge of the drops are q_1 = 0.019 pC and q_2 = 0.005 pC. Thus at the moment of DC application, both drops decelerated.

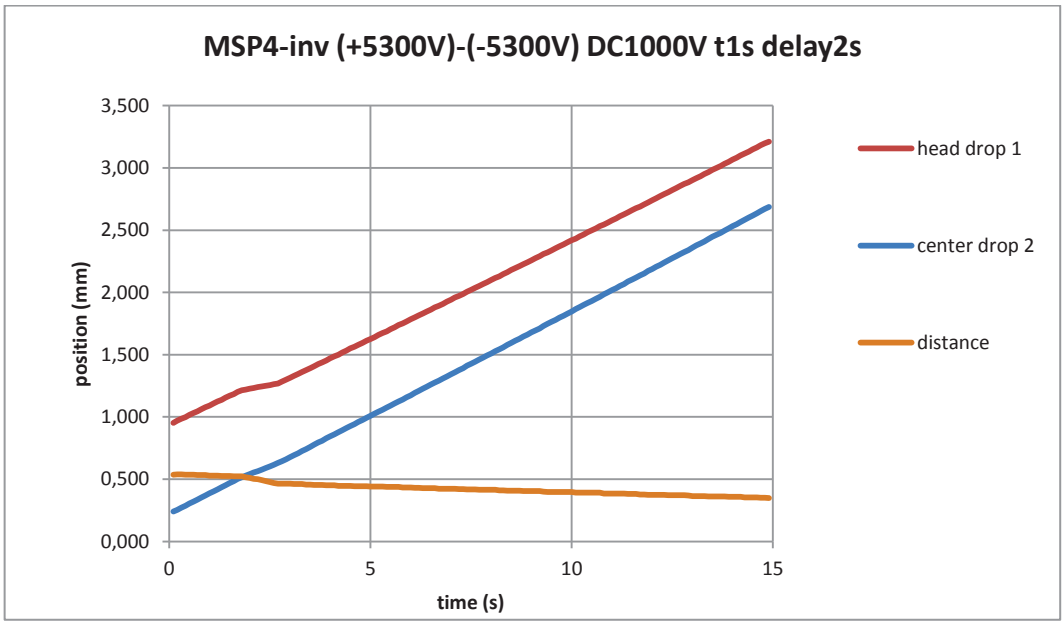

a)

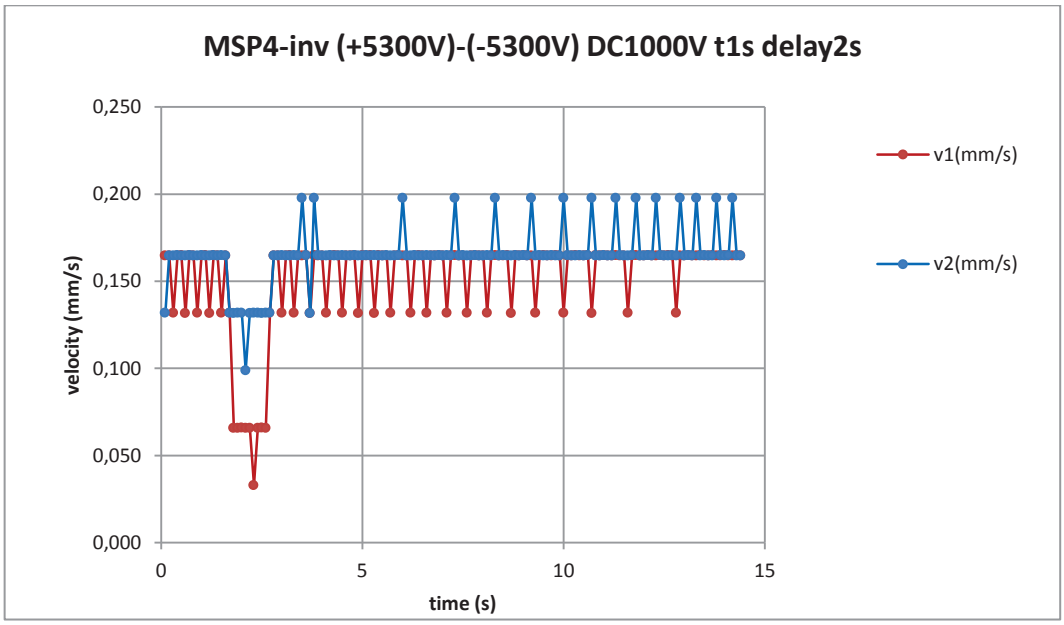

b)

Fig 4.13. Drop falling velocities with dual injection MSP4 – $MSP_{inverse}$ at +5300V and -5300V respectively, DC=1kV (29/05/2015, 23 °C ± 1 °C). Duration of application of DC voltage is 1 second. Velocities and position are positives from top to bottom. The position 0 corresponds to the upper entry of the video screen.

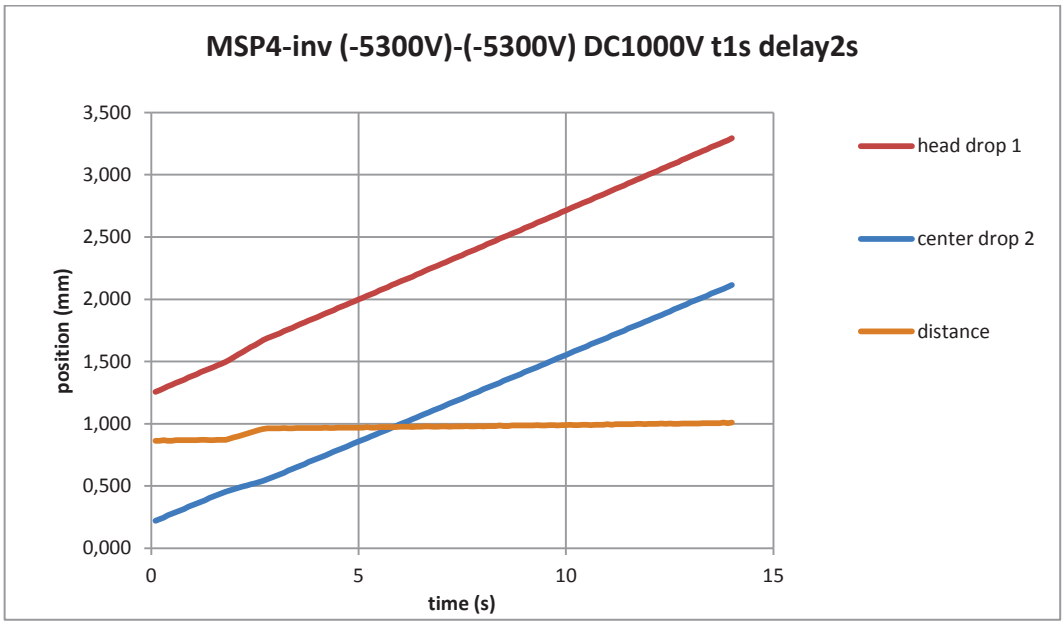

a)

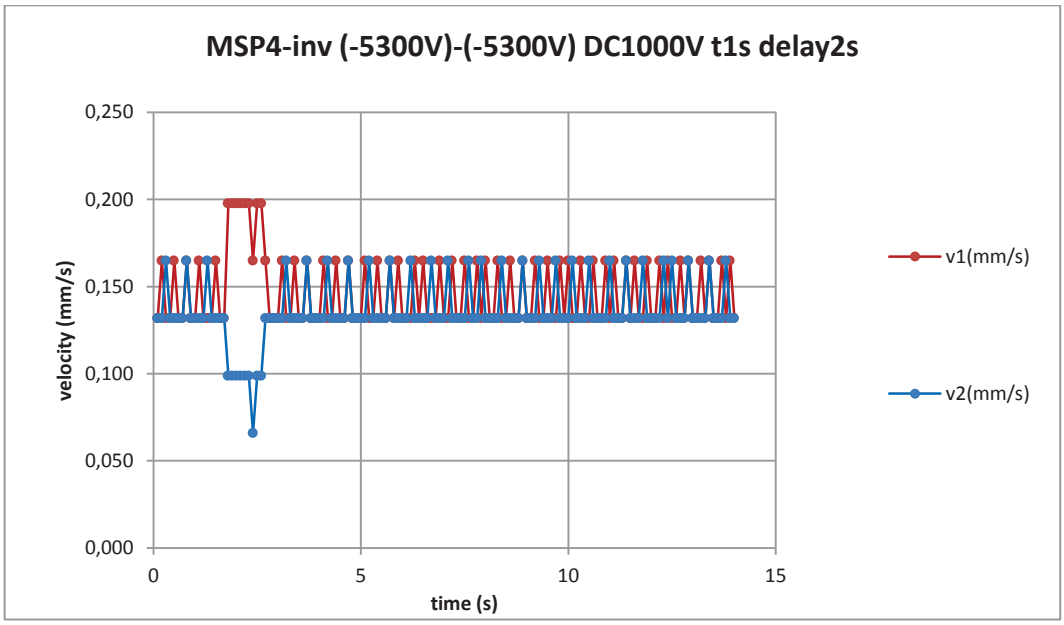

b)

Fig 4.14. Drop falling velocities with dual injection MSP4 – $MSP_{inverse}$ at -5300V and -5300V respectively, DC=1kV (29/05/2015, 23 °C ± 1 °C). Duration of application of DC voltage is 1 second. Velocities and position are positives from top to bottom. The position 0 corresponds to the upper entry of the video screen.

Fig 4.14 shows the injection of MSP4 – $MSP_{inverse}$ both at -5300V. The estimated drop diameters are D_1 = 0.114 mm and D_2 = 0.112 mm. The electric charge of the drops are q_1 = -0.012 pC and q_2 = 0.010 pC. It can be seen that during DC application, the first drop speeded up while the second drop slowed down.

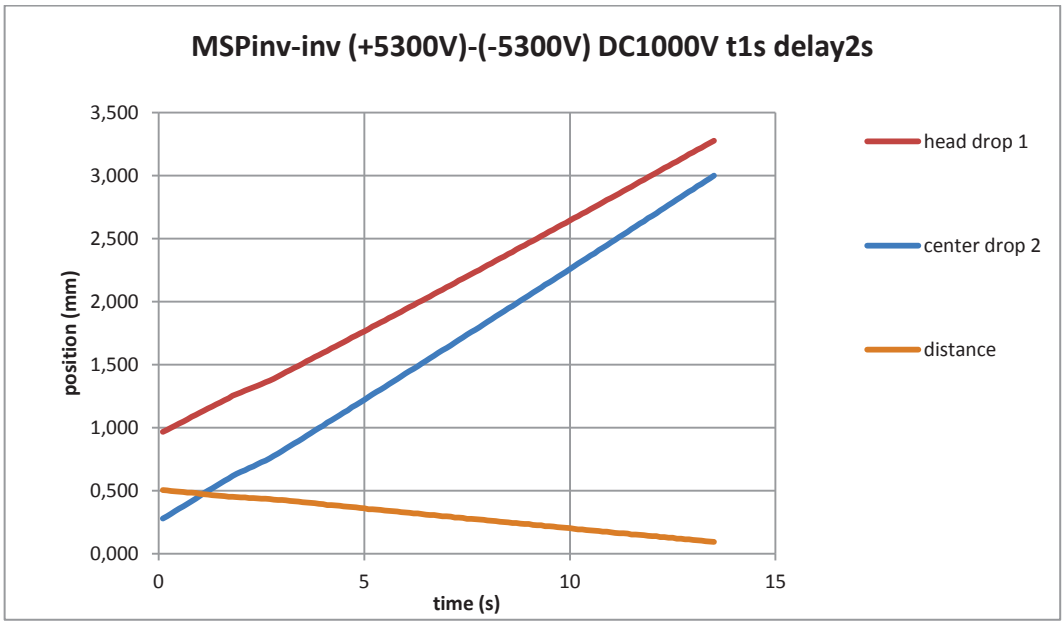

a)

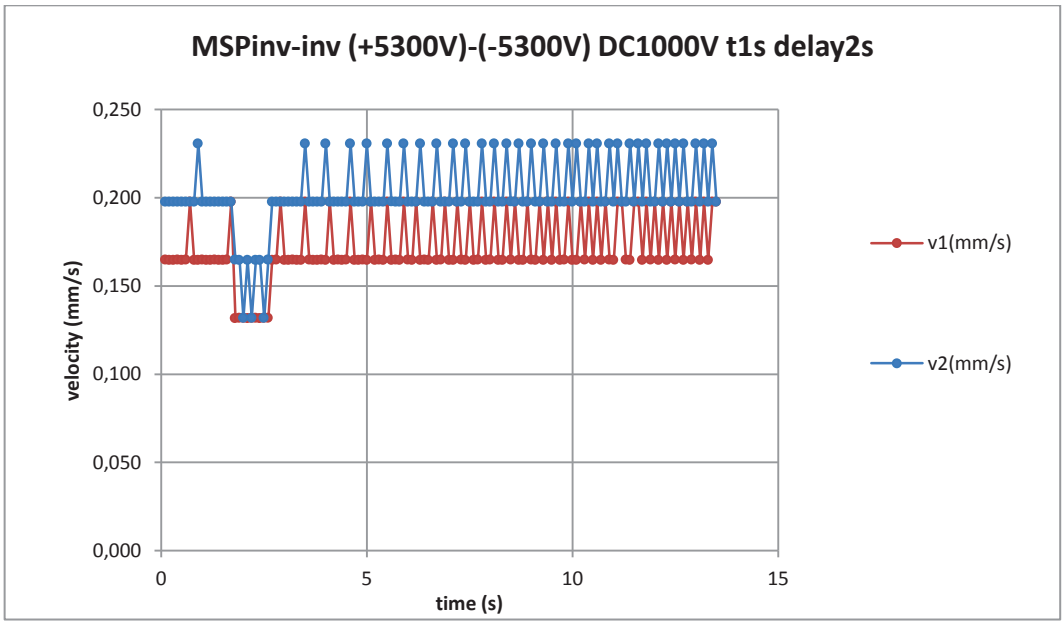

b)

Fig 4.15. Drop falling velocities with dual injection $MSP_{inverse}$ – $MSP_{inverse}$ at +5300V and -5300V respectively, DC=1kV (29/05/2015, 23 °C ± 1 °C). Duration of application of DC voltage is 1 second. Velocities and position are positives from top to bottom. The position 0 corresponds to the upper entry of the video screen.

Fig 4.15 shows the injection of $MSP_{inverse}$ – $MSP_{inverse}$ at +5300V and -5300V respectively. The estimated drop diameters are D_1 = 0.117 mm and D_2 = 0.133 mm. The electric charge of the drops are q_1 = 0.006 pC and q_2 = 0.011 pC.

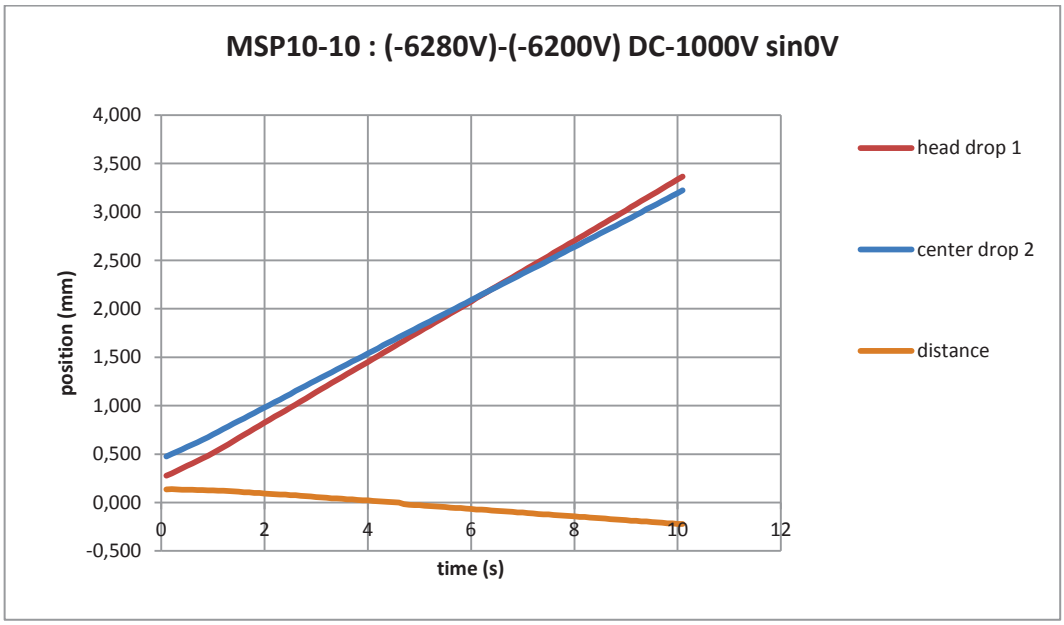

a)

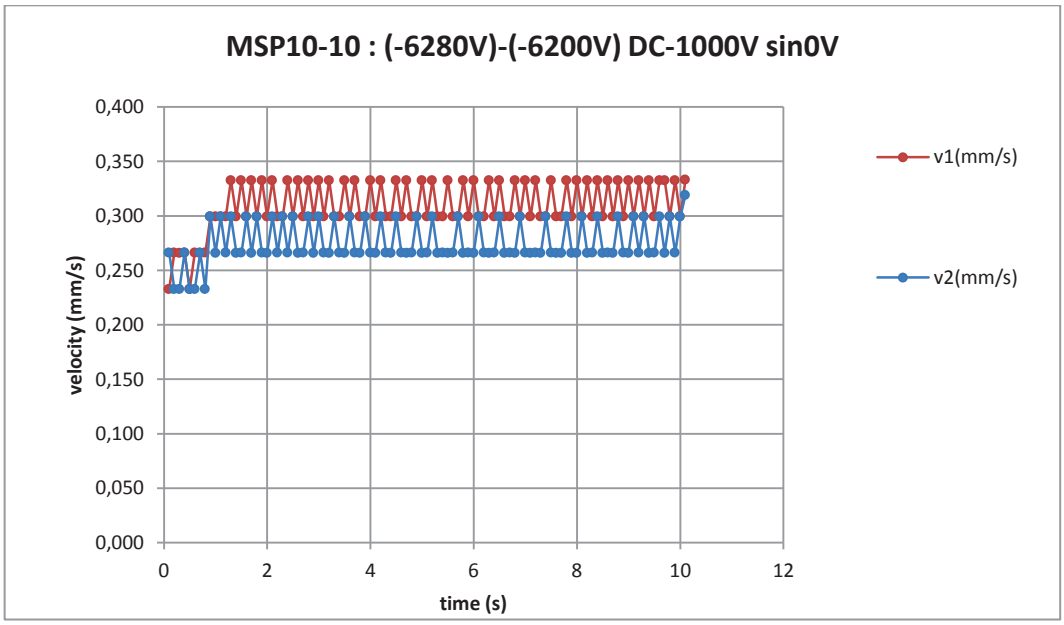

b)

Fig 4.16. Drop falling velocities with dual injection MSP10 – MSP10 at -6280V and -6200V respectively, DC=-1kV (12/06/2015, 25 °C ± 1 °C). Duration of application of DC voltage is 1 second. Velocities and position are positives from top to bottom. The position 0 corresponds to the upper entry of the video screen.

Finally, one experiment done by MSP10 – MSP10 drop injection is illustrated Fig 4.16. In that case, for technical reasons the DC field application of 1 second duration is applied directly when the drops entered the Dalsa vision field. After DC field application, no other electric fields were imposed and

the two drops were in their free fall. The drops were injected by MSP10 at -6280V and -6200V. The drop diameters are D_1 = 0.14 mm and D_2 = 0.16 mm, measured directly by visualisation on Spotlight because the initial distance between the two drops is very small, (less than one radius, giving a non-dimensional parameter s < 3). The drop mass or charge calculations are not accurate because the hydrodynamic interaction model used for force calculations is only valid when the distance between the two drops is large enough (s > 4).

4.6 Conclusion

EHD injection of drops pair from the same needle was performed successfully. At very low Reynolds number, due to the very small size of the droplets and their associated small falling velocity, the hydrodynamic interaction between the two droplets is very strong. Under electric field, the combination of hydrodynamic and electrostatic drops interactions further complicates the analysis.

A method of identifying the drops diameter and charge is proposed, based on the coupled analysis of the falling velocity of the two droplets, with and without application of external DC electric field. Validity of the hydrodynamic and electrostatic used models and possible simplifications are discussed Different examples of application to the characterization of injected drops pairs are presented.

Chapter 5. Drop electrocoalescence

5.1 Introduction

Water-oil emulsions, drop electrocoalescence occurs under application of an electric field when two drops come in close contact and merge into a bigger one. In our experiments of drop electrocoalescence, the drops pair are injected in oil by the EHD drop injection method. All of the experiments in this chapter are performed in the drop coalescence set-up and the model oil used is Marcol 52 with 0.001 wt% Span80. The drops are of tap water with 3.5 wt% NaCl. When the injected drops pair is falling inside oil medium in the axisymmetric system, a DC or AC field is applied at the electrode. Under influence of the electric field the two drops coalesce, and the process is recorded by two Dalsa cameras and an AOS camera. In this chapter the first section shows experimental results of drop coalescence visualized by the Dalsa cameras. The drop charges are calculated using the method described in Chapter 4. The second section presents AOS fast camera recordings in which we zoom in on the drop coalescence process. The third section summarizes the results obtained and problems encountered during experiments and suggestions for future improvement.

5.2 Global review of electrocoalescence experimental results

In petroleum industry research, electrocoalescence is thought to be the best way to break up water in crude oil emulsions because the electric fields can promote an efficient, clean and fast phase separation (Eow et al. 2001). For experiments with crude oil, (Hellesø et al. 2015) used an infrared

camera to visualize the drop coalescence process. Crude oil is transparent to near infrared rays while water is opaque to them. In their experiments, they used droplets, of about one half to one millimeter diameter, falling on a big stationary drop posed at the bottom of the test cell. It has been found that with increasing voltage on the electrode, the total coalescence is first fastened, but evolves to partial coalescence, or even no coalescence. Since experiments in crude oil require a high level of camera imaging due to oil opacity to visible light, more experiments have been done in transparent model oils to investigate the electrocoalescence process. In existing experiments two configurations were discussed: one drop falling onto a stationary one, as in (Hellesø et al. 2015) experiment , and two drops falling side-by-side. The first arrangement was studied in detail over the last ten years, after the early experiments of Charles and Masson (1960): (Chiesa et al. 2006), (Aryafar & Kavehpour 2009), Ristenpart et al. (2009), (Mousavichoubeh et al. 2011), Hamlin et al (2012), (Hellesø et al. 2015)... The second configuration was much less studied : in Eow & Ghadiri (2003) the drop diameter is about 1.8 $\pm$ 0.3 mm and they carried out 19 experiments. In (Pedersen 2008), the drop diameter is around 0.5 mm for 2 experiments of drops pair coalescence…. and very recently in (Mohammadi et al. 2014) the diameter of the drops was close to 1.25 mm and 8 cases are described and commented. In experiments presented by (Guo & He 2014), 30 – 40 different cases with varying electric field strengths were tested with drop diameters from 1.72 mm to 1.8 mm. They observed both coalescence and non-coalescence. The latter happened above threshold field strength of 200 kV/m.

For all experiments carried out to date, only large drops have been used. The number of tests is limited, and among them most experiments are of one drop falling onto a bigger stationary one. For drops falling side by side, the flux inside the test cell is not in the same direction as the applied electric fields. Such cases are three dimensional non-axisymmetric systems. Thus it will be difficult to perform simulations corresponding to such a configuration. In our experiments, up to 70 cases have been done in the axisymmetric system, and these will be compared to simulations done in Norway.

5.3 Electrocoalescence in axisymmetric system

Electrocoalescence experiments are performed in the drop coalescence set-up with Marcol 52 containing 0.001 wt% Span80 as model oil and tap water with 3.5 wt% NaCl droplets. The system is theoretically axisymmetric as described in Chapter 4. Two cameras register drops falling and coalescence processes in two plans rotated by 45 or 90 degrees around the vertical axis, allowing the

verification of the alignment of the drops center axis with the electric field and the gravity. The cameras used are one or two Dalsa cameras to record the falling velocities of the drops pair over a large distance, and one AOS high speed camera to zoom in on drop coalescence to analyze the coalescence processes at 8000 fps. Because of the strong zoom and the variations on droplet diameter and charge and on their initial distance, the location of the coalescence phenomenon is not always in the field of the AOS camera, and only a few cases have been possible to study. Under sufficiently high electric field, the two drops attract each other and coalesce. In experiments, the distance between the two drops should be adjusted to ensure on the one hand the minimum distance during drop injection, on the other hand the sufficiently short distance to let two drops approach and coalesce with each other under electric fields before crossing the total inter electrode distance. This needs controls over drop sizes through injection processes.

5.3.1 Electrocoalescence under DC/AC electric fields

5.3.1.1 Tracking of falling droplets

For data analyses, Spotlight needs the initial definition around the droplet of rectangular ''areas of interest (AOI)'' which serves to follow drop motions by detecting gray levels. These areas of interest move then automatically with the droplets on the successive images of the records. Following a number of attempts, the best results were obtained with the combination of a border threshold applied to track the first drop leading edge (Fig 5.1: right droplet) and a center tracking applied to the second droplet (Fig 5.1: left droplet).

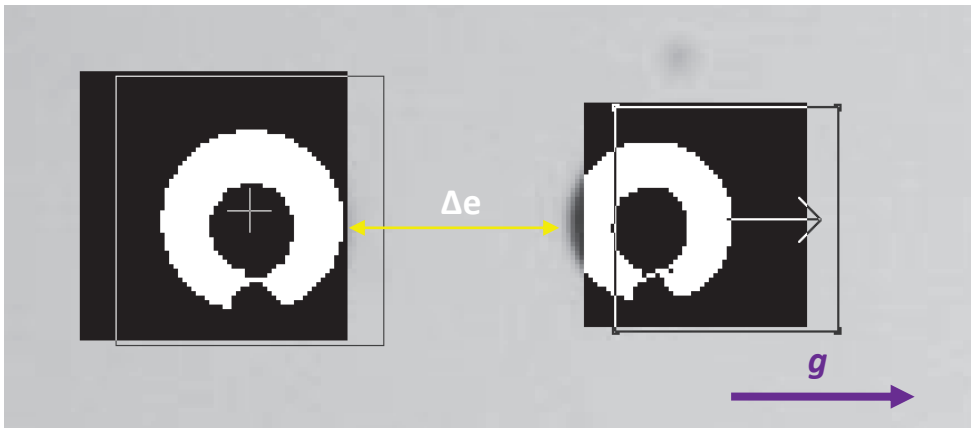

Fig 5.1. AOIs on drops pair for drop coalescence of MSP_{inv} – MSP_{inv} case No. 47 (03/06/2015, 25 °C ± 1 °C). Gravity is from left to right.

Fig 5.1 shows two drops tracked by AOI with threshold value of 128 applied on 256 inverse grey levels. Generally in AOIs, values of thresholds could be adjusted to give best border recognition. This tracking method is better than border threshold tracking and center tracking because at the moment when the two drops jump together to form one drop, the two AOIs continue following the drop locations instead of losing the track. The inter drop distance before drop coalescence is shown as Δe on Fig 5.1. The calculation of this distance is the distance between drop locations x_1 and x_2 minus the first drop diameter D_1 and half of second drop diameter D_2.

$$\Delta e = x_1 - x_2 - D_1 - \frac{D_2}{2} \tag{5.1}$$

After coalescence, the two AOI overlap on the same drop, and it is the same for the thresholds. Thus the locations of the drop are not well determined and the inter drop distance may be larger than reality.

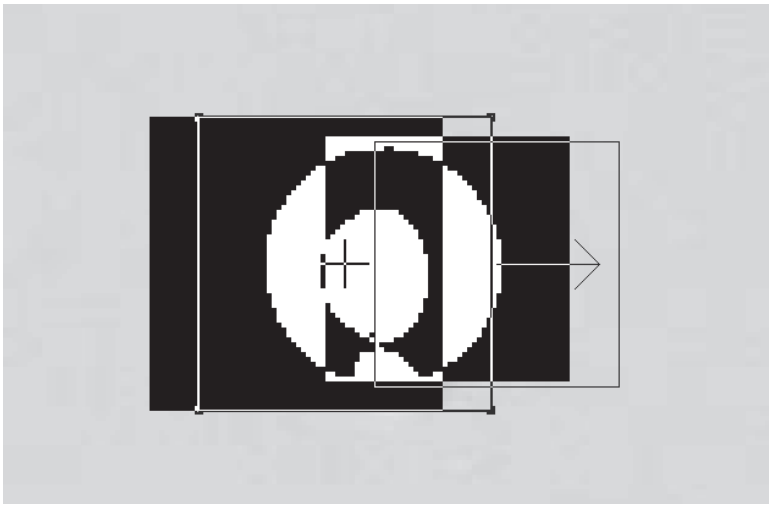

Fig 5.2. AOI overlaps on coalesced drop. Drop coalescence of MSP_{inv} – MSP_{inv} case No. 47 (03/06/2015, 25 °C ± 1 °C).

Fig 5.2 showed the overlap of two AOI with thresholds of 128 applied on 256 inverse grey levels. The distance Δe is calculated as follows.

$$\Delta e = x_1 - x_2 - \frac{D_3}{2} \tag{5.2}$$

Here D_3 is the diameter of the coalesced drop. The first AOI is threshold tracking and the second is center tracking. It is seen that the position of the latter is not well placed due to the overlap of the two AOIs and associated image processing. The center positioned by Spotlight on the coalesced drop is shifted with respect to the real center. Thus the calculated inter distance Δe is not exactly equal to zero.

Using the distance Δe between the two droplets, the non-dimensional parameter $s = 2\,l\,/(r_1+r_2)$ (see equations 4.11 and 4.12) can be calculated as $s = 2 + (4\Delta e)/(D_1+D_2)$. The initial non dimensional distance between the two drops s_0, is taken at the time when the DC or AC voltage is turned on.

5.3.1.2 Electrocoalescence under DC fields

The procedure for dealing with the falling drops pair falling and coalescence in model oil is similar to that described in Chapter 4. The difference is the duration of the applied DC field. For electrocoalescence experiments, the DC duration is stretched to tens of seconds until drop coalescence is complete. Results of drop falling velocities before and after coalescence deduced from the recording by the Dalsa camera are presented in the next figures. As explained in the previous chapter, the difference between velocities with or without application of DC electric field allows us to deduce the electric charges of the drops.

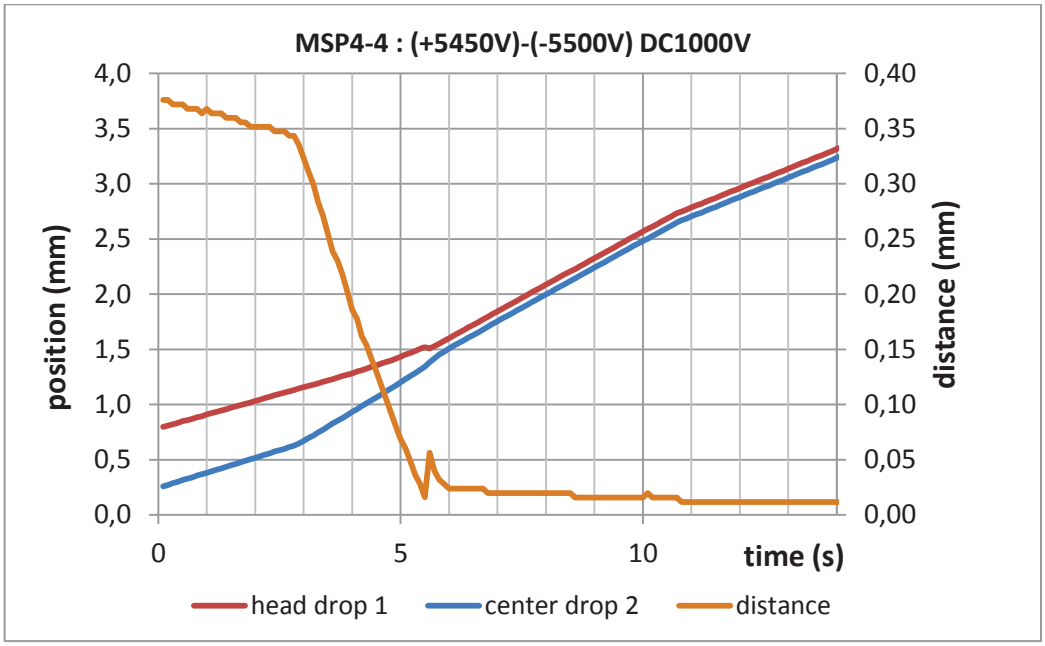

a)

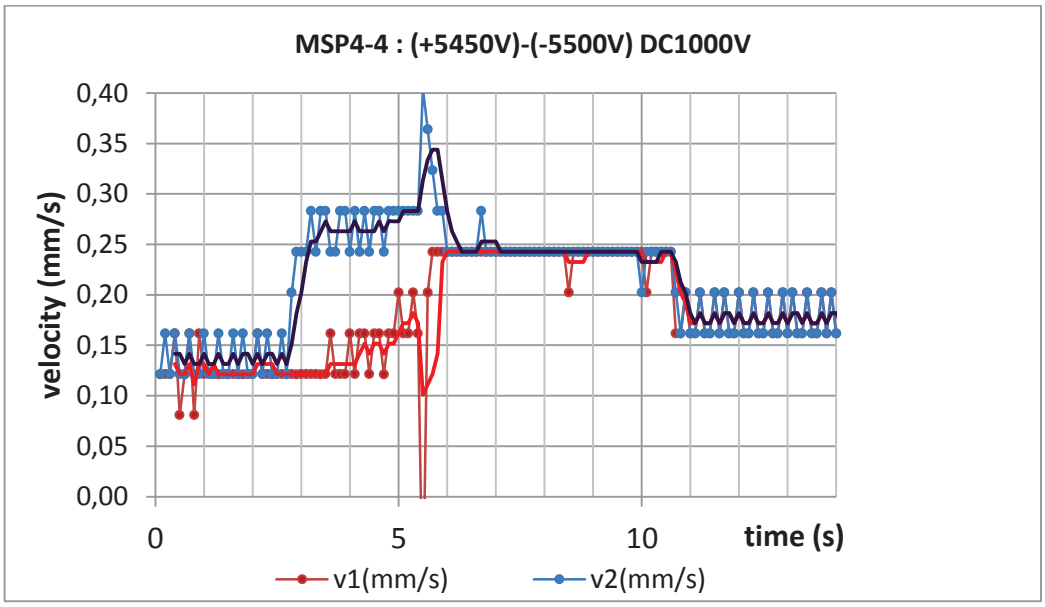

b)

Fig 5.3. Drop coalescence of MSP4 – MSP4 with drop diameters of D_1 = 0.105 mm, D_2 = 0.113 mm; charges of q_1 = 0.005 pC, q_2 = -0.026 pC; $\Delta m/m$ = 1.9 %, $\Delta q/q$ = 0.8 %, DC=1.2kV (24/03/2015, 21 °C ± 1 °C, case No. 6).

Fig 5.3 shows the electrocoalescence of oppositely charged droplets injected by MSP4 – MSP4 pulses, with resulting drop diameters of D_1 = 0.105 mm, D_2 = 0.113 mm, and charges q_1 = 0.005 pC and q_2 = -0.026 pC. These parameters are deduced from the analysis of the first part of the record, without and then with DC electric field, as was previously done in chapter 4. The effect of the strong viscous interaction is taken into account to deduce the net forces acting separately on each droplet. One visible effect of this interaction is the increase of the falling velocities of the two droplets when their distance decreases, as can be seen on Fig 5.3b between the time 4 and 6 s. On Fig 5.3a, the curve 'distance' which represents the inter drop distance Δe shows a small peak at time close to 6s. For the first part of the curve, preceding the peak, the calculation is based on equation (5.1). The peak corresponds to sudden switch from equation (5.1) to equation (5.2) which serves for the rest part of the curve 'distance'. As it was explained in 5.3.2.1, the locations of the two tracking points may then not be exact, thus a slight derivation can be found from coalesced drop radius. This leads to the non-zero value of the second part of the curve 'distance'. Moreover, the switch moment is obtained when $\Delta e < 0$, the equation used is immediately switched from (5.1) to (5.2). However, it is possible that in some cases the two drops are not perfectly aligned and a slight overlap occurs when they are in close vicinity. At this moment the equation is switched to (5.2) a little too early, which can explain the more or less pronounced peak on the curve.

Increasing the duration of the applied DC electric field leads to the coalescence of the droplets, and the resulting single droplet continues its falling trajectory, first under the same DC electric field, and later without. Thus, the analysis of the single drop velocity during the second part of the record allows us to deduce its mass and associated diameter and its electric charge by comparing the velocities with and without electric field.

The results deduced from the analysis of the four stages of the record (falling drops pair without and with DC electric field, then falling coalesced droplet with and without DC electric field) can be used to verify the mass and electric charge balance between initial drops pair and final coalesced droplet. We propose to define the two following non-dimensional imbalance parameters:

- Mass imbalance:

$$\frac{\Delta m}{m} = \frac{m_3}{m_1 + m_2} - 1 \tag{5.3}$$

Here m_1, m_2 and m_3 are the masses for the two initial droplets and the final coalesced one taken from calculations from drop different falling velocities. The values are calculated from the different velocities deduced from the analysis of the initial and final stages of the record, without DC electric field. For large droplets the coalesced drop fell out of the camera vision field so fast that the last stage cannot be registered. The mass of the coalesced drop cannot be calculated from drop falling velocity. Then the mass of the coalesced droplet is supposed to be equal to those of the pair of droplets, and the mass imbalance is 0.0%. That artifact allows us to calculate the charge imbalance as if the mass of the coalesced droplet was deduced from its last velocity.

- Charge imbalance:

$$\frac{\Delta q}{q} = \frac{|q_3 - (q_1 + q_2)|}{Max(|q_1|, |q_2|)} \tag{5.4}$$

Here q_1, q_2 and q_3 are the charge of the two initial droplets and of the final coalesced one. Because q_1 and q_2 are often of opposite sign, $|q_3|$ can be much smaller than $|q_1|$ or $|q_2|$, or even equal to zero. Thus the $|q_3|$ is not chosen as the denominator in equation expression (5.4).

The imbalances of mass and charge corresponding to Fig 5.3 are respectively $\Delta m/m$ = 0.2 % and $\Delta q/q$ = 28.3 %. The three continuous curves drawn on Fig 5.3 a) are the positions of the first drop

leading edge, the center of the second drop and the distance between the closest boundaries of the two drops. For the velocity curves, an average over four successive measurement points is drawn for each droplet to facilitate the analyses.

From Fig 5.3, we can comment on the different stages of drop motion: drop free fall, application of DC field, drop coalescence, coalesced drop under DC field and coalesced drop free fall. For the first stage, the velocities of the two drops are nearly the same because the drops are the same size. When a DC field is applied, the second drop immediately increases its falling velocity while the first does not change its motion so much because the electric charge of the first drop is much smaller (0.004 pC) leading to a weaker response to the DC field. When the second drop approaches the first one the viscous interaction increases. Because of the very small Reynolds number, the hydrodynamic interaction is symmetric and the second droplet repels the first one as the first attracts the second. The hydrodynamic drag of the drops pair becomes smaller with respect to the cumulative weight and both velocities increase. Despite the electric charge of the droplets, the Coulomb effect remains small up to a very short distance between the facing interfaces (Fig 4.10). When the two drops are close enough, the coalescence takes place which can be seen as two strong peaks in the velocity curves, in opposite directions. The two peaks illustrate that the first drop suddenly decelerates and the second drop accelerates to catch the other. After the coalescence, the single resulting droplet is still subjected into DC field and its falling velocity is immediately constant. Some seconds later, a sudden decrease of velocity plateau corresponds to the shutdown of DC voltage and at this time the coalesced drop is in free fall.

Fig 5.4a shows the drop positions and distance between the facing interfaces, and Fig 5.4b shows that the two positively charged drops decelerated immediately under positive DC field.

The injections are performed by MSP4 – MSP_{inv}, with drop diameters of D_1 = 0.159 mm, D_2 = 0.171 mm, and charges of q_1 = 0.026 pC, q_2 = 0.006 pC. The imbalances of mass and charges are respectively $\Delta m/m$ = 0.6 % and $\Delta q/q$ = 22.4 %.

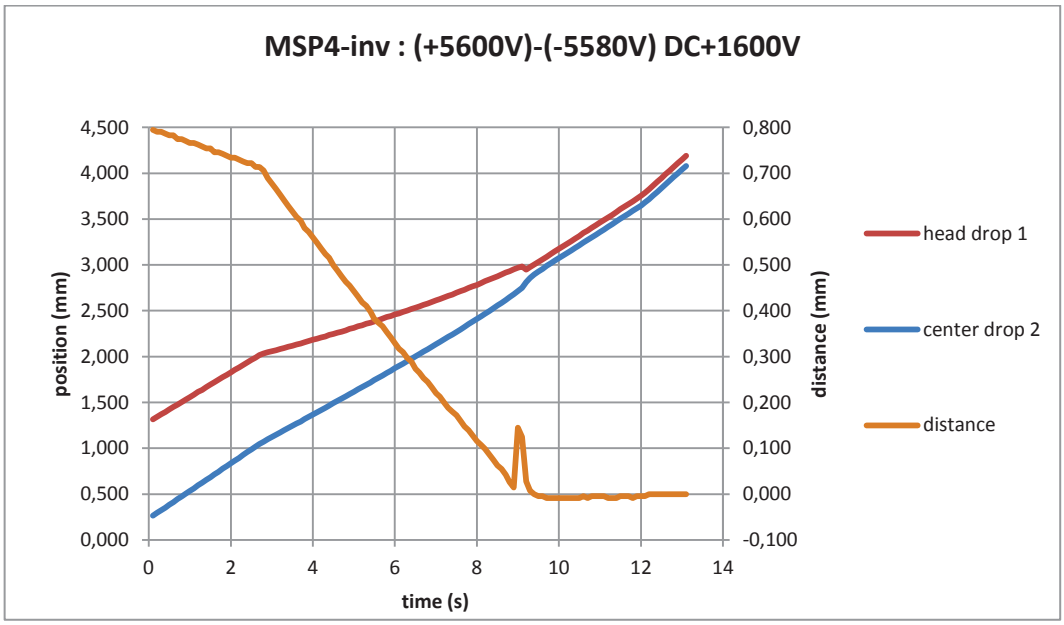

a)

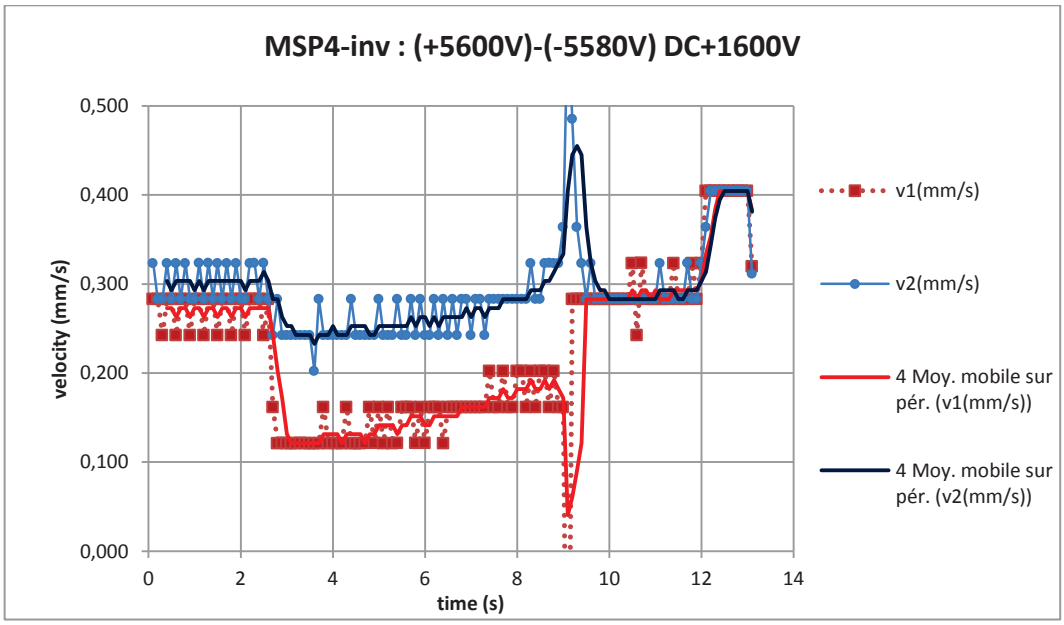

b)

Fig 5.4. Drop coalescence of MSP4 – MSP_{inv} with drop diameters of D_1 = 0.159 mm, D_2 = 0.171 mm; charges of q_1 = 0.026 pC, q_2 = 0.006 pC; $\Delta m/m$ = 0.6 %, $\Delta q/q$ = 22.4%, DC=1.6kV (08/04/2015, 21 °C ± 1 °C, case No. 21).

When a stronger DC field is applied at the electrode, the drop behaviors are shown on Fig 5.5.

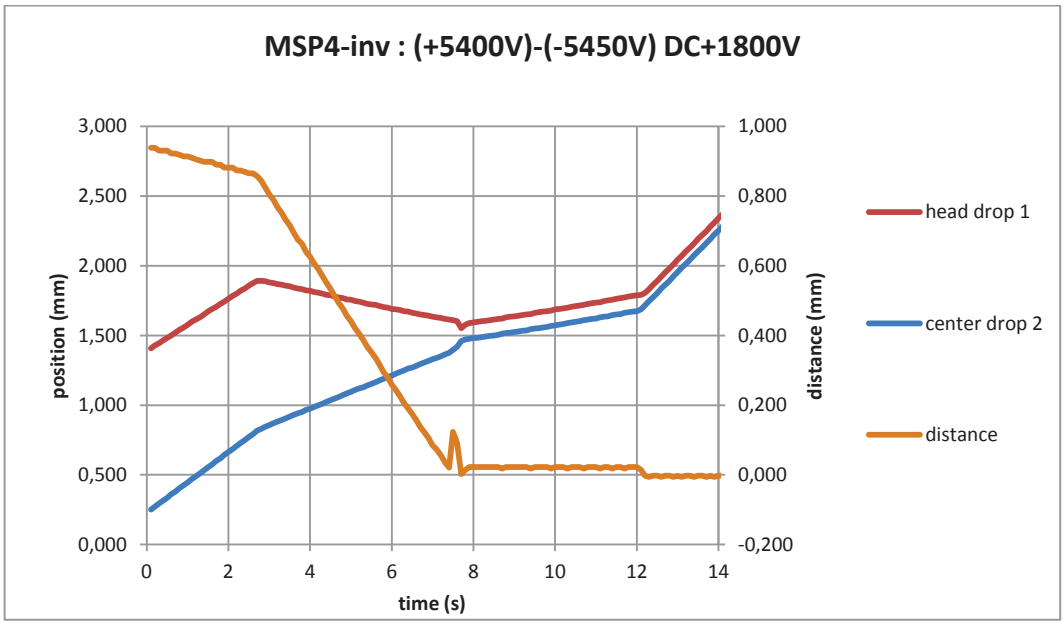

a)

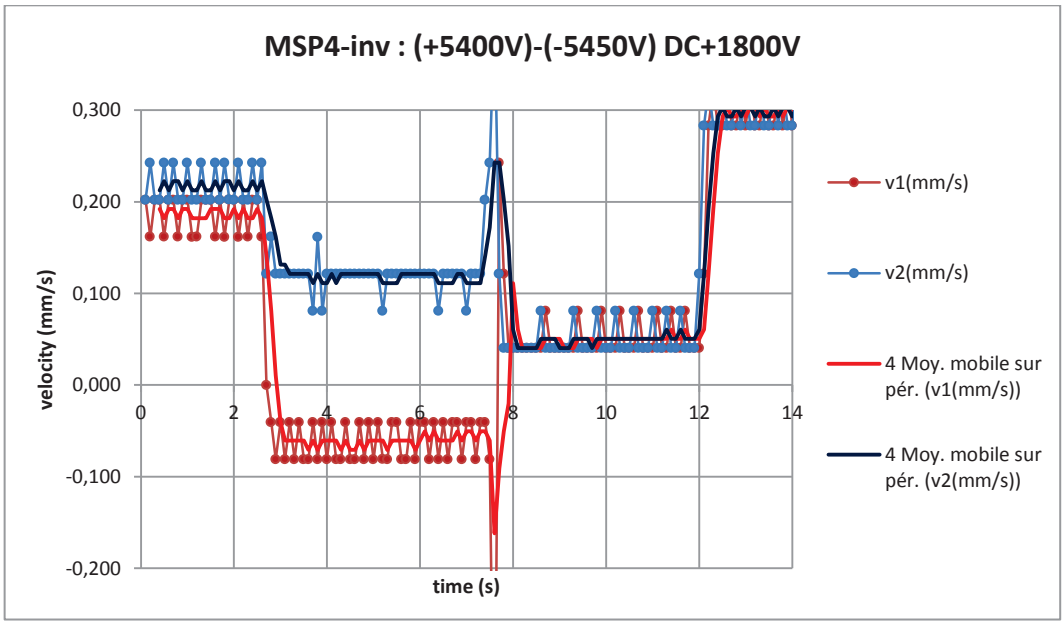

b)

Fig 5.5. Drop coalescence of MSP4 – MSP_{inv} with drop diameters of D_1 = 0.130 mm, D_2 = 0.142 mm; charges of q_1 = 0.030 pC, q_2 = 0.009 pC; $\Delta m/m$ = -7.6 %, $\Delta q/q$ = 6.9%, DC=1.8kV (15/04/2015, 23 °C ± 1 °C, case No. 27).

It can be seen that under DC field, the first drop went upwards because the strong electrophoresis is larger than the other forces. Under DC field, the average falling velocity of the two droplets and the falling velocity of the coalesced droplet are very small and there is no visible effect of the decreasing

distance before coalescence. The injections are performed by MSP4 – MSP_{inv}, with drop diameters of D_1 = 0.130 mm, D_2 = 0.142 mm, and charges of q_1 = 0.030 pC, q_2 = 0.009 pC. The imbalances of mass and charges are respectively Δm/m = -7.6 % and Δq/q = 6.9 %.

5.3.1.3 Electrocoalescence under AC fields

Experiments on drop electrocoalescence under AC fields is an improvement of that under DC fields because the former can eliminate the electrophoresis effect of the charged drops (Chabert et al. 2005). Thus it is expected that electrocoalescence will be more similar to that of uncharged droplets in oil medium. In experiments, peak voltage is fixed to 1414 V which corresponds to 1000 V in DC fields. During the first experiments the AC frequencies did not seem to influence the drop coalescence process. Thereafter, the frequency was set to the fixed value f = 1000 Hz. To reveal drop charges a short DC field of one second is applied at the moment when the two drops fall inside the Dalsa camera vision field. After the application of the DC field the drops pair enters into the free fall regime for a duration of two seconds, and then the AC field is applied.

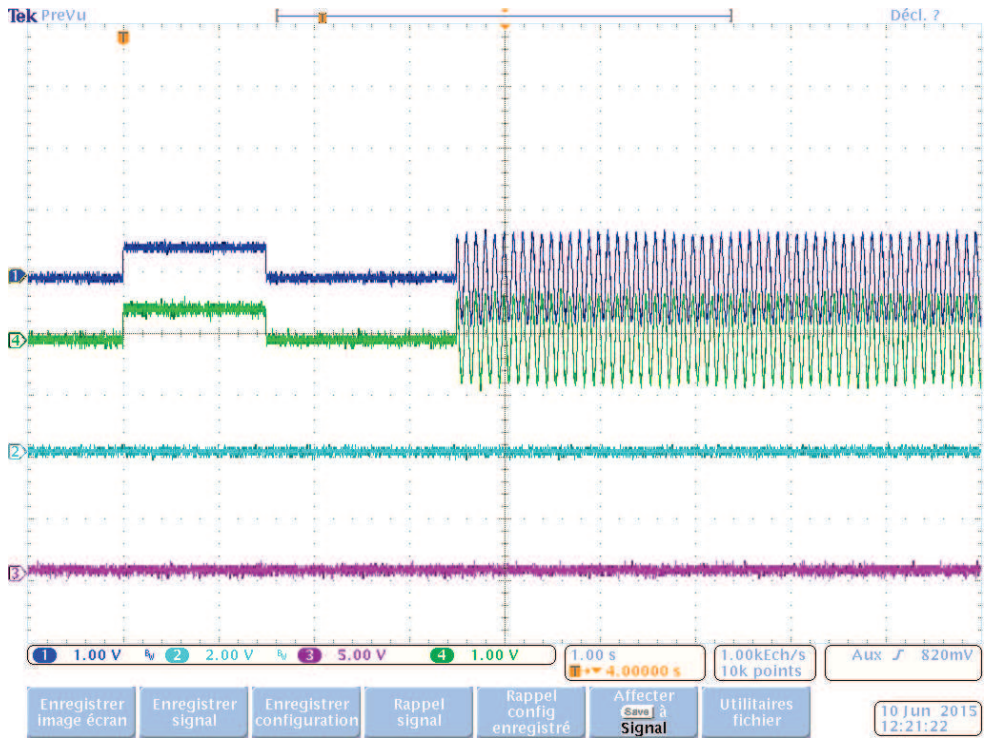

Fig 5.6. Application of DC field and AC field on the electrode: at the beginning of the trigger a DC field is applied with duration of 1.5 seconds. Then the voltage is cut off for about 2 seconds. Then the AC field is applied as oscillations on the figure.

Fig 5.6 shows the order of application of DC and AC fields on the electrode. The inconvenient aspect of AC field is that as the drop coalescence processes occur during the AC application, the charge on the coalesced drops cannot be revealed. Moreover, in the previous cases electrophoresis under DC field tended to increase the approach velocity of the two droplets. The drop approaching process takes more time under AC fields and the initial distances between the two drops should be reduced in order to allow them coalesce before reaching the bottom of the test cell. Some results of this electrocoalescence are shown below.

AC frequency testing without drop charge calculation

The following two figures present the frequency influences of the applied AC field on electrocoalescence. However in these first experiments the short DC voltage was not applied on the electrode, thus no drop charges could be calculated from drop falling velocities.

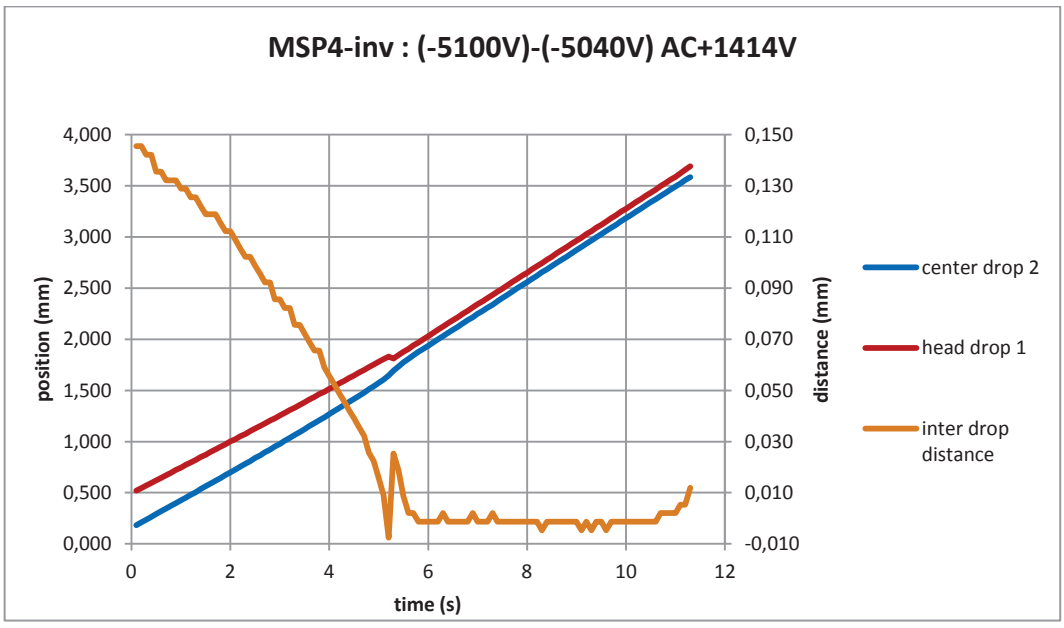

a)

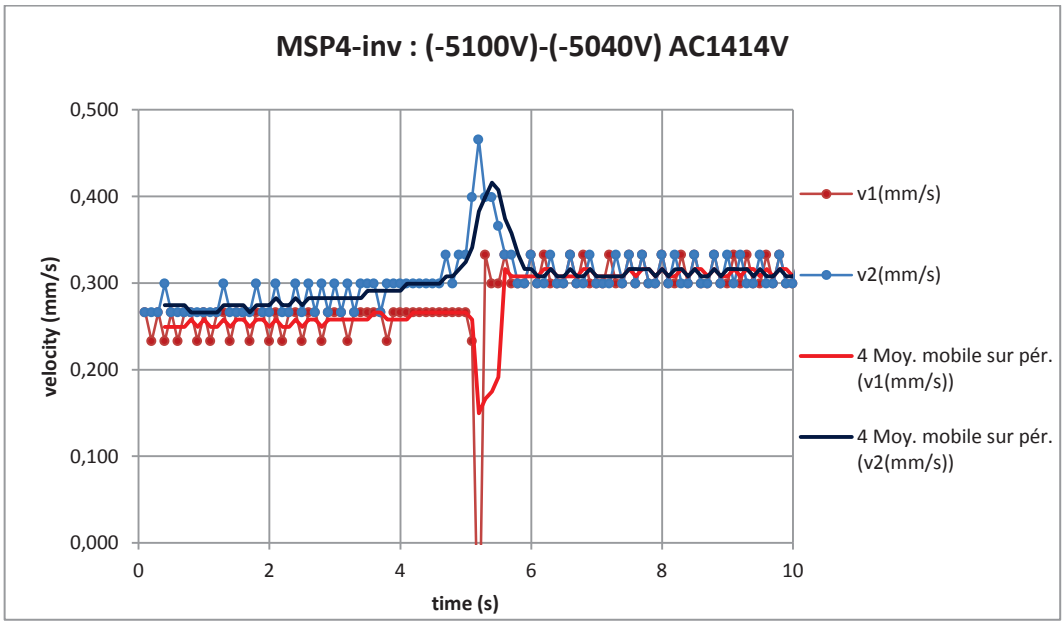

b)

Fig 5.7. Drop coalescence of MSP4 – MSP_{inv} with drop diameters of D_1 = 0.13 mm, D_2 = 0.14 mm; frequency of the AC field is of f = 1000 Hz, AC=1.414kV (09/06/2015, 25 °C ± 1 °C, case No. 61).

Fig 5.7 shows electrocoalescence of drops pair under AC field with frequency f = 1000 Hz. The injections are performed by MSP4 – MSP_{inv}, with drop diameters D_1 = 0.13 mm and D_2 = 0.14 mm.

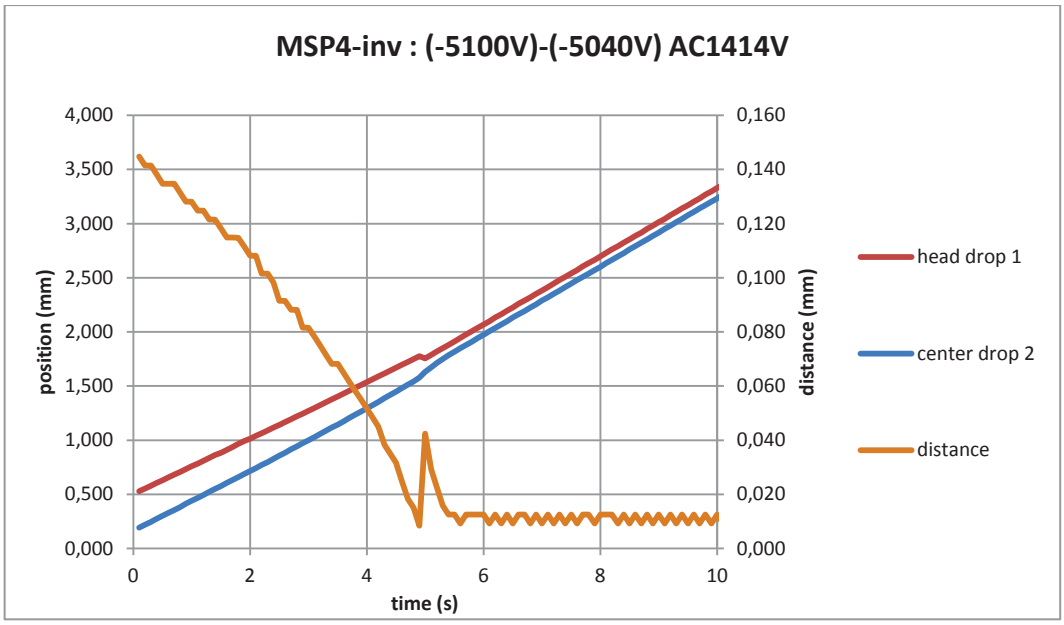

a)

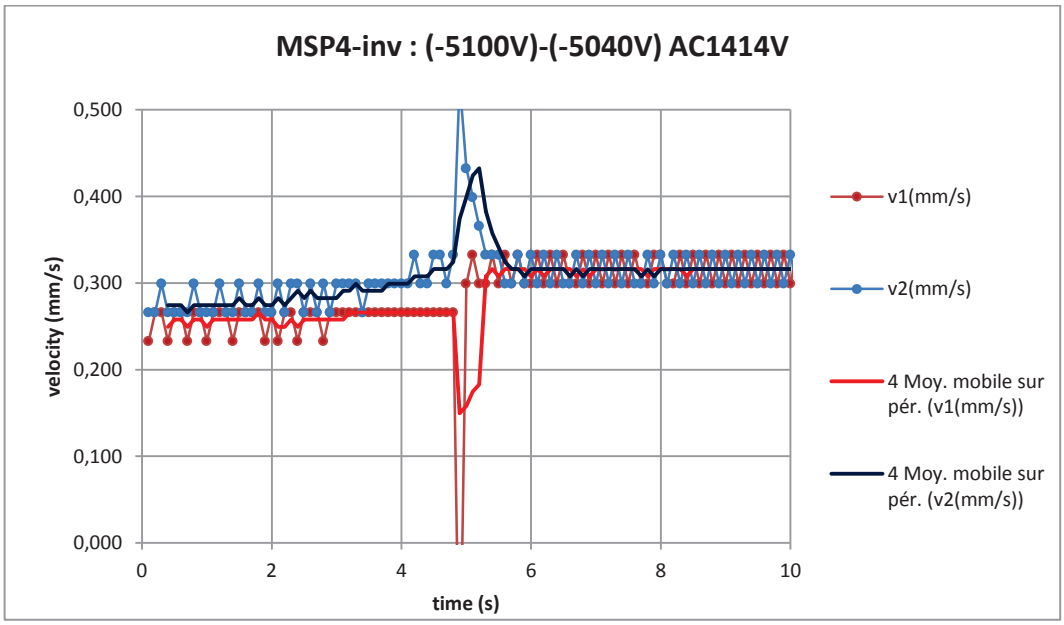

b)

Fig 5.8. Drop coalescence of MSP4 – MSP_{inv} with drop diameters of D_1 = 0.13 mm, D_2 = 0.14 mm; frequency of the AC field is of f = 1500 Hz, AC=1.414kV (09/06/2015, 25 °C ± 1 °C, case No. 62).

The Fig 5.8 shows electrocoalescence of drops pair under AC field with frequency f = 1500 Hz. The injection are performed by MSP4 – MSP_{inv}, with drop diameters D_1 = 0.13 mm and D_2 = 0.14 mm as in the previous case. For Fig 5.7 and Fig 5.8, the drop coalescence looks quite identical, thus it can be concluded that the AC field frequency does not affect drop coalescence process. The drop diameters used in these cases are of visual diameters because the initial distance between the drops pair is very small (s < 4), thus the calculated diameters are not exact.

5.3.1.4 Acceleration and approach velocity

Under electric field, the distance between the two droplets decreases with time up to contact and coalescence. The distance can be fitted by a second order polynomial function of time, as illustrated by Fig 5.9. From the function, we propose to identify two terms: the acceleration a (mm/s^2), as the second derivative of the function, and the drop approach velocity at the contact time, called 'ΔU near contact (mm/s)' calculated as the first derivative of the function at the last time point before drop coalescence.

When the droplets get closer, the approach velocity is negative. The consequence is that a negative value of acceleration a means that the approaching droplets are slowed down by oil film drainage: the hydrodynamic force being stronger than the electrocoalescence force. A positive value of acceleration means that the electrocoalescence force increases faster than the hydrodynamic interaction.

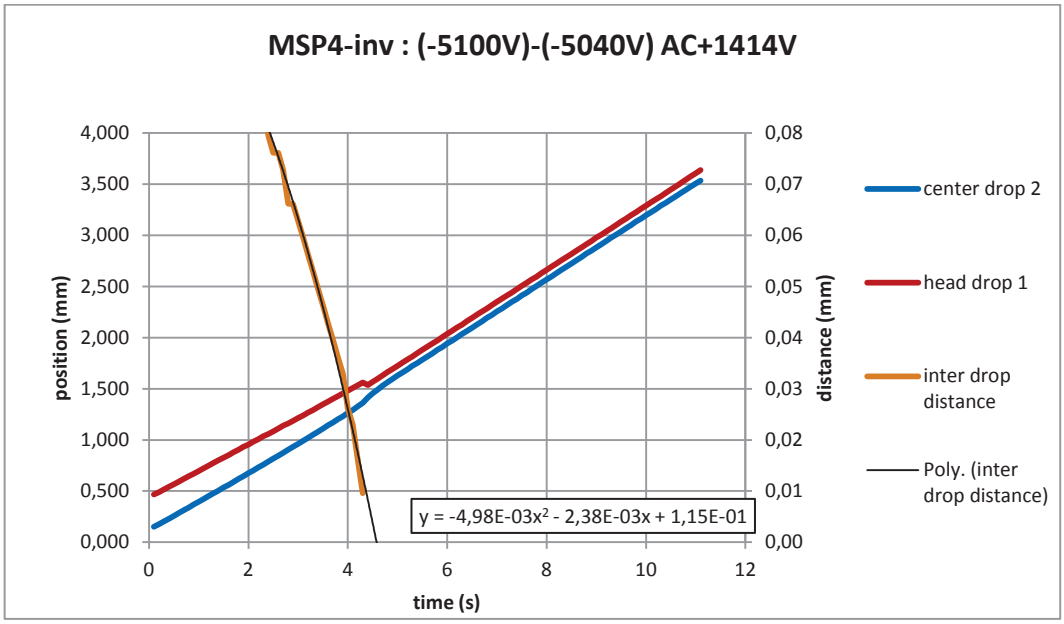

Fig 5.9. Distance of the drops for drop coalescence of MSP4 – MSP_{inv} with drop diameters of D_1 = 0.13 mm, D_2 = 0.14 mm; frequency of the AC field is of f = 1500 Hz, AC=1.414kV (09/06/2015, 25 °C ± 1 °C, case No. 62).

The curve 'distance' is fitted with a polynomial equation, and a $=2*(-4.98*10^{-3}) = -0.010$ mm/s^2 ΔU is calculated from application of AC field until drop contact time, and the result at drop contact is ΔU = -0.045 mm/s.

5.3.1.5 Sum up table for AC fields

All experimental results carried out for different AC field frequencies are shown in Table 5.1. From that table it can be seen that for small values of s, the calculated diameters for the first drop are different from visualized diameters. The largest discrepancy occurs for f = 800 Hz. For the four other cases, the diameters are comparable for the different frequencies and the results (time to coalescence, acceleration and final approach velocity) remain quite close to each other.

	D_1 (mm) Visual / calculated	D_2 (mm) Visual / calculated	s	t (s)	a (mm/s^2)	ΔU near contact (mm/s)
f = 800 Hz	0.13 / 0.113	0.13 / 0.130	2.556	3.2	-0.0037	-0.028
f = 1000 Hz	0.13 / 0.123	0.14 / 0.136	3.000	3.2	-0.0082	-0.044
f = 1500 Hz	0.13 / 0.122	0.14 / 0.137	2.947	2.9	-0.0098	-0.047
f = 2300 Hz	0.13 / 0.122	0.14 / 0.137	2.671	2.3	-0.0100	-0.045
f = 5000 Hz	0.13 / 0.128	0.15 / 0.143	2.488	1.7	-0.0126	-0.051

Table 5.1. Electrocoalescence with different applied AC frequencies.

5.3.1.6 Drop electrocoalescence under AC fields with detection of charge

The frequency of the AC field is chosen to be 1000 Hz and electrocoalescence of drops pair with small electric charges and large electric charges may be compared.

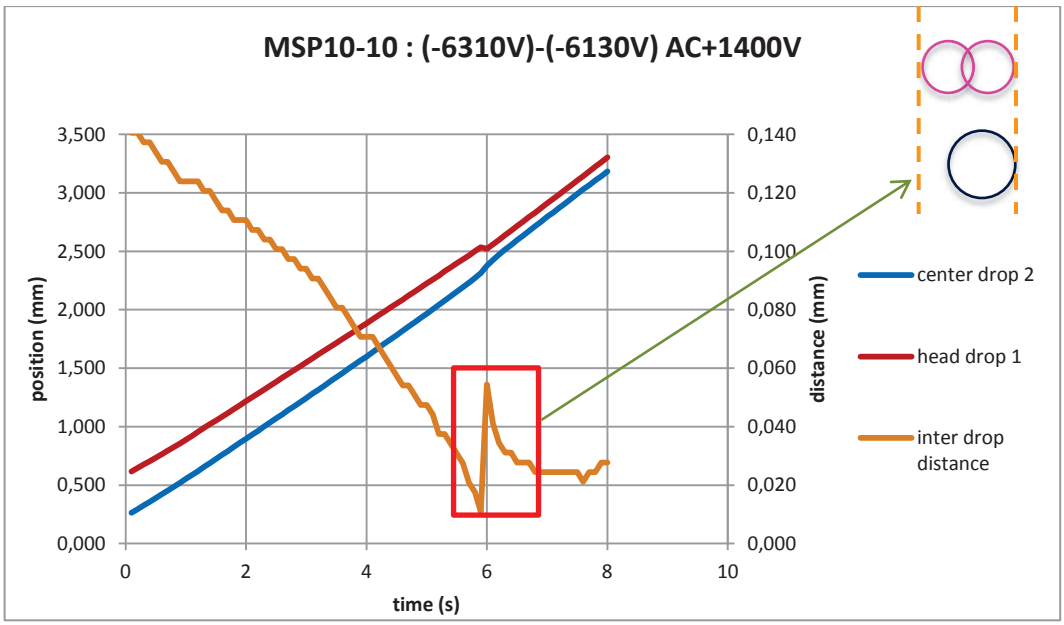

a)

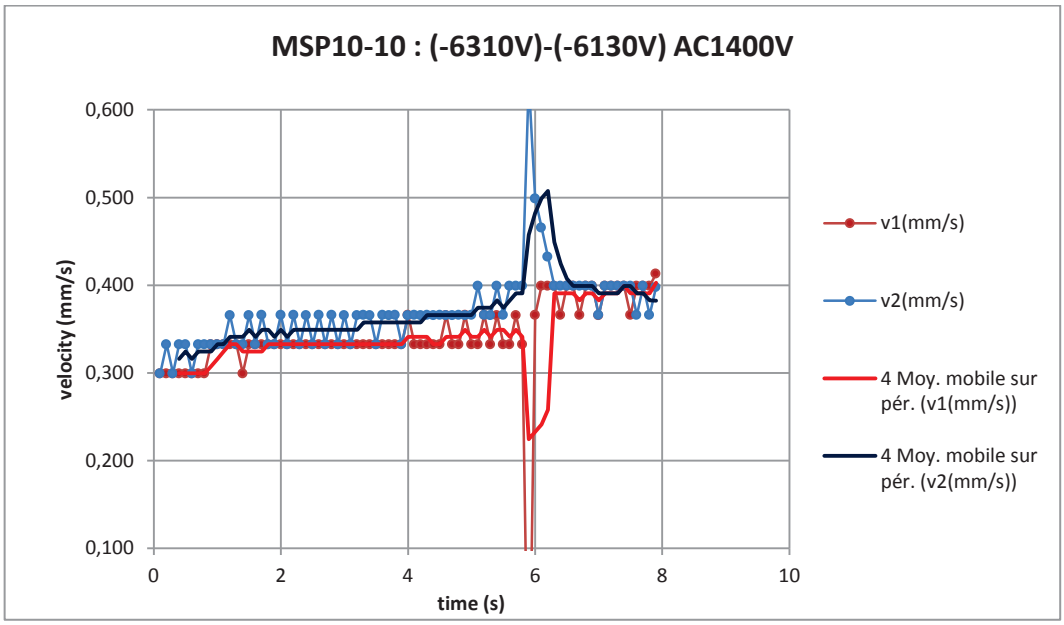

b)

Fig 5.10. Drop coalescence of MSP10 – MSP10 with drop diameters of D_1 = 0.15 mm, D_2 = 0.15 mm; frequency of the AC field is of f = 1000 Hz, AC=1.4kV (12/06/2015, 25 °C ± 1 °C, case No. 69).

The drop diameters are revealed by visualization and image processing using Spotlight. The initial distance between the two drops is very small and s < 3. Thus the calculations on drop diameters and charges may be not very accurate. From calculations, the drop diameters are D_1 = 0.138 mm, D_2 = 0.151 mm while the measured diameters are D_1 = 0.15 mm, D_2 = 0.15 mm. The charges are found to be q_1 = -0.001 pC and q_2 = -0.004 pC. This jump of distance at t ≈ 6s is due to the switch of equations through distance calculations, identical to the 'jumps' of drop distance previously presented for electrocoalescence under DC fields.

5.3.2 Table of results

The 70 different cases studied are summed up in the two following tables:

- Table 5.2 gives the initial state of the generated droplet pair, with the two drop diameters and charges, and the conditions of the injection pulses.

- Table 5.3 gives the conditions of electrocoalescence, applied electric field (DC or AC), coalesced droplet obtained, mass and charge imbalance and acceleration and final approach velocity.

All the results presented are cases where electrocoalescence is achieved. Their parameters are then not randomly distributed, but affected by the fact that effect of the difference in weight and charge of the two droplets should mainly favor their approach, and in any case does not prevent possible contact. The second droplet is generally larger than the first one, and there are combinations that are better than others for droplet charge and polarity of the DC electric field applied.

case No.	Pulse shape	Date	MSP Maximum Voltage (V)		Drop 1		Drop 2	
			V_1	V_2	D_1(mm)	q_1(pC)	D_2(mm)	q_2(pC)
DC								
1	MSP4-MSP4	3/20/2015	5400	-5400	0.129	0.013	0.132	-0.033
2	MSP4-MSP4		-5400	5400	0.124	-0.012	0.133	0.025
3	MSP4-MSP4	3/24/2015	5450	-5500	0.105	0.000	0.113	-0.016
4	MSP4-MSP4		5450	-5500	0.103	0.008	0.113	-0.011
5	MSP4-MSP4		5450	-5500	0.110	0.002	0.114	-0.024
6	MSP4-MSP4		5450	-5500	0.105	0.005	0.113	-0.026
7	MSP4-MSP4		5450	-5500	0.112	0.004	0.118	-0.027
8	MSP4-MSP4		5450	-5500	0.111	0.000	0.119	-0.026
9	MSP4-MSP4		5450	-5500	0.112	0.004	0.119	-0.026
10	MSP4-MSP4		5450	-5500	0.111	-0.007	0.117	-0.027
11	MSP4-MSP4		5450	-5500	0.118	-0.007	0.121	-0.035
12	MSP_{inv}-MSP_{inv}	4/2/2015	5600	-5600	0.134	-0.004	0.187	-0.062
13	MSP_{inv}-MSP_{inv}		5600	-5600	0.155	-0.026	0.188	-0.015
14	MSP_{inv}-MSP_{inv}		5600	-5600	0.165	-0.016	0.188	0.021
15	MSP_{inv}-MSP_{inv}		5600	-5600	0.167	-0.020	0.184	-0.021
16	MSP_{inv}-MSP_{inv}		5600	-5600	0.167	-0.001	0.195	0.000
17	MSP4-MSP_{inv}	4/8/2015	5600	-5580	0.140	0.033	0.164	0.003
18	MSP4-MSP_{inv}		5600	-5500	0.146	0.025	0.164	-0.010
19	MSP4-MSP_{inv}		5600	-5580	0.152	0.028	0.166	0.014
20	MSP4-MSP_{inv}		5600	-5580	0.156	0.030	0.177	-0.012
21	MSP4-MSP_{inv}		5600	-5580	0.159	0.026	0.171	0.006
22	MSP4-MSP_{inv}	4/15/2015	5400	-5450	0.116	-0.003	0.132	-0.023
23	MSP4-MSP_{inv}		5400	-5450	0.132	0.021	0.155	0.009
24	MSP4-MSP_{inv}		5400	-5450	0.141	0.023	0.161	0.012
25	MSP4-MSP_{inv}		5400	-5450	0.141	0.028	0.163	0.017
26	MSP4-MSP_{inv}		5400	-5450	0.120	0.033	0.142	0.007
27	MSP4-MSP_{inv}		5400	-5450	0.130	0.030	0.142	0.009
28	MSP4-MSP_{inv}	4/16/2015	5200	-5280	0.082	0.012	0.092	0.005
29	MSP4-MSP_{inv}		5200	-5280	0.106	0.018	0.112	0.011
30	MSP4-MSP_{inv}	5/11/2015	5400	5450	0.120	0.015	0.137	-0.019
31	MSP4-MSP_{inv}		5400	-5450	0.122	0.010	0.140	-0.020
32	MSP4-MSP_{inv}		-5400	5450	0.119	-0.035	0.138	-0.018
33	MSP4-MSP_{inv}		-5400	-5450	0.126	0.022	0.143	-0.021

34	MSP_{inv}-MSP_{inv}	5/13/2015	5400	5450	0.175	0.021	0.205	0.001
35	MSP_{inv}-MSP_{inv}		5400	-5450	0.143	-0.012	0.175	0.018
36	MSP4-MSP_{inv}	5/30/2015	5100	5100	0.114	0.029	0.131	0.006
37	MSP4-MSP_{inv}		5100	-5100	0.130	0.035	0.126	-0.026
38	MSP4-MSP_{inv}		-5100	5100	0.114	-0.022	0.127	0.008
39	MSP4-MSP_{inv}		-5100	-5100	0.120	-0.028	0.133	0.013
40	MSP4-MSP_{inv}	6/1/2015	-5100	-5100	0.122	-0.042	0.129	-0.021
41	MSP4-MSP_{inv}		-5200	-5200	0.128	-0.045	0.136	0.007
42	MSP4-MSP_{inv}		-5100	-5100	0.110	-0.025	0.120	0.015
43	MSP4-MSP_{inv}		-5200	-5200	0.113	-0.019	0.125	-0.004
44	MSP4-MSP_{inv}		-5150	-5200	0.127	-0.064	0.125	0.005
45	MSP_{inv}-MSP_{inv}		5100	-5070	0.128	0.005	0.145	0.007
46	MSP_{inv}-MSP_{inv}		5100	-5100	0.136	-0.007	0.148	-0.005
47	MSP_{inv}-MSP_{inv}	6/3/2015	5100	-5040	0.123	0.002	0.135	0.012
48	MSP_{inv}-MSP_{inv}		5010	-5060	0.113	-0.003	0.159	-0.001
49	MSP_{inv}-MSP_{inv}		5030	-5030	0.135	-0.037	0.146	-0.030
50	MSP4-MSP_{inv}		-4930	-4910	0.105	-0.021	0.112	-0.008
51	MSP4-MSP_{inv}		-4930	-4910	0.109	-0.023	0.114	0.003
52	MSP10-MSP10	6/5/2015	6420	6250	0.122	0.005	0.149	0.003
53	MSP10-MSP10		-6420	-6250	0.123	-0.006	0.153	0.000
54	MSP10-MSP10	6/7/2015	6450	6200	0.128	0.011	0.145	0.006
55	MSP10-MSP10		6440	6230	0.120	0.005	0.133	0.008
56	MSP10-MSP10		-6280	-6080	0.119	-0.005	0.132	-0.007
57	MSP10-MSP10		-6350	-6280	0.093	0.000	0.104	-0.002
58	MSP10-MSP10		-6450	6300	0.113	-0.006	0.131	-0.001
59	MSP10-MSP10	6/8/2015	6220	-6140	0.122	0.013	0.137	0.004
AC								
60	MSP4-MSP_{inv}	6/9/2015	-5100	-5020	0.113		0.130	
61	MSP4-MSP_{inv}		-5100	-5040	0.123		0.136	
62	MSP4-MSP_{inv}		-5100	-5040	0.122		0.137	
63	MSP4-MSP_{inv}		-5100	-5040	0.122		0.137	
64	MSP4-MSP_{inv}		-5100	-5040	0.128		0.143	
65	MSP4-MSP_{inv}	6/10/2015	-5070	-5060	0.139	-0.084	0.139	-0.023
66	MSP10-MSP10		-6350	6150	0.139	-0.033	0.153	-0.012
67	MSP_{inv}-MSP_{inv}		5100	-5060	0.146	-0.027	0.153	-0.035
68	MSP10-MSP10	6/12/2015	-6310	-6130	0.096	0.005	0.151	-0.004
69	MSP10-MSP10		-6310	-6130	0.138	-0.001	0.151	-0.004
70	MSP10-MSP10		-6310	-6150	0.119	0.004	0.157	-0.013

Table 5.2. Summation of initial conditions (multistage pulses shapes and amplitudes, date, droplets diameter and charge) for coalescence cases.

On Table 5.2 and Table 5.3, the drop diameter and charge are all from calculated values. In cases No. 60 – No. 64 there is no charge calculation for both drops because during experiments no DC field was

applied to change drop motion. The mass imbalances and charge imbalances cannot be calculated for these cases.

case No.	Voltage (V)	Drop 3		mass imbalance	charge imbalance	ΔU near contact (mm/s)	a (mm/s^2)
		D_3 (mm)	q_3 (pC)				
DC							
1	1000	0.166	-0.019	2.0%	2%	-0.103	0.014
2	-1000	0.164	0.013	3.4%	2%	-0.068	0.013
3	400	0.137	-0.032	0.0%	106%	-0.017	0.003
4	600	0.136	-0.007	0.0%	34%	-0.004	0.004
5	800	0.141	-0.026	0.8%	14%	-0.061	0.008
6	1000	0.138	-0.021	1.9%	1%	-0.103	0.017
7	1200	0.145	-0.030	0.2%	28%	-0.103	0.021
8	1400	0.148	-0.032	5.5%	23%	-0.112	0.018
9	1600	0.148	-0.027	4.2%	19%	-0.152	0.023
10	1800	0.144	-0.042	0.0%	31%	-0.115	0.016
11	2000	0.150	-0.046	0.0%	14%	-0.151	0.025
12	800	0.208	-0.088	0.0%	34%	-0.028	-0.006
13	1000	0.218	-0.053	0.0%	47%	-0.029	-0.003
14	-1000	0.223	0.006	0.0%	5%	-0.242	-0.013
15	-1800	0.222	-0.046	0.0%	27%	-0.067	-0.003
16	-2000	0.229	0.001	0.0%	140%	-0.102	-0.016
17	800	0.193	0.032	0.0%	15%	-0.073	0.002
18	1000	0.196	0.017	0.0%	7%	-0.090	0.011
19	1200	0.203	0.049	3.8%	22%	-0.062	0.002
20	1400	0.210	0.019	0.0%	5%	-0.144	0.015
21	1600	0.209	0.039	0.6%	22%	-0.103	0.003
22	800	0.155	-0.028	-2.3%	13%	-0.014	0.017
23	1000	0.181	0.033	-2.1%	14%	-0.067	0.007
24	1200	0.190	0.040	-0.9%	23%	-0.076	0.004
25	1400	0.191	0.050	-1.9%	18%	-0.102	0.004
26	1600	0.164	0.039	-3.5%	3.1%	-0.187	0.008
27	1800	0.170	0.039	-2.5%	0.9%	-0.171	0.003
28	1000	0.110	0.017	0.0%	4%	-0.063	0.002
29	1400	0.138	0.030	0.0%	7%	-0.075	0.000
30	1000	0.164	0.003	2.6%	38%	-0.114	0.012
31	1000	0.170	0.010	7.5%	102%	-0.096	0.015
32	-1000	0.163	-0.053	0.4%	1%	-0.102	-0.004
33	-1000	0.174	-0.005	7.3%	29%	-0.133	0.011
34	1000	0.241	0.014	0.0%	40%	-0.060	0.014
35	-1000	0.202	0.025	0.0%	100%	-0.079	-0.022
36	1000	0.155	0.038	-0.1%	10%	-0.085	0.010

37	1000	0.164	0.020	5.4%	32%	-0.139	0.010
38	-1000	0.154	-0.018	4.2%	18%	-0.091	0.012
39	-1000	0.162	-0.022	4.6%	22%	-0.117	0.018
40	-1000	0.160	-0.066	2.0%	7%	-0.079	0.005
41	-1000	0.165	-0.040	-2.0%	6%	-0.154	0.017
42	-1000	0.148	-0.013	5.0%	15%	-0.141	0.013
43	-1400	0.152	-0.025	2.6%	9%	-0.096	0.004
44	-600	0.159	-0.063	-0.6%	7%	-0.115	0.008
45	-1000	0.172	0.022	0.0%	142%	-0.031	0.000
46	-1000	0.179	-0.005	0.0%	106%	-0.001	-0.029
47	-1000	0.163	0.024	0.0%	83%	-0.047	-0.002
48	-1400	0.176	0.002	0.0%	191%	-0.099	-0.153
49	-600	0.182	-0.081	8.2%	37%	-0.039	-0.001
50	-1000	0.138	-0.038	3.1%	38%	-0.050	0.008
51	-1000	0.141	-0.024	0.6%	14%	-0.095	0.011
52	-1000	0.172	0.019	0.0%	247%	-0.023	0.003
53	-1000	0.176	0.009	0.0%	253%	-0.027	0.012
54	1400	0.176	0.020	5.5%	24%	-0.065	0.001
55	-1400	0.170	0.005	20.6%	93%	-0.041	-0.002
56	1400	0.158	-0.021	-2.3%	131%	-0.028	0.001
57	-1400	0.127	-0.003	6.6%	31%	-0.030	-0.005
58	-1400	0.159	-0.011	8.4%	44%	-0.062	-0.002
59	1400	0.166	0.019	3.9%	14%	-0.069	0.005
AC							
60	1414					-0.028	-0.004
61	1414					-0.044	-0.008
62	1414					-0.047	-0.010
63	1414					-0.045	-0.010
64	1414					-0.051	-0.013
65	1400	0.176	0.001	2.0%		-0.037	-0.018
66	1400	0.182	0.001	-3.8%		-0.069	-0.044
67	1400	0.186	0.001	-3.8%		-0.051	-0.022
68	2000	0.167	0.001	8.7%		-0.075	-0.135
69	1400	0.186	0.001	5.2%		-0.036	-0.006
70	1000	0.184	0.001	12.7%		-0.019	-0.003

Table 5.3. Summation of results on coalescence conditions (initial conditions in table 5.2) and mass and charge imbalances.

5.4 First analyses of drops pair behaviour to coalescence

5.4.1 Droplet diameters and mass conservation

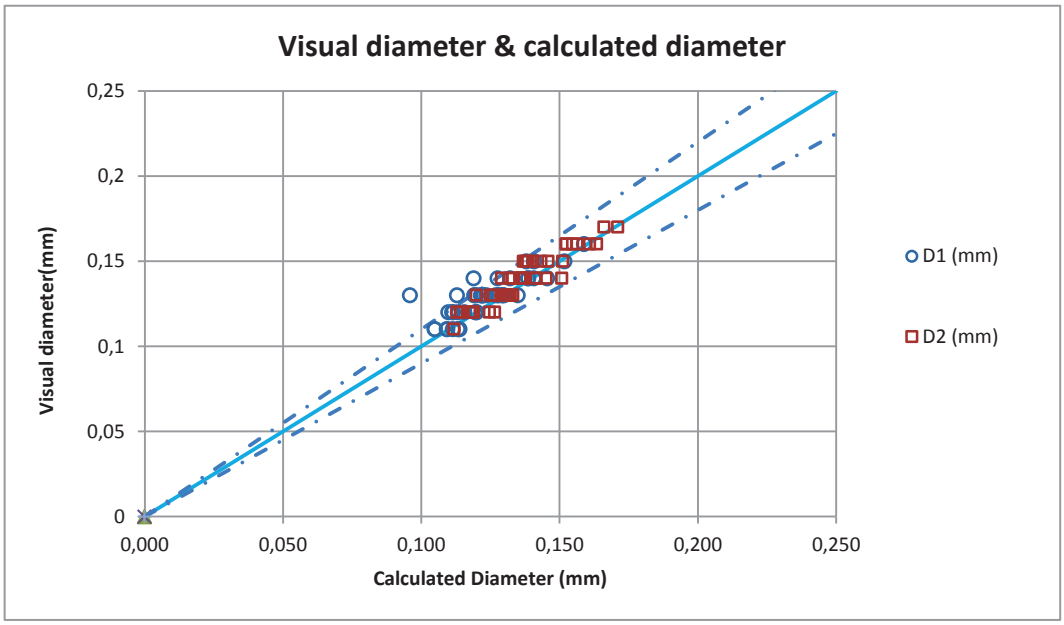

Fig 5.11. Comparison of droplet diameters deduced from direct analyses of photos and diameters calculated from falling velocities. The results are reported for drops pair injections: blue circles correspond to the droplet injected first and red squares to the second ones.

On Fig 5.11, the drop diameters determined from direct visualization are compared to these calculated from falling velocities. These two values coincide well except for four values which are outside the trend lines. Of the four values the initial distance between the two drops is very small (initial non dimensional distance $s_0 < 4$), which influences the calculated values of the diameters. The median blue line is defined as visual diameter equals calculated diameter, and the two dotted lines indicate variations of +/- 10%.

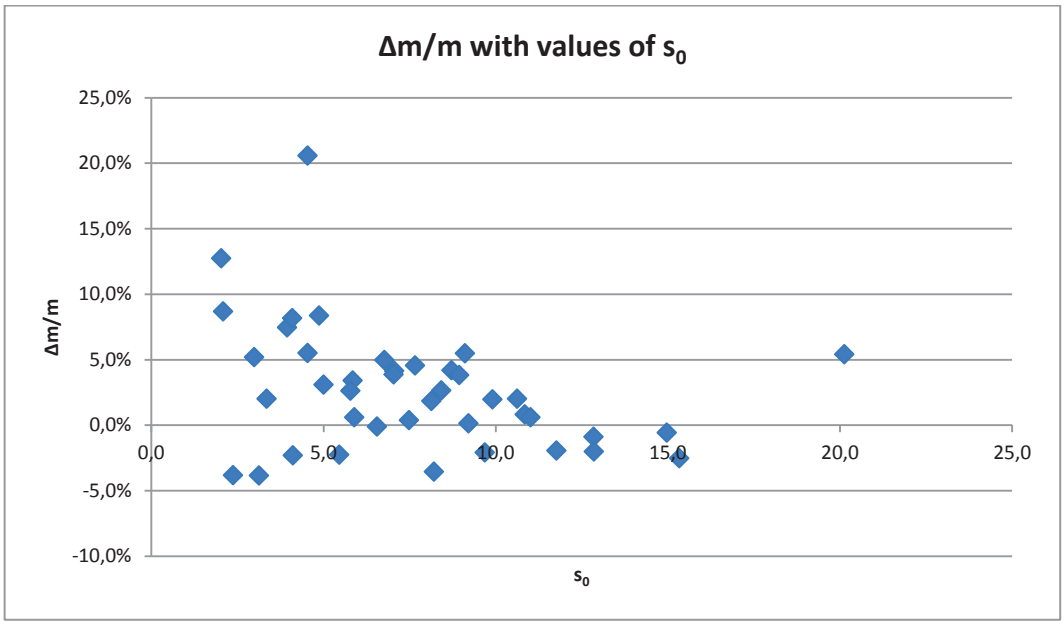

Fig 5.12. Mass balance with s_0 for the 70 cases of electrocoalescence.

Fig 5.12 shows that the mass imbalances Δm/m decreases with the parameter s_0. The mass imbalance exceeds 10% only for the smaller values of initial non dimensional distance s_0. This is because equations (4.11) and (4.12) are limited to $O(s^{-10})$ and $O(s^{-9})$. For the one point where the imbalance is larger than 20 % it was verified that the diameter of the coalesced drop was not well calculated because the duration of the drop falling path was too short to obtain a stable falling velocity. When the initial non dimensional distance s_0 is larger than 5, Δm/m is always smaller than 6 %. This value is good because the average time duration for revealing drop falling velocity is often only 1 second. According to equation (3.4) the uncertainty on the estimate of the droplet diameters is then 2.3%. The uncertainty on the drop mass is close to 7%.

5.4.2 Droplet electric charge and charge conservation

The calculation of drop charge follow application of the DC field, at the beginning of which the inter drop distance parameter is calculated as s_0. The calculation of drop charge is presented in section 4.4.2 and the model adopted is good for non-dimensional distance $s > 4$.

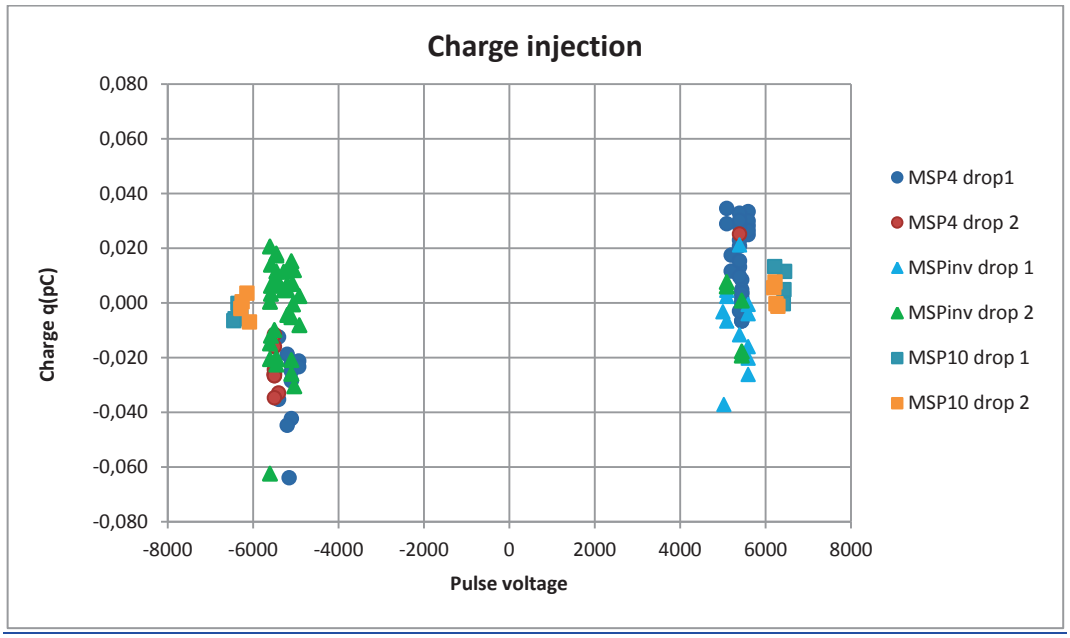

a)

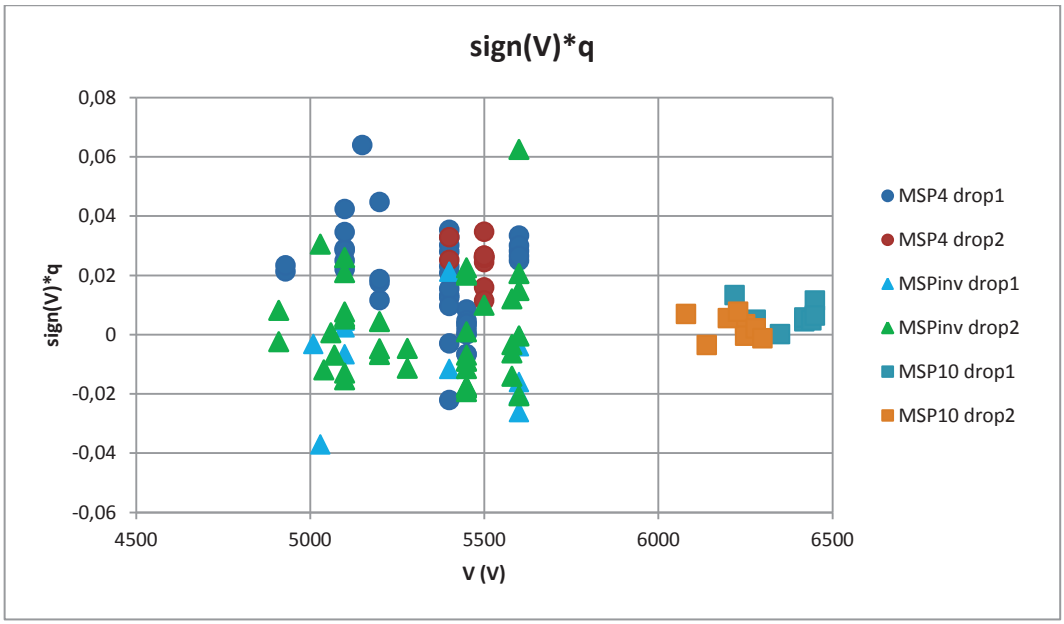

b)

Fig 5.13. Electric charge injection during EHD injection for different pulse shape used with different drop injections.

Drop injection is performed by different pulse shape with both positive and negative voltage. Thus, on Fig 5.13 a) the points showing the droplet charge with respect to the injection voltage are separated in two clusters. To facilitate the analysis, Fig 5.13 b) shows the charge multiplied by the

sign of the applied voltage. It can first be seen on that second figure that for a given pulse shape, the charges of injected droplets are in good accordance. The quantity of drop charge is influenced largely by used pulse shape, no matter the sign of applied voltage.

The shape of pulse MSP4, MSP_{inv} and MSP_{10} are respectively given on Fig 3.18, 3.19 and 3.32. For pulse MSP4, the polarity remained the same during the entire pulse duration, and the injected charge is of the same polarity as the applied voltage. The absolute value of electric charge is most often between 0.02 and 0.06 pC. Pulse MSP_{inv} aimed at limiting the injection by reversing the polarity between first and last part of the pulse. It can be seen that the charge of droplets injected by pulse MSP_{inv} does not depend so clearly on the polarity of the applied voltage. The absolute value of the charge is reduced but generally remains between 0.01 and 0.02 pC or a little larger. The reduction of the electric charge of the droplets using a kind of alternate pulse such as MSP10, gives the best results, with electric charges usually smaller than 0.01 pC.

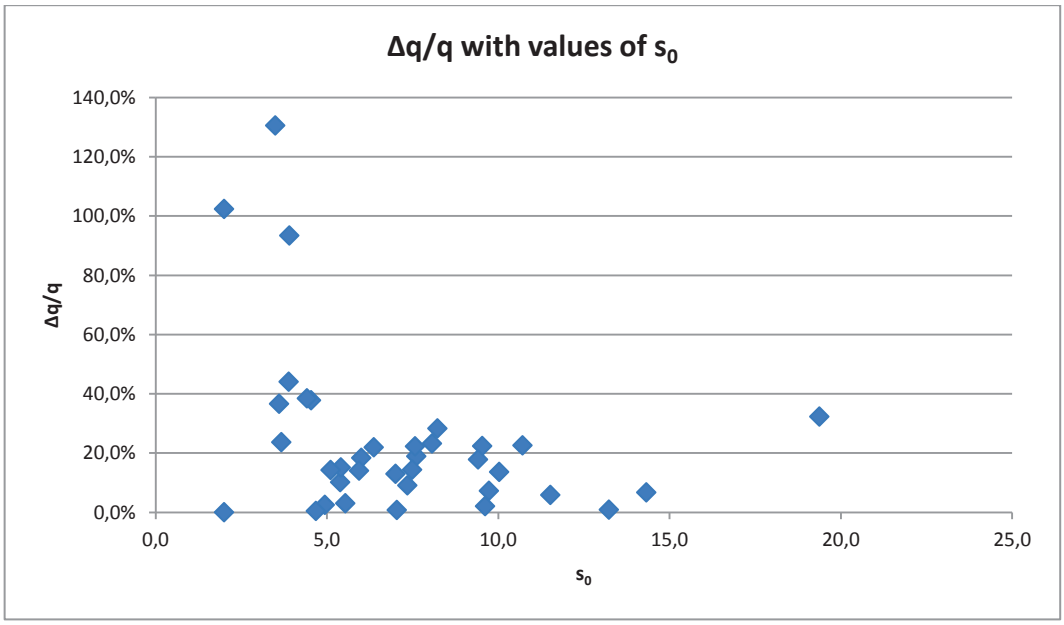

Fig 5.14. Charge imbalances with values of s_0.

The calculation of drop charge is after application of the DC field, at the beginning of which the inter drop distance parameter is calculated as s_0. The calculation of drop charge is presented in section 4.4.3 and the model adopted is considered good for $s_0 > 4$. On Fig 5.14 the charge imbalances $\Delta q/q$ decrease with s_0 and the imbalances remain smaller than 30 % for $s_0 > 5$. Only the cases where the mass imbalance has been verified have been drawn on the figure: when the diameter of a coalesced drop has not been calculated from the videos but from application of mass conservation the charge imbalances $\Delta q/q$ sometimes exceeds 200 % (Table 5.3). The three points remaining largely out of the

points cluster, with Δq/q around 100%, are due to the limited duration of coalesced drop falling path. Charge conservation is not as good as mass conservation. Estimation of charge uncertainty using equation (3.16) is not sufficient to explain the few cases where the charge imbalance is much larger than 30 %.

5.4.3 Droplet approach velocity

As proposed in section 5.3.1.4, the distance between the two droplets, decreasing with time up to contact, can be fitted by a 2nd order polynomial function, from which acceleration and approach velocity can be deduced. The acceleration a for two drops approaching each other up to contact under DC fields or AC fields is drawn on Fig 5.15 as a function of applied voltage. The voltage corresponds to the values applied directly on the electrode in the test cell, and for the value of AC field the applied peak voltage is divided by $\sqrt{2}$.

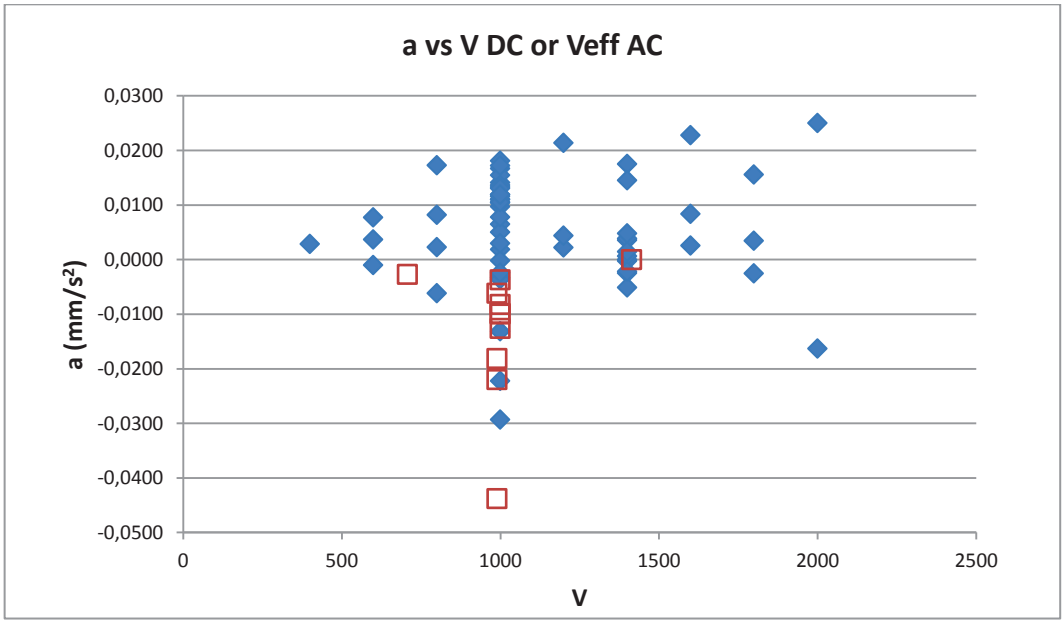

Fig 5.15. Acceleration vs applied voltage for DC (blue diamond) and AC (red square) applied electric fields.

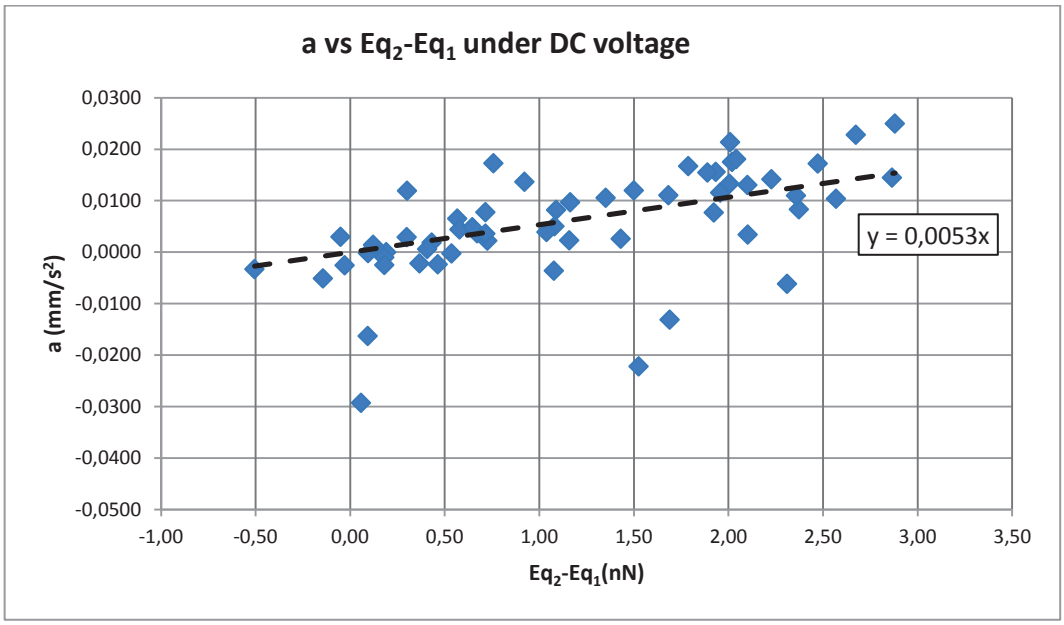

a)

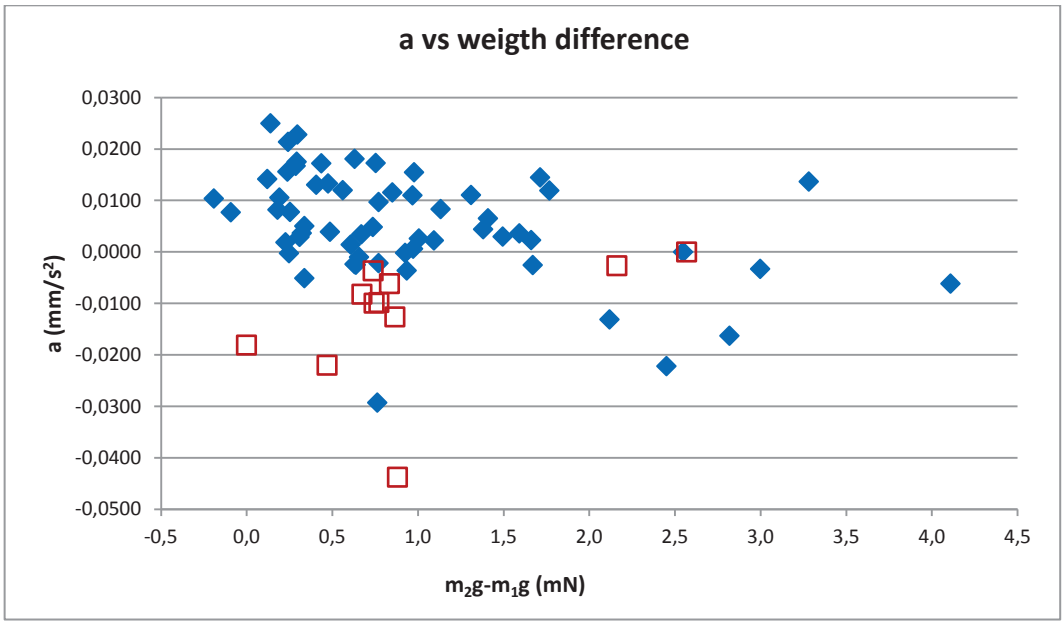

b)

Fig 5.16 : a) acceleration vs difference of electrophoresis force under DC applied electric fields; b) acceleration vs difference of droplets weight under DC (blue diamond) and AC (red square) applied electric field. Vertical component of electric field and gravity are positive when in the droplet falling direction.

On Fig 5.15, the acceleration values cluster at positive values under DC fields while they are always negative under AC fields. This illustrates the effect of the electrophoretic force, when droplet electric

charge is not equal to zero. It should be remembered that the results are biased by the fact that a positive force difference favors the approach of the droplet, while negative difference opposes it. Fig 5.16 a) and b) illustrate that there is a clear influence of the electrophoretic force difference on the acceleration term, but a more random distribution with respect to the weight difference.

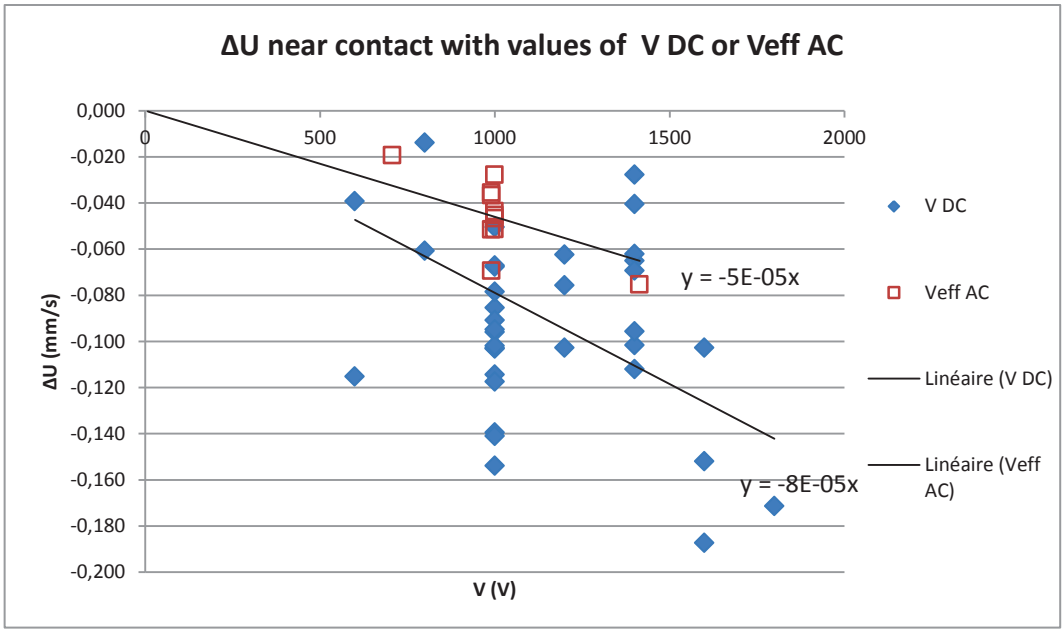

Fig 5.17. Approaching velocity ΔU near contact as function of V DC (blue diamond) and Veff AC (red square).

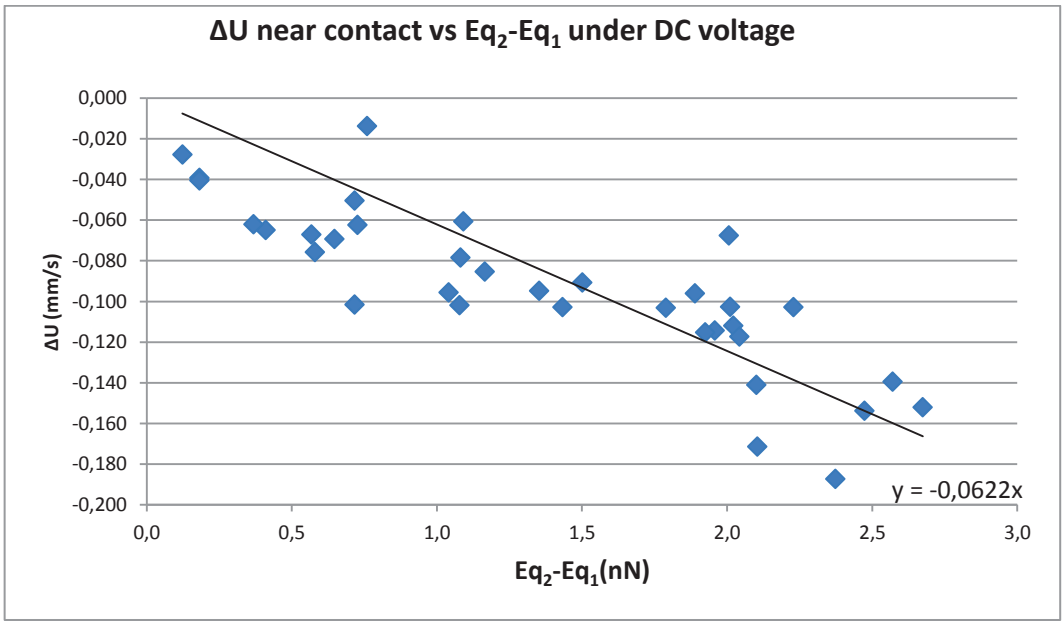

Fig 5.18. Approach velocity ΔU near contact as a function of the difference in electrophoretic force.

On Fig 5.17, the values of ΔU near contact increase much more (in absolute value) under DC field than under AC field. This is a new demonstration of the influence of electrophoresis on charged droplets, whose dependence is again clearly seen on Fig 5.18.

5.5 Zoom-in on drop coalescence

The electrocoalescence processes are recorded by AOS camera at 8000 fps with spatial resolution of 250*200 pixels. The frame rate cannot be increased further because increasing camera speed requires reduction of spatial resolution. 8000 frames per second is a compromise between spatial and temporal resolution. Since the electrocoalescence spot fluctuates on height in the cell from one case to the next, the sequence is often out of the camera vision field. An example of drop coalescence is shown on Fig 5.20 for injection of $MSP_{inverse}$ – $MSP_{inverse}$ case No. 47 on Table 5.2 and 5.3.

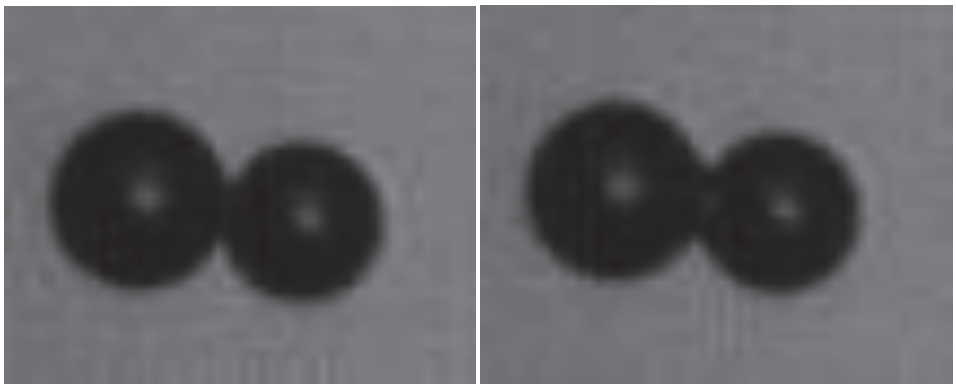

(a) (b)

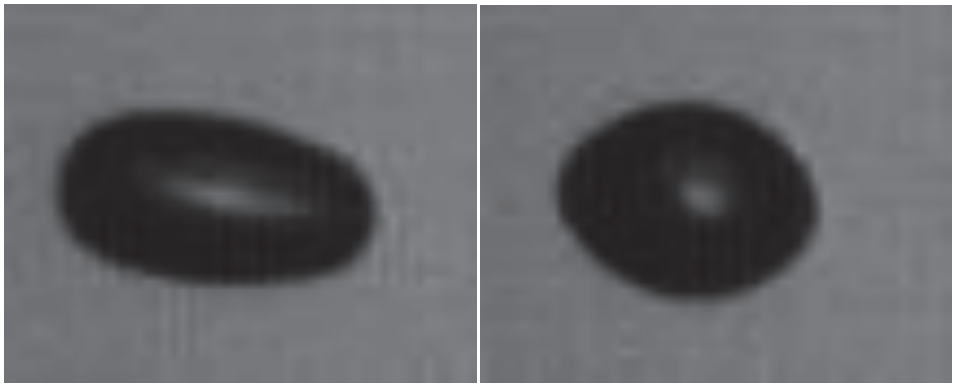

(c) (d)

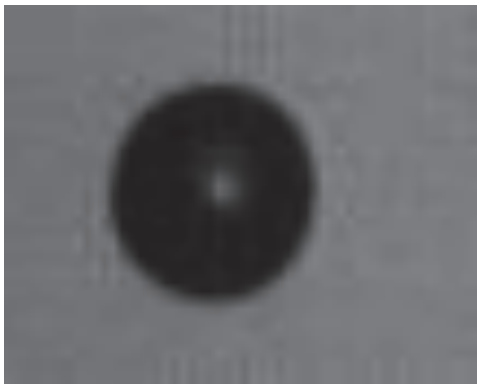

(e)

Fig 5.19. Coalescence of two drops viewed by AOS camera 8000 fps with 250*200, the photos above are successive frames, and the time interval between two photo is 0.125 ms, case No. 47 (03/06/2015).

5.5.1 Image processing of AOS high speed videos

The time interval between the two successive photos is 1/8000 = 0. 125 ms and the uncertainties in the measurements of 1 pixel correspond to 0.01 mm with this frame size. It can be seen on Fig 5.19 that the coalescence begins in photo (b) and is already completed by photo (c), the photos (d) and (e) illustrate the quick return to the spherical shape of the fused droplet. This sequence was selected because the beginning of the fusion, which is marked as a link formation between the two drops, is well seen on photo (b) whereas it was not captured in most of the other recorded sequences. With reduced spatial resolution of AOS camera at this frame rate, the boundaries of drops are not so clear. Thus the AMILab software (Trujillo-Pino et al. 2013) is used in association with classical image processing software ImageJ, for fixing drop boundaries in subpixel resolution. The measurement of the inter drop distance Δe from AOS camera data is performed using the following method sequence:

1. Draw the subpixel boundary of the droplets using AMIlab software, with the standard parameters proposed. That boundary appears as a dotted line made of red segments, superimposed on the initial frame (Fig 5.20).
2. Determine the length of cross sections drawn on the figures with the help of the subpixel boundary.

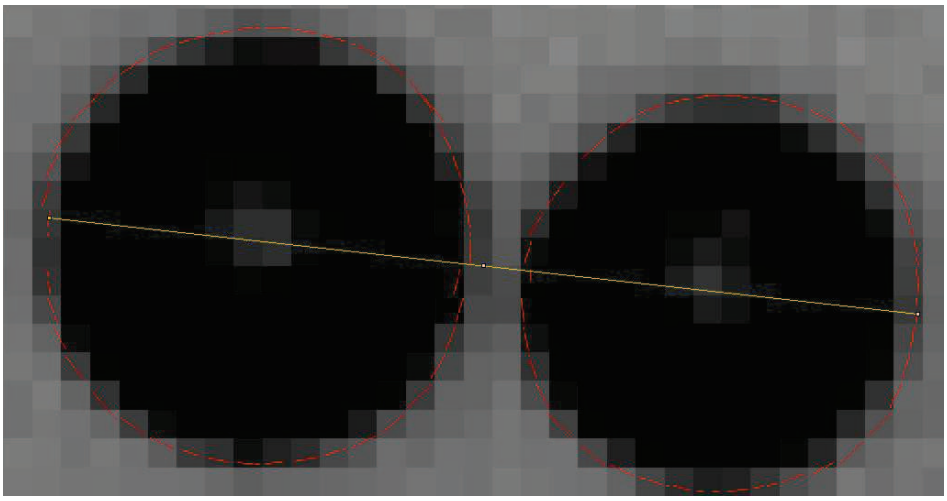

a)

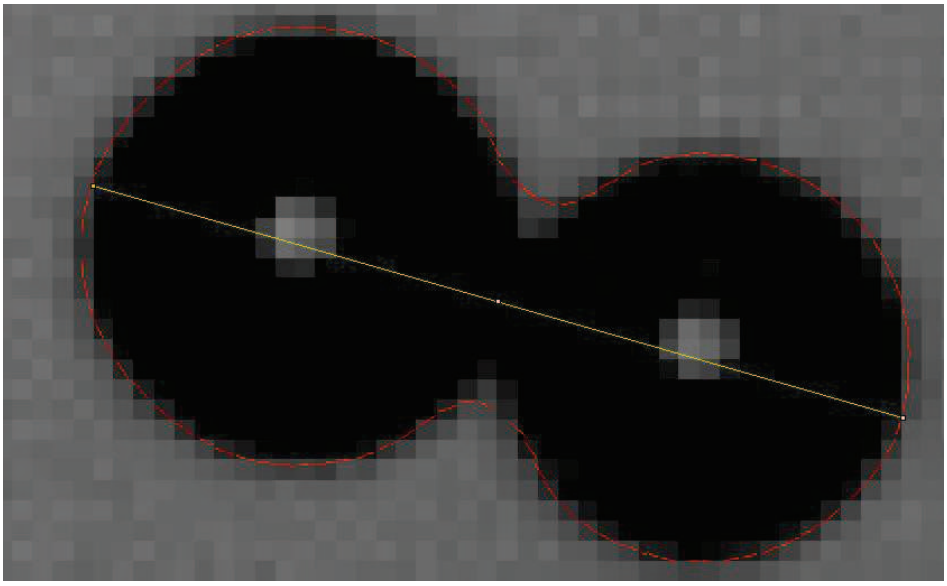

b)

Fig 5.20. Subpixel boundary (red segments drawn by AMIlab software) and maximum cross section (yellow line placed by eyes): a) before drop contact, b) after drop contact.

To measure inter drop distance Δe using AMILab combined with ImageJ, the length of maximum cross section of the two drops is first measured, as indicated by the yellow segment on Fig 5.20a and 5.20b. Then the drop diameters are measured by drawing separate lines crossing each droplet, as indicated by blue lines on Fig 5.21a (and thus can be compared to diameters obtained from the falling velocities). Finally the length of maximum cross section minus the two drop diameters equals the inter drop distance Δe. The position of the different cross sections is adjusted by eye. Thus it is possible to introduce small uncertainties. A little change in position of the extremities of the

segments drawn can induce slight change in the length of the cross sections, but certainly much smaller than the pixel size. Other errors can be attributed either to the lack of sphericity of the droplets, as illustrated by Fig 5.21, or to an overlap of the droplets, in lateral view, when they are not perfectly aligned with the vertical axis.

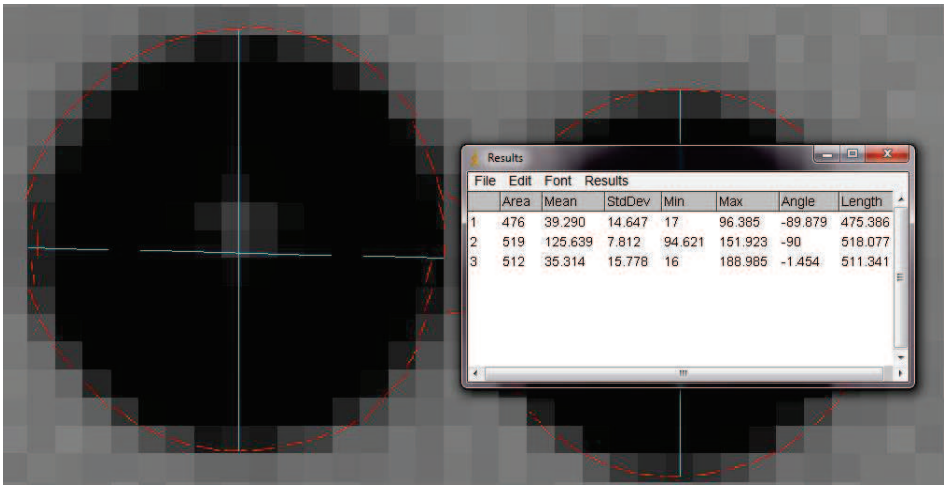

a)

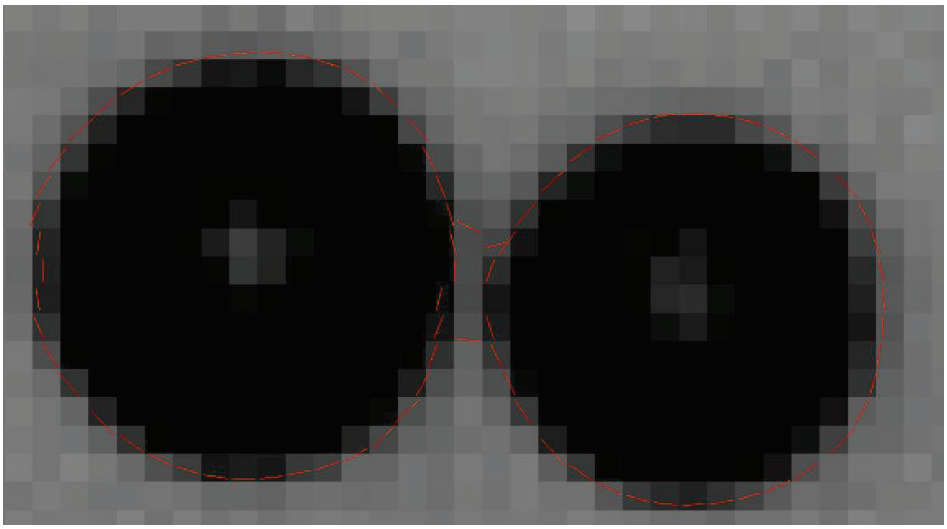

b)

Fig 5.21. a) Illustration of the lack of sphericity of observed droplet: there is about 2% difference between vertical and horizontal segment lengths on the left droplet. b) Cone-like shape of the leftpole of the right droplet under AC field (2015-06-10, 25 °C ± 1 °C, test1, case No. 65).

The drops sometimes appear slightly deformed when they are in close proximity. Thus the diameter estimate could be different along the two axes of the drop, as illustrated on Fig 5.21b, where the

shape of the drops is a little flattened as if pushed by the trapped oil film. Contrarily it can sometimes be observed that facing poles deformed in a cone-like shape. This observation confirmed well the assumptions of (Ghazian et al. 2014) for the redistribution of electric charge.

5.5.2 Analyses of AOS camera data

The drop approach velocity and acceleration can be deduced from the data of the AOS camera, and can be compared to the results obtained previously by image processing of the Dalsa camera records. The decrease with time of the inter droplet distance Δe is drawn on Fig 5.22. Because of uncertainty sources discussed previously, the value Δe can take negative values when approaching contact. Because there is no exact time matching between Dalsa and AOS records, the correspondence of the two sets of points is adjusted manually.

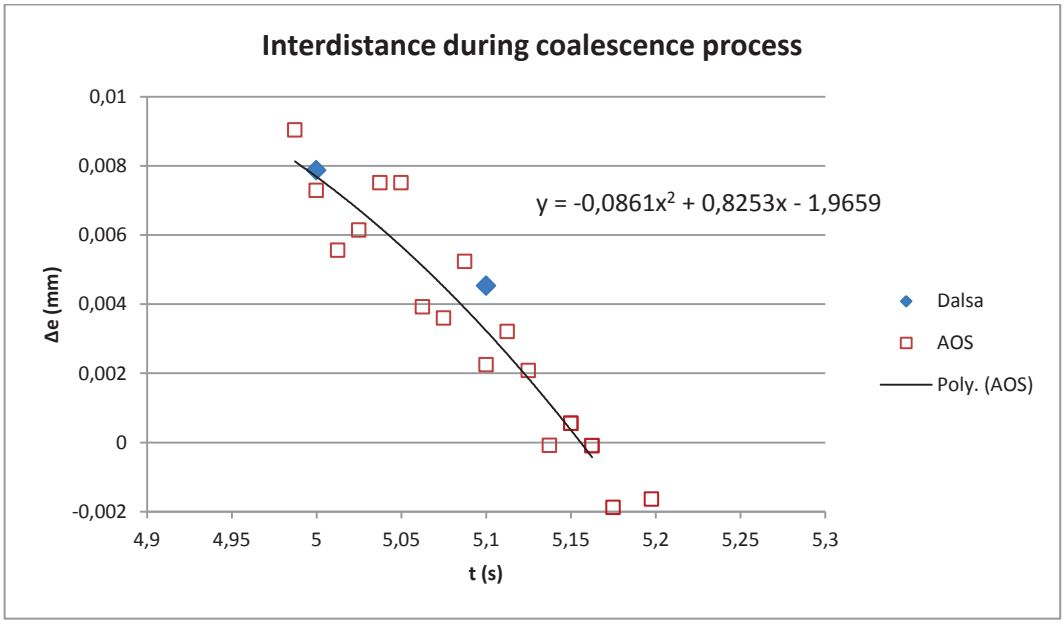

Fig 5.22. Inter drop distance during coalescence process. Blue points are data from Dalsa camera and red squares are extracted from AOS high speed video (2015-06-10, test1; case No. 65).

On Fig 5.22 the blue points from the Dalsa data have larger time spacing (0.1 ms) than the red ones. These red points, extracted from AOS high speed video, complement the data of the Dalsa camera just before the contact and coalescence of the two droplets. The drop approach velocity and acceleration can be calculated from the trend curve, as was previously done in chapter 5.3: ΔU_{AOS} = -0.059 mm/s, a_{AOS} = -0.172 mm/s^2. This corresponds to case No. 65 on Table 5.3 where ΔU = -0.037

mm/s and a = -0.018 mm/s^2. The values obtained from the two videos are very different. That is why a more accurate analysis can be proposed for the data from the Dalsa camera. Starting again with the curve 'distance' vs time a new fit can be tested, using a polynomial function of 4th order instead of a parabolic one as drawn on Fig 5.9. The result drawn Fig 5.23 shows a better fit just before the contact time than the previous one.

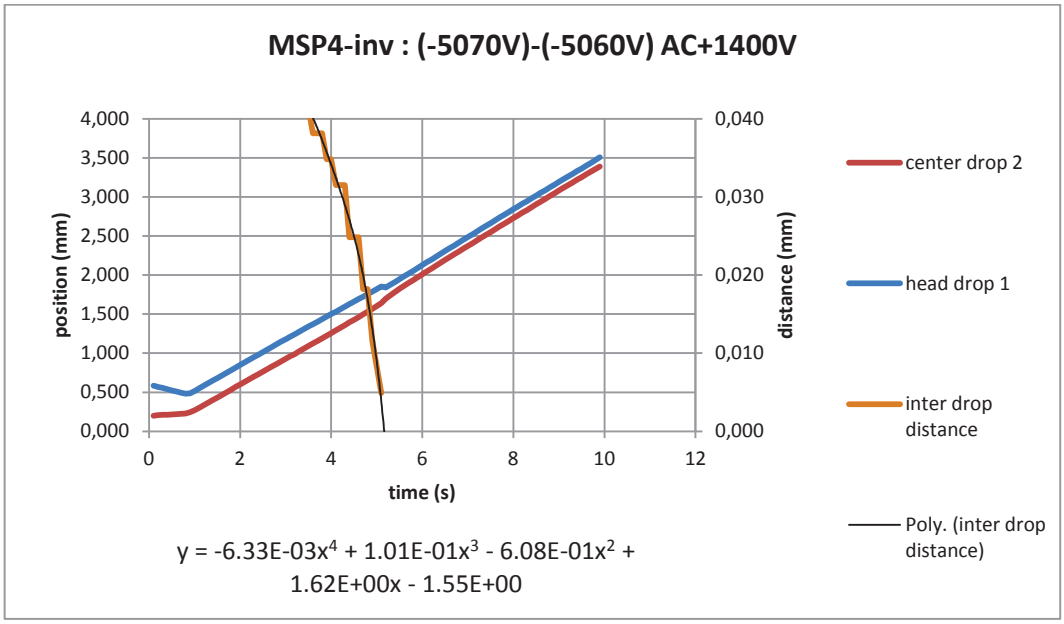

Fig 5.23. Inter drop distance during coalescence process, AC=1.4kV (2015-06-10, test1; case No. 65).

Using the equation indicated on Fig 5.23, the calculated velocity and acceleration just before contact are found to be ΔU_{4th} = -0.059 mm/s and a_{4th} = -0.101 mm/s^2. The velocity value is then in good accordance with the value deduced from the AOS camera data and the order of magnitude of the acceleration terms is in better agreement. The figures presenting ΔU and a obtained respectively with parabolic and 4th order polynomial fittings are drawn on Fig 5.24.

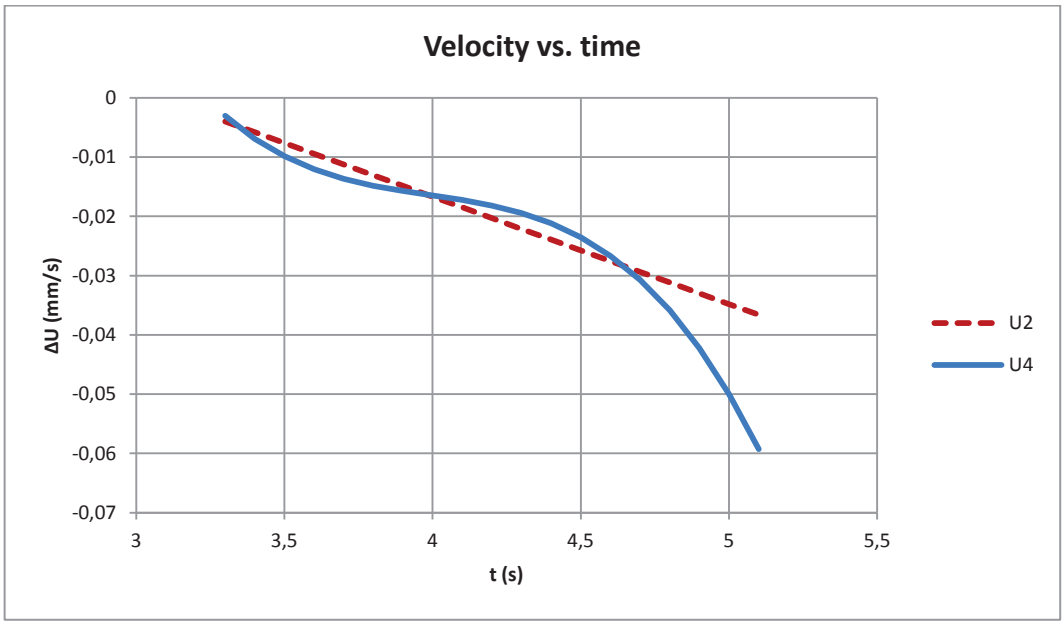

a)

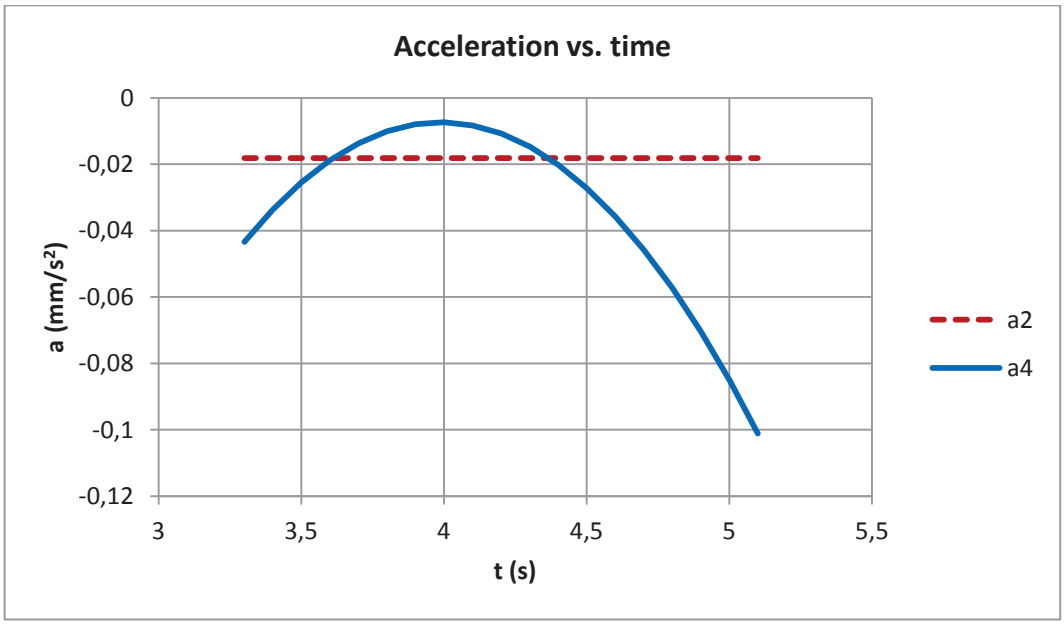

b)

Fig 5.24. Drop approaching velocity and acceleration vs time (2015-06-10, test1; case No. 65). Red dotted line are obtained from parabolic fitting (constant acceleration and linear variation of approaching velocity), while blue full lines correspond to a 4th order polynomial fitting.

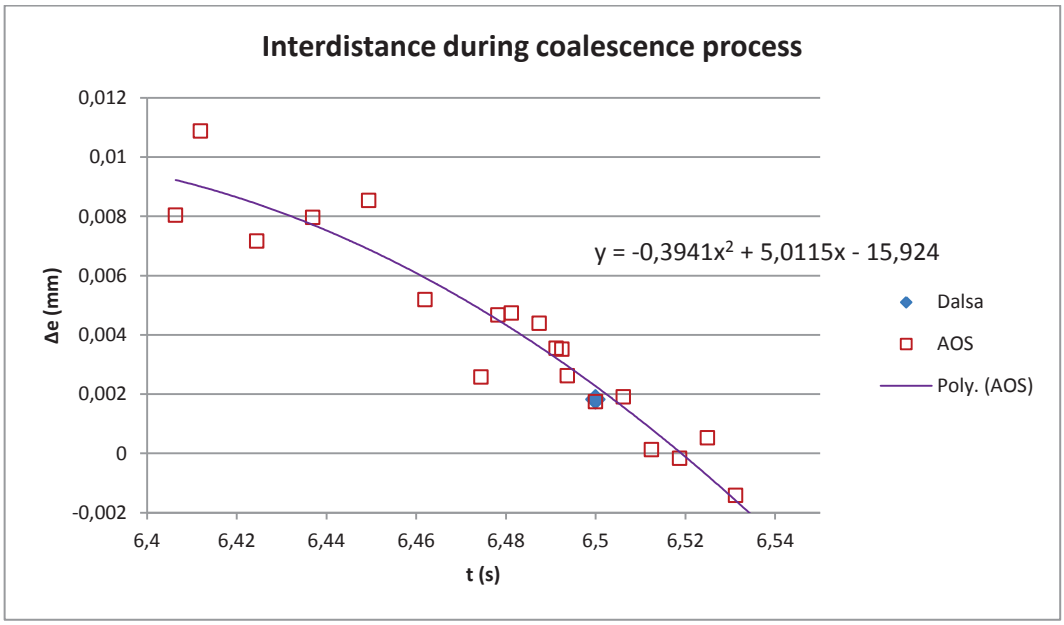

Fig 5.25. Inter drop distance during coalescence process (2015-06-07, test4; case No. 57).

On Fig 5.25 the drop approach velocity and acceleration are: U = -0.143 mm/s, a = -0.788 mm/s^2. This corresponds to case No.57 on Table 5.3. For case No. 57 the 'distance' is also fitted by a function of polynomial order 4, and it gives ΔU = -0.050 mm/s and a = -0.041 mm/s^2.

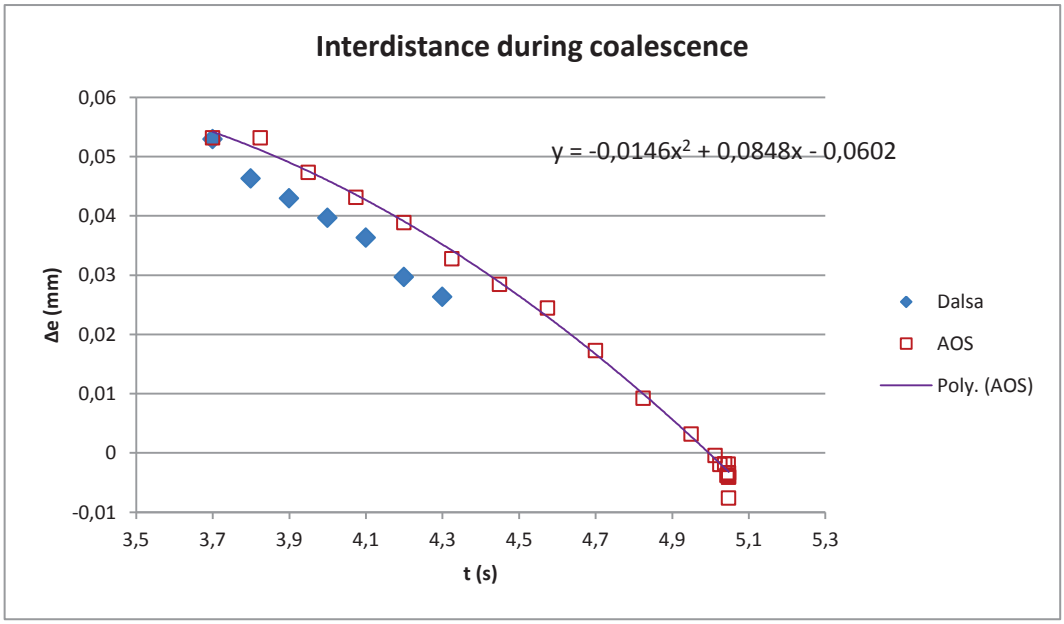

Fig 5.26. Inter drop distance during coalescence process (2015-06-10, test2; case No. 67).

On Fig 5.26 the drop approaching velocity and acceleration are: U = -0.063 mm/s, a = -0.029 mm/s^2. This corresponds to case No.67 on Table 5.3 where U = -0.047 mm/s and a = 0.001 mm/s^2.

Case No.	ΔU_{2nd} (mm/s)	ΔU_{4th} (mm/s)	ΔU_{aos} (mm/s)	Δa_{2nd} (mm/s^2)	Δa_{4th} (mm/s^2)	Δa_{aos} (mm/s^2)
65	-0.037	-0.059	-0.059	-0.018	-0.101	-0.172
57	-0.030	-0.050	-0.143	-0.005	-0.041	-0.788
67	-0.051	-0.047	-0.063	-0.022	0.001	-0.029

Table 5.4. Approaching velocities and acceleration obtain by fitting of Dalsa (2^{nd} and 4^{th} order) and AOS data (2^{nd} order).

On Table 5.4, the values of approach velocity and acceleration deduced from 4^{th} order polynomial fitting on the Dalsa data are clearly closer to the values determined from the AOS camera for case No. 65. The same trend is observed for the case No. 57, but the differences remain very strong. The case No. 67 shows a different result: the time step chosen to extract points from the AOS camera data set is almost as large as the time step of the Dalsa camera records and the two curves present a very similar behavior. Thus the fit of the two data sets by parabolic curves directly gives quite a good agreement, and the 4^{th} order polynomial fitting applied on the Dalsa data diminishes this good agreements.

5.6 Discussion

5.6.1 Estimation of possible charge injection in the oil from the needle tip

It is confirmed that the injected droplets contain electric charge. Consequently the nature and provenance of the charge should be discussed.

First of all, it should be reminded that the shut-off of the multistage pulses, used to extract a droplet from the water meniscus, takes place before the neck breakdown and that the conductivity of water is in theory sufficient to relax all the surface charges. No offset of the high voltage supply was

observed with the oscilloscope, thus the voltage seems really returned to zero. During the successive stages of water drop injection, no jets either lateral or axial were observed. Thus the questionable point is whether the application of the high voltage on the electrode can induce jets of electric charge at the needle tip since it has the smallest curvature of the whole system. For the calculations of injected charge by the needle tip curvature, one example is taken in drop coalescence setup, and the applied voltage on the electrode is 5 kV for H = 8 mm. Under this condition, if positive or negative ions are injected, then the mobility of one ion can be calculated.

$$k = \frac{e}{4\pi\mu x} \tag{5.3}$$

Here the k is mobility coefficient, e is one electron charge with e = $1.602*10^{-19}$ C. x is the radius of the anion with x ≈ 10^{-10} m. Calculation gives, k ≈ 10^{-8} m^2/Vs.

The electric field was assumed to be E ≈ V/L with V the voltage applied on the electrode, L the distance around the needle concerned with charge injection, seen here as a variable. It is assumed that the injected charge neutralized the electric fields around the needle tip, then the space charge density ρ verifies divE = ρ/ε, with ε = $\varepsilon_0\varepsilon_r$. With divE ≈ E/L, it can be written ρ ≈ $\varepsilon V/L^2$. The current density is j = kρE, and the electric current limited by the space charge I = $j*\pi L^2$ if the surface is supposed to be a disc of radius L. We deduce the expression:

$$I \approx \pi k \epsilon \frac{V^2}{L} \tag{5.4}$$

Taking L = H the numerical applications gives I ≈ $\pi*10^{-8}*2.1*8.85*10^{-12}*5000^2/(8*10^{-3})$ ≈ 10^{-9} A. Then the total injected charge is Q = I*t with t the duration of the pulse, of about 1 ms. Then Q ≈ 2 10^{-12} C. In fact this supposes that the system has the time to stabilize itself: with this indicated mobility the spatial charge injected from the needle tip has moved (during 1 ms under 5 kV, and L = 8 mm) of a distance of k*U/L*t = 6 microns.

The above calculations only give an order of magnitude of injected charge. The charge of the injected drops can then be explained in two different ways. The first possibility relates to the fact that when the high voltage was applied on the bottom electrode, electric charges of the opposite polarity are injected around the needle tip. After the shut-down of the electrode voltage, for electroneutrality purposes, the needle should be of the opposite polarity to the surrounding charge and thus of the

same polarity as the electrode. The water droplet has the same potential as the needle, thus it is charged with the same polarity as the initially applied voltage. The second possibility is that the injected charge around the needle tip neutralized the electric field around it, and this electric-field screening charge is absorbed by falling drops through its journey. This effect may cause the drops to have the opposite polarity to the electrode.

During experiments drops were observed to have the same polarity as the bottom electrode, which confirmed the first possibility. However, through series of injection or DC applications on the electrode, the charge on drops lost their concordance with the electrode polarity. This is because the accumulation of injected charge in oil medium cannot be evacuated easily due to low conductivity of the oil. Then the resultant electric charge of the accumulation is not as clearly linked to the applied voltage, and needs to be defined through drop falling velocities under DC field.

The Fig 5.27 presents the electric charge density around the needle tip with total charge of +0.25 pC distributed within a tenths of a millimeter thick layer. Fig 5.27a is the distributed charge density and Fig 5.27b is the induced charge on the water meniscus surface induced by the charge density on Fig 5.27a.

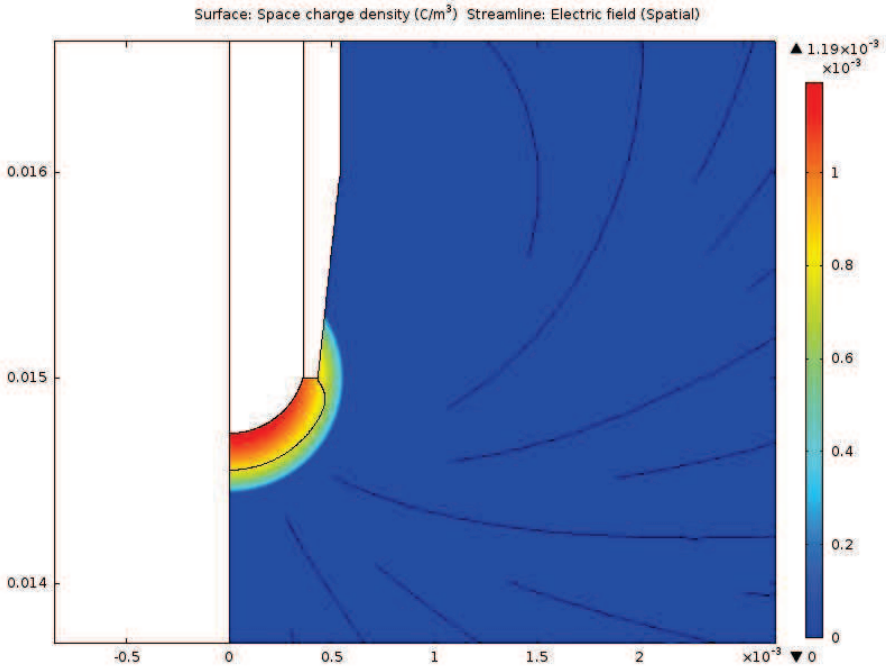

a)

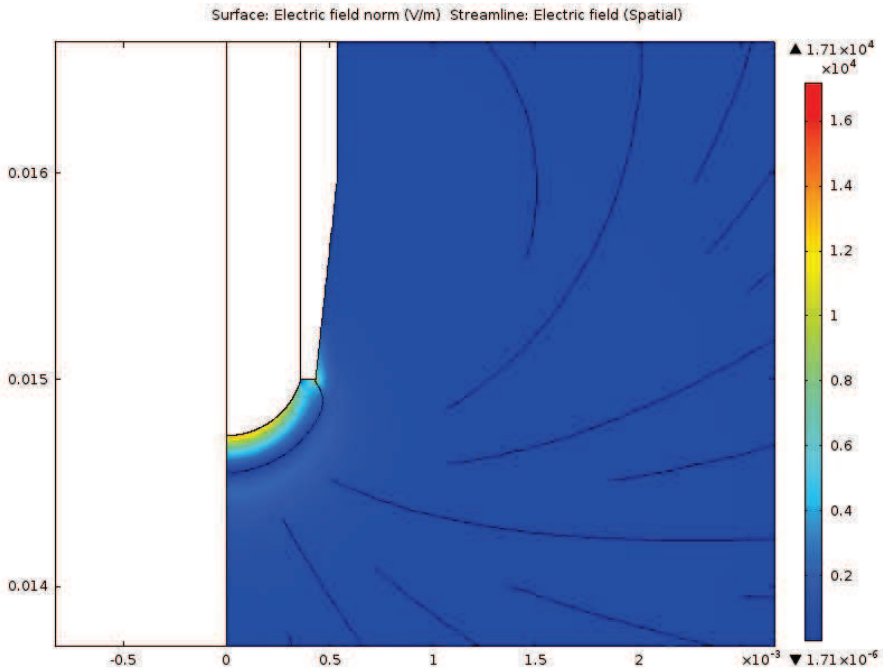

b)

Fig 5.27. Simulated electric fields around the needle tip with spatial charge. a) Spatial distribution of electric charge density around the needle tip: total charge + 0.25 pC. b) electric fields around the needle tip induced by the spatial charge distribution.

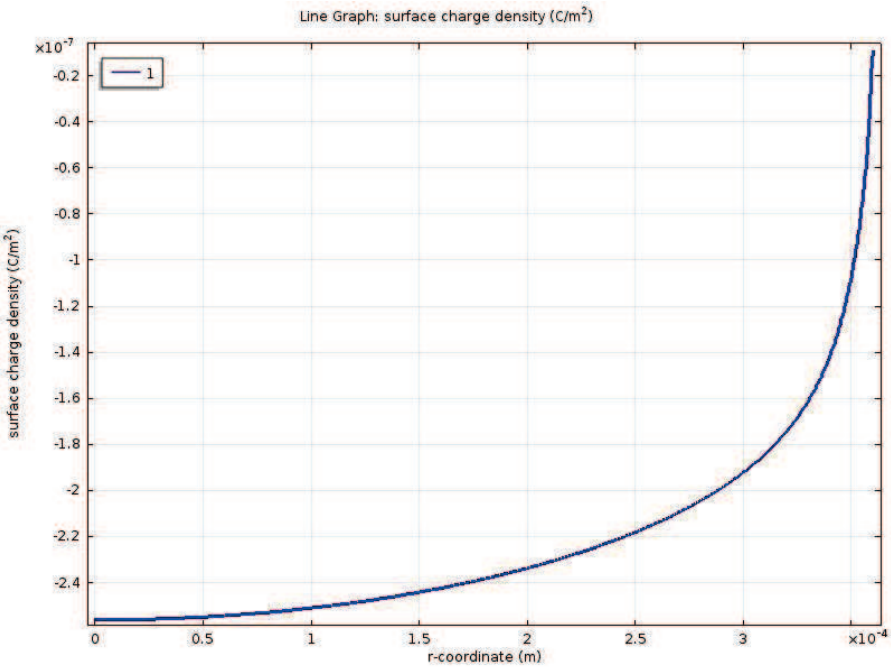

a)

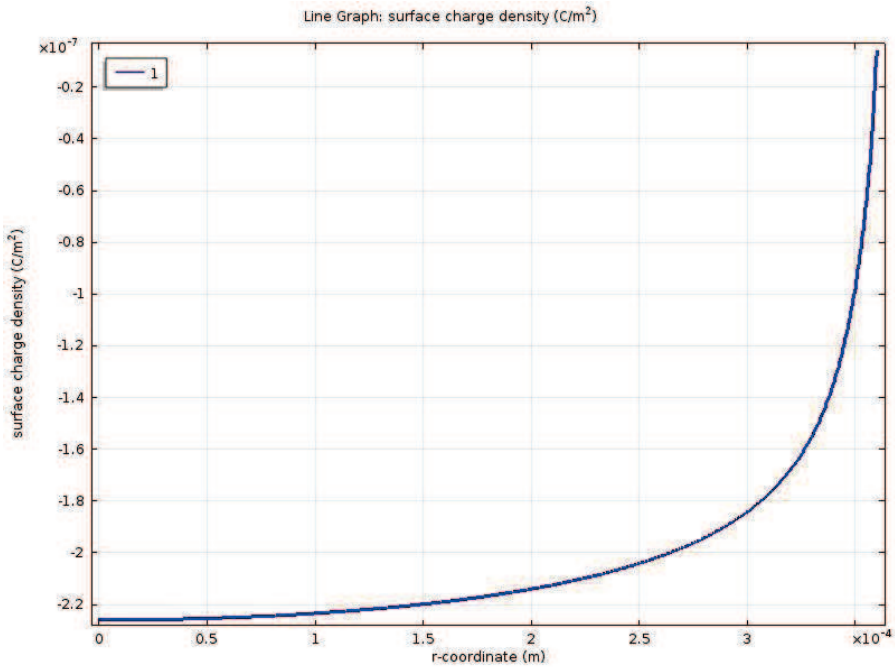

b)

Fig 5.28. Calculated electric field density at water meniscus apex. a) Surface electric charge density on the meniscus (the polarity of the charge is opposite to the injected charge). b) Induced surface charge on the water meniscus by an application of +10VDC on the electrode below.

The electric charge is calculated on the water meniscus. On Fig 5.28 the 0 corresponds to the center apex of the meniscus because of its symmetry. This charge density decreases when reaching the border of the needle cone. Fig 5.28 a) is the induced charge calculation. With this surface charge density value, one water drop of 0.15 mm diameter can carry electric charge of order of -0.02 pC. Fig 5.28 b) is the electric charge density induced by a residual voltage on the electrode, without a charge cloud around the needle tip.

5.6.2 Comparison with numerical simulation of falling droplet pair under electric field

In sections 5.4 and 5.5, it was seen that, despite the large number of configurations studied, it remains difficult to extract some of the main features of electrocoalescence behavior. In analyses it is particularly difficult to distinguish the different influences: effects of weight difference and of electrophoresis due to the charged droplets, strong non-linear interactions between droplets. That is

why a direct comparison of the records with numerical simulations would probably be the best way to improve the knowledge of the physical interactions and to develop prediction capabilities. As an example, we can compare the results of case n° 6, already illustrated in Fig 5.3 reproduced hereafter in Fig 5.30 a and b for convenience.

Simulation is carried out there using Comsol Multiphysics, version 5.0. The model takes into account the two water droplets and the oil medium through resolution of Navier-Stokes equations in a mesh moving at constant velocity to follow approximately the falling droplet pair. The resolution of electrostatic equations is performed in the oil, the water being considered as pure conductive medium and the droplet carrying the electric charge deduced from experiment. The model is Arbitrary Lagrangian-Eulerian, which means that the boundary of the droplet is described by deformable lines on which the deforming mesh is attached. The clear identification of the water-oil interfaces, as described in (Raisin et al. 2011), allows the direct application of the electrostatic pressure on the surface. In the case presented in Fig 5.29 the coupling of the different equations takes into account a no slip velocity condition at the droplet surface to deal with the effect of surfactant described in chapter 1.4.4 (Fig 1.24). The result of droplet trajectories and velocities are compared to the measurements in Fig 5.30, almost up to the contact of the drop boundaries where the numerical simulation stopped. Other numerical models, as for example those based on Volume-of-Fluid or Level-Set methods, would allow continuing the computation after the droplet coalescence.

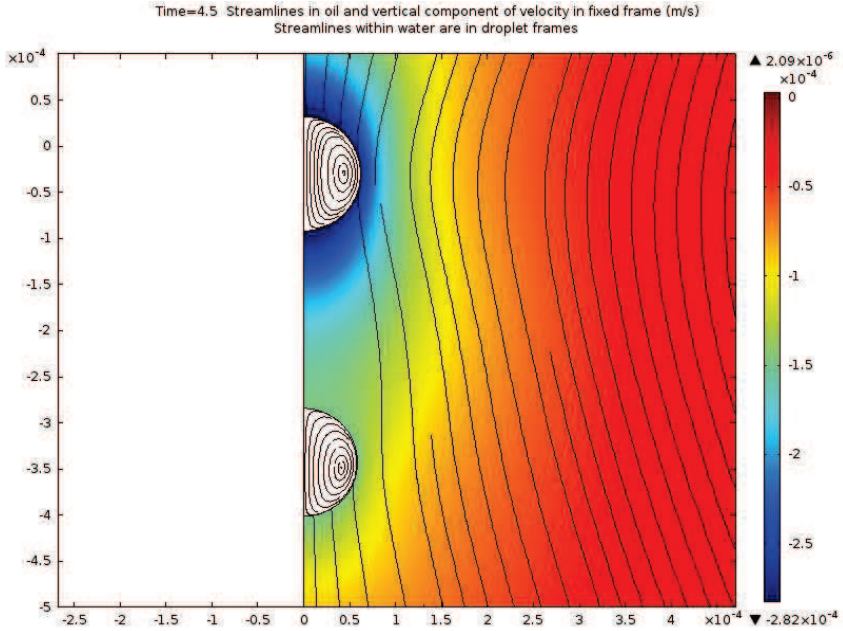

a)

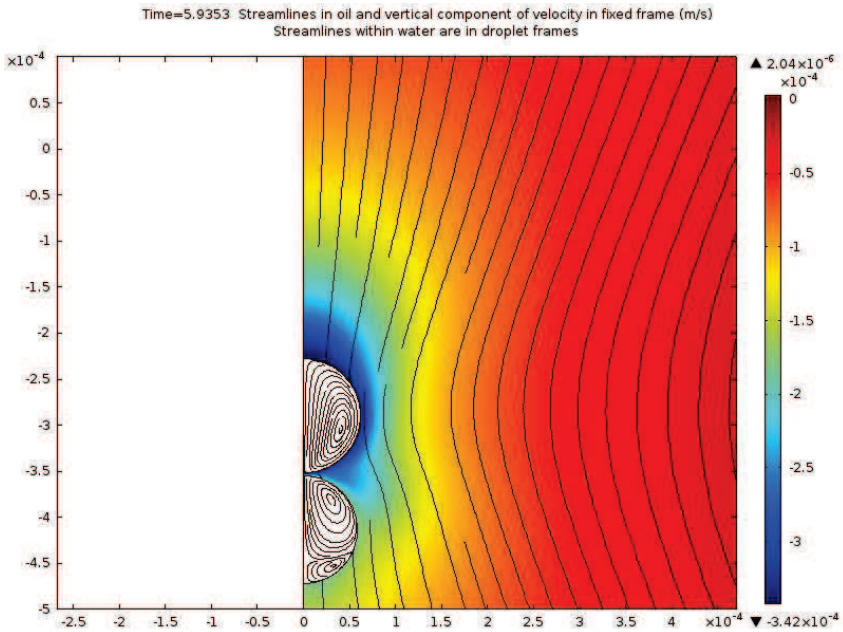

b)

5.29. Simulation of falling drops pair up to contact: drop diameters of D_1 = 0.105 mm, D_2 = 0.113 mm; charges of q_1 = 0.005 pC, q_2 = -0.026 pC; (24/03/2015, 21 °C ± 1 °C, case No. 6).

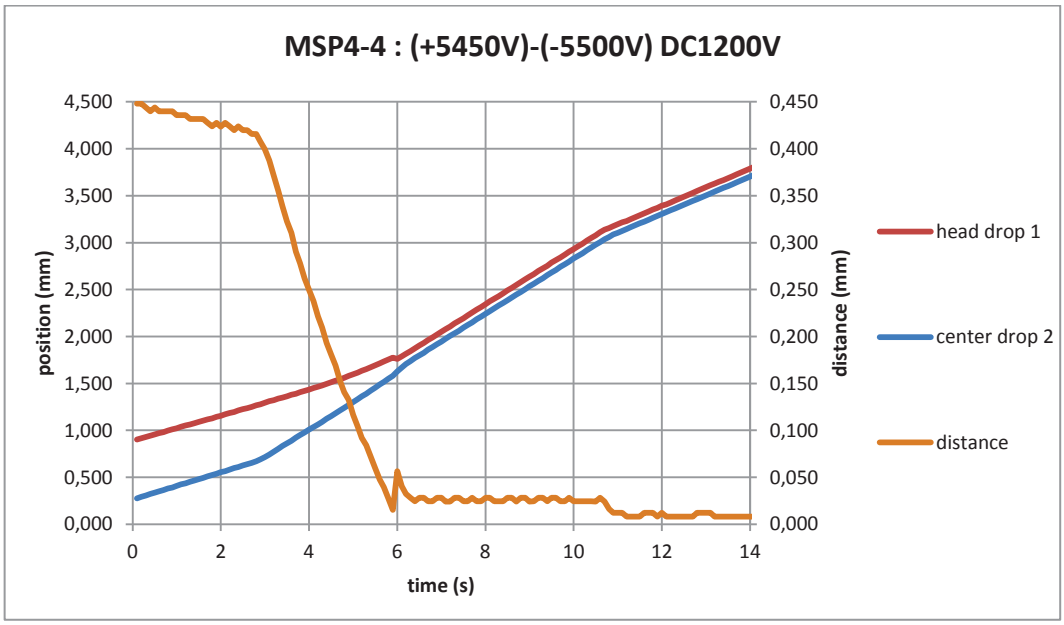
MSP4-4 : (+5450V)-(-5500V) DC1200V
position (mm)
distance (mm)
time (s)
head drop 1
center drop 2
distance

a)

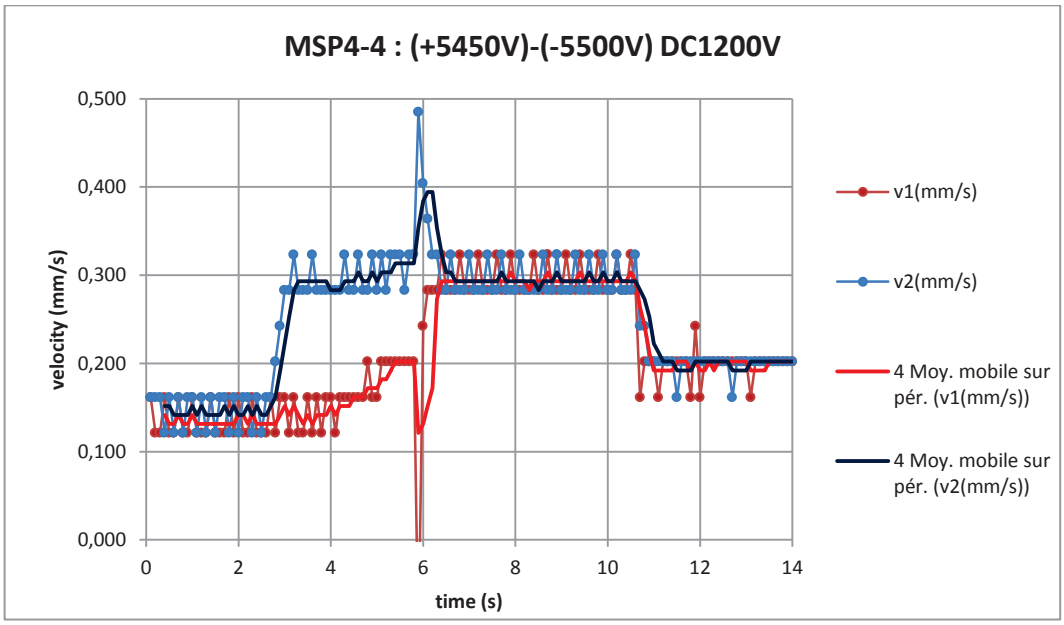
MSP4-4 : (+5450V)-(-5500V) DC1200V
velocity (mm/s)
time (s)
v1(mm/s)
v2(mm/s)
4 Moy. mobile sur pér. (v1(mm/s))
4 Moy. mobile sur pér. (v2(mm/s))

b)

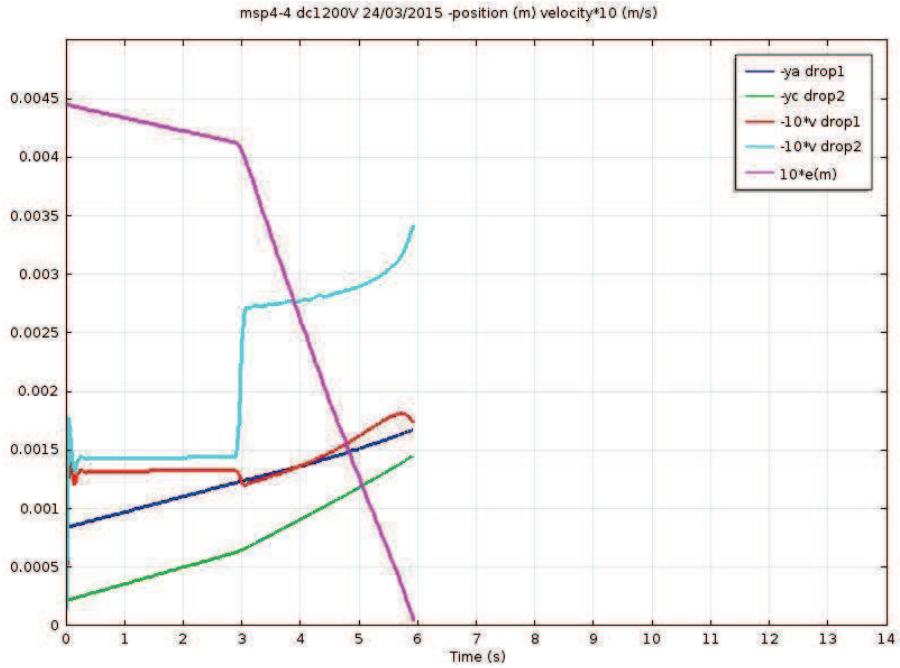

c)

5.30. Drop coalescence of MSP4 – MSP4 with drop diameters of D_1 = 0.105 mm, D_2 = 0.113 mm; charges of q_1 = 0.005 pC, q_2 = -0.026 pC; $\Delta m/m$ = 1.9 %, $\Delta q/q$ = 0.8 % (24/03/2015, 21 °C $\pm$ 1 °C, case No. 6).

Comparisons between Fig 5.30 c) and 5.30 a) and b) shows there is a fairly good agreement between simulation and experimental data (time of contact, velocities with and without applied DC electric field, increase of the falling drops pair velocity when the inter-droplet distance decreases...). Simulation then gives access to supplementary data, as for example the radial velocities during the last stages of drainage of the oil film (Fig 5.31).

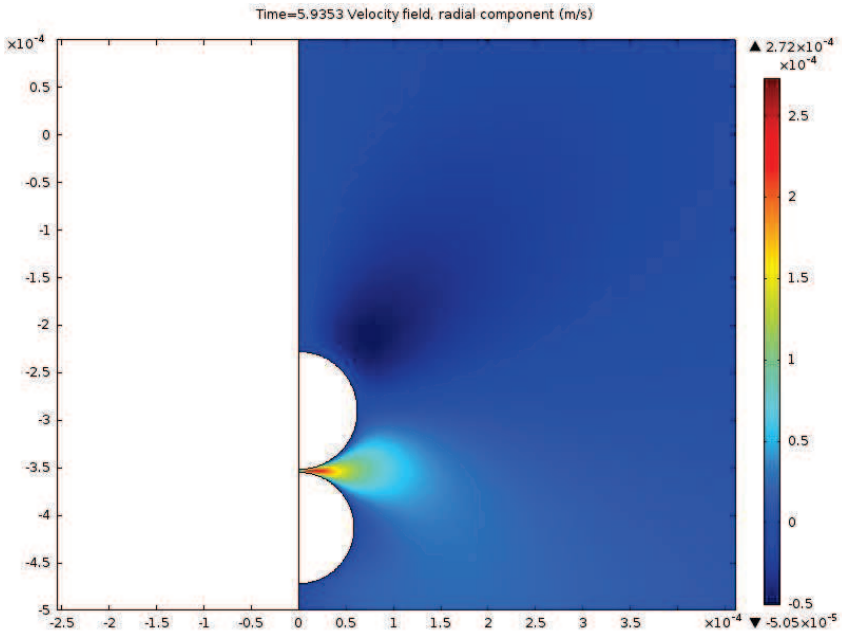

5.31. Drop coalescence of MSP4 – MSP4 with drop diameters of D_1 = 0.105 mm, D_2 = 0.113 mm; charges of q_1 = 0.005 pC, q_2 = -0.026 pC; $\Delta m/m$ = 1.9 %, $\Delta q/q$ = 0.8 % (24/03/2015, 21 °C ± 1 °C, case No. 6). Radial velocity just before contact (drainage of the oil fime between the two facing water-oil interfaces).

5.6.3 Additional experiments

For drop coalescence under electric fields, most experiments were done in the region between the injection needle and the intermediate high voltage electrode. However, in this region the electric field is not perfectly uniform, its intensity decreasing from the needle tip to the electrode. To have a constant electric field environment, in the drop coalescence set-up test cell, some experiments were done between the high voltage electrode and the bottom grounded metallic plate. The free falling droplet pair traveled through the hole in the middle of the high voltage electrode and the DC voltage is applied on the electrode only when the two droplets have reached the other side. Thus the electric fields are generated between the two parallel metallic plates and are far more uniform as expected. The distance between the two plates is 1.5 cm, and it increases the total time of observation with respect to previous experiments. However, it was far more difficult to catch good droplet pair configurations (good alignment with the vertical axis, good range of the inter-drop distance) in the vision fields of the cameras after a longer journey from the injection point. An example is presented in Fig 5.32.

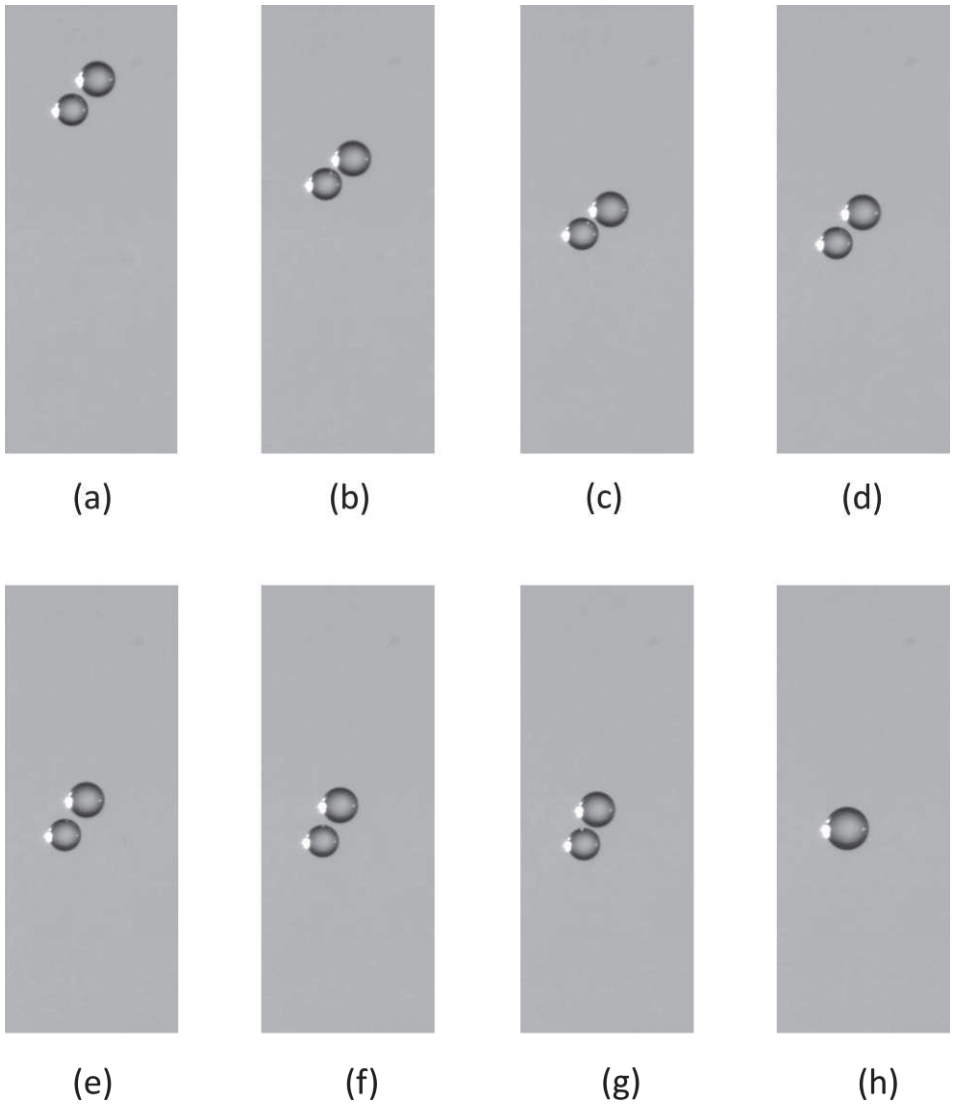

Fig 5.32. Drops are oriented under electric fields to be parallel to these field lines. The time intervals between the photos are not the same: from (a) to (e) the time interval is of 1s; from photo (e) to (h) the time interval is decreased to 0.5s 0.3s and finally 0.2s. Injection of the drops are of MSP_{inv} – MSP_{inv} with drop diameters of D_1 = 0.19 mm and D_2 = 0.21 mm, measured directly from images (2015-02-23). A 1kV DC voltage is applied just before image c).

Fig 5.32 shows the beginning of the self-alignment of the droplet pair when subjected to vertical electric field. The drops were injected by MSP_{inv} – MSP_{inv} with drop diameters of D_1 = 0.19 mm and D_2 = 0.21 mm, measured directly from images. During their free fall, from (a) to (c), the angles between the drop center line and the vertical axis remains quite large (> 30°), and the falling velocity is high. When the DC field is applied on the electrode, from (c) to (h), the falling motion of the drops is slowed down while the drops began to rotate their center line to align with electric field, as

predicted theoretically (Lundgaard & Berg 2003). There, the initial distance between droplets is not sufficient to obtain a perfect alignment before their final coalescence.

5.7 Conclusion and recommendations for further experiments

In this chapter, 70 different cases of drops coalescence under DC or AC fields are presented. First analysis of data from Dalsa and AOS camera are proposed to describe the near contact drop approaching process. Discussions on the origin of the droplet charge, on the possible comparisons with numerical simulations, and on a better configuration for additional experiments, are also proposed.

For further research of electrocoalescence in the configuration depicted in this PhD, analysis of the results allows proposing different aspects to be improved:

- Reducing the uncertainty related to temperature effects on viscosity and density. The temperature should be registered separately for each case and adjustment of the viscosity and density should be taken into account for data analysis.
- Managing the variations of surface tension. First a special attention should be paid to the prevention of oils dust contamination. Secondly, a primary ejection of a large droplet can be applied to clean the meniscus interface from surface active component, after that the injection of the droplets pair can be done with a fixed delay. This procedure will allow the comparison with the time dependent interfacial tension measured with the pendant drop tensiometer. A better alternative would consist in verifying in situ the surface tension by transient analysis of droplets oscillations under application of square DC voltage. However, it will be difficult to visualize because of the droplets' small size and their associated high frequency oscillations.
- Working on longer time period of falling droplet pair and on more uniform electric field. It can be done by recording the electrocoalescence process between HV electrode and bottom of the cell as illustrated in chapter 5.6.3.
- Reducing the uncertainties on the droplet diameter and velocity estimations by improving the spatial resolution (mainly for high speed camera) or by developing improved image

processing, for example by using correlation technique of the images with moving template circles.

- Improving the use of alternate pulses for drop-on-demand generation to minimize the droplet charge. That can be based on MSP10 pulse, but needs reducing the capacitive effect of the HV cable to enable the increase of the frequency.
- Applying AC electric fields, instead of DC, to minimize the effect of droplet electric charge.

Conclusion

When electric fields are applied in oil-water mixtures small water droplets are attracted to others and merge in larger drops. This electrocoalescence process makes more efficient the oil-water separation by sedimentation.

Experimental data on the electrocoalescence of very small droplets will be useful to improve the understanding of the dynamics of water-oil interface and to validate numerical models. The simple studied configuration consists in a small droplet pair falling in stagnant model oil, under electric field aligned with the symmetry axis of the droplet pair and the direction of gravity.

First part of the work consisted in the well-controlled generation of very small droplet pair (range 20-200 micrometers) aligned with electric field. Droplet-on-Demand generation by EHD method was improved for a better control of the diameter and electric charge of droplets injected from a single metallic needle. This was obtained by applying to a pendant water meniscus optimized multistage high voltage electric pulses.

Then, electrical and hydrodynamic characterization of the droplet pairs and their coalescence are mainly deduced from the analysis of falling velocities, with and without applied DC electric field. A complete data set of droplet position and velocity is deduced from video. A special attention was paid to the visualizations of very small droplet and small falling velocities, involving multiple angles of view, strong zooming and high speed video.

Modelling the different terms of hydrodynamic and electrostatic interactions between droplets allows deducing, from the recorded velocities, their respective mass and electric charge. When coalescence occurs, a record of the resulting single droplet velocity, with and without applied voltage, allows controlling the mass and charge conservations and validating the method.

A first data set of about 70 different cases, taking into account the variation of droplets pair diameter (with a limited range in order to maintain falling velocities between 0.1 and 0.3 mm/s) and different

applied voltage types (DC or AC), was established. Analyses of the results and experimental uncertainties, and example of possible comparison with numerical simulations using Comsol Multiphysics™ software, allow performing some recommendations for future work.

Appendix

A. Drop injection in Primol 352

Primol 352 is a mixture of saturated hydrocarbons, products of petroleum refinery, and it is also stable in terms of oxidation. For Primol 352, the remarkable difference compared to Marcol 52 is the high viscosity value, of about 0.193 Pa.s, ten times higher than that of Marcol 52. Thus the influence of oil viscosity is much more important than the capillary effect on drop injection dynamics. On Table 2.3, the only high value of Ohnesorge number corresponds to Primol 352, which signifies that the viscosity takes a dominating role over all. The calculations of capillary time and viscous time show that t_{cap}=0.535 ms while t_{μ}=0.275 ms, the viscous time is smaller than the capillary time. Generally the pulse duration is defined between the two extremities presented by the capillary time and the viscous time, however this is not the case for Primol 352. Experiments of tap water drop injection into primol 352 were done in EHD injection setups. Due to the high viscosity of the model oil, the water meniscus which should be formed by pressure difference between the water recipient and the oil-water interface could not be got anymore. Thus the water recipient was replaced by a micro-syringe through which a quantity of water could be pushed out manually to adjust the height of the meniscus.

A.1 Characteristics of Primol 352 model oil

On Table A.1, the uncertainties of the parameters are not revealed because the interfacial tension was measured by Du Noüy Ring method and the oil viscosity, density was not measured with temperature increase. Since Primol 352 has a high viscosity, it is decided not to use this oil to

perform drop coalescence experiments. Thus further investigations on oil characteristics have not been done.

	Primol (4.2ms, 3.4ms)	Primol (3.2ms, 3.0ms)
ε_r	2.1786 (taken from document)	2.1786 (taken from document)
σ (N/m)	0.043	0.041
μ (Pa.s)	0.193 (taken from document)	0.193 (taken from document)
ρ_o (kg/m^3)	863	863
R_{cap} (mm)	0.23	0.23
H (mm)	6	6
V_{low} (kV)	3.332	3.254
t_{cap} (ms)	0.535	0.548
t_μ (ms)	0.275	0.275
$h/R_{cap} = 0.75$	MSP1	MSP1
t (ms)	4.2; 3.4	3.2; 3.0
V_{min} (kV)	3.90	4.24
$V_{0.1mm}$ (kV)	4.07	4.46
V_{max} (kV)	4.98	4.98
t/t_{cap}	7.85; 6.36	5.84; 5.47
V_{min}/V_{low}	1.17	1.30
$V_{0.1mm}/V_{low}$	1.22	1.37
V_{max}/V_{low}	1.49	1.53
figures	Fig A.2	Fig A.2

Table A.1. Summed up of the characteristics of Primol 352 performed for injection on Fig A.2.

A.2 Drop injection in Primol 352 model oil

For drop injection, a pulse shape was fixed to be MSP1 because this pulse can give good drop injection. As the model oil is changed, the experimental parameters should be changed with. First, the height of the hanging needle should be determined by calculations of V_{low}. The needle was not changed from drop injection in Marcol 52, thus R_{cap} = 0.23 mm. in experiments. The pulse generator was the Wavetek 395 model with an amplification of 1000 times. The upper limit of the possible applied voltage is of 5 kV. By determining V_{low} = 5 kV, the corresponding needle height H could be as high as 25 mm. In reality, the applied voltage should be higher than the calculated values, thus the height of the needle should be reduced to assure a sufficient electrostatic pressure. From many experimental tests, the distance of the needle height was fixed to H = 6 mm, which corresponds to V_{low} = 3.4 kV.

After having confirmed the distance H, the pulse durations is put in question. During experiments, it was found that values between the capillary time and the viscous time calculated on Table 2.3, as for Marcol 52, could not give successful drop injection due to lack of applied electric energy on the meniscus. Thus increasing the pulse durations was tested up to 3 ms to 4ms, values with which drops are injected successfully into Primol 352. The injection process is shown below with one example of MSP1 3.4 ms at 4.8 kV, with a relative meniscus height of h/R_{cap}=0.75.

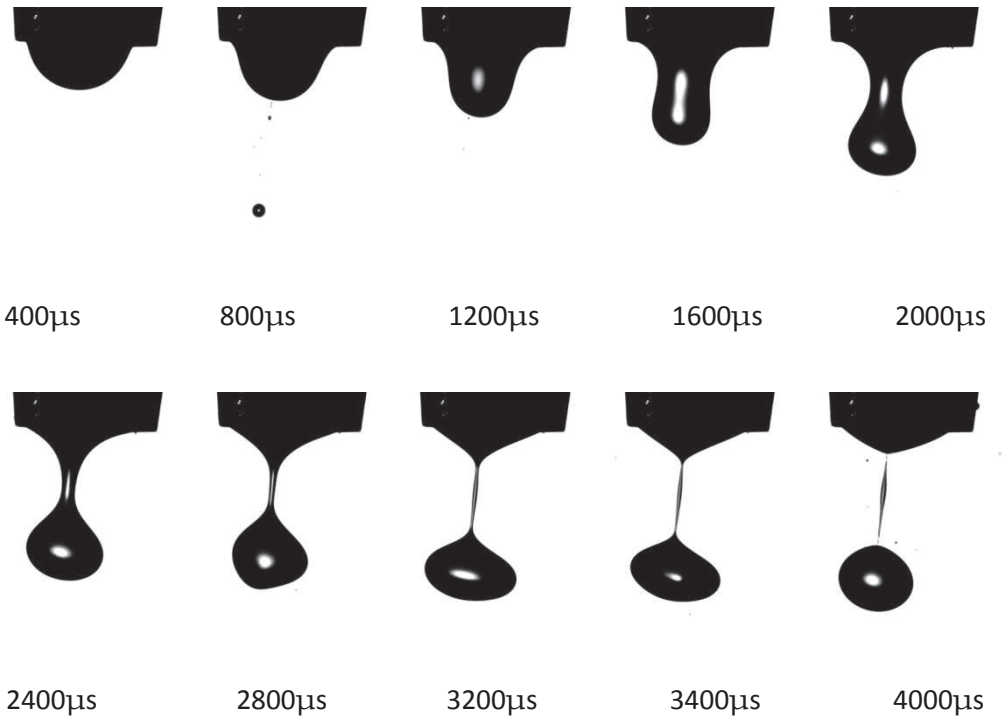

Fig A.1 Injection process in Primol 352, using MSP1 at 4.8 kV, with a total pulse duration of 3.4 ms.

On the photos above, the deformations of the meniscus are different than that in Marcol 52, because in Primol 352 it is the viscosity which constrains these water dynamics. In other cases of injection, the drop should be extracted by meniscus inertial force. But in this case the injection is mainly based on electrical force. Due to the high viscosity, the meniscus deforms very slowly during injection. The blunt-tip meniscus is not formed as it was observed with Marcol 52. All through the process, only the head of the meniscus grows with a longing and thinning necking. Part 3 of the pulse ensured the jet, but in this case it extends the duration of the connection time of drop with the rest of the meniscus due to the high viscosity environment. The necking doesn't break off easily. The break up takes place later than the voltage shut down, and the drops are not electrically charged. Moreover, with this comportment of necking, only small satellites formed. The curves of drop diameters with applied voltage are shown below.

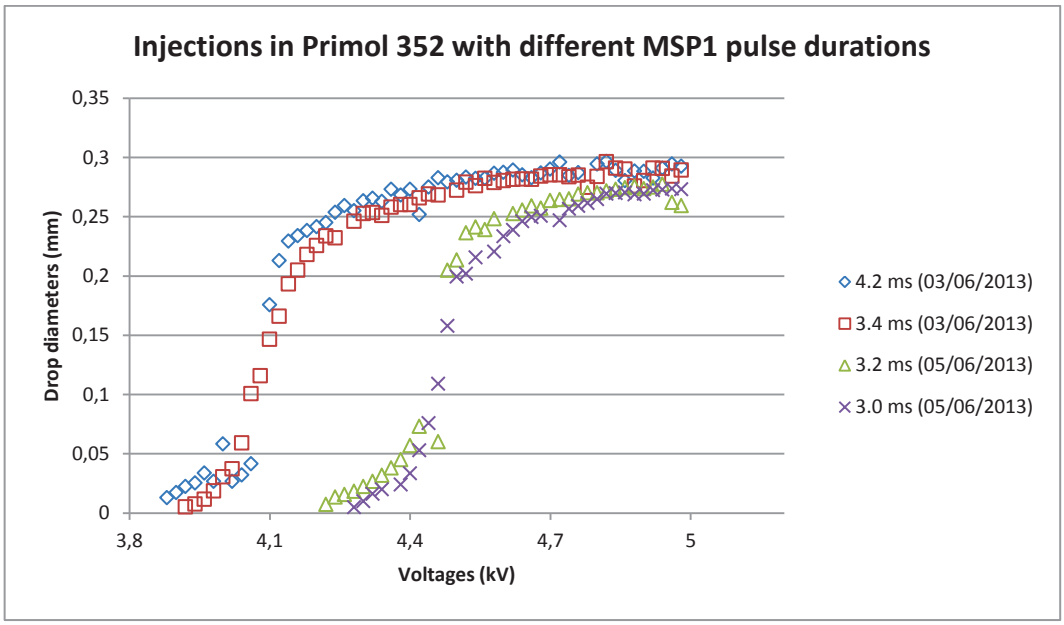

Fig A.2. Drop injection in Primol 352 by MSP1 with different pulse durations. The temperature is taken of 21 °C ± 1 °C, the interfacial tension is σ = 43 to 41 mN/m, H = 6 mm.

On Fig A.2 all the curves have almost the same diameters range, from about 0.005 mm up to 0.300 mm. The curves are all smooth and for large drop diameters, they all converged to an upper value. This plateau showed no increase in main drop sizes, however the hidden information is that with increasing voltage, water thread became longer and longer, then thread breakup caused big satellites formations. Among the four curves, the curve of 3.4 ms does not have any 'hole' inside. Thus the pulse duration for drop injection into Primol 352 was fixed to be 3.4 ms. The four curves are placed two by two with a certain distance between, which correspond to different dates for experiments.

The two series of 4.2 ms and 3.4 ms done two days earlier are placed before the other two curves 3.2 ms and 3.0 ms done later. This phenomenon may be due to changes of water-oil interfacial tension. The refractive index was from 1.473 to 1.479 (Anon n.d., p.35). Then for calculations of relative permittivity, the refractive index was chosen to be 1.476. For Primol 352 $\varepsilon_r \approx n^2 = 2.1786$. This relative permittivity value is used for V_{low} calculation. The V_{low} corresponding to the curves of 43 mN/m is 3.33 kV and to the curves of 41 mN/m is 3.25 kV.

Curves are drawn in function of pulse energies W to test curve horizontal positions with different given pulse energies.

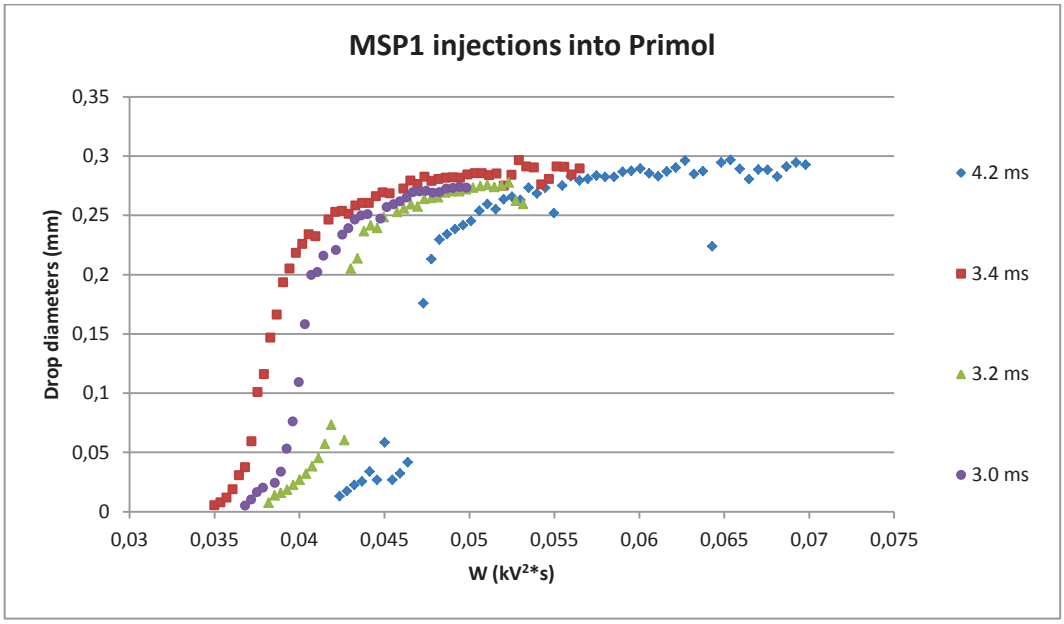

Fig A.3. Drop injection in Primol 352 by MSP1 with different pulse durations. The temperature is taken of 21 °C ± 1 °C, the interfacial tension is σ = 43 mN/m, H = 6 mm.

On Fig A.3 the horizontal positions of the four curves have changed, comparing to the curve positions on Fig A.2. The series with the largest pulse duration is placed to a higher W number while the series with the lowest pulse duration is placed in between the extremities. For the experiments on the same date, the series of 3.4 ms was done before that of 4.2 ms, and the series of 3.2 ms was done before that of 3.0 ms. This seemed not due to the accumulated charge inside bulk oil because the behaviors of series done in order are not the same, for the experiments on the two dates respectively. It is supposed that the dynamic influence which relates to the used pulse shape played the role to influence the injected drop sizes.

Primol 352 has large viscosity value, and the injection distance between the needle tip and the bottom electrode is too small to do any drop coalescence experiments. Thus this high viscous oil is not the best choice for the following study of electrocoalescence.

B. Résumé de la thèse en français

B.1 Introduction

Le pétrole brut est un liquide de couleur bronze foncé, avec une haute viscosité. Ce liquide se trouve dans des cavités dans le sous-sol de la terre où il s'est formé sous haute pression et température durant des millions d'années. L'eau est présente naturellement dans ces cavités, mélangée avec le pétrole brut. La figure B.1 illustre l'extraction par des puits du pétrole contenu dans la cavité remplie également de gaz et d'eau.

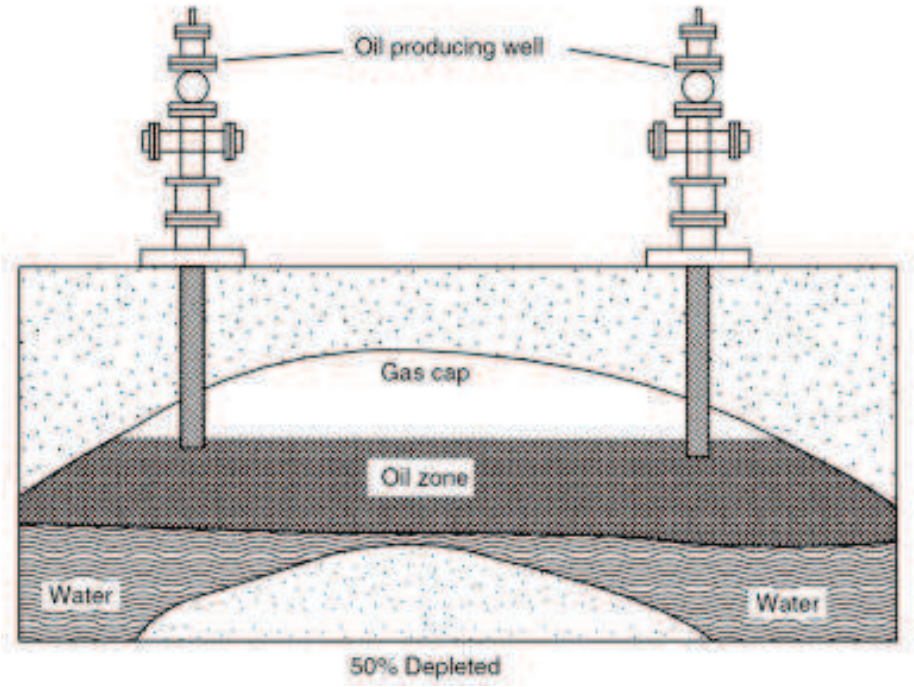

Fig B.1. Extraction du pétrole brut du sous-sol de la terre (Speight 2014).

Au fur et à mesure de l'extraction, la pression dans la cavité diminue, défavorisant l'extraction. Pour surmonter ce problème, on peut procéder à l'injection d'eau ou de gaz dans la cavité pour maintenir la pression. Mais cette injection favorise le mélange de l'eau avec le pétrole brut. A la sortie des puits d'extraction, on obtient ainsi un mélange d'eau, de pétrole et de gaz.

Une fois ce mélange extrait, la séparation préliminaire des différentes phases est nécessaire. A l'aide de la gravité, on sépare eau, pétrole et le gaz dont les densités sont différentes. Mais cette séparation n'est pas complète parce que le pétrole brut contient encore des fines gouttelettes d'eau. De plus, une injection d'eau douce peut encore être utilisée pour dissoudre les sels minéraux, comme l'illustre la figure B.2 qui présente le principe de prétraitement du pétrole brut. L'ensemble du procédé va ainsi générer une émulsion très stable de très fines gouttelettes d'eau dans le pétrole. L'émulsion résultante doit être encore traitée pour diminuer la quantité d'eau contenue dans le pétrole avant le raffinage.

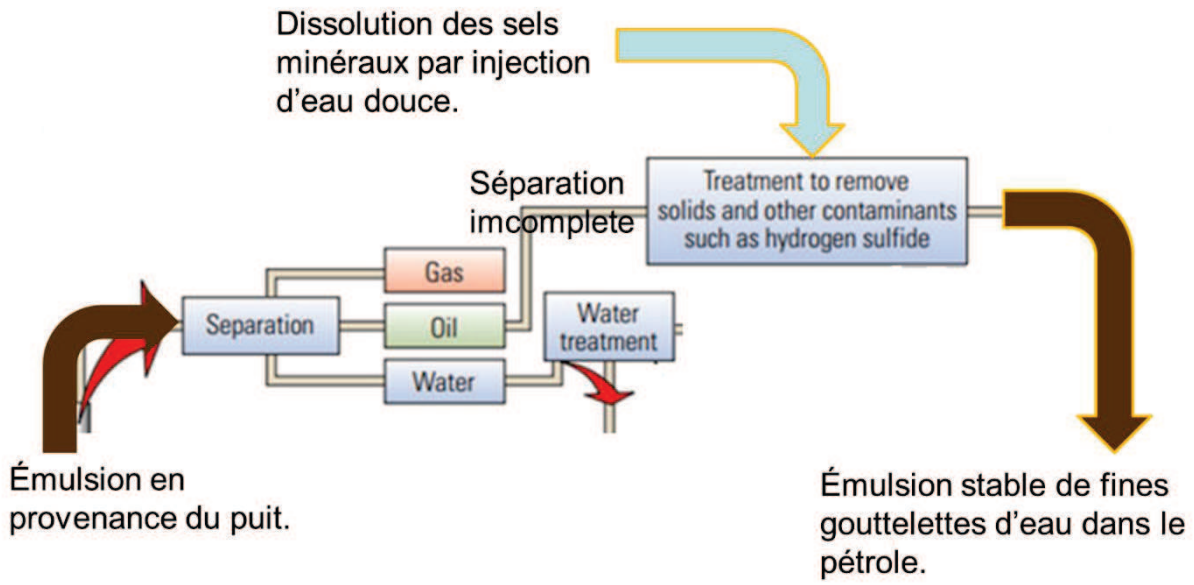

Fig B.2. Séparation préliminaire du pétrole brut (Arnold et al. 2004).

Normalement la séparation d'émulsion est réalisée par sédimentation à l'aide de la gravité et de la différence de densité. Un exemple est illustré Figure B.3. Quand le pétrole brut est échauffé à 60˚C, la viscosité décroit à 25mPa.s. Les gouttelettes d'eau salée présentent une différence de masse volumique de 100kg/m^3 par rapport au pétrole brut. En chutant sous l'effet de la gravité les gouttes suivent un régime visqueux de Stokes. Pour une grosse goutte de diamètre D=1mm, la vitesse de

chute est d'environ 2mm/s. Pour une gouttelette d'eau dix fois plus petite (D=100µm), la vitesse de chute est beaucoup réduite, de l'ordre de 20µm/s. Cette vitesse est très petite et la séparation par sédimentation est très lente, ou même impossible s'il y a des légères vitesses de convection dans la cuve.

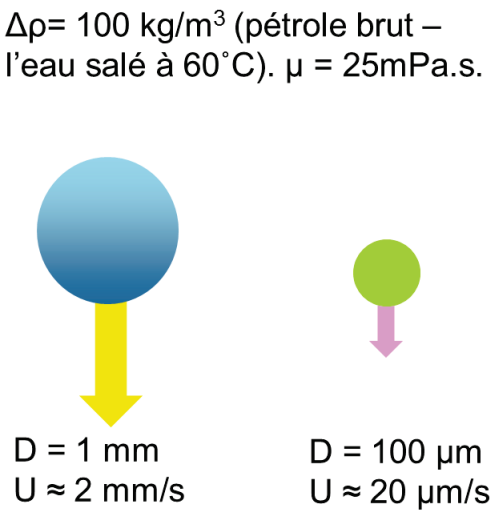

Fig B.3. Vitesse de chute pour deux tailles de gouttelette d'eau dans du pétrole brut chauffé à 60˚C.

Pour raccourcir le temps de séparation on cherche à fusionner les plus petites gouttelettes en gouttes plus grosses, dont la vitesse de sédimentation est plus grande, et on applique pour cela une méthode d'électrocoalescence, suivant un principe connu depuis plusieurs dizaines d'années.

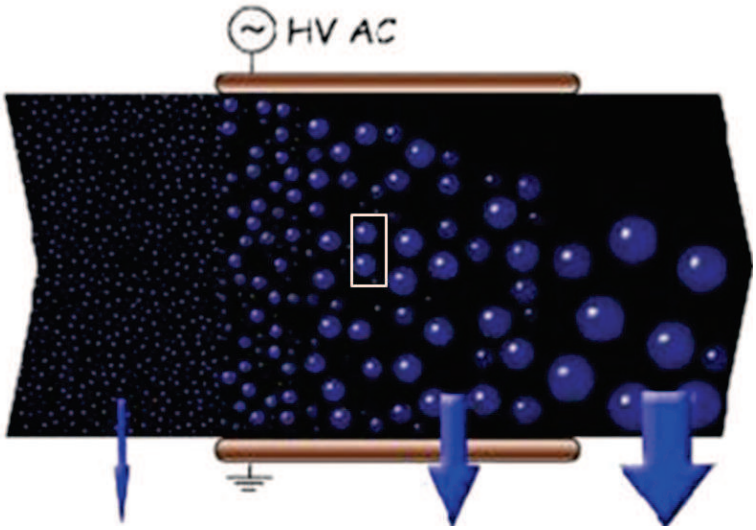

Fig B.4. Séparation de l'émulsion d'eau dans le pétrole par la méthode d'électrocoalescence (https://www.sintef.no/en/projects/compact-separation/by/electrocoalescence-/).

L'électrocoalescence consiste à appliquer un champ électrique, continu ou alternatif, à l'écoulement de l'émulsion de pétrole brut. Les fines gouttelettes d'eau vont être attirées et fusionner sous l'effet des forces électrostatiques créées par ce champ électrique pour former des grosses gouttes. Puis sous l'effet de la gravité, les grosses gouttes sédimentent rapidement. Le champ électrique typique est de l'ordre de 2 à 10kV/cm avec réchauffement du pétrole pour diminuer sa viscosité. L'objectif du traitement de desémulsification est de rendre la quantité d'eau inférieure à 0.1-1%.

Dans la thèse on s'intéresse à l'électrocoalescence de deux gouttes, à une échelle de quelques dizaines de microns. Les travaux expérimentaux antérieurs cités dans la littérature traitent deux configurations : deux gouttes tombant parallèlement avec un champ électrique perpendiculaire à leur direction de chute, présenté à gauche Figure B.5; une gouttelette tombant sur une goutte plus grosse posée au fond d'une cuve, avec un champ parallèle à la direction de chute, présenté à droite Figure B.5.

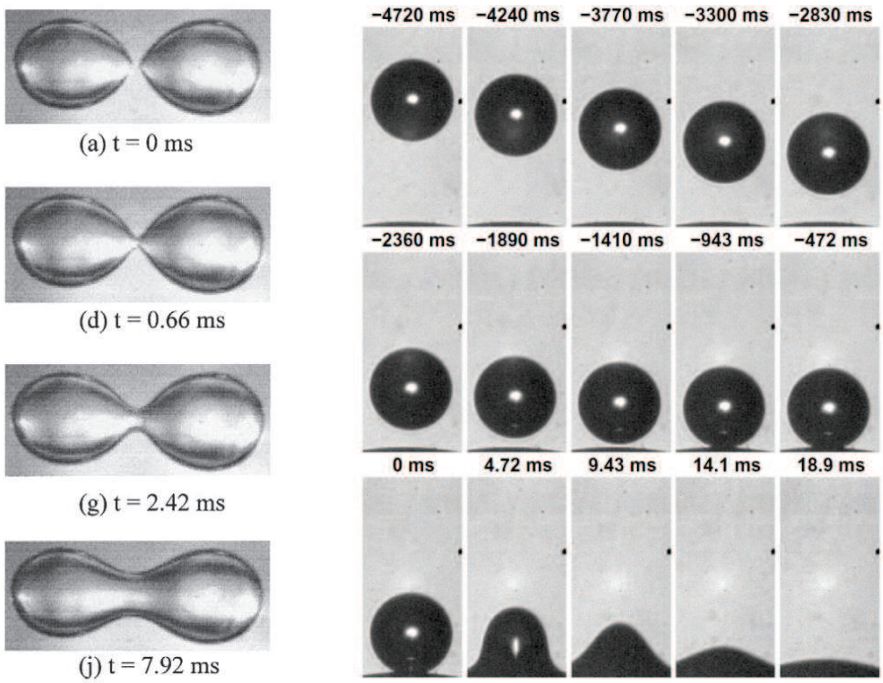

Fig B.5. A gauche, deux gouttes tombant parallèlement avec un champ électrique appliqué perpendiculairement à la direction de chute (Eow & Ghadiri, 2003); à droite, une goutte tombant sur une grosse goutte posée au fond de la cuve (Helleso et al, 2015).

Figure B.5, à gauche les expériences sont réalisée dans une huile modèle avec des gouttes de diamètre D≈2mm, le champ électrique E vaut 1.0kV/cm ; à droite les expériences sont faite dans le pétrole brut avec visualisation par caméra infrarouge, le diamètre de la goutte tombante est D=0.7mm et le diamètre de la goutte sur le fond D=4mm, le champ électrique vaut E=0.25kV/cm. Les inconvénients des expériences est que la taille des gouttes est très grande, ce qui n'est pas en accord

avec la composition réelle des émulsions. En effets les tailles de gouttelettes d'eau observée dans les émulsions sont de l'ordre quelques microns à quelques dizaines de micron (Aichele et al, 2007 ; Less & Vilagines 2013 ; Rodionova et al, 2014). De plus pour la configuration de deux gouttes tombant parallèlement, le problème est complètement tridimensionnel parce que le champ électrique est perpendiculaire à leur direction de chute. Cela alourdit beaucoup les calculs qui devraient être fait pour développer des modèles de simulation. Dans cette thèse on cherche donc à diminuer la taille des gouttelettes étudiées expérimentalement, passant de diamètres de l'ordre du millimètre à quelques dizaine de microns. On va chercher à générer et suivre des paires de gouttelettes tombant dans une huile modèle stagnant dans une cuve, alignées avec le champ électrique et la gravité. Durant la thèse on génèrera ainsi des bases de données expérimentales qui pourront ainsi être comparées avec des modèles numériques en géométrie axisymétrique.

B.2 Montage expérimental et mesures

La figure B.6 montre la cellule expérimentale. La cellule est remplie d'huile Marcol 52 ou Primol 352 suivant les expériences. Oon ajoute parfois un surfactant (Span 80) pour modifier la tension interfaciale. Au fond de la cellule l'électrode est reliée à la haute tension. L'aiguille plongée dans l'huile est reliée à la masse. Cette aiguille est remplit de l'eau salée (solution contenant 3.5 %(en poids) de NaCl).

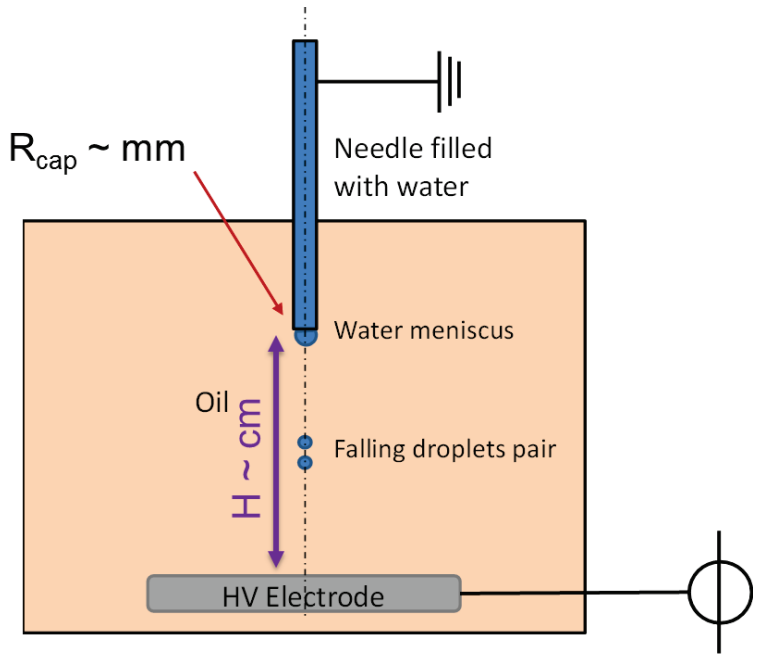

Fig B.6. Schéma de la cellule d'essai.

L'ordre de grandeur de la distance H entre l'aiguille et l'électrode est de l'ordre du cm et le rayon interieur R_{cap} de l'aiguille de l'ordre du mm. La tension appliquée sur l'électrode est de l'ordre du kV et les gouttes injectées ont des diamètres compris entre environ 20 et 200µm. Cette cellule est relié à l'ensemble des appareils présentés Figure B.7.

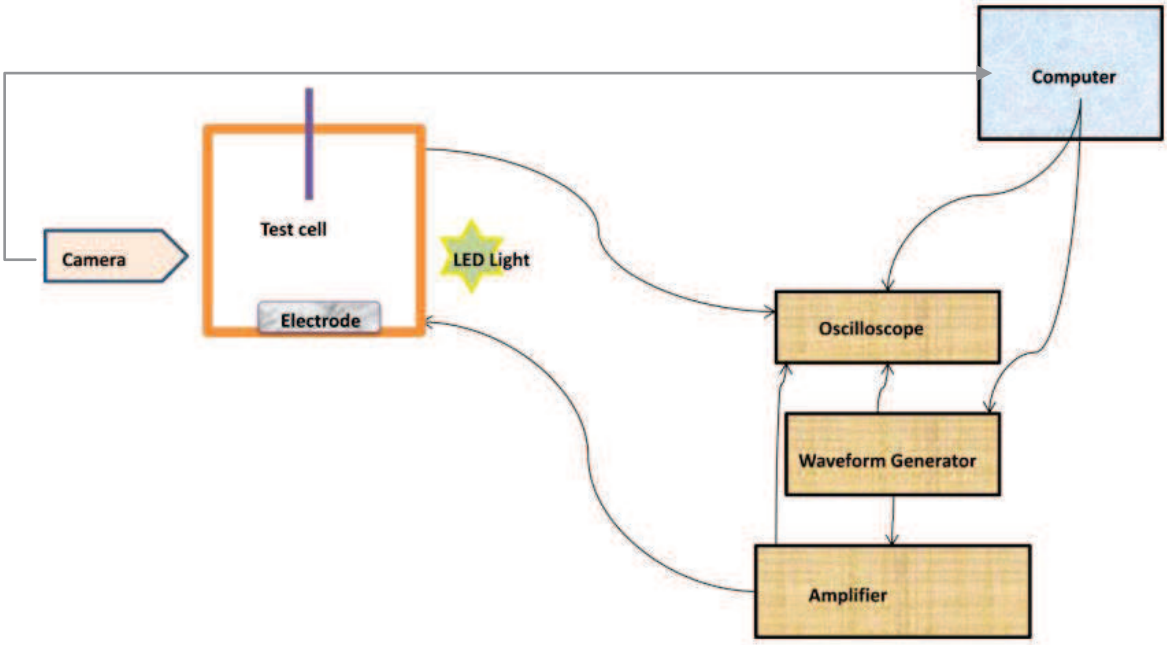

Fig B.7. Connexion des différents appareils électriques.

La visualisation du comportement est réalisée simultanément par plusieurs caméras. Un microordinateur génère les différents signaux trigger nécessaire au générateur d'impulsion et enregistre les images. Le générateur d'impulsion va créer des signaux de formes déterminées et les envoie à l'amplificateur. L'amplificateur va augmenter la tension électrique des signaux d'un facteur 2000 et l'appliquer à l'électrode plate de la cellule. Tous les signaux provenant des caméras, de l'amplificateur, de générateur d'impulsion et de l'ordinateur sont enregistrés par l'oscilloscope pour vérification du bon fonctionnement et de la synchronisation.

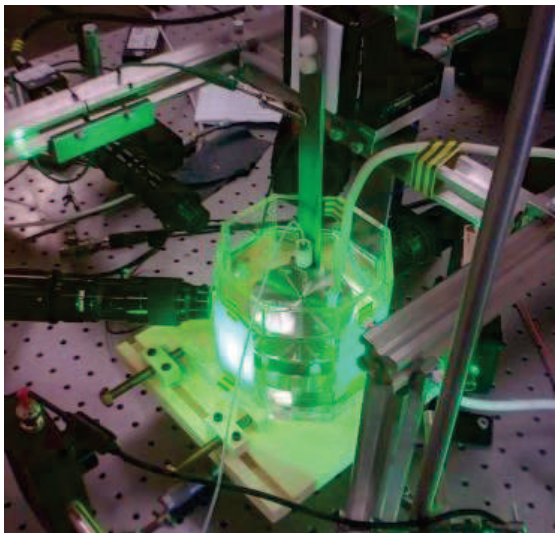

Fig B.8. Visualisation de la cellule d'essai.

La figure B.8 présente une photo de la cellule expérimentale. Elle permet de voir les caméras assurant différents angles de visualisation selon les axes de symétrie de la cellule octogonale.

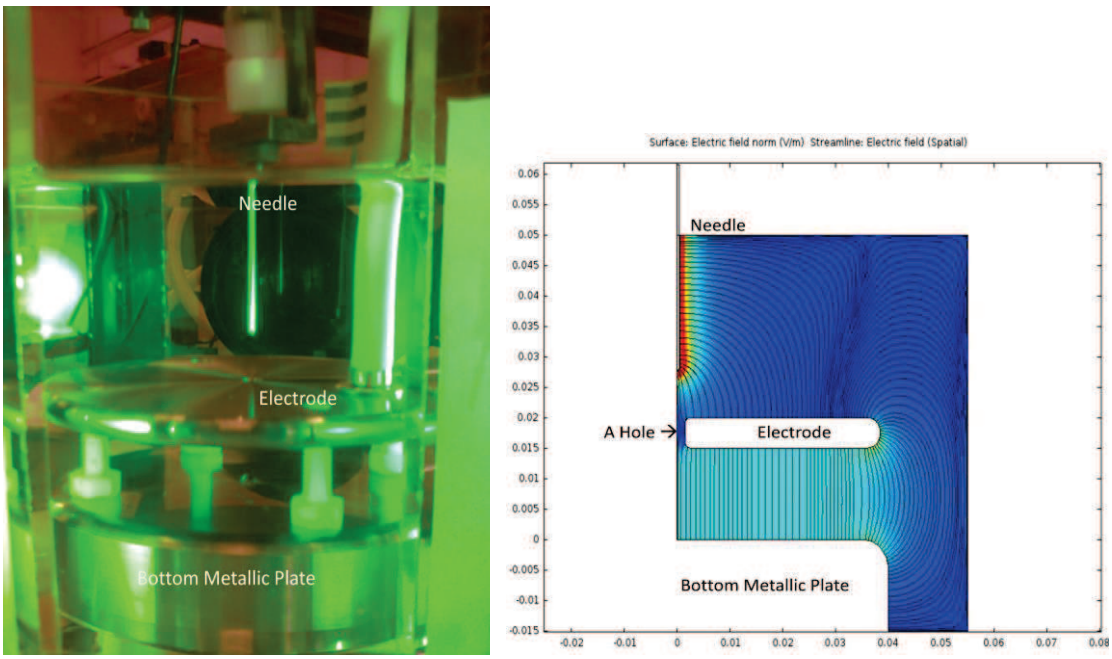

Fig B.9. Cellule d'électrocoalescence visualisé sous lumière verte générée par LED (gauche) et vue d'un demi plan méridien de la cellule (considérée comme cylindrique) tracé par COMSOL (droite). Dans ce montage, l'électrode, percée d'un petit trou en son centre, est à 1,5 cm du fond de la cellule. La haute tension est appliquée à l'électrode, avec la plaque métallique du fond de la cuve et l'aiguille reliées à la terre. La norme du champ électrique calculé est tracée en couleur.

La figure B.9 à droite présente le résultat d'un calcul de champ électrostatique en appliquant applique la haute tension sur l'électrode. On peut voir les lignes de champs dans la cellule. On s'intéresse principalement à trois domaines : le domaine autour de l'aiguille où le champ électrique est plus fort, pour effectuer des injections électrohydrodynamiques de gouttelettes ; le domaine entre l'électrode et l'aiguille où le champ électrique est plus uniforme, pour étudier l'interaction et l'électrocoalescence de deux gouttelettes ; le domaine entre l'électrode et la plaque métallique en du fond sera évoqué dans la conclusion de ce travail.

On a mesuré les caractéristiques des liquides utilisés, résumés Table B.1.

	T (˚C)	μ (mPa.s)	ρ (kg/m^3)	ε_r	Temps de relaxation électrique (s)	σ (mN/m) (after 2 mn)
3.5 wt% NaCl solution (taken from document)	20	1.070	1029.1	--	--	--
	25	0.955	1027.6			
0.001 wt% Span80 in Marcol 52	21 ± 1	11.43 ± 3.8 %	828.7 ± 0.03%	2.1	1000 – 5000	42 ± 6.7 %
	23 ± 1	10.62 ± 3.5 %	828.0 ± 0.03%			
	25 ± 1	9.93 ± 3.2 %	827.3 ± 0.03%			
	27 ± 1	9.33 ± 2.9 %	826.7 ± 0.03%			

Table B.1. Les différentes caractéristiques des liquides mesurés.

Les valeurs de l'eau salée sont tirées de documents, celles pour les huiles mesurées. On constate qu'avec l'augmentation de la température, la viscosité et la masse volumique de l'huile diminuent. La permittivité relative de l'huile et de 2.1 et le temps de relaxation électrique est compris entre 1000 et 5000 s. La tension interfaciale entre l'huile Marcol 52 avec 0.001wt% de surfactant Span80 et l'eau salée est de 42mN/m, avec une incertitude de 6.7%. La mesure de la tension interfaciale est effectuée par la méthode de la goutte pendante comme présenté figure B.10.

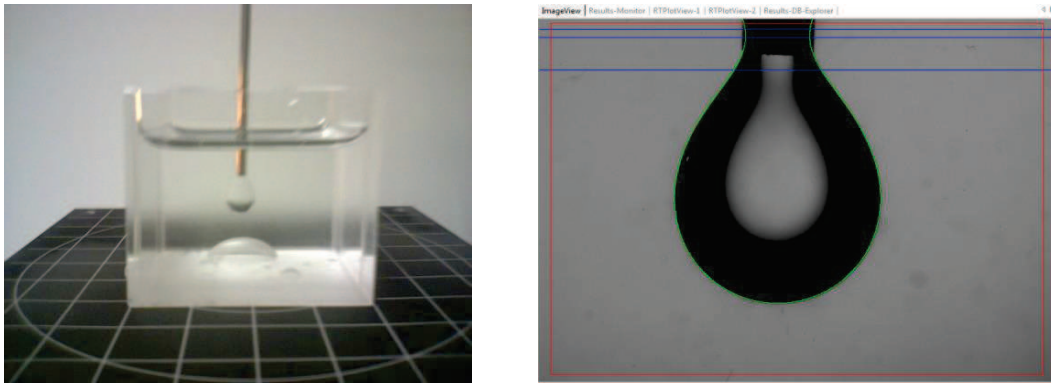

Fig B.10. Méthode de la goutte pendante pour mesurer la tension interfaciale. A gauche, une photo prise de l'expérience. A droite, une image acquise sur l'écran avec l'extraction du contour de la goutte d'eau.

Sur la figure B.10 à gauche on montre une aiguille plongée dans l'huile, au bout de laquelle une goutte est formée. A droite on montre l'image acquise par une caméra CMOS. En mesurant la forme de la goutte, on peut déduire la tension interfaciale. On a regroupé les mesures réalisées sur la figure B.11.

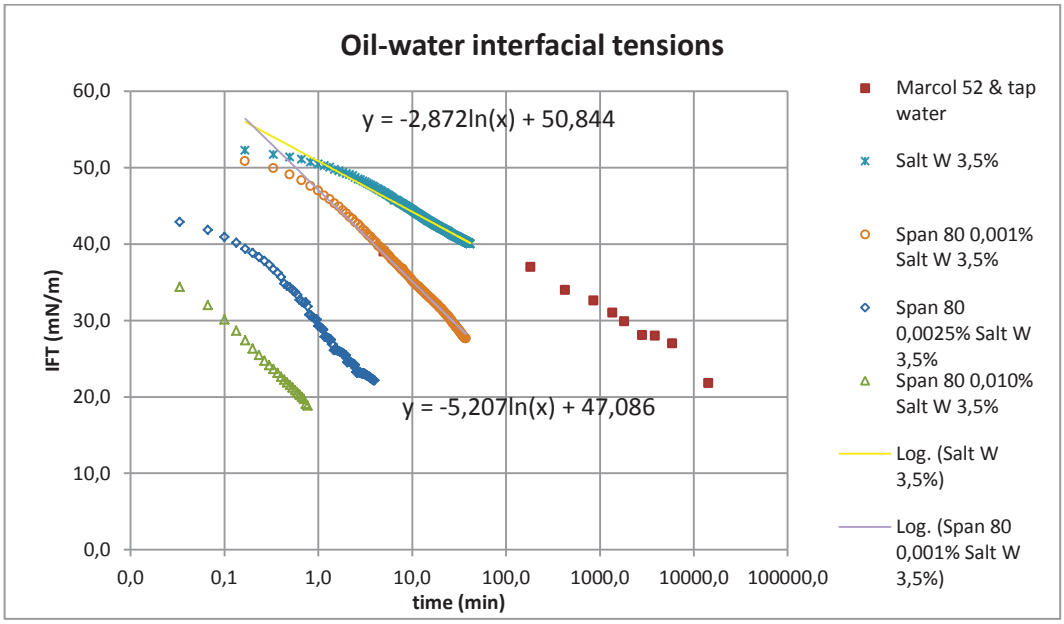

Fig B.11. Evolutions en fonction du temps des tensions interfaciale eau/huile pour différentes proportions de surfactant.

La figure B.11 illustre que l'augmentation de la proportion de surfactant Span80 ajouté à l'huile se traduit par une diminution plus rapide de la tension interfaciale. La fin des courbes correspond au détachement de la goutte pendante de l'aiguille. Ici on s'intéresse seulement à la courbe a) où il n'y a pas de surfactant, et b) où on a ajouté 0.001wt% de Span80. Les deux courbes peuvent être lissées par des équations polynomiales. Pour avoir une valeur de la tension interfaciale au cours de nos

expériences d'injection EHD de gouttelette, il faudra évaluer l'age de l'interface eau/huile pour exploiter nos mesures reportées Figure B.11. On estime pour cela que l'intervalle de temps entre deux injections que nous avons réalisé lors des expériences qui seront décrites ensuite est compris entre 1 et 5 mn. A chaque injection d'une gouttelette on estime également que les surfactants sont entièrement drainés du ménisque. On estime ainsi la tension interfaciale à un temps de 3mn ± 2mn, ce qui donne : σ_a=48mN/m±3.4% ; σ_b=42mN/m±6.7%.

B.3 Injection électrohydrodynamique (EHD)

B.3.1 Injection d'une goutte

La configuration de l'injection d'une seule goutte est présentée par la figure B.12. En appliquant une tension électrique sur l'électrode en bas de la cellule, il y aura des charges induites sur la surface du ménisque. La force électrostatique va déformer le ménisque comme l'illustre la forme pointillée sur la figure B.12. Ensuite avec l'inertie, une goutte peut être détachée du bout de l'aiguille.

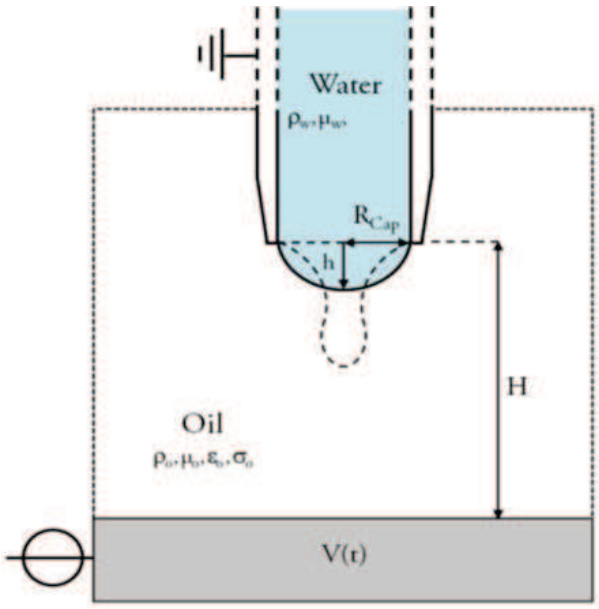

Fig B.12. Schéma de l'injection d'une seule goutte (Raisin, 2011).

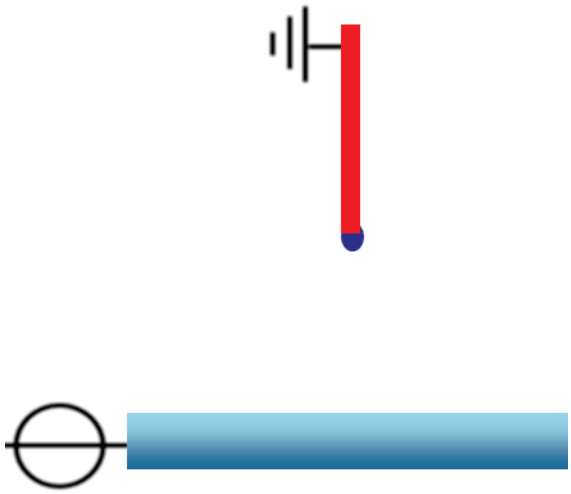

Fig B.13. Schéma de la cellule d'essai.

Le schéma de la cellule d'essai est de type pointe-plan, comme monté par la figure B.13. Pour déformer le ménisque, la pression électrostatique doit être supérieure à la pression capillaire $p_E > p_{cap}$. Ce qui peut être réécrit comme :

$$\frac{1}{2}\epsilon_r\epsilon_0 E^2 > \frac{2\sigma}{R_{cap}} \tag{B.1}$$

En assumant que le ménisque est d'une forme demi-sphérique $h \sim R_{cap}$, on obtient :

$$E_{Max} = \frac{2V}{R_{cap} ln\left(\frac{4H}{R_{cap}}\right)} \tag{B.2}$$

E_{Max} est le champ électrique maximum. Et on en déduit la tension minimum à appliquer sur l'électrode :

$$V_{low} = \sqrt{\frac{\sigma R_{cap}}{\varepsilon_r \varepsilon_0}} ln\left(\frac{4H}{R_{cap}}\right) \tag{B.3}$$

Avec les valeurs H=15mm, R_{cap}=0.23mm, ε_r=2.1, σ=48mN/m, on peut calculer que V_{low}=4kV.

On applique cette tension sur une durée finie de l'ordre de temps capillaire t_{cap} qui désigne le temps caractéristique de la dynamique de l'interface entre les liquides.

$$t_{cap} = \sqrt{\frac{\rho_w R_{cap}^3}{\sigma}} \tag{B.4}$$

Avec l'application numérique, t_{cap}=0.5ms.

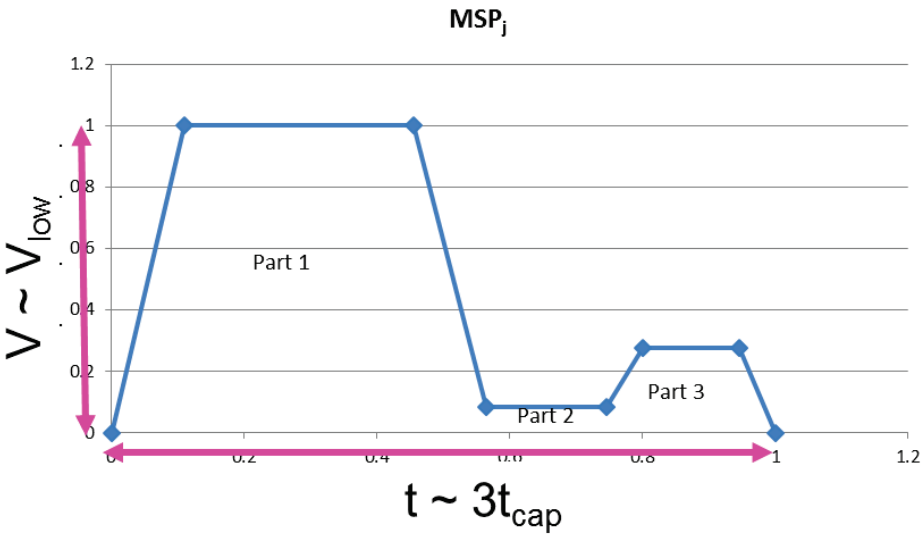

Fig B.14. Forme d'impulsion utilisée (Raisin, 2011).

La forme d'impulsion utilisée est présentée Figure B.14. Il y a trois plateaux successif, et l'amplitude maximale est de l'ordre de V_{low} avec une durée totale de l'ordre de $3t_{cap}$.

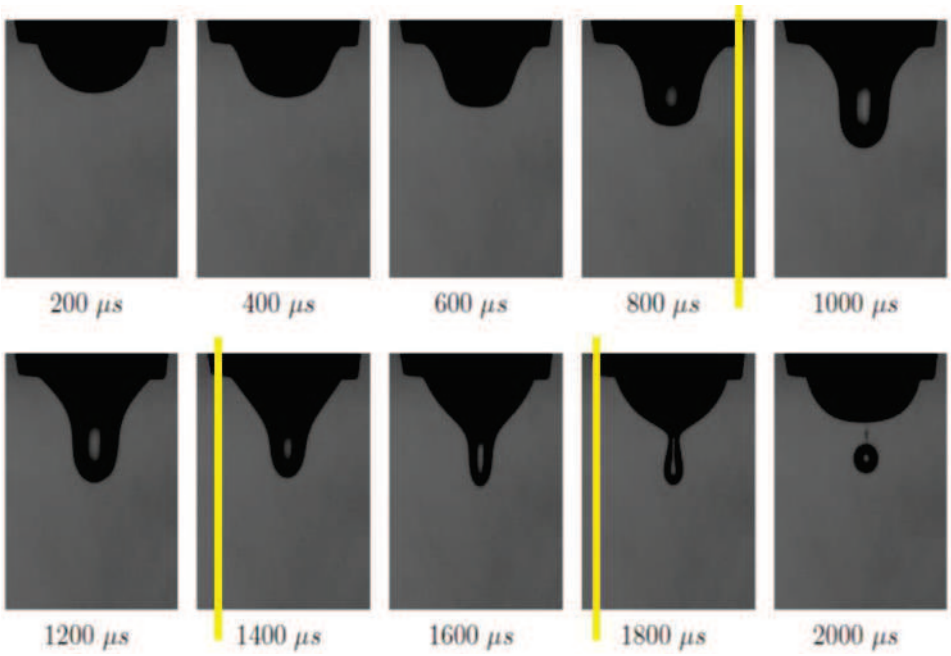

Fig B.15. Procès d'injection électrohydrodynamique (Raisin, 2011).

Le processus d'injection d'une goutte est illustré par la figure B.15 (Raisin, 2011). Le premier plateau sert à déformer sous l'effet de la pression électrostatique le ménisque, qui prend une forme plus carrée. Durant l'application du second plateau, de faible tension, le ménisque continue sa déformation sous l'effet de l'inertie et la force capillaire. Le troisième plateau sert à redonner une impulsion sur l'apex du ménisque et génère l'élongation en pointe. Il est important que la fin de l'impulsion ait lieu avant la coupure du ligament du ménisque pour s'assurer que les charges induites par l'électrostatique aient un temps suffisant pour se relaxer et pour permettre de former une goutte électriquement neutre (Raisin, 2011). En réalité on a observé que les gouttes étaient malgré tout légèrement chargées à cause de l'influence des charges injectées dans l'huile lors de l'applications des tensions élevées.

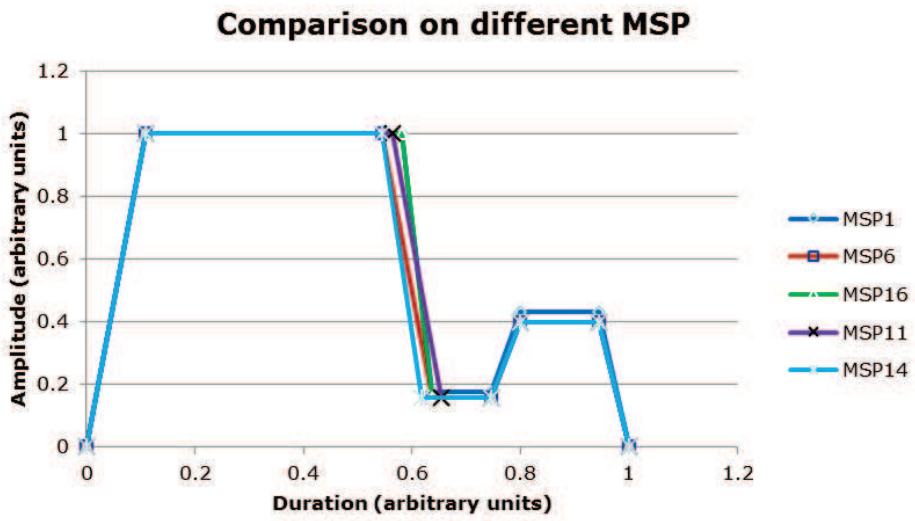

Fig B.16. Les différentes formes d'impulsions testées.

Par rapport aux travaux précédents (PHD de Raisin, 2011), le changement d'huile a rendu nécessaire des améliorations de la forme de l'impulsion EHD, notamment en raison de grandes différences de tension interfaciale. On a testé les différentes formes d'impulsion illustrées Figure B.16. On a constaté qu'une petite modification sur la forme d'impulsion peut entrainer une grande différence d'injection.

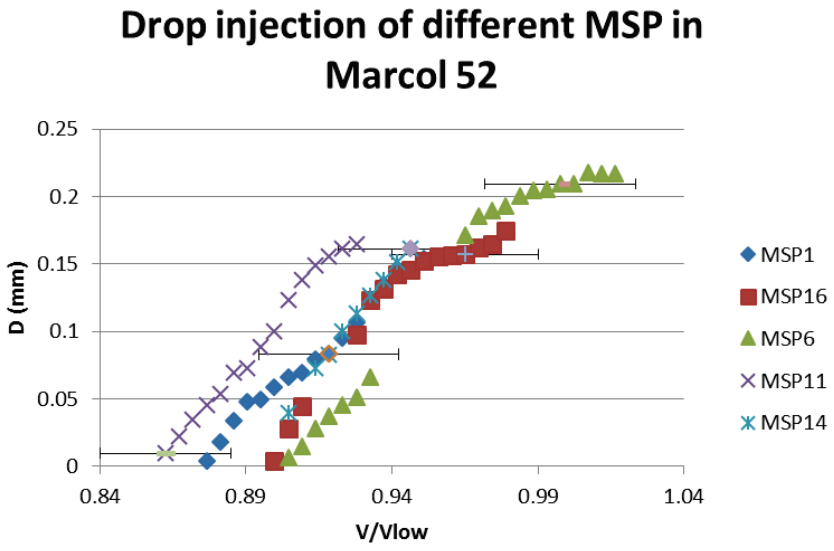

Fig B.17. Les différentes injections par les différentes formes d'impulsion.

Les incertitudes tracées Figure B.17 sont reliées aux incertitudes sur la tension interfaciale. Les courbes sont dans la gamme d'incertitude. Mais on a observé les irrégularités, comme pour la courbe

MSP6 pour laquelle il n'y a pas de goutte de taille intermédiaire extraite. C'est pourquoi dans ce travail une attention particulière a été portée dans un premier temps à améliorer les injections des gouttelettes.

Une fois les gouttes extraites, il faut mesurer précisément leur diamètre. Il y a deux méthodes. La première consiste à mesurer les diamètres par visualisation, comme illustré Figure B.18. Les valeurs de gris sur la goutte définissent le bord de goutte. Le bord de goutte est non lissé, donc l'incertitude est estimée à ± 1 pixel. Pour la goutte sur la figure, l'incertitude est ainsi de 5%. Mais pour cette méthode de visualisation, une erreur systématique est possible sur la calibration et le réglage du plan focal.

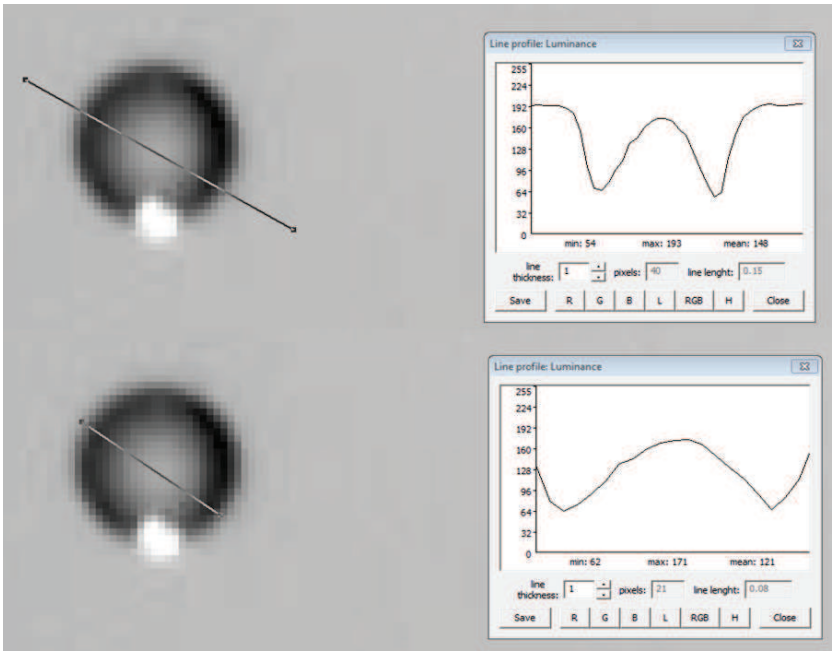

Fig B.18. Mesure des diamètres de goutte par la méthode de visualisation.

La seconde méthode pour obtenir le diamètre est basée sur le calcul. Puisqu'on est en régime de Reynolds très faible (Re << 1), l'écoulement est laminaire. De plus les surfactants présents sur la goutte tendent à bloquer l'écoulement à l'interface (par un effet Marangoni), si bien que les gouttes peuvent être considérées comme des particules solides. On est dans un régime de Stokes ce qui permet de relier la force de frottement à la vitesse de chute.

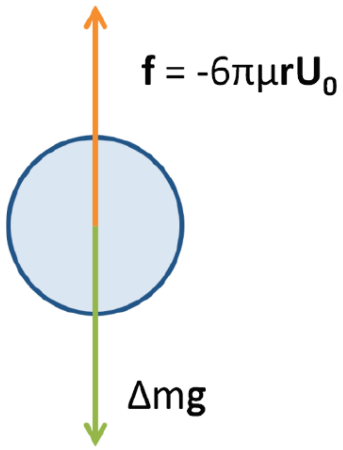

Fig B.19. La goutte est en état d'équilibre.

A l'équilibre, la force de frottement égale à la différence du poids.

$$-\Delta m\boldsymbol{g} + 6\pi\mu_o r\boldsymbol{U}_0 = 0 \tag{B.5}$$

On peut en déduire le diamètre à partir de la vitesse de chute.

$$D = 6\sqrt{\frac{\mu_o U_0}{2(\rho_w - \rho_o)g}} \tag{B.6}$$

Et on peut calculer l'incertitude sur le diamètre.

$$\frac{\delta D}{D} = \frac{1}{2}\sqrt{\left(\frac{\delta\mu_o}{\mu_o}\right)^2 + \left(\frac{\delta U_0}{U_0}\right)^2 + \left(\frac{\delta(\rho_w - \rho_o)}{\rho_w - \rho_o}\right)^2} \tag{B.7}$$

Avec δU=δx/δt.

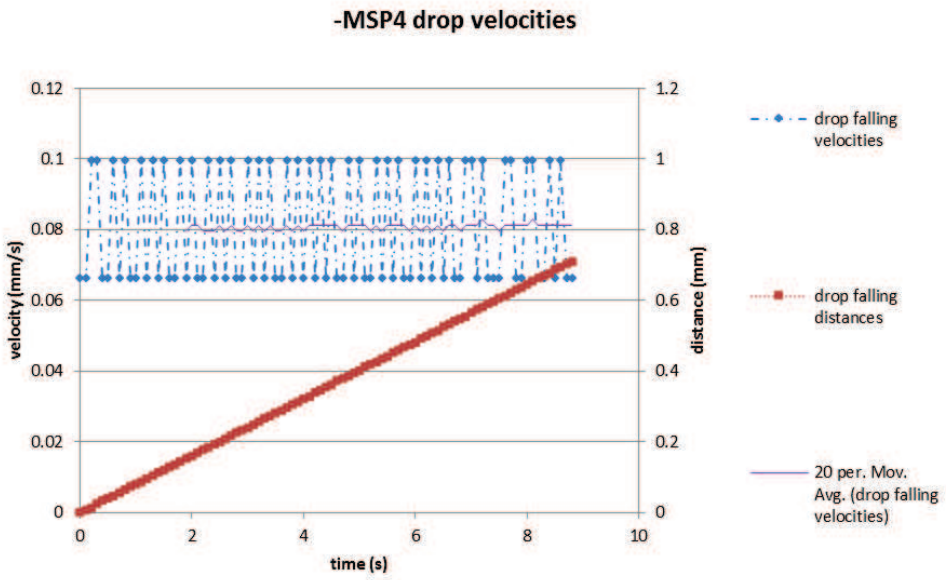

Fig B.20. Chute de goutte à l'équilibre dans l'huile modèle.

On utilise le logiciel Spotlight pour suivre le déplacement de la goutte. Sur Spotlight on a δx=3.3µm (correspondant à 1 pixel). L'analyse de la chute sur une durée courte de 0.1s, conduit à une incertitude sur la vitesse δU=33µm/s. Pour une durée de 1s, l'incertitude diminue à δU=3.3µm/s. et pour une durée de 2s δU=1.65µm/s. Dans le cas de la figure B.20, on a moyenné sur 2 secondes. En comparant avec le diamètre de visualisation, on a : δD_{cal} = 2% pour δD_{visu} = 3.5% et on s'affranchit des erreurs systématiques possibles de la première méthode.

Contrairement à ce qui était supposé on constate que les gouttelettes ne sont pas électriquement neutres. C'est pourquoi on applique un champ continu après l'injection de la goutte pour étudier sa charge électrique. On s'intéresse sur la zone entre l'aiguille et l'électrode comme sur la figure B.21.

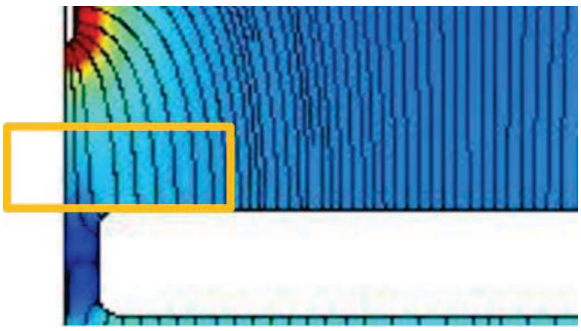

Fig B.21. Repérage de la région entre l'électrode et l'aiguille.

Dans cette région pour tension de 1kV appliqué sur l'électrode, E(y) varie de 40V/m à 60V/m. Pour une goutte à l'équilibre sous champ électrique, on peut calculer sa charge.

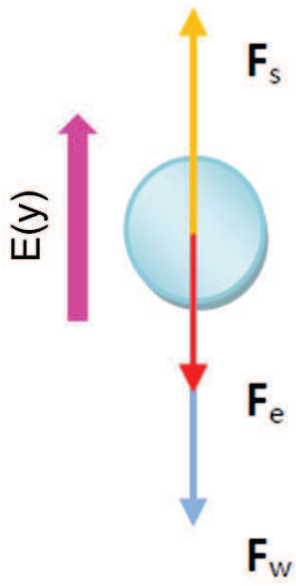

Fig B.22. Chute de goutte à l'équilibre sous champ électrique.

On a à présent équilibre entre le poids F_w, la force de frottement F_s et la force électrostatique F_e. De plus :

$$\boldsymbol{F}_w = \Delta m\boldsymbol{g} = 6\pi\mu_o r\boldsymbol{U}_0 \tag{B.8}$$

Avec $\mathbf{U}_0$ la vitesse terminale sans champ.

$$\boldsymbol{F}_s = -6\pi\mu_o r\boldsymbol{U} \tag{B.9}$$

Avec U la vitesse terminale avec le champ.

$$\boldsymbol{F}_e = q\boldsymbol{E} \tag{B.10}$$

Le champ n'étant pas exactement uniforme la force diélectrophorétique F_{dep} doit aussi être considérée.

$$\boldsymbol{F}_{dep} = \frac{\pi}{4}\varepsilon_o D^3 K\overrightarrow{grad}\boldsymbol{E}^2 \tag{B.11}$$

On vérifie ainsi quelle reste négligeable (moins de 4% de la force F_e). Donc on a :

$$\boldsymbol{F}_w + \boldsymbol{F}_e + \boldsymbol{F}_s = 0 \tag{B.12}$$

$$\boldsymbol{F}_e = -\Delta m\boldsymbol{g} \pm 6\pi\mu_o r\boldsymbol{U} \tag{B.13}$$

On peut en déduire la charge q :

$$q = \frac{6\pi\mu_o r(U - U_0)}{E} \tag{B.14}$$

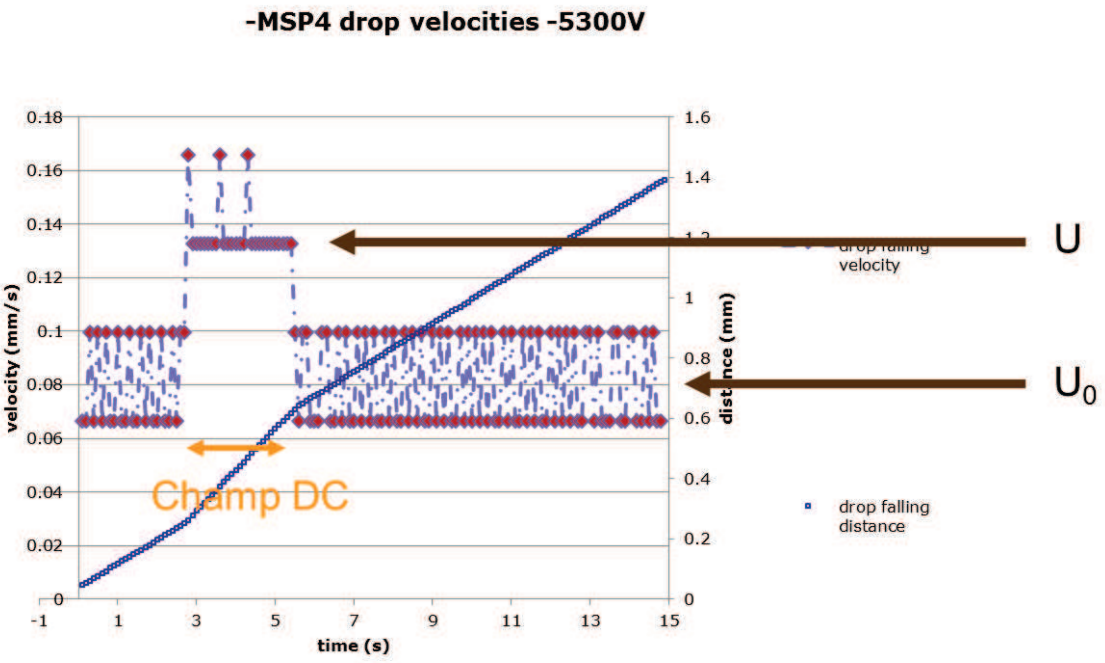

Fig B.23. Chute de goutte à l'équilibre sous le champ électrique.

On peut voir sur l'exemple de la Figure B.23 l'augmentation de vitesse correspondant au moment d'application du champ électrique. A la fin de l'application du champ, la goutte retrouve sa vitesse de chute initiale. Dans ce cas la charge déduite est q=-0.008 pC.

On peut calculer l'incertitude sur la charge de goutte.

$$\frac{\delta q}{q} = \sqrt{\left(\frac{\delta \mu_o}{\mu_o}\right)^2 + \left(\frac{\delta D}{D}\right)^2 + \left(\frac{\delta (U - U_0)}{U - U_0}\right)^2 + \left(\frac{\delta E}{E}\right)^2} \quad \text{(B.15)}$$

On peut réécrire le terme d'incertitude sur le diamètre.

$$\frac{\delta q}{q} = \sqrt{\left(\frac{\delta \mu_o}{\mu_o}\right)^2 + \frac{1}{4}\left(\left(\frac{\delta \mu_o}{\mu_o}\right)^2 + \left(\frac{\delta U_0}{U_0}\right)^2 + \left(\frac{\delta (\rho_w - \rho_o)}{\rho_w - \rho_o}\right)^2\right) + 2\left(\frac{\delta U_0}{U - U_0}\right)^2 + \left(\frac{\delta E}{E}\right)^2} \quad \text{(B.16)}$$

En recombiner les différents termes et négligeant le terme sur la différence de masse volumique, on a :

$$\frac{\delta q}{q} = \sqrt{\frac{5}{4}\left(\frac{\delta \mu_o}{\mu_o}\right)^2 + \frac{1}{4}\left(\frac{\delta U_0}{U_0}\right)^2 + 2\left(\frac{\delta U_0}{U - U_0}\right)^2 + \left(\frac{\delta E}{E}\right)^2} \quad \text{(B.17)}$$

On note que si le changement de vitesse de chute n'est pas remarquable $U \approx U_0$, le terme sur l'incertitude de vitesse diverge et cela entraine la divergence de δq/q.

Pour améliorer la linéarité des courbes diamètre/tension et contrôler la charge de la goutte on a testé plusieurs types d'impulsions nouvelles.

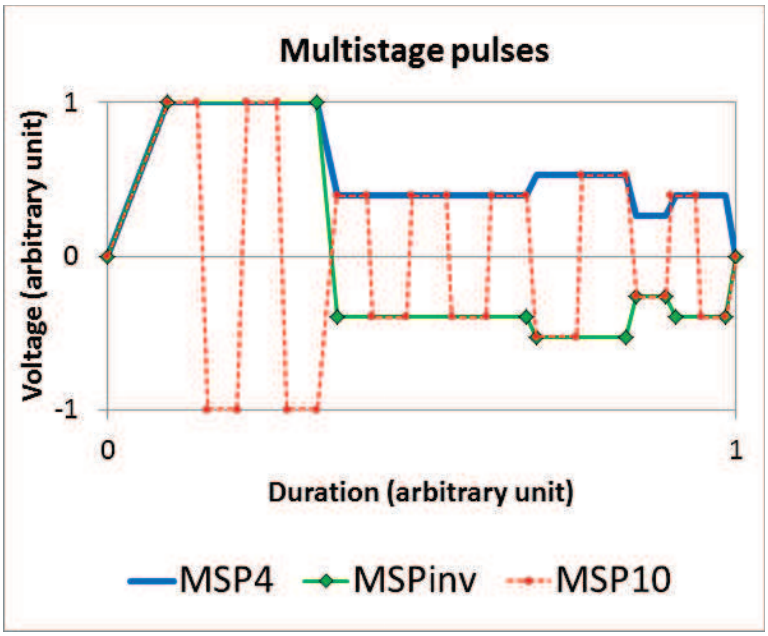

Fig B.24. Les améliorations des formes d'impulsions.

L'impulsion MSP4 a la même polarité, MSPinv a une polarité inversée et MSP10 a une polarité alternée.

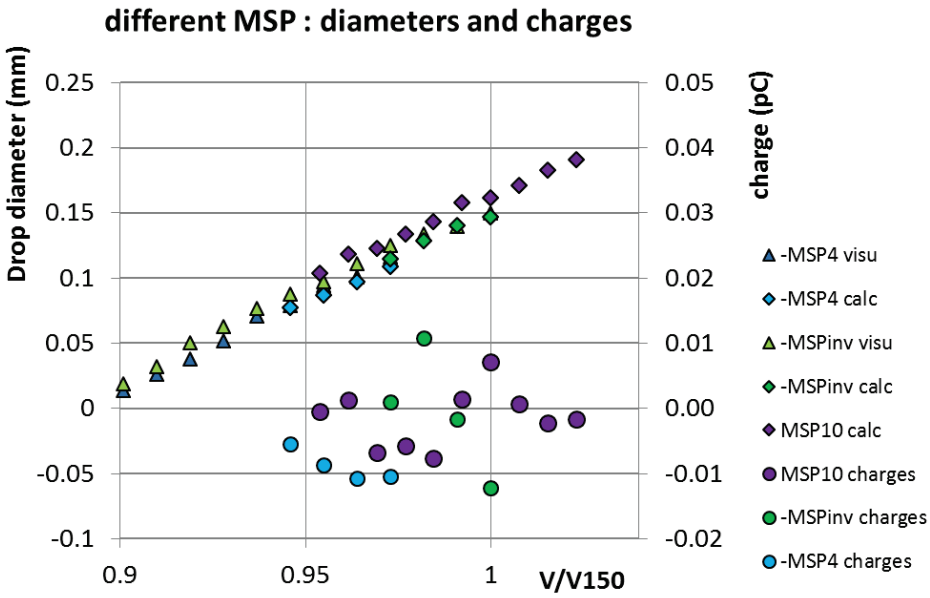

Fig B.25. Injection de goutte par les formes d'impulsion améliorée.

Avec les nouvelles formes d'impulsion, on voit que les diamètres de goutte augmentent linéairement avec la tension et il n'y a pas d'irrégularités dans les courbes. Les diamètres calculés sont en bon accord avec les diamètres de visualisation. Les gouttes injectées sont dans la gamme de 15-200µm et les charges des gouttes injectées restent dans un intervalle de ± 0.01 pC.

B.3.2 Injection d'une paire de goutte

On cherche à injecter une paire de goutte alignée avec le champ électrique comme montré Figure B.26. Puis en appliquant le champ électrique nous étudierons leur rapprochement et leur coalescence.

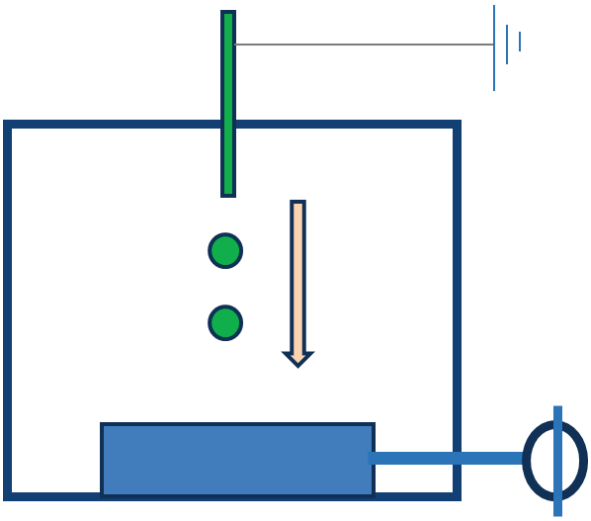

Fig B.26. Schéma de l'injection d'une paire de goutte.

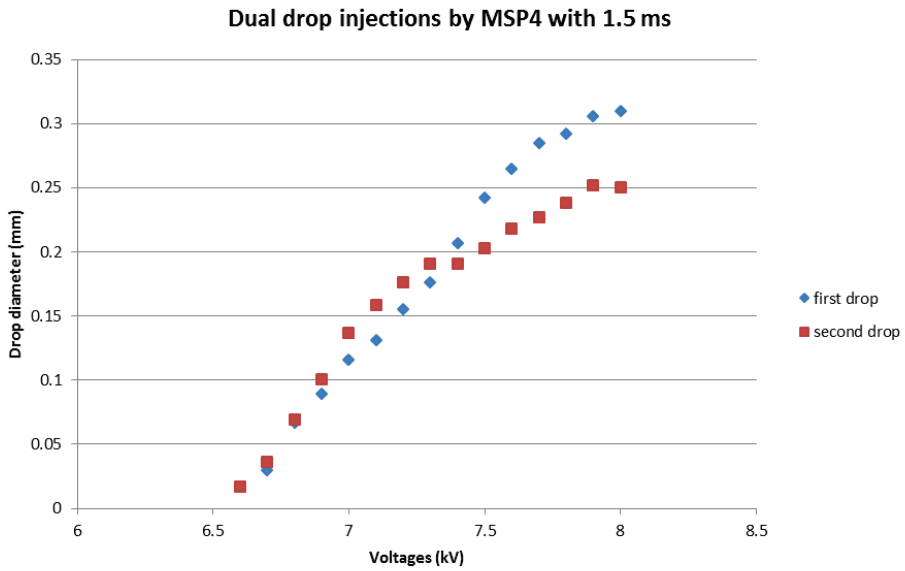

Fig B.27. Injection d'une paire de gouttes issues de la même aiguille.

On a injecté une paire de gouttes issue d'une même aiguille en appliquant deux fois la même tension, on voit que la taille des deux gouttes n'est pas identique, comme montré Figure B.27. On définit la hauteur du ménisque h, et le rayon de l'aiguille R_{cap} présenté en Fig B.28.

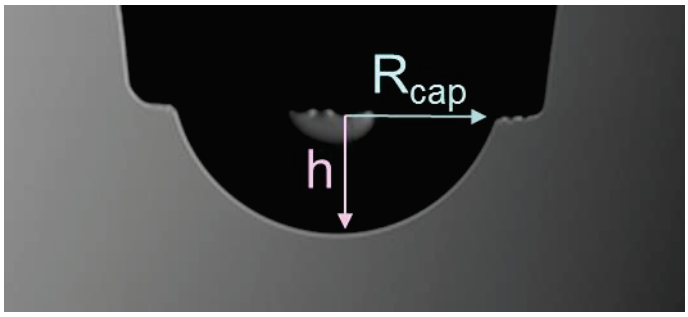

Fig B.28. Définition des paramètres du ménisque.

En fixant la tension appliquée et variant la hauteur du ménisque, on a obtenu différentes tailles de gouttes comme illustré Figure B.29.

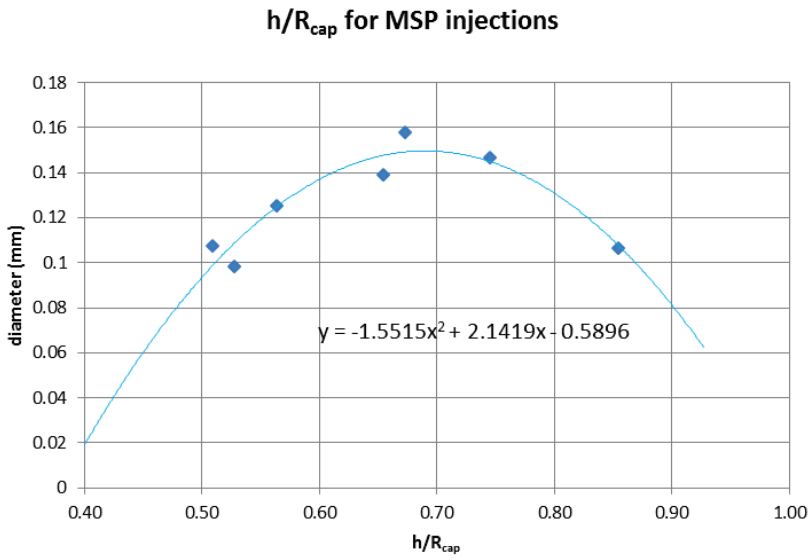

Fig B.29. Injection des gouttes en variant la hauteur du ménisque.

Cela permet d'expliquer que les deux gouttes injectées avec une impulsion identique ne sont pas de même taille : l'injection de la première goutte affecte la hauteur du ménisque qui n'a pas le temps de se rétablir à sa valeur initiale avant l'injection de la seconde

B.4 Chute d'une paire de goutte alignée avec le champ électrique

B.4.1 Chute d'une paire de goutte

Fig B.29. Chute d'une paire de goutte dans l'huile modèle. Deux gouttes tombent dans l'huile modèle verticalement, se rapprochent et coalescent sous l'effet du champ électrique.

Comme illustré Figure B.30, la chute de la première goutte va créer un champ de vitesse qui va influencer la vitesse de chute de la deuxième goutte. La chute de la deuxième goutte va réciproquement influencer la vitesse de chute de la première goutte. L'écoulement est laminaire à très faible Reynolds, il n'y a pas d'effet de sillage et l'influence est symétrique.

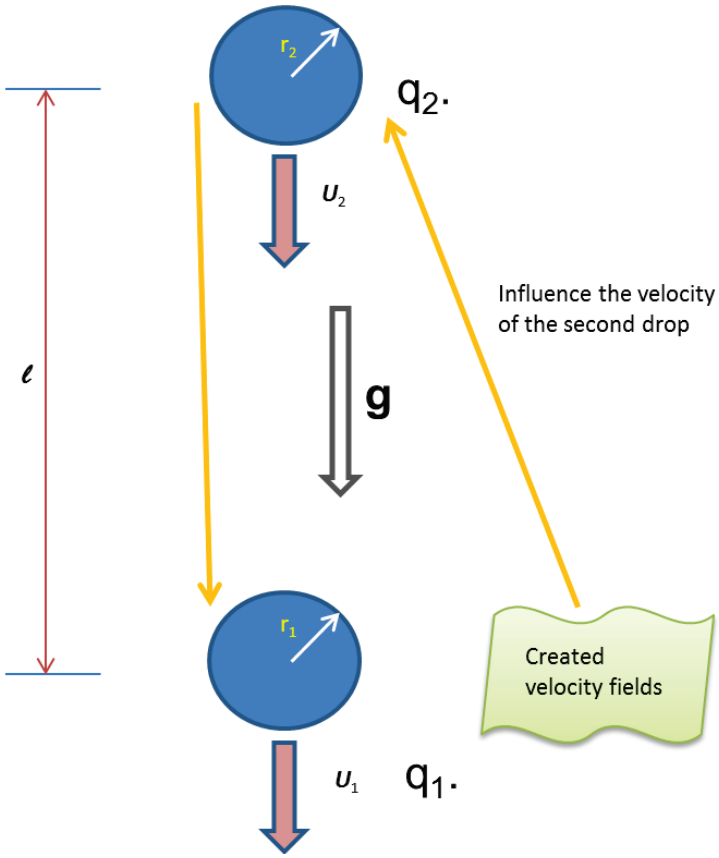

Fig B.30. Interaction hydrodynamique entre les deux gouttes.

L'expression des forces exercées sur les deux gouttes est donnée par (Batchelor, 1982) :

$$F_1 = 6\pi\mu_o \frac{r_1 X_{11} U_1 - \frac{2r_1 r_2}{r_1+r_2} X_{12} U_2}{X_{11}^2 - \frac{4r_1 r_2}{(r_1+r_2)^2} X_{12}^2} \tag{B.18}$$

$$F_2 = 6\pi\mu_o \frac{r_2 X_{11} U_2 - \frac{2r_1 r_2}{r_1+r_2} X_{12} U_1}{X_{11}^2 - \frac{4r_1 r_2}{(r_1+r_2)^2} X_{12}^2} \tag{B.19}$$

où X_{ij} sont les coefficients de mobilité, dépendant des paramètre sans dimension $\lambda = r_2/r_1$ et $s = 2\,l\,/(r_1+r_2)$. On peut en déduire les forces à partir des vitesses de chute U_1 et U_2, avec une influence non linéaire des tailles de gouttes r_1 et r_2.

Quand on applique le champ électrique, il y a aussi une interaction électrostatique. On peut utiliser pour la caractériser le modèle de Davis (1964).

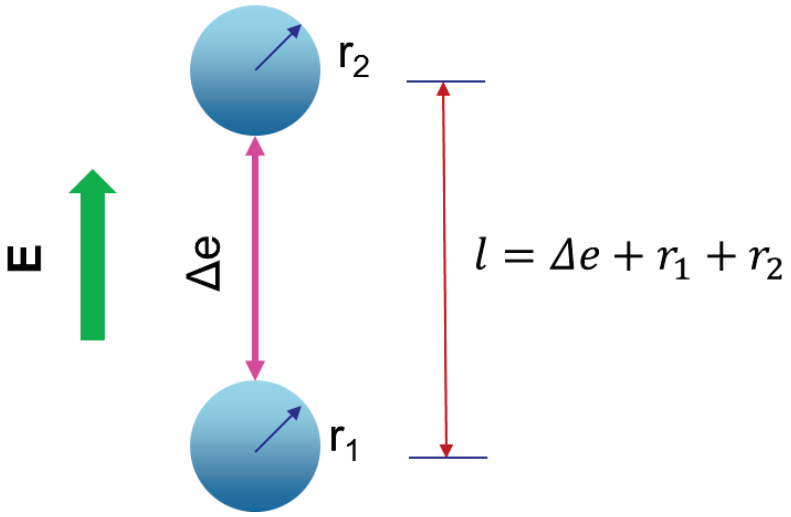

Fig B.31. Interaction des deux gouttes sous champ électrique.

L'expression de force est (Davis, 1964) :

$$F_z(1) = 4\pi\varepsilon r_1^2 E^2 F_1' + E(F_3' q_2 + F_4' q_1) + E q_1 + \frac{1}{4\pi\varepsilon r_1^2}(F_5' q_2^2 + F_6' q_1 q_2 + F_7' q_1^2) \quad \text{(B.20)}$$

Les termes F_j' résultent de séries mathématiques complexes, lentes à converger. Si $\Delta e > r_1+r_2$, on peut utiliser un modèle simplifié.

Le premier terme est simplifié par la force dipôle-dipôle :

$$F_{dd}(1) = 24\pi\varepsilon_0\varepsilon_r r_1^3 E^2 \left(\frac{r_2^3}{l^4}\right) \quad \text{(B.21)}$$

Le deuxième et le troisième terme sont simplifiés par la force électrique :

$$F_c(1) = E q_1 \quad \text{(B.22)}$$

Le quatrième terme est simplifié par la force électrostatique :

$$F_{es} = \frac{1}{4\pi\varepsilon_0\varepsilon_r}\frac{q_1 q_2}{l^2} \quad \text{(B.23)}$$

Ce modèle simplifié donne une erreur relative de moins de 5% par rapport au modèle complet pour $\Delta e > r_1+r_2$, comme montré Figure B.32.

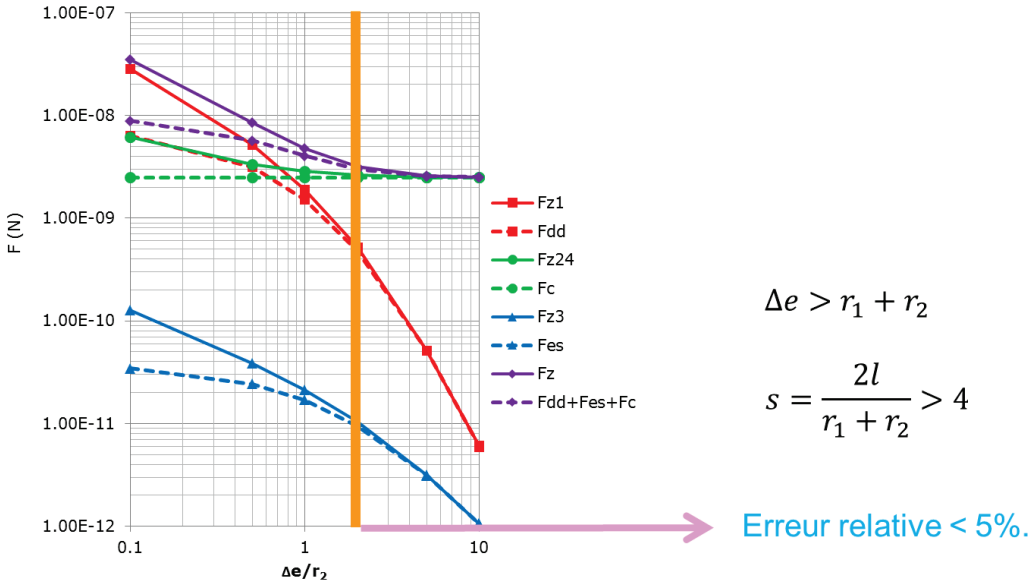

Fig B.32. Comparaison de la force issue de modèle simplifié et de modèle de Davis en fonction de la distance entre les deux gouttes.

On prend un exemple pour la première goutte, à l'état d'équilibre, on a la relation :

$$F_{dd}(1) + F_{es}(1) + F_{dep}(1) + F_1 + F_c(1) + F_w(1) = 0 \tag{B.24}$$

Sans champ électrique, le poids est en équilibre avec la force hydrodynamique F_1 :

$$F_1 \approx -F_w(1) = -g(\rho_w - \rho_o)\frac{4}{3}\pi r_1^3 \tag{B.25}$$

De cette équation on déduit une première valeur de r_1 et U_1. On procède de même pour la goutte 2. En prenant en compte les interactions hydrodynamiques, on corrige de façon itérative les rayons et les vitesses des deux gouttes. Dans un deuxième temps, avec le champ électrique, on a la relation :

$$F_1 = -F_w(1) - F_c(1) - F_{dep}(1) - F_{es}(1) - F_{dd}(1) \tag{B.26}$$

Avec les valeurs des rayons r et des vitesses associées U, on peut en déduire les charges q_1 et q_2.

B.4.2 Electrocoalescence

On utilise le logiciel Spotlight pour suivre les trajectoires des deux gouttes, comme montré Figure B.33.

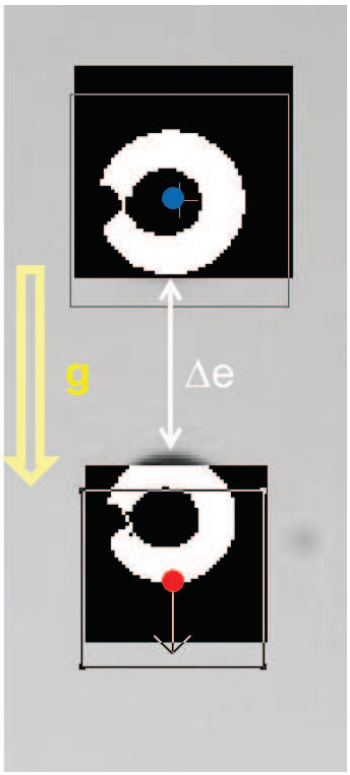

Fig B.33. Suivi des deux gouttes avec les aires d'intérêt définies dans Spotlight.

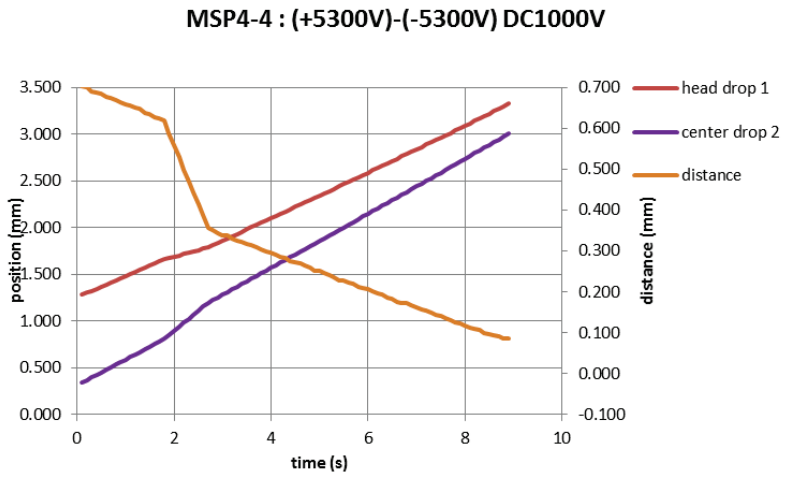

a)

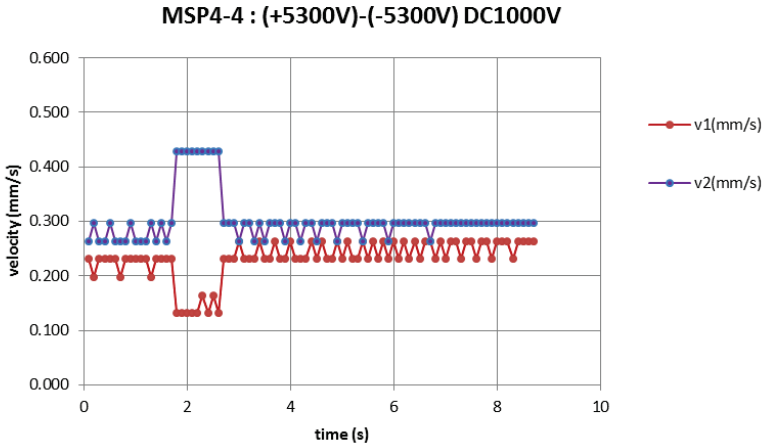

b)

Fig B.34. a) Position et distance des deux gouttes. b) vitesse de chute des deux gouttes.

La figure B.34 montre un exemple de relevé de la position et de la distance des deux gouttes, avec la modification des vitesses lors qu'on applique le champ électrique.

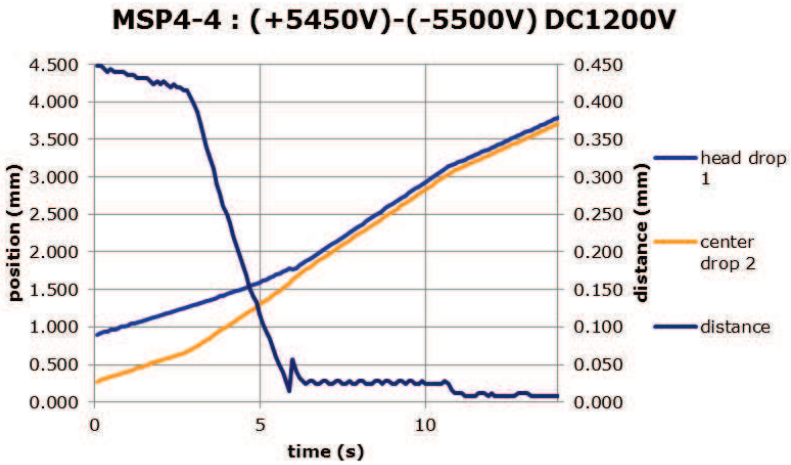

a)

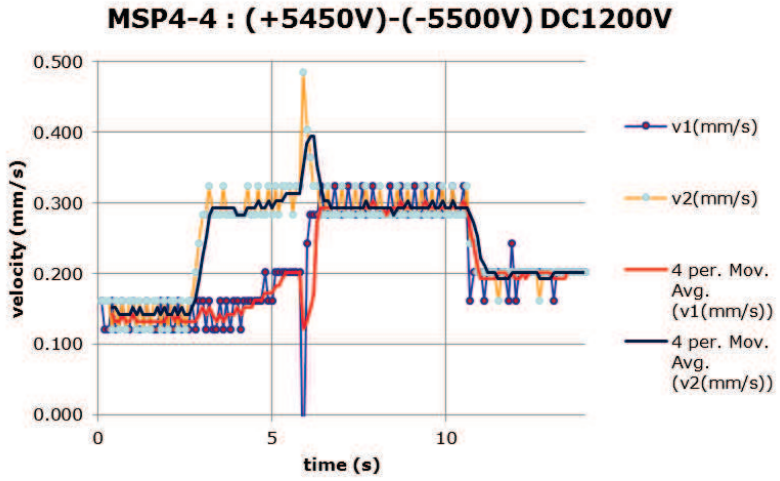

b)

Fig B.35. a) position et distance des deux gouttes. b) électrocoalescence des deux gouttes sous le champ DC.

Figure B.35, on montre les vitesses des deux gouttes sous champ électrique continu. Le premier et deuxième plateau montre que les gouttes changent de vitesse de chute lorsque le champ est appliqué. Les deux pics correspondent au moment de la coalescence. Puis la goutte unique générée par coalescence poursuit sa chute sous champ électrique. A la fin de l'application de ce champ la grosse goutte tombe librement. Les deux premières parties permettent de calculer les rayons et les charges des gouttes. La troisième et la quatrième partie donnent des informations sur la goutte coalescée.

Pour s'assurer de la conservation de la masse et de la charge électrique, on peut calculer les écarts de masse et de charge, définies comme suit :

$$\frac{\Delta m}{m} = \frac{m_3}{m_1 + m_2} - 1 = 1.9\% \tag{B.27}$$

$$\frac{\Delta q}{q} = \frac{|q_3 - (q_1 + q_2)|}{Max(|q_1|, |q_2|)} = 0.8\% \tag{B.28}$$

Pour l'électrocoalescence sous champ alternatif, on a la même allure des courbes. LA principale différence est que les modifications des vitesses de chute sous le champ alternatif, comme montré Figure B.36, est beaucoup moins marquée que celle obtenue sous champ continu (Figure B.35).

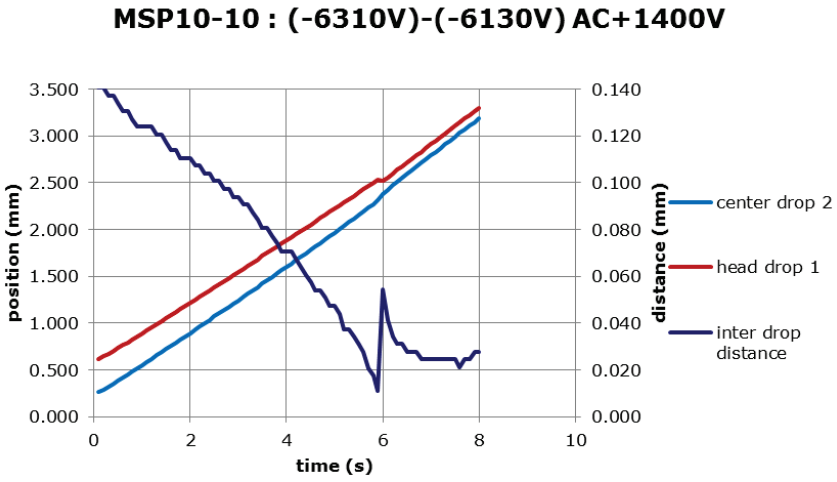

a)

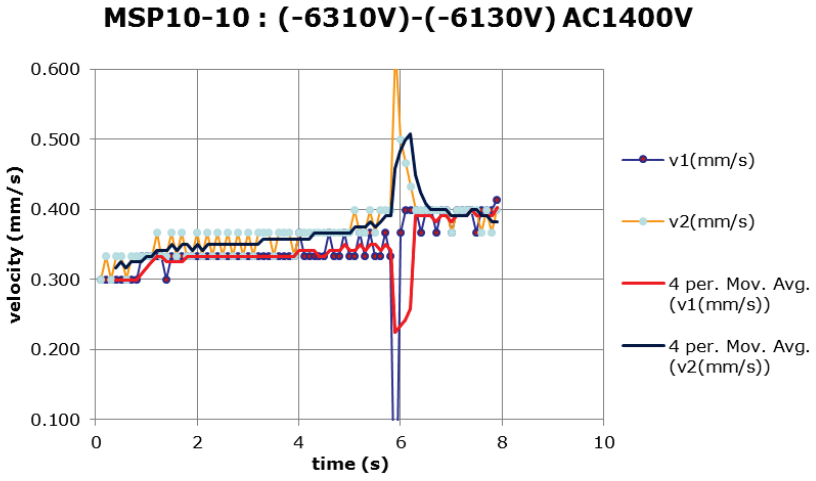

b)

Fig B.36. a) la position et la distance entre les deux gouttes. b) les vitesses de chute des deux gouttes.

On a combiné ensemble de nos résultats et analysé l'influence des différents paramètres.

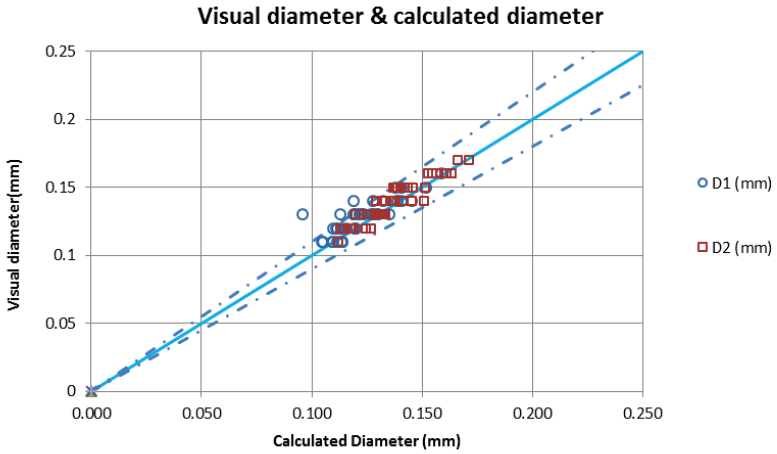

Fig B.37. Comparaison des diamètres déduits des visualisations et des diamètres calculés à partir des vitesses de chute.

Sur la figure B.37 on voit que les diamètres relevés par visualisation sont en bon accord avec les diamètres calculés à partir des vitesses de chutes. Il y a seulement quelques points pour lesquels l'accord est moins bon. Ces points correspondent à des cas où le paramètre de distance initiale s est inférieur à 4 et que le modèle d'interaction simplifié n'est pas valide.

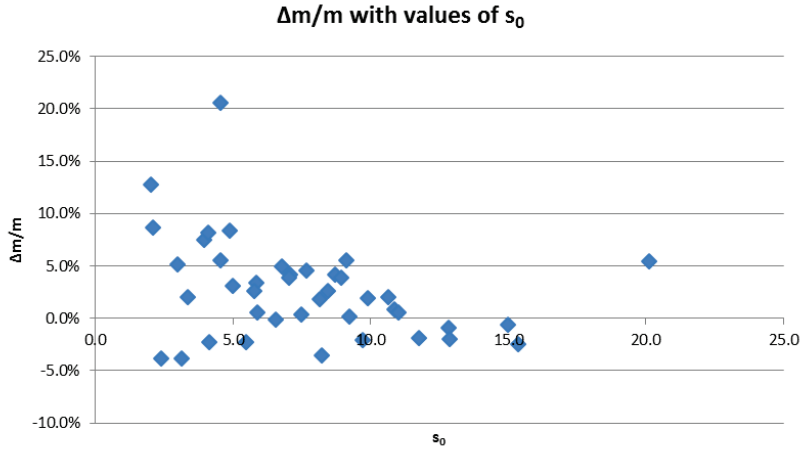

Fig B.38. Conservation de masse en fonction de s.

Sur la figure B.38 on voit que la conservation de masse est assurée avec une bonne précision pour les grandes valeurs de s, mais quand s est petit, la vérification de la conservation est moins bonne.

C’est pareil pour la conservation de charge, comme montré Figure B.39.

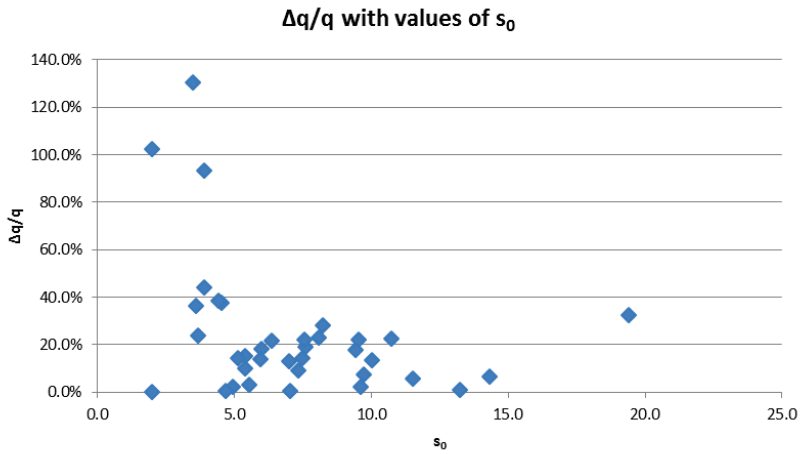

Fig B.39. Conservation de charge en fonction de s.

La conservation de charge dépend d’une part de la conservation de masse, d’autre part de l’incertitude sur le calcul de la charge. Là encore, les résultats sont meilleurs quand la distance de départ entre les deux gouttes est suffisamment grande.

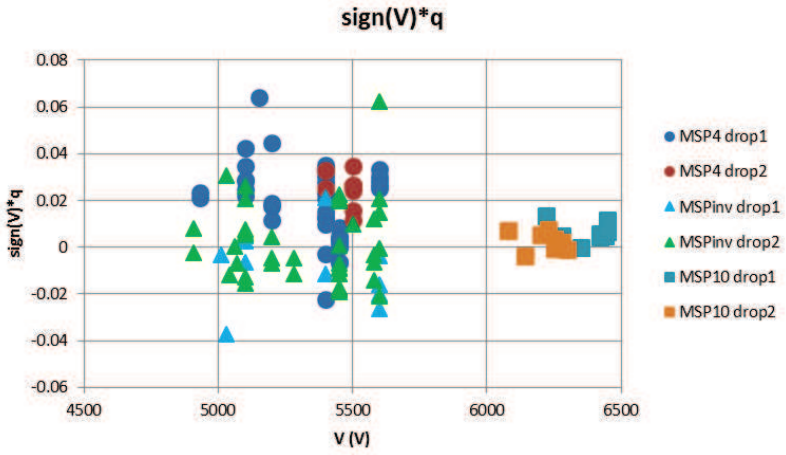

Fig B.40. Charges électriques des gouttelettes mesurées en fonction des types d’impulsion EHD appliqués.

Toutes les valeurs de charge des gouttes mesurées ont été tracés Figure B.40. On voit que pour l’impulsion MSP4 qui est une impulsion d’une seule polarité, les signes de charge correspondent à la polarité de l’impulsion. MSPinv est une impulsion dont la polarité est inversée à mi-impulsion, et les signes de charge varient. MSP10 est une impulsion alternée, et les charges sont bien plus petites que dans les deux cas précédents.

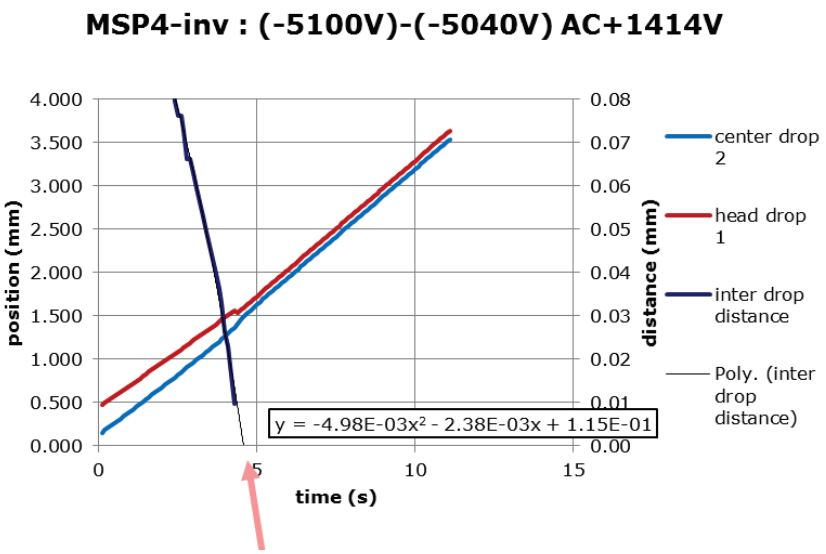

Fig B.41. Exemple de calcul des vitesses et accélérations des gouttes juste avant contact.

La figure B.41 montre que la distance entre les deux gouttes peut être décrite avant le contact par une équation polynomiale d'ordre 2 en temps. En se basant sur cette équation, on peut déduire la vitesse et l'accélération du mouvement de rapprochement des gouttes juste avant contact.

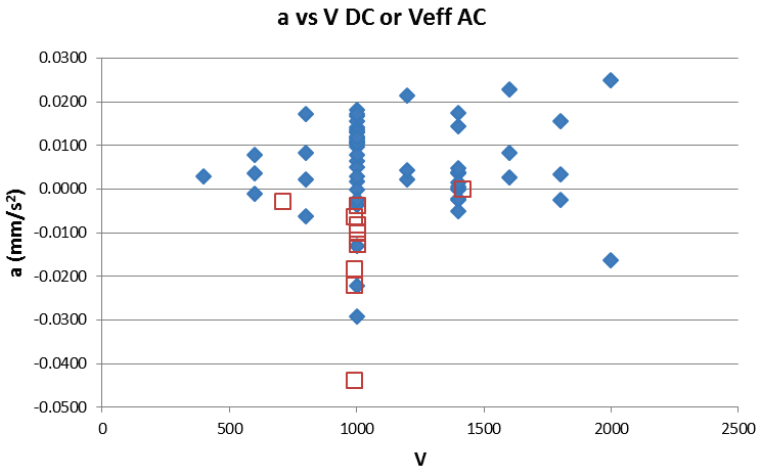

Fig B.42. Accélération en fonction de tension appliquée.

On note en particulier Figure B.42 que les accélérations sous champ continu sont centrées sur les valeurs positives alors qu'elles sont centrées sur les valeurs négatives sous champ alternatif. Cette différence illustre l'influence du champ continu sur les gouttes en raison de leur charge électrique.

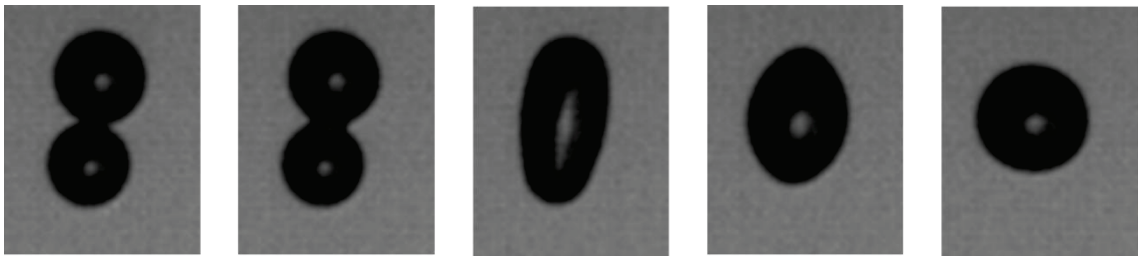

Fig B.43. Séquence de photos de l'électrocoalescence d'une paire de gouttelettes de diamètre environ 150 µm, tirées d'une vidéo rapide (8000 images/s).

Pour analyser plus en détail l'électrocoalescence des gouttelettes une vidéo par caméra rapide à 8000 images/s avec une résolution spatiale de 250x200 pixels est utilisée. La figure B.43 en présente une suite de photos successives, séparées de 125 µs. L'incertitude liée à la résolution spatiale correspond à la taille d'un pixel soit 10 µm. Une méthode de traitement d'image sub-pixel sera donc nécessaire pour obtenir des informations plus précises.

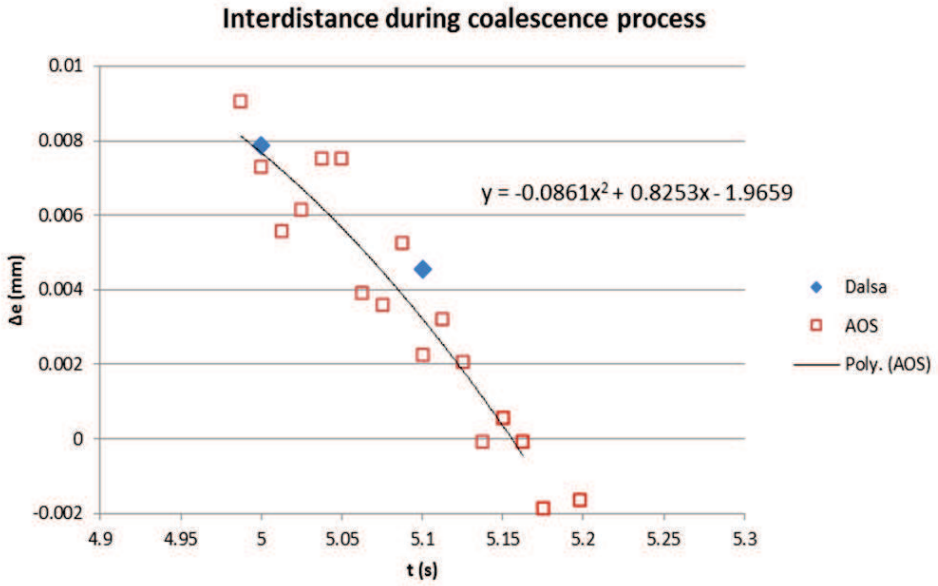

Fig B.44. Distance entre les deux gouttes en fonction du temps durant la phase d'électrocoalescence.

Figure B.44 les points rouges sont obtenus par caméra rapide, alors que les points bleus sont obtenus par caméra Dalsa (CMOS) à la cadence de 10 images par seconde. Les points rouges montrent des fluctuations aléatoires à cause de l'incertitude, mais cette dispersion est plus petite que l'incertitude de ±1 pixel.

La figure B.45 illustre les résultats des simulations faites avec le logiciel COMSOL Multiphysics par (Reboud, 2016).

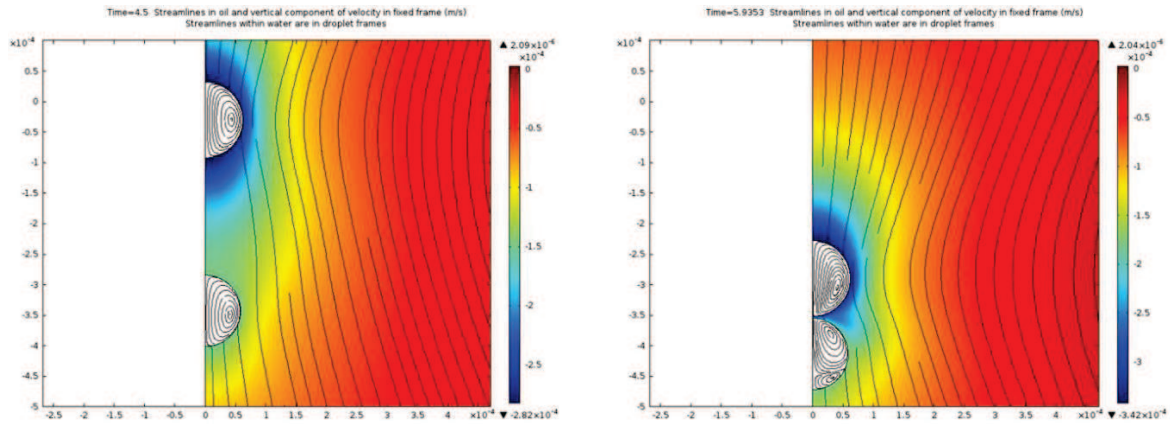

Fig B.45. Chute et contact de deux gouttelettes sous champ électrique (simulation COMSOL Multiphysics).

Les simulations sont basées sur l'hypothèse que les gouttes sont déformables mais sans glissement à l'interface. Les équations de Navier-Stockes sont appliquées dans l'eau et l'huile, le champ électrique est calculé dans l'huile isolante pour pouvoir appliquer la pression électrostatique à l'interface des gouttes d'eau salée, considérée comme un conducteur parfait. Le calcul transitoire en maillage déformable avec remaillage automatique, se poursuit jusqu'au contact des gouttes.

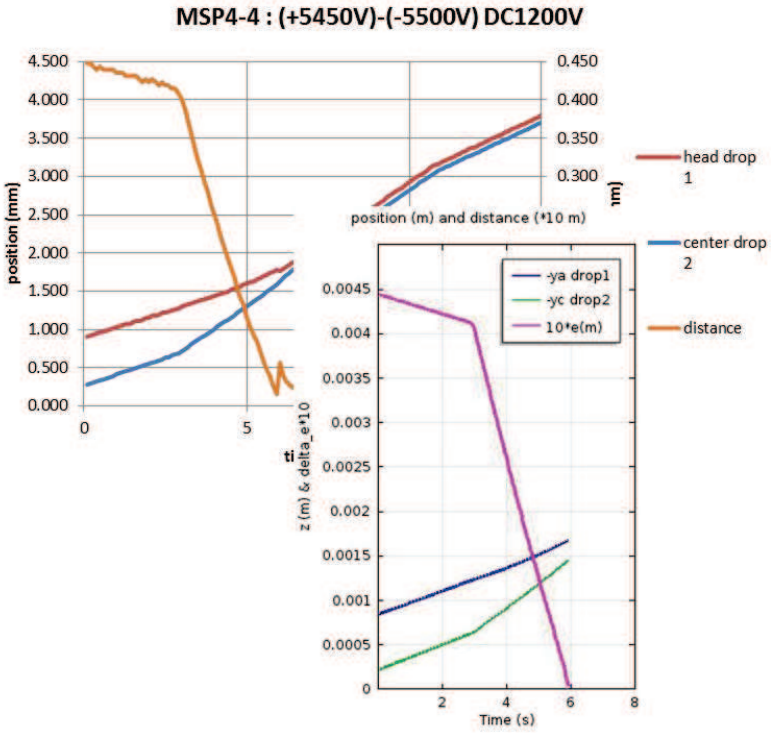

a)

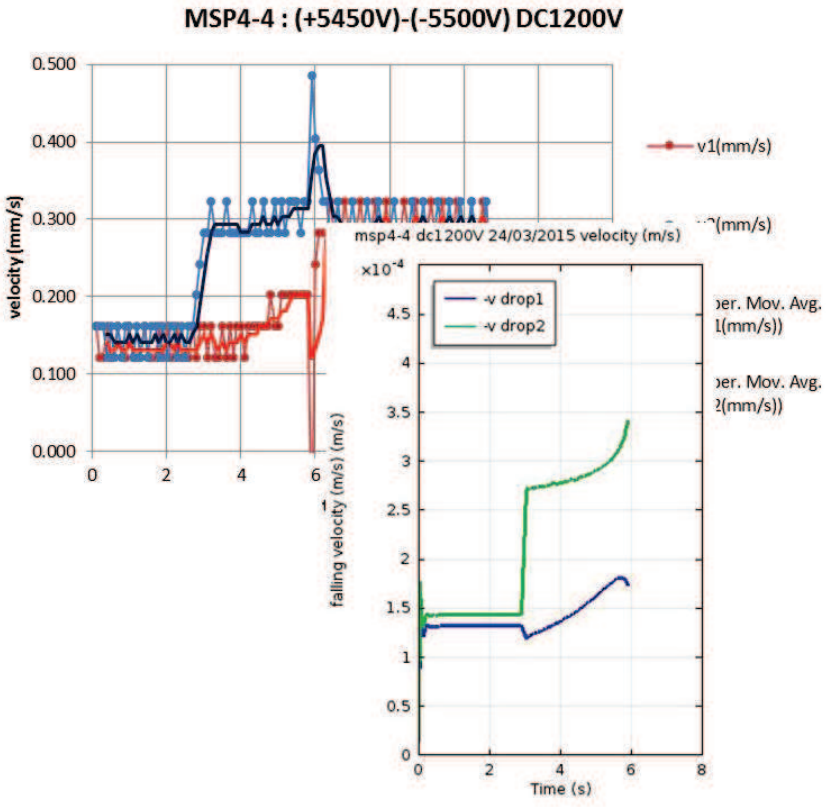

b)

Fig B.46. Comparaison des résultats de simulation avec les résultats expérimentaux. a) comparaison de position et distance des gouttes. b) comparaison de vitesse des gouttes.

On voit que les simulations sont en bon accord avec les résultats expérimentaux, en position et en vitesse.

Quelques expériences préliminaires supplémentaires ont été faites en appliquant le champ électrique lorsque la paire de gouttelettes est passée par l'orifice percé dans l'électrode haute tension et entre dans la région située entre cette électrode et le fond de la cuve. Dans cette région le champ électrique est plus uniforme. Le schéma est illustré Figure B.47.

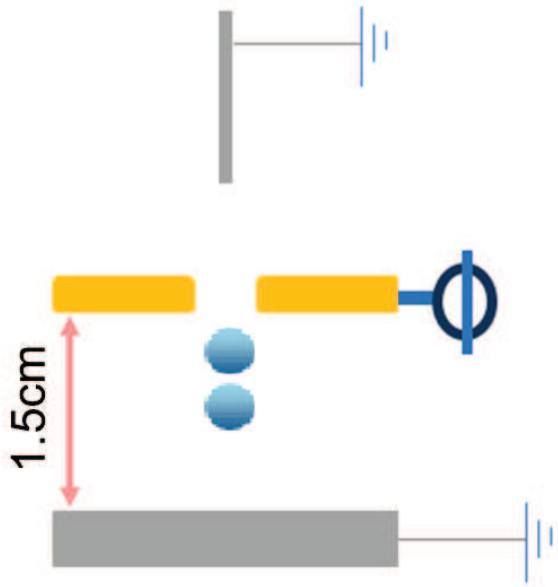

Fig B.47. Schéma de la cellule pour les expériences supplémentaires.

La réalisation d'expériences dans cette région rend très difficile de contrôler la distance des deux gouttes, leur alignement vertical et le moment de coalescence.

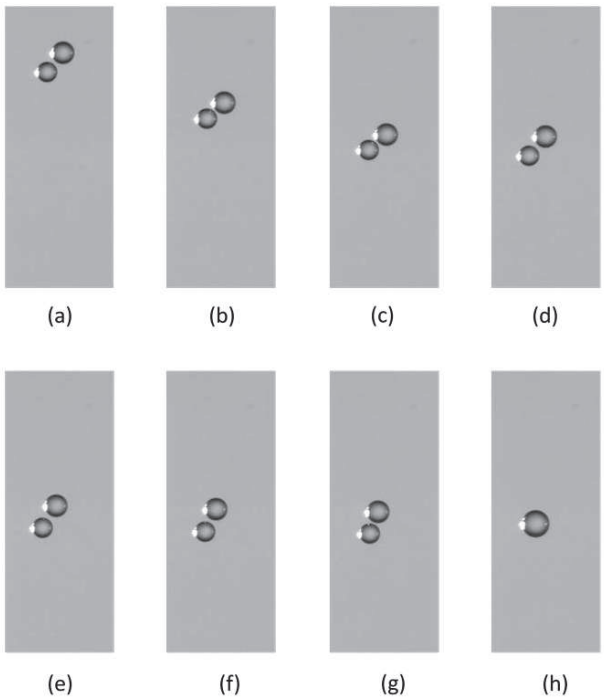

Fig B.48. Electrocoalescence des deux gouttes dans la région comprise entre l'électrode haute tension et le fond de la cuve. On constate que l'alignement vertical n'a pas pu être assuré pour cet essai.

B.5 Conclusion

Dans cette thèse on a cherché à produire une base de données expérimentales sur l'électrocoalescence de paires de très petites gouttelettes tombant dans une cuve d'huile stagnante en configuration axisymétrique. On a pour cela dans un premier temps amélioré une méthode d'injection EHD pour obtenir des très petites gouttes (20-200 microns) dans des conditions de forte tension interfaciale eau/huile. On a appliqué cette méthode pour parvenir à l'injection d'une paire de gouttelettes depuis la même aiguille. Grace à la prise en compte des interactions hydrodynamiques et électrostatiques on a pu caractériser précisément les propriétés de la paire de goutte (taille/charge électrique). On a ainsi généré une première base de données de 70 cas pour comparaison à des simulations numérique.

Pour le futur, l'analyse des résultats obtenus nous permet de suggérer des pistes d'améliorations :

- réduire l'incertitude liée à la température sur la viscosité et la masse volumique.
- mieux contrôler la tension interfaciale en fixant la durée entre deux éjections de goutte.
- réduire l'incertitude sur le diamètre de goutte et la vitesse par un traitement d'images amélioré (sub-pixel).
- réaliser les expériences de coalescence dans la région située entre l'électrode haute tension et le fond de la cuve, où le champ électrique est plus uniforme.
- appliquer de préférence un champ alternatif et générer les gouttes en utilisant l'impulsion alternée (MSP10) pour réduire la charge des gouttelettes et les effets qui y sont associés.

Bibliography

Abid, S. & Chesters, A.K., 1994. The drainage and rupture of partially-mobile films between colliding drops at constant approach velocity. *International Journal of Multiphase Flow*, 20(3), pp.613–629.

Adam, J.R., Lindblad, N.R. & Hendricks, C.D., 1968. The Collision, Coalescence, and Disruption of Water Droplets. *Journal of Applied Physics*, 39(11), pp.5173–5180.

Aichele, C.P., Flaum, M., Jiang, T., Hirasaki, G.J. & Chapman, W.G., 2007. Water in oil emulsion droplet size characterization using a pulsed field gradient with diffusion editing (PFG-DE) NMR technique. *Journal of Colloid and Interface Science*, 315(2), pp.607–619.

Amirzadeh, A. & Chandra, S., 2010a. Small droplet formation in a pneumatic drop-on-demand generator: Experiments and analysis. *Experimental Thermal and Fluid Science*, 34(8), pp.1488–1497.

Amirzadeh, A. & Chandra, S., 2010b. Small droplet formation in a pneumatic drop-on-demand generator: Experiments and analysis. *Experimental Thermal and Fluid Science*, 34(8), pp.1488–1497.

Anon, BEM Research -- Droplets. Available at: https://engineering.purdue.edu/~heister/weber.html [Accessed July 11, 2015a].

Anon, Compact Separation by Electrocoalescence. *SINTEF*. Available at: https://www.sintef.no/en/projects/compact-separation-by-electrocoalescence-/ [Accessed December 20, 2015b].

Anon, 2015a. Drop Shape Analyzer DSA30. Available at: http://www.kruss.de/products/contact-angle/dsa30/drop-shape-analyzer-dsa30/ [Accessed October 30, 2015].

Anon, Fossil Fuel Formation: Oil and Natural Gas. *Green Planet Solar Energy*. Available at: http://www.green-planet-solar-energy.com/fossil-fuel-formation.html [Accessed December 19, 2015c].

Anon, Oil & Gas Solutions: Specialty Silicones - Antifoams for Oil Production and Processing - Dow Corning. Available at: http://www.dowcorning.com/content/oilgas/antifoams.aspx [Accessed January 5, 2016d].

Anon, 2015b. Pendant drop. Available at: http://www.kruss.de/services/education-theory/glossary/pendant-drop/ [Accessed October 30, 2015].

Anon, Primol 352. Available at: http://www.exxonmobil.com/Denmark-English/Specialties/PDS/GLXXENSPCEMPrimol_352.aspx [Accessed July 6, 2015e].

Anon, Primol 352. Available at: http://www.exxonmobil.com/Denmark-English/Specialties/PDS/GLXXENSPCEMPrimol_352.aspx [Accessed November 12, 2015f].

Anon, Seawater. Available at: http://hyperphysics.phy-astr.gsu.edu/hbase/chemical/seawater.html [Accessed December 26, 2015g].

Anon, TREK Model 20/20C High-Voltage Power Amplifier. Available at: http://www.trekinc.com/products/20-20C.asp [Accessed October 27, 2015h].

Arnold, R. et al., 2004. *Managing Water - From Waste to Resource*,

Arrondo, J.L.R. & Alonso, A., 2007. *Advanced Techniques in Biophysics*, Springer Science & Business Media.

Aryafar, H. & Kavehpour, H.P., 2006. Drop coalescence through planar surfaces. *Physics of Fluids (1994-present)*, 18(7), p.72105.

Aryafar, H. & Kavehpour, H.P., 2009. Electrocoalescence: Effects of DC Electric Fields on Coalescence of Drops at Planar Interfaces. *Langmuir*, 25(21), pp.12460–12465.

Atten, P., 1993. Electrocoalescence of water droplets in an insulating liquid. *Journal of Electrostatics*, 30, pp.259–269.

Bailes, P.J. & Stitt, E.H., 1987. Column liquid contacting with vigorous agitation balanced by electrostatic coalescence. I: Intensified coalescence-redispersion. *Chemical engineering research & design*, 65(6), pp.514–523.

Bailles, P.J. & Larkai, S.K., 1981. An experimental investigation into the use of high voltage D.C. fields for liquid phase separation. *Chemical Engineering Research and Design*.

Balson, T. & Britain, R.S. of C. (Great, 2002. *Chemistry in the Oil Industry VII: Performance in a Challenging Environment*, Royal Society of Chemistry.

Basi, S., Hunsche, M., Damerow, L., Lammers, P.S. & Noga, G., 2012. Evaluation of a pneumatic drop-on-demand generator for application of agrochemical solutions. *Crop Protection*, 40, pp.121–125.

Batchelor, G.K., 1982. Sedimentation in a dilute polydisperse system of interacting spheres. Part 1. General theory. *Journal of Fluid Mechanics*, 119, pp.379–408.

Bell, S., 2001. *A Beginner's Guide to Uncertainty of Measurement*, NPL.

Benmekhbi, M., Simon, S. & Sjöblom, J., 2014. Dynamic and Rheological Properties of Span 80 at Liquid–Liquid Interfaces. *Journal of Dispersion Science and Technology*, 35(6), pp.765–776.

Benselama, A.M., Pham, P. & Atten, P., 2006. Calcul de la force diélectrophorétique dans les microsystèmes biologiques: comparaison du modèle dipolaire avec le modèle du tenseur de Maxwell. *Journal of Electrostatics*, 64(7–9), pp.437–444.

Bird, J.C., Ristenpart, W.D., Belmonte, A. & Stone, H.A., 2009. Critical Angle for Electrically Driven Coalescence of Two Conical Droplets. *Physical Review Letters*, 103(16), p.164502.

Bjørklund, E., 2009. The level-set method applied to droplet dynamics in the presence of an electric field. *Computers & Fluids*, 38(2), pp.358–369.

Bogy, D.B. & Talke, F.E., 1984. Experimental and Theoretical Study of Wave Propagation Phenomena in Drop-on-Demand Ink Jet Devices. *IBM Journal of Research and Development*, 28(3), pp.314–321.

Borges, G.R., Farias, G.B., Braz, T.M., Santos, L.M., Amaral, M.J., Fortuny, M., Franceschi, E., Dariva, C. & Santos, A.F., 2015. Use of near infrared for evaluation of droplet size distribution and water content in water-in-crude oil emulsions in pressurized pipeline. *Fuel*, 147, pp.43–52.

Brazier-Smith, P.R., Jennings, S.G. & Latham, J., 1972. The Interaction of Falling Water Drops: Coalescence. *Proceedings of the Royal Society of London A: Mathematical, Physical and Engineering Sciences*, 326(1566), pp.393–408.

Brenn, G. & Kolobaric, V., 2006. Satellite droplet formation by unstable binary drop collisions. *Physics of Fluids (1994-present)*, 18(8), p.87101.

Brennen, C.E., 2005. *Fundamentals of Multiphase Flow*, Cambridge University Press.

Chabert, M., Dorfman, K.D. & Viovy, J.-L., 2005. Droplet fusion by alternating current (AC) field electrocoalescence in microchannels. *ELECTROPHORESIS*, 26(19), pp.3706–3715.

Charles, G.E. & Mason, S.G., 1960. The mechanism of partial coalescence of liquid drops at liquid/liquid interfaces. *Journal of Colloid Science*, 15(2), pp.105–122.

Chen, A.U. & Basaran, O.A., 2002. A new method for significantly reducing drop radius without reducing nozzle radius in drop-on-demand drop production. *Physics of Fluids (1994-present)*, 14(1), pp.L1–L4.

Chen, D., Cardinaels, R. & Moldenaers, P., 2009. Effect of Confinement on Droplet Coalescence in Shear Flow. *Langmuir*, 25(22), pp.12885–12893.

Chen, P.-H., Chen, W.-C. & Chang, S.-H., 1997. Bubble growth and ink ejection process of a thermal ink jet printhead. *International Journal of Mechanical Sciences*, 39(6), pp.683–695.

Chen, T.Y., Mohammed, R.A., Bailey, A.I., Luckham, P.F. & Taylor, S.E., 1994. Dewatering of crude oil emulsions 4. Emulsion resolution by the application of an electric field. *Colloids and Surfaces A: Physicochemical and Engineering Aspects*, 83(3), pp.273–284.

Cheng, S.X., Li, T. & Chandra, S., 2005. Producing molten metal droplets with a pneumatic droplet-on-demand generator. *Journal of Materials Processing Technology*, 159(3), pp.295–302.

Chesters, A.K., 1975. The applicability of dynamic-similarity criteria to isothermal, liquid-gas, two-phase flows without mass transfer. *International Journal of Multiphase Flow*, 2(2), pp.191–212.

Chesters, A.K., 1991. The modelling of coalescence processes in fluid-liquid dispersions : a review of current understanding. *Chemical engineering research & design*, 69(A4), pp.259–270.

Chiesa, M., Ingebrigtsen, S., Melheim, J.A., Hemmingsen, P.V., Hansen, E.B. & Hestad, Ø., 2006. Investigation of the role of viscosity on electrocoalescence of water droplets in oil. *Separation and Purification Technology*, 50(2), pp.267–277.

Chiesa, M., Melheim, J.A., Pedersen, A., Ingebrigtsen, S. & Berg, G., 2005. Forces acting on water droplets falling in oil under the influence of an electric field: numerical predictions versus experimental observations. *European Journal of Mechanics - B/Fluids*, 24(6), pp.717–732.

Clift, R., Grace, J.R. & Weber, M.E., 2005. *Bubbles, Drops, and Particles*, Courier Corporation.

Coelho, R. & Debeau, J., 1971. Properties of the tip-plane configuration. *Journal of Physics D: Applied Physics*, 4(9), p.1266.

Copin-Montégut, G., 2002. Propriétés physique de l'eau de mer.

Cotrell, F.G., 1911. Process for separating and collecting particles of one liquid suspended in another liquid. *US Patent 987*.

Cottrell, F.G. & Speed, J.B., 1911. Separating and collecting particles of one liquid suspended in another liquid. *US Patent 987*.

Dadvand, A., Khoo, B.C. & Shervani-Tabar, M.T., 2008a. A collapsing bubble-induced microinjector: an experimental study. *Experiments in Fluids*, 46(3), pp.419–434.

Dadvand, A., Khoo, B.C. & Shervani-Tabar, M.T., 2008b. A collapsing bubble-induced microinjector: an experimental study. *Experiments in Fluids*, 46(3), pp.419–434.

Davis, M.H., 1964. Two Charged Spherical Conductors in a Uniform Electric Field: Forces and Field Strength. *The Quarterly Journal of Mechanics and Applied Mathematics*, 17(4), pp.499–511.

Dezhi, S., Shik Chung, J., Xiaodong, D. & Ding, Z., 1999. Demulsification of water-in-oil emulsion by wetting coalescence materials in stirred- and packed-columns. *Colloids and Surfaces A: Physicochemical and Engineering Aspects*, 150(1–3), pp.69–75.

Dong, J., Almeida, V.F. de & Tsouris, C., 2002. Effects of Applied Electric Fields on Drop—Interface and Drop—Drop Coalescence. *Journal of Dispersion Science and Technology*, 23(1–3), pp.155–166.

Ellson, R., 2002. Picoliter: enabling precise transfer of nanoliter and picoliter volumes. *Drug Discovery Today*, 7(5), pp.S32–S34.

Eow, J.S. & Ghadiri, M., 2003. Drop–drop coalescence in an electric field: the effects of applied electric field and electrode geometry. *Colloids and Surfaces A: Physicochemical and Engineering Aspects*, 219(1–3), pp.253–279.

Eow, J.S., Ghadiri, M. & Sharif, A.O., 2002. Electrostatic and hydrodynamic separation of aqueous drops in a flowing viscous oil. *Chemical Engineering and Processing: Process Intensification*, 41(8), pp.649–657.

Eow, J.S., Ghadiri, M., Sharif, A.O. & Williams, T.J., 2001. Electrostatic enhancement of coalescence of water droplets in oil: a review of the current understanding. *Chemical Engineering Journal*, 84(3), pp.173–192.

Erik Teigen, K., Song, P., Lowengrub, J. & Voigt, A., 2011. A diffuse-interface method for two-phase flows with soluble surfactants. *Journal of Computational Physics*, 230(2), pp.375–393.

Ervik, A., 2016. *Multiscale modelling using molecular dynamics and interface-capturing methods for two-phase flow simulation of droplets covered with surfactants or asphaltenes, and applications to electrocoalescence*. Trondheim, Norway.

Ervik, Å., Hellesø, S.M., Munkejord, S.T. & Müller, B., 2014. Experimental and computational studies of water drops falling through model oil with surfactant and subjected to an electric field. *arXiv:1405.0911 [physics]*, pp.1–6.

Fahim, M.A., Al-Sahhaf, T. & Elkilani, A.., 2010. *Fundamentals of Petroleum Refining*, Elsevier.

Fakhari, A. & Rahimian, M.H., 2009. Simulation of falling droplet by the lattice Boltzmann method. *Communications in Nonlinear Science and Numerical Simulation*, 14(7), pp.3046–3055.

Fedorchenko, A.I. & Wang, A.-B., 2004. On some common features of drop impact on liquid surfaces. *Physics of Fluids (1994-present)*, 16(5), pp.1349–1365.

Furbank, R.J. & Morris, J.F., 2007. Pendant drop thread dynamics of particle-laden liquids. *International Journal of Multiphase Flow*, 33(4), pp.448–468.

Galvin, C.P., 1986. Design principles for electrical coalescers. In IChemE Symp. pp. 101–113.

Ghazian, O., Adamiak, K. & Castle, G.S.., 2014. Head-on collision of electrically charged droplets. *Journal of Electrostatics*, 73.

Gilet, T. & Bush, J.W.M., 2012. Droplets bouncing on a wet, inclined surface. *Physics of Fluids (1994-present)*, 24(12), p.122103.

Gotaas, C., Havelka, P., Jakobsen, H.A. & Svendsen, H.F., 2007. Evaluation of the impact parameter in droplet-droplet collision experiments by the aliasing method. *Physics of Fluids (1994-present)*, 19(10), p.102105.

Gotaas, C., Havelka, P., Jakobsen, H.A., Svendsen, H.F., Hase, M., Roth, N. & Weigand, B., 2007. Effect of viscosity on droplet-droplet collision outcome: Experimental study and numerical comparison. *Physics of Fluids (1994-present)*, 19(10), p.102106.

Guo, C. & He, L., 2014. Coalescence behaviour of two large water-drops in viscous oil under a DC electric field. *Journal of Electrostatics*, 72(6), pp.470–476.

Hamlin, B.S., Creasey, J.C. & Ristenpart, W.D., 2012. Electrically Tunable Partial Coalescence of Oppositely Charged Drops. *Physical Review Letters*, 109(9), p.94501.

Hamlin, B.S. & Ristenpart, W.D., 2012. Transient reduction of the drag coefficient of charged droplets via the convective reversal of stagnant caps. *Physics of Fluids (1994-present)*, 24(1), p.12101.

Harris, D.M., Liu, T. & Bush, J.W.M., 2015. A low-cost, precise piezoelectric droplet-on-demand generator. *Experiments in Fluids*, 56(4), pp.1–7.

Hazlehurst, T.H. & Neville, H.A., 1937. Liquid Drops on Liquid Surfaces. *The Journal of Physical Chemistry*, 41(9), pp.1205–1214.

Hellesø, S.M., Atten, P., Berg, G. & Lundgaard, L.E., 2015. Experimental study of electrocoalescence of water drops in crude oil using near-infrared camera. *Experiments in Fluids*, 56(6), pp.1–16.

Herodotus, 457AD. *The History*,

Howarth, W.., 1964. Coalescence of drops in a turbulent flow field. *Chemical Engineering Science*. Available at: http://www.sciencedirect.com/science/article/pii/000925096485003X [Accessed March 6, 2015].

Hsiao, M., Lichter, S. & Quintero, L.G., 1988. The critical Weber number for vortex and jet formation for drops impinging on a liquid pool. *Physics of Fluids (1958-1988)*, 31(12), pp.3560–3562.

Ingebrigtsen, S., Berg, G. & Lundgaard, L., 2005. *The Electrocoalescence of two water drops in oil*, SINTEF Energy Research.

Jiang, Y.J., Umemura, A. & Law, C.K., 1992. An experimental investigation on the collision behaviour of hydrocarbon droplets. *Journal of Fluid Mechanics*, 234, pp.171–190.

Jones, T.J., Neustadter, E.L. & Whittingham, K.P., 1978. Water-In-Crude Oil Emulsion Stability And Emulsion Destabilization By Chemical Demulsifiers. *Journal of Canadian Petroleum Technology*, 17.

Jose, B.M. & Cubaud, T., 2011. Droplet arrangement and coalescence in diverging/converging microchannels. *Microfluidics and Nanofluidics*, 12(5), pp.687–696.

Jung, Y.-M. & Kang, I.S., 2009. A novel actuation method of transporting droplets by using electrical charging of droplet in a dielectric fluid. *Biomicrofluidics*, 3(2), p.22402.

Klimin, N.N., Rivkind, V.Y. & Pachin, V.A., 1994. Collision efficiency calculation model as a software tool for microphysics of electrified clouds. *Meteorology and Atmospheric Physics*, 53(1–2), pp.111–120.

Ko, G.H., Ryou, H.S., Hur, N.K., Ko, S.W. & Youn, M.O., 2007. Numerical study on bouncing and separation collision between two droplets considering the collision-induced breakup. *Journal of Mechanical Science and Technology*, 21(4), pp.585–592.

Krause, K.., 1973. Focusing Ink Jet Head.

Lee, E.R., 2002. *Microdrop Generation*, CRC Press.

Lefebvre, A., 1988. *Atomization and Sprays*, CRC Press.

Less, S., H, A. & S, J., 2010. Dehydration Efficiency of Water-in-Crude Oil Emulsions in Alternating Current Electrical Fields. *Journal of Dispersion Science and Technology*, 31(3), pp.265–272.

Less, S. & Vilagines, R., 2013. Light beam reflectance measurement of droplets diameter distribution in crude oil emulsions. *Fuel*, 109, pp.542–550.

Less, S. & Vilagines, R., 2012. The electrocoalescers' technology: Advances, strengths and limitations for crude oil separation. *Journal of Petroleum Science and Engineering*, 81, pp.57–63.

Levan, M.D., 1981. Motion of a droplet with a newtonian interface. *Journal of Colloid and Interface Science*, 83(1), pp.11–17.

Levan, M.D. & Holbrook, J.A., 1989. Motion of a droplet containing surfactant. *Journal of Colloid and Interface Science*.

Lévin, L. & Agneray, A., 1999. Micro-Injection System Using Ultrasonic Vibrations for Drop on Demand Ejection. In D. D. E. Ricken & W. Gessner, eds. *Advanced Microsystems for Automotive Applications 99*. Springer and the environment. Springer Berlin Heidelberg, pp. 87–95. Available at: http://link.springer.com/chapter/10.1007/978-3-662-03838-3_7 [Accessed June 27, 2015].

Li, D. ed., 2008. Ohnesorge Number. In *Encyclopedia of Microfluidics and Nanofluidics*. Springer US, pp. 1513–1513. Available at: http://link.springer.com/referenceworkentry/10.1007/978-0-387-48998-8_1141 [Accessed October 31, 2015].

Lin, Y., Skjetne, P. & Carlson, A., 2012. A phase field model for multiphase electro-hydrodynamic flow. *International Journal of Multiphase Flow*, 45, pp.1–11.

Low, T.B. & List, R., 1982. Collision, Coalescence and Breakup of Raindrops. Part I: Experimentally Established Coalescence Efficiencies and Fragment Size Distributions in Breakup. *Journal of the Atmospheric Sciences*, 39(7), pp.1591–1606.

Lundgaard, L. & Berg, G., 2003. Coalescence efficiency of water drop pairs in oil influenced by electric field. In 4th intervational conference on petroleum phase behaviour and fouling. Trondheim, Norway.

Lundgaard, L.E., Berg, G., Pedersen, A. & Nilsen, P.J., 2002. Electrocoalescence of water drop pairs in oil. In Proceedings of 14th International Conference on Dielelctric Liquids. (ICDL 2002), Graz (Austria).

Mahajan, L.D. & Katalinie, M., 1931. Liquid Drops on the Same Liquid Surface. Available at: http://www.nature.com/nature/journal/v129/n3245/abs/129059a0.html [Accessed February 27, 2015].

Manning, F.S., (Ph.D.), R.E.T. & Thompson, R.E., 1995. *Oilfield Processing of Petroleum: Crude oil*, PennWell Books.

Manzello, S.L. & Yang, J.C., 2002. An experimental study of a water droplet impinging on a liquid surface. *Experiments in Fluids*, 32(5), pp.580–589.

Martin, J.J., Wang, P.K., Pruppacher, H.R. & Pitter, R.L., 1981. A Numerical Study of the Effect of Electric Charges on the Efficiency with which Planar Ice Crystals Collect Supercooled Cloud Drops. *JOURNAL OF THE ATMOSPHERIC SCIENCES*, 38.

McKinley, G.H., 2005. Visco-Elasto-Capillary Thinning and Break-Up of Complex Fluids. Available at: http://dspace.mit.edu/handle/1721.1/18085 [Accessed July 9, 2015].

McKinley, G.H. & Renardy, M., 2011. Wolfgang von Ohnesorge. *Physics of Fluids (1994-present)*, 23(12), p.127101.

Meacham, J.. & Vara, M.., 2005. Droplet formation and ejection from a micromachined ultrasonic droplet generator: Visualization and scaling.

Mem, R.S. & Loomis, A.L., 1927. XXXVIII. The physical and biological effects of high-frequency sound-waves of great intensity. *The London, Edinburgh, and Dublin Philosophical Magazine and Journal of Science*, 4(22), pp.417–436.

Mhatre, S., Vivacqua, V., Ghadiri, M., Abdullah, A.M., Al-Marri, M.J., Hassanpour, A., Hewakandamby, B., Azzopardi, B. & Kermani, B., 2015. Electrostatic phase separation: A review. *Chemical Engineering Research and Design*, 96, pp.177–195.

Milliken, W.J., Stone, H.A. & Leal, L.G., 1993. The effect of surfactant on the transient motion of Newtonian drops. *Physics of Fluids A: Fluid Dynamics (1989-1993)*, 5(1), pp.69–79.

Mohammadi, M., Shahhosseini, S. & Bayat, M., 2012. Direct numerical simulation of water droplet coalescence in the oil. *International Journal of Heat and Fluid Flow*, 36, pp.58–71.

Mohammadi, M., Shahhosseini, S. & Bayat, M., 2014. Electrocoalescence of binary water droplets falling in oil: Experimental study. *Chemical Engineering Research and Design*, 92(11), pp.2694–2704.

Mohammadi, M., Shahhosseini, S. & Bayat, M., 2013. Numerical prediction of the electrical waveform effect on electrocoalescence kinetic. *Chemical Engineering Research and Design*, 91(5), pp.904–918.

Mohammed, R.A., Bailey, A.I., Luckham, P.F. & Taylor, S.E., 1993a. Dewatering of crude oil emulsions 1. Rheological behaviour of the crude oil—water interface. *Colloids and Surfaces A: Physicochemical and Engineering Aspects*, 80(2–3), pp.223–235.

Mohammed, R.A., Bailey, A.I., Luckham, P.F. & Taylor, S.E., 1993b. Dewatering of crude oil emulsions 2. Interfacial properties of the asphaltic constituents of crude oil. *Colloids and Surfaces A: Physicochemical and Engineering Aspects*, 80(2–3), pp.237–242.

Mohammed, R.A., Bailey, A.I., Luckham, P.F. & Taylor, S.E., 1994. Dewatering of crude oil emulsions 3. Emulsion resolution by chemical means. *Colloids and Surfaces A: Physicochemical and Engineering Aspects*, 83(3), pp.261–271.

Mölders, N. & Kramm, G., 2014. *Lectures in Meteorology*, Springer.

Moradi, M., Alvarado, V. & Huzurbazar, S., 2011. Effect of Salinity on Water-in-Crude Oil Emulsion: Evaluation through Drop-Size Distribution Proxy. *Energy & Fuels*, 25(1), pp.260–268.

Mordy, W.A., 1959. Differences in Coalescence Tendencies in Computed Condensation Cloud Droplet Spectra. In *Proceedings of the cloud physics conference*. Physics of precipitation. Woods Hole, Massachusetts: American Geophysical Union.

Mousavi, S.H., Ghadiri, M. & Buckley, M., 2014. Electro-coalescence of water drops in oils under pulsatile electric fields. *Chemical Engineering Science*, 120, pp.130–142.

Mousavichoubeh, M., Ghadiri, M. & Shariaty-Niassar, M., 2011. Electro-coalescence of an aqueous droplet at an oil–water interface. *Chemical Engineering and Processing: Process Intensification*, 50(3), pp.338–344.

Mundo, C., Sommerfeld, M. & Tropea, C., 1995. Droplet-wall collisions: Experimental studies of the deformation and breakup process. *International Journal of Multiphase Flow*, 21(2), pp.151–173.

Nisisako, T., Torii, T. & Higuchi, T., 2002. Droplet formation in a microchannel network. *Lab on a Chip*, 2(1), pp.24–26.

Pan, Y. & Suga, K., 2005. Numerical simulation of binary liquid droplet collision. *Physics of Fluids (1994-present)*, 17(8), p.82105.

Pawar, Y. & Stebe, K.J., 1996. Marangoni effects on drop deformation in an extensional flow: The role of surfactant physical chemistry. I. Insoluble surfactants. *Physics of Fluids (1994-present)*, 8(7), pp.1738–1751.

Pearce, C.A.R., 1954. The mechanism of the resolution of water-in-oil emulsions by electrical treatment. *British Journal of Applied Physics*, 5(4), p.136.

Pedersen, A., 2008. *Forces Acting on Water Droplets in Electrically Energized Oil Emulsions*. Trondheim, Norway: Norweigian University of Science and Technology.

Pedersen, A., Ildstad, E. & Nysveen, A., 2004. Forces and movement of water droplets in oil caused by applied electric field. In 2004 Annual Report Conference on Electrical Insulation and Dielectric Phenomena.

Pilch, M. & Erdman, C.A., 1987. Use of breakup time data and velocity history data to predict the maximum size of stable fragments for acceleration-induced breakup of a liquid drop. *International Journal of Multiphase Flow*, 13(6), pp.741–757.

Priest, C., Herminghaus, S. & Seemann, R., 2006. Controlled electrocoalescence in microfluidics: Targeting a single lamella. *Applied Physics Letters*, 89(13), p.134101.

Qian, J. & Law, C.K., 1997. Regimes of coalescence and separation in droplet collision. *Journal of Fluid Mechanics*, null, pp.59–80.

Rabe, C., Malet, J. & Feuillebois, F., 2010. Experimental investigation of water droplet binary collisions and description of outcomes with a symmetric Weber number. *Physics of Fluids (1994-present)*, 22(4), p.47101.

Rahman, K., Khan, A., Nam, N.M., Choi, K.H. & Kim, D.-S., 2011. Study of drop-on-demand printing through multi-step pulse voltage. *International Journal of Precision Engineering and Manufacturing*, 12(4), pp.663–669.

Raisin, J., 2011. *Electrocoalescence in Water-in-Oil Emulsions: Toward an Efficiency Criterion*. Universite de Grenoble.

Raisin, J., Atten, P. & Reboud, J.-L., 2013. A novel actuation technique for the on-demand injection of charge-free conducting droplets in a viscous dielectric liquid. *Experiments in Fluids*, 54(3), pp.1–14.

Rayleigh, L., 1882. *Further Observations upon Liquid Jets, in Continuation of Those Recorded in the Royal Society's "Proceedings" for March and May, 1879*, Royal Society of London. Available at: http://archive.org/details/philtrans03401853 [Accessed February 26, 2015].

Ristenpart, W.D., Bird, J.C., Belmonte, A., Dollar, F. & Stone, H.A., 2009. Non-coalescence of oppositely charged drops. *Nature*, 461(7262), pp.377–380.

Rodionova, G., Pettersen, B., Kelesoğlu, S. & Sjöblom, J., 2014. Preparation and characterization of reference fluid mimicking behavior of North Sea heavy crude oil. *Fuel*, 135, pp.308–314.

Sartor, D., 1954. A laboratory investigation of collision efficiencies, coalescence and electrical charging simulated cloud droplets. *Journal of Meteorology*, 11(2), pp.91–103.

Schramm, L., 1992. *Petroleum Emulsions Basic Principles*, Petroleum Recovery Institute.

Shafrir, U. & Gal-Chen, T., 1971. A Numerical Study of Collision Efficiencies and Coalescence Parameters for Droplet Paris with Radii up to 300 Microns. *JOURNAL OF THE ATMOSPHERIC SCIENCES*, 28.

Shardt, O., Derksen, J.J. & Mitra, S.K., 2013. Simulations of Droplet Coalescence in Simple Shear Flow. *Langmuir*, 29(21), pp.6201–6212.

Shardt, O., Mitra, S.K. & Derksen, J.J., 2014. The Critical Conditions for Coalescence in Phase Field Simulations of Colliding Droplets in Shear. *Langmuir*, 30(48), pp.14416–14426.

Shinnar, R. & Church, J.M., 1960. Statistical Theories of Turbulence in Predicting Particle Size in Agitated Dispersions. *Industrial & Engineering Chemistry*, 52(3), pp.253–256.

Silset, A., 2008. *Emulsions (w/o and o/w) of heavy Crude Oil. Characterization, Stabilization, Destabilization and Produced Water Quality.* Trondheim, Norway: Norweigian University.

Simanzhenkov, V. & Idem, R., 2003. *Crude Oil Chemistry*, CRC Press.

Speight, J.G., 2015. *Handbook of Petroleum Product Analysis*, John Wiley & Sons.

Speight, J.G., 2014. *The Chemistry and Technology of Petroleum, Fifth Edition*, CRC Press.

Srivastava, R.C., 1967. On the Role of Coalescence between Raindrops in Shaping Their Size Distribution1. *Journal of Atmospheric Sciences*, 24, pp.287–292.

von Szyszkowski, B., 1908. Experimentelle Studien über kapillare Eigenschaften der wasserigen Losungen von Fettsauren. *Zeitschrift für Physikalische Chemie*, 64, pp.385–414.

Tan, Y.-C., Ho, Y.L. & Lee, A.P., 2006. Droplet coalescence by geometrically mediated flow in microfluidic channels. *Microfluidics and Nanofluidics*, 3(4), pp.495–499.

Tang, C., Zhang, P. & Law, C.K., 2012. Bouncing, coalescence, and separation in head-on collision of unequal-size droplets. *Physics of Fluids (1994-present)*, 24(2), p.22101.

Taylor, G., 1964. Disintegration of Water Drops in an Electric Field. *Proceedings of the Royal Society of London A: Mathematical, Physical and Engineering Sciences*, 280(1382), pp.383–397.

Taylor, G. & Spenser, E., 1988. Investigations into the electrical and coalescence behaviour of water-in-crude oil emulsions in high voltage gradients. *Colloids and Surfaces*, 29(1), pp.29–51.

Teigen, K.E. & Munkejord, S.T., 2010. Influence of surfactant on drop deformation in an electric field. *Physics of Fluids (1994-present)*, 22(11), p.112104.

Thompson, D.G., Taylor, A.S. & Graham, D.E., 1985. Emulsification and demulsification related to crude oil production. *Colloids and Surfaces*, 15, pp.175–189.

Tissot, B.P. & Welte, D.H., 2013. *Petroleum Formation and Occurrence*, Springer Science & Business Media.

Tjahjadi, M., Stone, H.A. & Ottino, J.M., 1992. Satellite and subsatellite formation in capillary breakup. *Journal of Fluid Mechanics*, 243, pp.297–317.

Trujillo-Pino, A., Krissian, K., Alemán-Flores, M. & Santana-Cedrés, D., 2013. Accurate subpixel edge location based on partial area effect. *Image and Vision Computing*, 31(1), pp.72–90.

Vandewalle, N., Terwagne, D., Mulleners, K., Gilet, T. & Dorbolo, S., 2006. Dancing droplets onto liquid surfaces. *Physics of Fluids (1994-present)*, 18(9), p.91106.

Vicent, L., Duchemin, L., Le Dizes, S. & Villermaux, E., 2013. Dynamique de ligaments fortement étirés. In 21 Congrès Français de Mécanique. Bordeaux.

Wright, G.S., Krein, P.T. & Chato, J.C., 1995. Self-consistent modeling of the electrohydrodynamics of a conductive meniscus. *IEEE Transactions on Industry Applications*, 31(4), pp.768–777.

Zhang, Y., Liu, Y., Ji, R., Cai, B., Wang, F. & Liu, R., 2012. Discussion of the Drop Rest Phenomenon at Millimeter Scale and Coalescence of Droplets at Micrometer Scale. *Journal of Dispersion Science and Technology*, 33(12), pp.1700–1707.

Abstract

When electric fields are applied in oil-water mixtures small water droplets are attracted to others and merge in larger drops. This electrocoalescence process makes more efficient the oil-water separation by sedimentation. Experimental data on the electrocoalescence of very small droplets will be useful to improve the understanding of the dynamics of water-oil interface and to validate numerical models. The simple studied configuration consists in a small droplet pair falling in stagnant model oil, under electric field aligned with their symmetry axis.
First part of the work consisted in the well-controlled generation of very small droplet pair (range 20-200 micrometers). Droplet-on-Demand generation by EHD method was improved for a better control of the diameter and electric charge of droplets injected from a single metallic needle. This was obtained by applying to a pendant water meniscus optimized multistage high voltage electric pulses.
Then, electrical and hydrodynamic characterization of the droplet pairs and their coalescence are mainly deduced from the analysis of falling velocities, with and without applied DC electric field. A complete data set of droplet position and velocity is deduced from video. A special attention was paid to the visualizations of very small droplet and small falling velocities, involving multiple angles of view, strong zooming and high speed video.
Modelling the different terms of hydrodynamic and electrostatic interactions between droplets allows deducing, from the recorded velocities, their respective mass and electric charge. When coalescence occurs, a record of the resulting single droplet velocity, with and without applied voltage, allows controlling the mass and charge conservations and validating the method.
A first data set of about 70 different cases, taking into account the variation of droplets pair diameter and different applied voltage types (DC or AC), was established. Analyses of the results and experimental uncertainties, and example of possible comparison with numerical simulations using Comsol Multiphysics™ software, allow performing some recommendations for future work.

Résumé

Lorsque des champs électriques sont appliqués à des mélanges eau-huile, les petites gouttelettes d'eau sont attirées entre elles et se regroupent en gouttes plus grosses. Ce processus d'électrocoalescence rend plus efficace la séparation huile-eau par sédimentation. Des données expérimentales sur l'électrocoalescence de très petites gouttelettes sont nécessaires pour améliorer la compréhension de la dynamique de l'interface eau-huile et pour valider les modèles numériques. La configuration simple étudiée dans ce travail de thèse concerne une petite paire de gouttelettes tombant dans une cuve d'huile modèle et soumise à un champ électrique aligné avec leur axe de symétrie.
La première partie du travail a consisté à générer de façon contrôlée une paire de très petites gouttelettes (dans la gamme de diamètres 20-200 microns). La génération de goutte à la demande, par méthode électrohydrodynamique (EHD), a été améliorée pour un meilleur contrôle du diamètre et de la charge électrique des gouttelettes injectées à partir d'une aiguille métallique unique. Ceci a été obtenu en appliquant à un ménisque d'eau pendant à l'extrémité de l'aiguille des impulsions électriques de forme optimisée.
La caractérisation électrique et hydrodynamique des paires de gouttelettes et leur coalescence sont alors principalement déduites de l'analyse des vitesses de chute, avec et sans application d'un champ électrique à courant continu. Des données complètes de positions des gouttelettes et de leur vitesse en fonction du temps sont déduites de prises de vues vidéo. Une attention particulière a été accordée aux visualisations de très petites gouttelettes tombant à petites vitesses, associant des angles multiples de prise de vue, de forts zooms et des vidéos à grande vitesse.
La modélisation des différents termes d'interactions hydrodynamiques et électrostatiques entre les gouttelettes permet de déduire des vitesses enregistrées leur masse charge électrique respectives. Quand se produit une coalescence des deux gouttelettes, un enregistrement de la vitesse de la gouttelette résultante, avec et sans tension électrique appliquée, permet de contrôler la conservation de la masse et de la charge électrique, et la validation du procédé.
Un premier ensemble de données est constitué d'environ 70 cas différents, avec différentes paire de gouttelettes et en faisant varier la tension appliquée à courant continu ou alternatif. L'analyse des résultats et des incertitudes expérimentales et un exemple de comparaison possible avec des simulations numériques utilisant le logiciel Comsol Multiphysics ™, permettent d'effectuer des recommandations pour les travaux futurs.